Dissertation zur Erlangung des Doktorgrades

der Fakultät für Chemie und Pharmazie

der Ludwig-Maximilians-Universität München

INVESTIGATIONS ON THE STRUCTURE, EXFOLIATION BEHAVIOR AND ELECTRONIC PROPERTIES OF LAYERED TIN SULFIDES

Tanja Holzmann

aus

Lauingen (Donau), Deutschland

2016

Erklärung

Diese Dissertation wurde im Sinne von § 7 der Promotionsordnung vom 28. November 2011 von Frau Prof. Dr. Bettina V. Lotsch betreut.

Eidesstattliche Versicherung

Diese Dissertation wurde eigenständig und ohne unerlaubte Hilfe erarbeitet.

München, 15.12.2016

……………………………………………

(Tanja Holzmann)

Dissertation eingereicht am 20.12.2016

1. Gutachter:	Prof. Dr. Bettina V. Lotsch
2. Gutachter:	Prof. Dr. Christina Scheu
Mündliche Prüfung am	16.02.2017

It doesn’t matter how beautiful your theory is, it doesn’t matter how smart you are.
If it doesn’t agree with experiment, it is wrong.

— Richard P. Feynman

ACKNOWLEDGEMENTS

First, I would like to thank Prof. Dr. Bettina V. Lotsch for giving me the opportunity to do my PhD thesis in your kind research group. Throughout my entire work, I appreciated the freedom in research and your extraordinary expertise which was always inspiring and helpful for any kind of scientific problems.

Further, I want to thank Prof. Scheu for being my second reviewer and Prof. Schnick, Prof. Karaghiosoff, Prof. Johrendt and Prof. Kornath for being available as examiners in my PhD defense.

I especially want to thank my two day-to-day supervisors Dr. Alexander Kuhn and Dr. Leslie Schoop. Both of you are outstanding scientists full of motivation and passion for research. I am glad that I got the chance to work with you – I really learned a lot during this time!

I also want to thank my collaboration partners:

- Dr. Ute Zschieschang and Dr. Hagen Klauk for our collaboration on building transistors out of SnS_2. My project with your group was one of my favorites, as you both have so pleasant personalities and your motivation was always infectious. Also the “speed” with which Ute is contacting crystals is simply not to beat!
- Dr. Giuliano Gregori for the help with electrical measurements on my many samples. Although everything seemed to be “komisch” or “nicht ohmisch” in the beginning, your cheerful personality and your know-how made it way easier to clear all hurdles. Many thanks also to Dr. Robert Usiskin and Prof. Joachim Maier for the help with interpreting my electrochemical measurements and the assistance for my papers.
- Dr. Igor Moudrakovski for a whole bunch of ssNMR measurements. I appreciated your friendly manner, your exceptional expertise and your help in interpreting all of our (sometimes really confusing) data.

I further want to thank Dr. Marko Burkhardt for being my second internal supervisor at the Max Planck Institute for Solid State Research.

I want to thank my students Mazheva Giullevic, Marie Däntl and Anna-Katharina Hatz for their hard and self-sufficent work.

For further support I want to thank the *Chemical Service Group* and Christine Stefani from the *X-ray Diffraction Service Group.*

I also want to express my gratitude to our technicians. Vio, thanks for all the TEM and SEM measurements and of course thanks for just being you. With your calm and relaxed manner you always prevented us from freaking out. Willi, thanks for the help with all of my "engineering problems" and also for the assistance in taking care of our gloveboxes. Marie-Luise, thanks for the many ICP analyses and the kind support whenever I was starting an almost-organic wet-chemistry experiment. Roland, thanks for your scientific support and for cheering me up whenever I was sad or frustrated – I hope you can enjoy your retirement now although you would prefer to work in the lab forever. Finally, Claudia, thanks for being our "group mama". You are such an adorable person so please stay just as you are and be lenient towards us and every following PhD student whenever we (again) destroy your order!

I sincerely want to thank the people who were cheering up my daily life – the Lotsch group. I had a great time with all of you (inside and outside of the institute) and I am glad that I was allowed to do my PhD thesis in such a friendly group. Vincent, thanks for proof-reading all of my stuff and for every activity in- and outside the institute…there's nothing more to say than "meow". Katha, you were an awesome office neighbour and I had a really fun time with you. Thanks for every coffee break and every scientific or non-scientific discussion. You always helped me to see the bright side of life! I also want to thank our former Master's student Chrissi: I am grateful for the day you walked into our office with your ridiculously large suitcase. I really enjoyed the time we three had together and I will never forget our girl's dinners at *Il Pomodoro*, our gossip coffee sessions, etc. I have no idea how I would have been able to survive my PhD without you!

I also want to express my gratitude to my sister Carina for her day-to-day support *via* whatsapp, my parents for spoiling me with delicious food whenever I went home and, of course, my friends in Wertingen and Munich for the great time we had together – I'm glad that we are still friends although my education tried to keep me at bay all the time.

Finally, I would like to express my deep gratitude to Sepp. I am certainly grateful that I found you. We both had to sacrifice a lot of our "Gemeinsamzeit" but I hope that we will never be parted again. Thank you for your personal and scientific support and for making me laugh even in the darkest moments.

Keine Schuld ist dringender als die, Danke zu sagen.

− Marcus Tullius Cicero

ABBREVIATIONS AND SYMBOLS

Abbreviations

Abbreviation	Description
ASS	All-solid-state
LIB	Li^+ ion battery
MAS	Magic Angle Spinning
NS	Nanosheet
LGPS	$Li_{10}GeP_2S_{12}$
SS	Solid-state
PFG	Pulsed field gradient
NMR	Nuclear magnetic resonance
FET	Field-effect transistor
SAM	Self-assembled monolayer
MOS	Metal-oxide-semiconductor
SEM	Scanning electron microscope
EDX	Energy-dispersive X-ray
TEM	Transmission electron microscope
SXRD	Single crystal X-ray diffraction
PXRD	Powder X-ray diffraction
TMD	Transition metal dichalcogenide
2D	Two-dimensional
3D	Three-dimensional

ALD	Atomic layer deposition
AFM	Atomic force microscope
SAED	Selected area electron diffraction
TFT	Thin-film transistor
UV/Vis	Ultraviolet/visible
NIR	Near infrared
ICP-AES	Inductively coupled plasma atomic emission spectroscopy
ICP-OES	inductively coupled plasma optical emission spectrometry
LISICON	Lithium superionic conductor
SE	Secondary electrons
e.g.	For example
***h*, H**	Hexagonal
T	Trigonal
R	Rhombohedral
LDH	Layered double hydroxide
TMO	Transition metal oxide
CHP	Cyclohexyl-pyrrolidinone
DMSO	Dimethylsulfoxide
DS	Dodecylsulfate
TBA	Tetrabutylammonium
PTI	Poly(triazine imide)

BJT	Bipolar junction transistor
i.e.	That means
EC	Ethylene carbonate
DEC	Diethyl carbonate
NASICON	Sodium superionic conductor
LGPS	Lithium germanium phosphorus sulfide; $Li_{10}GeP_2S_{12}$
TFT	Thin film transistor
ESI	Electronic supporting information
VdW	Van der Waals

Symbols

Symbol	**Description**	**Unit/Value**
$\boldsymbol{\sigma}$	Conductivity	S cm^{-1}
$\boldsymbol{I}$	Current	A
$\boldsymbol{U}$	Voltage	V
$\boldsymbol{M}$	Molar mass	g mol^{-1}
$\boldsymbol{C}$	Capacity	m A h g^{-1}
$\boldsymbol{t_e}$	Electron transference number	–
$\boldsymbol{E}$	Energy	eV
$\boldsymbol{k_B}$	Boltzmann constant	$1.380 \cdot 10^{-23}$ J/K
$\boldsymbol{T}$	Temperature	K or °C
$\boldsymbol{v}$	Mobility	cm^2 V^{-1} s^{-1}

λ	Wavelength	Nm
I	Intensity	a.u.
θ	Diffraction angle	°
c	Concentration	g L^{-1}
h, k, l	Miller indices	–
β	Cell angle	°
a, b, c	Cell parameters	Å or nm
t	Time	s or min or h
D	Diffusion constant	m^{2} s^{-1}
B	Magnetic field	T
T_1	Spin-lattice relaxation	s
T_2	Spin-spin relaxation	s
γ	Gyromagnetic ratio	rad s^{-1} T^{-1}
δ	Pulse duration	s
Δ	Duration during pulses	s
δ	Chemical shift	ppm
Z'	Real part of impedance	Ohm
Z''	Imaginary part of impedance	Ohm
R	Resistance	Ohm
F	Electron density	m^{-3}
n	Concentration of mobile ions	m^{-3}
z	Charge number	–

$\boldsymbol{L}$	Diffusion length	m
$\boldsymbol{\tau}$	Characteristic chemical diffusion time	s

TABLE OF CONTENTS

Summary

This thesis is divided into four different research projects. In the following, a summary of each project is presented.

Transistor built from SnS_2 (Chapter 2)

"Threshold-voltage control and enhancement-mode characteristics in multilayer tin disulfide field-effect transistors by gate-oxide passivation with an alkylphosphonic acid self-assembled monolayer" by Ute Zschieschang, Tanja Holzmann, Alexander Kuhn, Mahdieh Aghamohammadi, Bettina V. Lotsch, and Hagen Klauk. Published in *J. Appl. Phys.* **2015**, *117*, 104509-1 - 104509-5.

SnS_2 is a layered semiconductor with a bandgap of ~2 eV and therefore a possible candidate for next-generation FETs. The larger bandgap compared to MoS_2 may translate into transistors with smaller off-state leakage currents and larger on/off current ratios. In Chapter 2 we present a FET using SnS_2 as semiconducting layer. The SnS_2 crystals were synthesized by a typical chemical vapor transport reaction and were afterwards characterized by SEM, XRD and UV/Vis measurements. Using the Kubelka-Munk formalism, the bandgap was determined to 2.2 eV (Figure 1). To construct the FET, the SnS_2 crystals were deposited on a Si/SiO_2 (100 nm; heavily boron doped) substrate, covered with a hydrophobic self-assembled monolayer (SAM), using the scotch-tape method and the source/drain contacts were added *via* electron beam lithography and subsequent metal deposition. A schematic representation of the FET is presented in Figure 2.

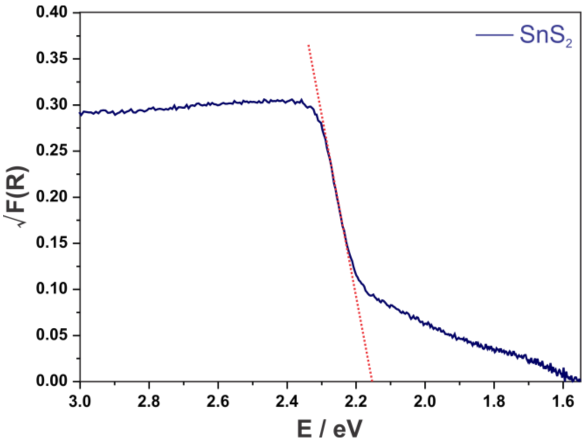

Figure 1. UV/Vis spectrum of SnS_2 plotted according to the Kubelka-Munk formalism for indirect bandgaps. The fit corresponds to a bandgap of 2.15 eV.

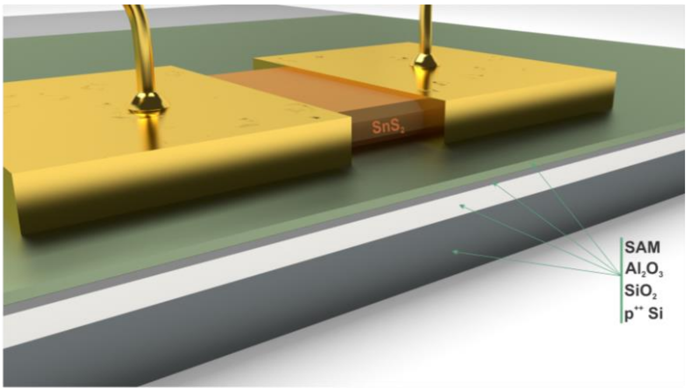

Figure 2. Schematic representation of the FET prepared from SnS_2 crystals. The thermally oxidized silicon substrate is coated with an Al_2O_3 layer and a hydrophobic alkylphosphonic acid SAM before the SnS_2 is deposited by the scotch tape method.

We could demonstrate that a passivation of the gate-oxide surface with Al_2O_3 and alkylphosphonic acid prior to the deposition of the SnS_2 flakes results in a FET with desirable enhancement-mode characteristics (Figure 3). This hydrophobic SAM serves as a clean and well-defined interface and further avoids the adsorption of water molecules between semiconductor and gate, which often results in a high density of trap states. By using the SAM, the depletion mode behavior that is commonly seen in these thin film transistors was avoided. Although the prepared transistor shows high on/off current ratios of 10^6 and a steep subthreshold swing (4V/decade), a small field-effect mobility (< 0.4 cm^2/Vs) was observed that arises from the thickness of the SnS_2 nanosheet (~380 nm height). Thinner crystals (< 100 nm) usually had a lateral size of less than 1 µm and where not useful for device fabrication. The strong access resistance between source/drain contacts and the gate-induced carrier channel could be avoided in future if large sheets with small height (several nanometers) can be produced. This is expected to strongly raise the field-effect mobility.

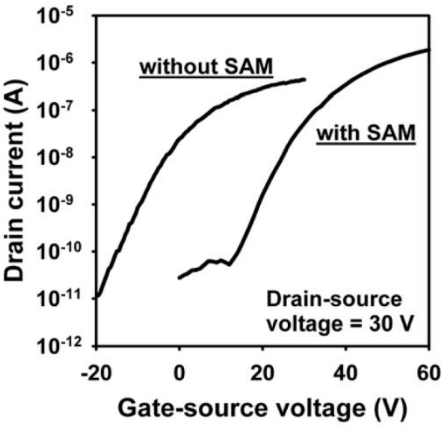

Figure 3. Transfer characteristics of multilayer SnS_2 FETs with and without SAM passivation of the gate oxide, both measured at a drain-source voltage of 30 V. The enhancement-mode behavior is only visible in the SAM coated device.

Exfoliation of $Li_{3x}[Li_xSn_{1-x}S_2]$ (Chapter 3)

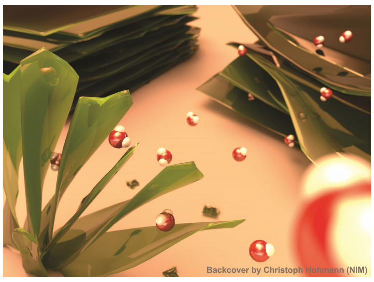

"*A facile wet chemistry approach towards unilamellar tin sulfide nanosheets from $Li_{4x}Sn_{1-x}S_2$ solid solutions*" by Alexander Kuhn, Tanja Holzmann, Jürgen Nuss, and Bettina V. Lotsch. Published in *J. Mater. Chem. A* **2014**, *2*, 6100 - 6106.

Since the discovery of graphene's exotic electronic properties, the interest in nanosheets is steadily growing. Especially semiconducting layered van der Waals (VdW) materials gained a lot of attention due to their possible application in thin film FETs, solar cells or photocatalysis. However, the mechanical exfoliation of these materials (e.g. the scotch-tape method) can hardly be upscaled and (electro-) chemical intercalation of lithium is time-consuming and often needs special conditions such as the handling under inert gas. In Chapter 3 we have tested a direct solid-state lithium intercalation into SnS_2 using Li_2S as precursor. We discovered a new solid solution $Li_{3x}[Li_xSn_{1-x}S_2]$ (x = 0.11-0.33) showing outstanding exfoliation properties for certain x values. The structure of the mother compound Li_2SnS_3 (x = 0.33) was determined by single crystal X-ray diffraction and is isotypic to Li_2SnO_3 (Figure 4). The chemical composition was analyzed by SEM/EDX and ICP-AES measurements. Li_2SnS_3 crystallizes in the monoclinic space group $C2/c$ (no. 15) with a = 6.3961(7), b = 11.0893(13), c = 12.4157(14) Å, and β = 99.860(2)°. The covalent layers are built up by edge-sharing SnS_6 octahedra whereby 1/3 of the tin atoms are substituted by lithium (LiS_6). These covalent layers ($[Li_xSn_{1-x}S_2]^{3x-}$) display the tendency for a honeycomb order and are negatively charged. The covalent layers are connected *via* lithium ions (Li_{3x}^{3x+}) through electrostatic forces.

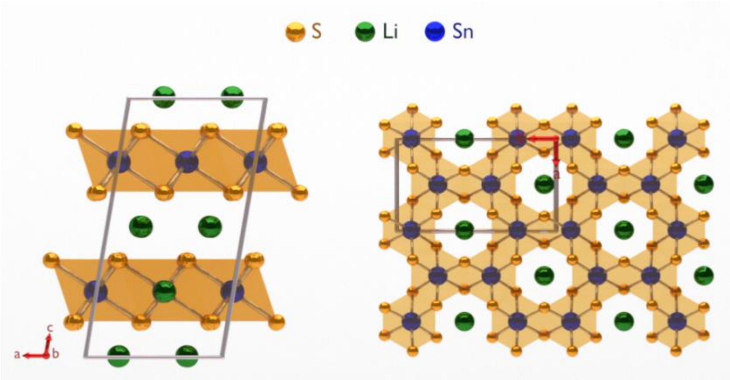

Figure 4. Crystal structure of Li_2SnS_3 in $C2/c$ (no. 15). Left: side view along [010] displaying the layered structure. Right: top view along [001]. The monoclinic cell arises from honeycomb ordered covalent layers. The structure shows the ideal honeycomb order (all intralayerlayer Li/Sn positions are fully occupied).

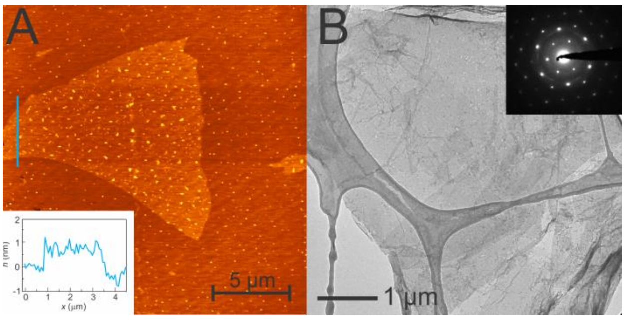

Figure 5. Characterization of the $[Sn_2S_5]^{2-}$ nanosheets. (A) AFM image of a nanosheet on a Si/SiO_2(300 nm) wafer. The inset picture shows the height of the nanosheet of somewhat less than a nanometer, as expected for a single-layer nanosheet. (B) TEM images and SAED patterns. By electron diffraction the maintained crystallinity is displayed.

While all of the prepared compounds could be exfoliated in water, $Li_{0.6}[Li_{0.2}Sn_{0.8}S_2]$ ($x = 0.2$) showed the best exfoliation behavior, namely a spontaneous quantitative exfoliation into single layered nanosheets simply by pouring the compound into water ($c = 1$ g L^{-1}) and shaking the suspension after several hours of swelling. By AFM measurements, we were able to demonstrate that the obtained nanosheets display a lateral size of up to 15 µm and that they are quantitatively exfoliated into single-layered nanosheets with a height of less than 1 nm, which is in good agreement with the expected height from the crystal structure (Figure 5). TEM measurements confirmed the maintained crystallinity of the layers (Figure 5). By centrifugation of the nanosheet suspension and subsequent drying we were able to produce freestanding thin films. PXRD measurements further confirmed the quantitative exfoliation into single-layered nanosheets. SEM/EDX measurements show that the sulfur content decreases from 2:5 to 2:4, presumably due to lithium removal or a substitution of sulfur by oxygen. Rietveld refinements of the freestanding film resulted in a “defective” SnS_2 type structure. This is supported by the fact that after annealing the film at 450 °C the PXRD pattern is in good agreement with the reference of SnS_2. Finally, we determined the band gap of $Li_{0.6}[Li_{0.2}Sn_{0.8}S_2]$ and the nanosheet film before and after annealing. By using the Kubelka-Munk formalism we obtain a bandgap of 1.9 eV for the bulk material, 2.1 eV for the nanosheet film before and 1.9 eV after annealing. Our direct lithium intercalation during the solid-state synthesis can be seen as a means for achieving exfoliation in layered solids through hydration of the interlayer lithium ions as a driving force. Lithium intercalation results in an electrostatically bound layered structure that spontaneously exfoliates in water. To the best of our knowledge a quantitative exfoliation of layered bulk material into single-layered nanosheets has not been observed yet for layered VdW solids. The presented concept will be widely applicable also for other layered chalcogenides, facilitating the excess to thin nanosheets with large lateral size.

Li^+ conduction in $Li_{0.6}[Li_{0.2}Sn_{0.8}S_2]$ (Chapter 4)

“*$Li_{0.6}[Li_{0.2}Sn_{0.8}S_2]$ – a layered lithium superionic conductor*” by T. Holzmann, L. M. Schoop, M. N. Ali, I. Moudrakovski, G. Gregori, J. Maier, R. J. Cava, and B. V. Lotsch. Published in *Energy Environ. Sci.* **2016**, *9*, 2578 - 2585.

Cover image by Christoph Hohmann

One of the key challenges in energy storage research is finding solid-state Li^+ ion conductors with conductivities comparable to liquid electrolytes. Therefore, the development of new structural families that show Li^+ ion conduction and the identification of structural descriptors for fast Li^+ ion migration is important to build all-solid-state batteries. In Chapter 4 we show that $Li_{0.6}[Li_{0.2}Sn_{0.8}S_2]$ does not only display an outstanding exfoliation behavior (see Chapter 3), it is further an anisotropic lithium superionic conductor with conductivities up to 10^{-2} S cm^{-1}. We were able to solve the crystal structure by single-crystal X-ray diffraction. It shows a monoclinic *C*2/*m* (no. 12) cell with $a = 19.217(7)$, $b = 3.6996(14)$, $c = 6.529(2)$ Å, and $\beta = 109.056(4)°$. As in Li_2SnS_3, the covalent layers are built up by edge-sharing SnS_6 octahedra whereby 20% of the tin atoms are substituted by lithium. However, $Li_{0.6}[Li_{0.2}Sn_{0.8}S_2]$ does not show a honeycomb intralayer ordering. The monoclinic cell rather arises from preferred occupancies of the intralayer Li/Sn sites (Figure 6) by either Li or Sn. We confirmed our structure solution by chemical analysis using SEM/EDX and ICP-AES as well as solid-state NMR measurements.

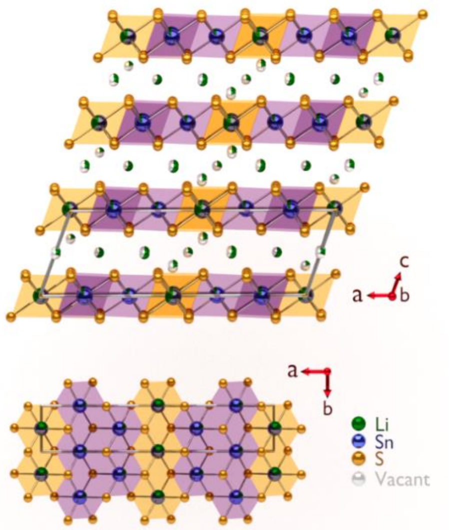

Figure 6. Crystal structure of $Li_{0.6}[Li_{0.2}Sn_{0.8}S_2]$ viewd along [001] (top) with partially substituted tin positions (yellow and purple polyhedra for two different tin positions) and O1 type stacking. A vertical top-view of the layers is shown underneath. The monoclinic unit cell arises from the intralayer ordering (two different Sn/Li occupations).

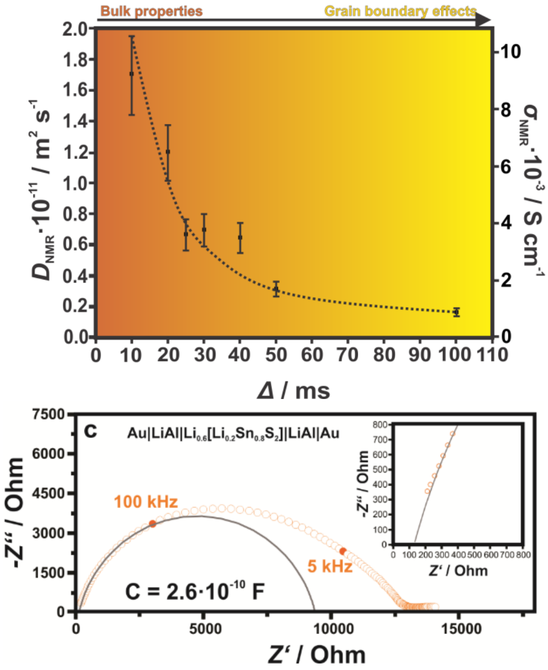

Figure 7. Top: Diffusion coefficient D_{NMR} determined with PFG NMR at various diffusion times Δ. D_{NMR} is lowered with longer Δ, indicating grain boundary effects that hinder the diffusion. The maximum bulk conductivity is $\sigma_{\mathrm{NMR}} = 9$ mS cm^{-1}. Bottom: Impedance spectrum of $Li_{0.6}[Li_{0.2}Sn_{0.8}S_2]$ at 298 K under argon. The measurement was performed between 1 MHz and 0.01 Hz on a non-blocking configuration. The finite intercept of 130 Ω (see inset) corresponds to a bulk conductivity of 15 mS cm^{-1}. The intercept at 12500 Ω most likely belongs to grain boundary resistance (~10^{-4} S cm^{-1}).

In contrast to Li_2SnS_3, only 38% of the interlayer lithium positions are occupied but lithium does not only occupy octahedral, but also tetrahedrally coordinated sites. The resulting vacancies are assumed to facilitate Li^+ motion. We investigated the Li^+ ion conduction by both PFG NMR and electrical conductivity measurements (Figure 7). In both measurements we see a grain boundary effect, arising from the fact that we measured polycrystalline powder. This effect could be avoided by measuring large single crystals. The conductivity goes up to 10^{-2} S cm^{-1} and the activation energy was determined by ^{7}Li T_1 relaxation time measurements at temperatures between 320 - 440 K. Like the high ionic conductivity, the obtained E_A of 0.17 eV is close to the currently best LISICONs such as LGPS (0.21 eV). With our investigations we show that Li depletion facilitates Li^+ ion migration in the solid-state compound. Compared to Li_2SnS_3, having a Li^+ ion conductivity of σ_{298K} ~ 10^{-5} S cm^{-1}, the migration in $Li_{0.6}[Li_{0.2}Sn_{0.8}S_2]$ is 3 orders of magnitude faster. This arises from the fact that interlayer Li does not only occupy the octahedral but also tetrahedral sites, which is critical for facile ion movement. We further supported this argument with calculation of possible lithium migration pathways, showing that Li hopping is only possible from octahedral to tetrahedral sites and *vice versa*. This insight can be very important for further studies on those materials since many Delafossite-related compounds have been reported to also exist in cation depleted versions. Our work points to a generic design principle for new layered Li^+ ion conductors based on the controlled depletion of Li^+ ions in the interlayer space.

Hydration of $Li_{0.6}[Li_{0.2}Sn_{0.8}S_2]$ (Chapter 5)

"*Air-tolerant Li ion conduction in the superionic conductor $Li_{0.6}[Li_{0.2}Sn_{0.8}S_2]$*" by T. Holzmann, L. M. Schoop, I. Moudrakovski, M. N. Ali, R. J. Cava, and B. V. Lotsch. *To be submitted.*

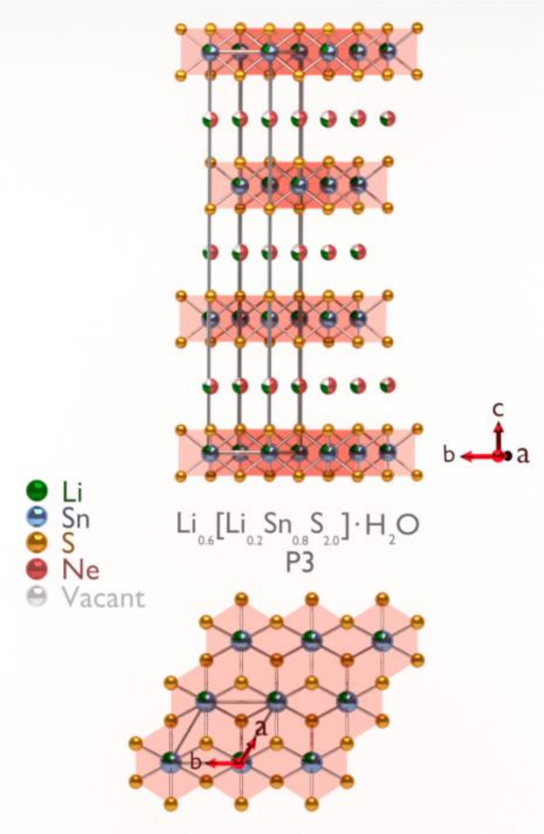

Figure 8. Crystal structure of the monohydrate $Li_{0.6}[Li_{0.2}Sn_{0.8}S_2]\cdot H_2O$ in $R\bar{3}m$ with P3 type stacking (top: view along [100], bottom: top view to one layer). Water was substituted by neon atoms for the calculations to ensure charge neutrality.

Solid-state Li ion conductors with negligible electronic conduction are of high importance in developing advanced energy storage technologies, such as batteries, supercapacitors or electrochemical sensors. However, most of the currently best Li ion conductors need to be handled under inert gas as they are unstable in air. In Chapter 5 we report the hydration of $Li_{0.6}[Li_{0.2}Sn_{0.8}S_2]$ in air, which leads to a two-step hydration process, first forming the monohydrate $Li_{0.6}[Li_{0.2}Sn_{0.8}S_2]\cdot H_2O$ while after longer air exposure a swollen phase with 1.6 H_2O molecules per formulate unit is obtained. $Li_{0.6}[Li_{0.2}Sn_{0.8}S_2]\cdot H_2O$ is found to crystallize in the space group $R\bar{3}m$ (no. 166) with $a = 3.685(3)$ Å and $c = 25.164$ Å and shows a P3 type stacking (Figure 8). ^1H NMR measurements reveal that the water molecules are strongly fixed like, for example, observed in gypsum. In contrast, the water molecules in the swollen phase $Li_{0.6}[Li_{0.2}Sn_{0.8}S_2]\cdot 1.6\ H_2O$ are highly mobile. ^6Li NMR and PXRD measurements display that there is no intermediate phase between anhydrate and monohydrate with less than one water molecule per formula unit, however, after the formation of the monohydrate the sample continuously absorbs further water. In air, an equilibrium state with 1.6 H_2O molecules per formula unit is obtained while, under argon/water gas flow, an uptake of at least 4.3 H_2O molecules could be reached. It is expected that this hydration is a continuous process, finally leading to the exfoliation of the powder. We exfoliated the powder by pouring it into water and analyzed the single-layer nanosheets. From SAED patterns it is clearly visible that the presented rhombohedral space group is only an average structure and the preferred occupancies of the $[Li_{0.2}Sn_{0.8}S_2]^{3x-}$ layers as observed in anhydrous $Li_{0.6}[Li_{0.2}Sn_{0.8}S_2]$ are still present. As $Li_{0.6}[Li_{0.2}Sn_{0.8}S_2]$ is known to be a fast Li^+ conductor we finally tested the influence of the hydration on the ion conducting properties (Figure 9). While the anhydrous sample displays a bulk conductivity of 8.6 mS cm^{-1}, the conductivity decreases to 1.7 mS cm^{-1} in the monohydrate caused by the simultaneous effects of the steric hindrance of water and the stacking change, which has been known to affect Li^+ ion migration. After prolonged contact with air, the sample absorbs more water, reaching a final uptake of 1.6 H_2O molecules per formula unit. This causes an increase in conductivity to 10 mS cm^{-1}, thus slightly exceeding the values for the anhydrous starting material. Thus, these results display the air-tolerant Li^+ conductivity of $Li_{0.6}[Li_{0.2}Sn_{0.8}S_2]$. The re-established conductivity presumably results from the largely increased layer distance of 11.4 Å as it is known that with increasing c lattice parameter the Li^+ migration is facilitated. Further, the fact that mobile water molecules are present instead of strongly fixed ones (as in the monohydrate) reduces the steric hindrance to Li ion motion. We therefore show that $Li_{0.6}[Li_{0.2}Sn_{0.8}S_2]$ forms a monohydrate upon exposure to air which is accompanied by a stacking change and a large increase of layer distance. The Li ion conduction measurements reveal that hydration does not necessarily negatively influence Li ion conduction. To our knowledge, $Li_{0.6}[Li_{0.2}Sn_{0.8}S_2]$ is the first air stable lithium superionic conductor.

1 Introduction

1.1 From layered materials to two-dimensional nanosheets

1.1.1 Layered bulk materials

Mankind has been harnessing the properties of layered materials since at least 400 a.d., when the Mayans started to produce dyes out of layered clays without any knowledge of their crystal structure.[1] By now, due to the intriguing structural and physical properties, there has been a sustained academic and technical interest directed at layered materials and their intercalation compounds for more than 40 years.[2] This interest rapidly increased in 2004, when A. Geim and K. S. Novoselov investigated a monolayer of graphite, so-called graphene.[3] Graphite (from greek γράφειν [graphein] which means “to write”) is the hexagonal layered form of carbon which is widely used, e.g. as writing tool, lubricant or as anode material in Li^+ ion batteries. It is an indispensable part of everyday life but until 2004, it was not known that the delamination of the bulk material into monolayers results in vastly different materials properties.[3-4]

By definition, a layered or two-dimensional (2D) material is a material in which the bond strength and the atomic organization are similar along two dimensions but much stronger than those along the third dimension.[5] Many of their physical and chemical properties derive from the anisotropy of the structure, e.g. the insertion of ions or molecules between the individual layers is possible due to the weak interlayer bonding forces. The anisotropic nature also leads to characteristic and often technologically useful mechanical, electrical, magnetic and optical properties. Further, as a broad range of metals in various oxidation states is included in this class of materials, their properties are extraordinarily diverse. This is for example shown by the fact that layered metal chalcogenides cover the whole range of electronic behavior, from semiconductors and insulators to semimetals or even metals.[6-8] To give a better overview, these layered materials can be split into two general groups: van der Waals and ionic solids. In the following, some important examples of both groups are presented.

Layered van der Waals solids

In layered van der Waals solids the crystal structure consists of neutral (i.e. non-charged) layers of atoms with covalent or ionic intralayer and van der Waals interlayer bonding. Hexagonal boron nitride (*h*-BN, Figure 1.1.1.1a), graphite (Figure 1.1.1.1b) and molybdenum sulfide (MoS_2, Figure 1.1.1.1c) are prominent examples, but there are many other materials.[9-10] The largest subgroup is formed by layered metal chalcogenides, most of which comprise the transition metals.[8-10] An exception is tin sulfide, which is a well-known main group metal containing example and which shows a crystal structure similar to the transition metal dichalcogenides (see chapter *1.2 Tin sulfides*). The layered metal chalcogenide subgroup itself can be classified by their composition. The binary compounds include transition metal dichalcogenides (TMDs) MX_2 (M = Mo, W, Ti, Zr, Hf, V, Nb, Ta, Re; X = S, Se, Te) and transition metal trichalcogenides MX_3 (M = Nb, Zr; X = S, Se, Te). Ternary compounds are, for example, metal phosphorus trichalcogenides MPX_3 (M = Cd, Fe, Mg, Ca, Mn, Ni, V, Sn, Pb, Zn; X = S, Se).[8] These materials are produced by a wide range of synthesis methods, such as high-temperature synthesis,[11] vapor-phase reactions,[12-13] chemical vapor transport,[14-25] low-temperature synthesis[26-30] or more special techniques such as metal organic vapor deposition[31-32] or pulsed laser evaporation.[8, 33-34]

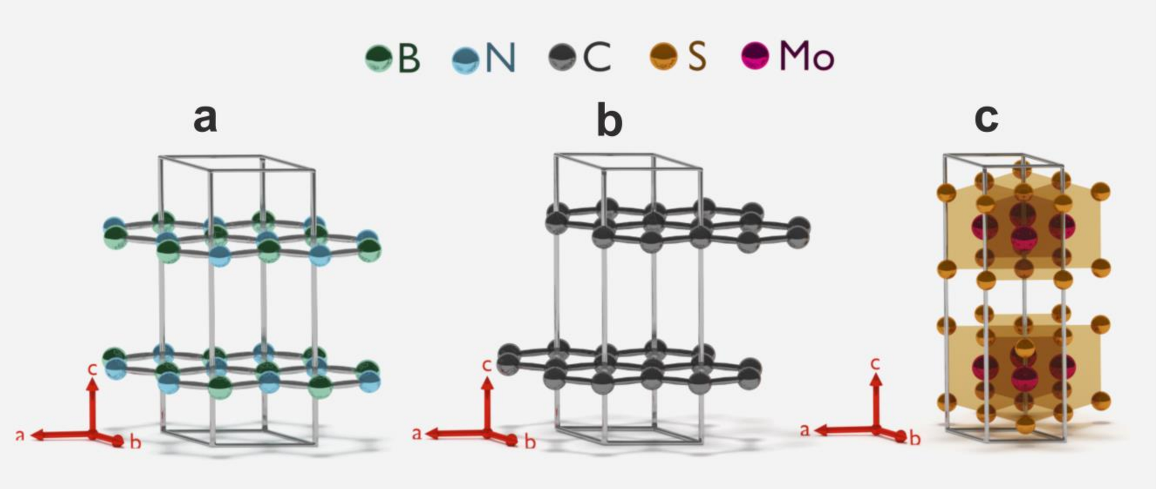

Figure 1.1.1.1 Schematic representation of the structures of three layered van der Waals solids: (a) *h*-BN ($P6_3/mmc$, no. 194), (b) graphite ($P6_3/mmc$, no. 194) and (c) MoS_2 ($P6_3/mmc$, no. 194). Each structure consists of covalent layers separated by van der Waals gaps. The covalent layers of graphite and *h*-BN are only one atom thick and display a hexagonal arrangement of C (in graphite) and alternating B-N (in *h*-BN) atoms. In the case of MoS_2, the covalent layer is built up by hexagonally arranged edge-sharing trigonal MoS_6 prisms. A top view of a graphene, *h*-BN and MoS_2 layer is presented in Figure 1.1.3.2.

Among layered van der Waals solids, metal dichalcogenides are of special interest as they exhibit versatile chemistry and have diverse properties ranging from metals and semimetals to semiconductors and insulators. This offers the possibility for fundamental and technological research in a wide field of applications, e.g. catalysis, energy storage, sensing or electronic devices such as field-effect transistors.[35] In particular, MoS_2 gained a lot of interest as an outstanding lubricant, catalyst (e.g. in petrochemistry, for water electrolysis, as co-catalyst in photocatalysis, or if nanostructured as substitute for platinum in fuel cells) and for its promising application in Li^+ ion batteries as anode or cathode material.[36-39]

The covalent layers of metal chalcogenides are built up of hexagonally arranged polyhedra (octahedra or trigonal prisms) with various stacking orders. The most common polymorphs are 1T, 2H and 3R – the letter stands for trigonal, hexagonal and rhombohedral, the digit describes the number of covalent layers within one unit cell.[35] In Figure 1.1.1.2, the three different polymorphs 1T, 2H and 3R of TaS_2 are displayed. Note that in the case of 2H- and 3R-TaS_2, the covalent layer consists of edge-sharing trigonal prisms, while in the case of 1T-TaS_2, the layers are built up by edge-sharing octahedra. This difference in coordination of the metal center and the stacking order of the covalent layers can drastically change the properties of a material. For example, under ambient conditions 2H-TaS_2 shows superconducting behavior while 1T-TaS_2 does not.[40-41]

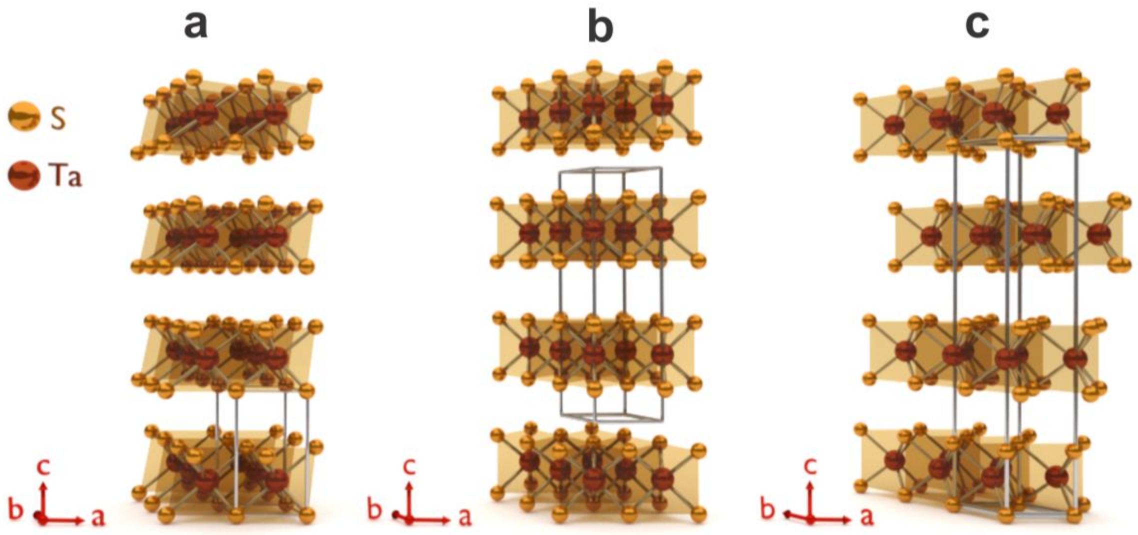

Figure 1.1.1.2 Schematic representation of three polymorphs of TaS_2: (a) 1T-TaS_2 ($P\bar{3}m$, no.164), (b) 2H-TaS_2 ($P6_3/mmc$, no. 194), and (c) 3R-TaS_2 ($R\bar{3}m$, no. 166). 1T-TaS_2 is built up by edge-sharing TaS_6 octahedra, 2H- and 3R-TaS_2 are built up by edge-sharing trigonal TaS_6 prisms. The digit (1, 2, 3) describes the

number of covalent layers within one unit cell. The letter stands for trigonal (T), hexagonal (H), and rhombohedral (R) phase.

Besides the 2D van der Waals solids, there also exist layered ionic solids. They have crystal structures with charged polyhedral slabs that are interleaved with ions and are thereby electrostatically bound.[9] They can be divided into two main groups, depending on the layer being positively or negatively charged. In the following, both groups are presented shortly.

Layered cationic solids

Although there are many examples for negatively charged layered materials, there are only few examples for positively charged ones – mainly the layered double hydroxides (LDHs). The general formula of LDHs is described by $[M^{y+}{}_{1-x}M^{3+}{}_{x}(OH)_2]^{z+}X^{n-}{}_{z/n}\cdot mH_2O$.[42] Usually $y = 2$, $z = x$, $M^{2+} = Ca^{2+}$, Mg^{2+}, Zn^{2+}, Ni^{2+}, Mn^{2+}, Co^{2+} or Fe^{2+} and $M^{3+} = Al^{3+}$, Cr^{3+}, Mn^{3+}, Fe^{3+}, Ga^{3+}, Co^{3+} or Ni^{3+}. The first part of the formula ($[M^{y+}{}_{1-x}M^{3+}{}_{x}(OH)_2]^{z+}$) describes the positively charged metal hydroxide layer; the second part ($X^{n-}{}_{z/n}\cdot mH_2O$) corresponds to the anions (e.g. CO_3^{2-}, NO_3^{-}, Cl^{-}) and the water molecules that are located between the covalent layers. They connect the separate layers by electrostatic forces.[43] This layered structure is closely related to that of Brucite, $Mg(OH)_2$. Each Mg^{2+} ion is octahedrally coordinated by 6 OH^{-} ions and the individual octahedra are connected *via* the edges. A partial exchange of Mg^{2+} by Fe^{3+} as in Pyroaurite ($[Mg_6Fe_2(OH)_{16}]CO_3\cdot 4H_2O$; in the following written as short form: Mg^{2+} Fe^{3+} LDH (CO_3)) or by Al^{3+} as in Hydrotalcite ($[Mg_6Al_2(OH)_{16}]CO_3\cdot 4H_2O$; Mg^{2+} Al^{3+} LDH (CO_3)) results in a positively charged layer which is charge-balanced by carbonate anions between the layers (Figure 1.1.1.3). The Brucite-like layers of LDHs can stack on top of each other with either hexagonal (2H; Figure 1.1.1.3a) or rhombohedral (3R; Figure 1.1.1.3b) sequence.[42, 44]

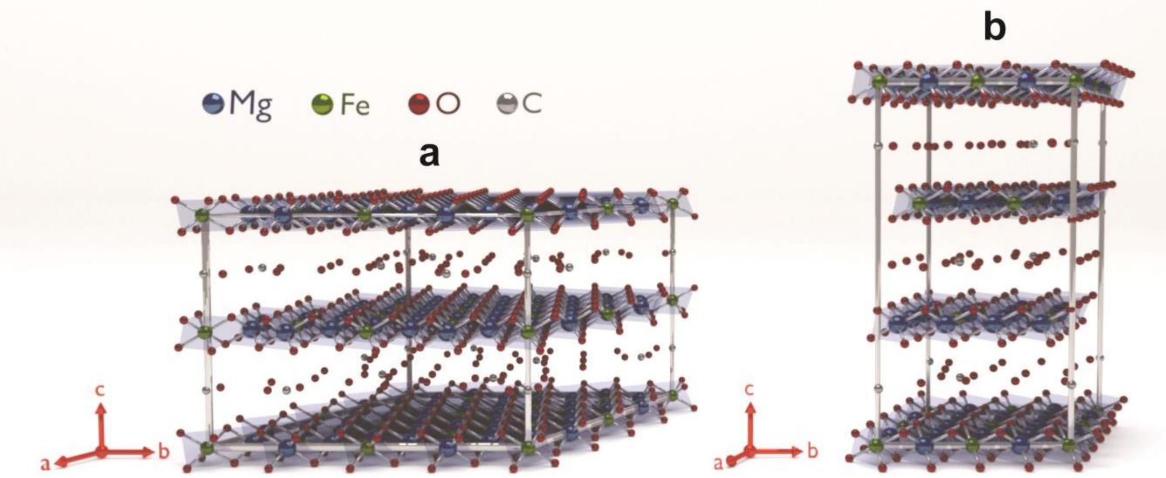

Figure 1.1.1.3 Structure of $[Mg_6Fe_2(OH)_{16}]CO_3{\cdot}4H_2O$ showing the Brucite-type layers consisting of edge-sharing MO_6 octahedra (M = Mg, Fe) and the polymorphic stacking patterns (a) Sjögrenite, hexagonal ($P6_3/mcm$, no. 193) and (b) Pyroaurite, rhombohedral ($R\bar{3}m$, no. 166). A top view of a LDH layer is presented in Figure 1.1.3.2. Note that the position of the H atoms is not determined.

An attractive feature of LDHs is their ability to catalyze reactions using relatively cheap and nonpolluting oxidants, such as peroxides or even oxygen itself. Hence, they are often used as catalysts for oxidation reactions. One reason for this feature is the stabilization of oxidation states within the LDH that are normally not stable in solutions. For example Cu^{3+} or Mn^{3+} are stabilized in the highly basic environment experienced by the metal ions.[8] Furthermore, Mg^{2+} Al^{3+}, Zn^{2+} Al^{3+} and Zn^{2+} Cr^{3+} LDH pillared with hetero- or isopolyoxometalates show high photocatalytic activity in the degradation of the organocholorine pesticide hexachlorocyclohexane.[8, 45-47]

Layered anionic solids

In contrast to LDHs which are amongst the very few layered materials featuring positively charged layers, there are many examples for negatively charged layered materials. One subgroup is the naturally occuring clays, e.g. montmorillonite[48] ($Ca_{1.2}Al_4(Si_8O_{20}(OH)_2)O_{2.2}(H_2O)_{3.1}$). Clay minerals belong to the class of phyllosilicates (silicate structures composed of sheets) and present a layered structure.[8, 49] Another large group of anionic layered materials can be summarized into a subgroup called layered transition metal oxides (TMO).[50-51] Some prominent examples are $K_4Nb_6O_{17}$, $KTiNbO_5$ and $Cs_{0.7}Ti_{1.825}O_4$ [50-52] but this subgroup also contains layered α-zirconium phosphates and phosphonates, layered manganese oxides and layered perovskites.[8] $KCa_2Nb_3O_{10}$ is a prominent example of layered perovskites, which gained a lot of academic interest due to its easy exfoliation into monolayered nanosheets and its photocatalytic properties (Figure 1.1.1.4a). The layered perovskites are in general built up by corner- or edge-sharing BO_6 octahedra (B = Ti, Nb, Mn, Ta, W) and the negatively charged layers are separated by cations which stabilize the structure *via* electrostatic forces. In rare cases, the octahedra can also be connected *via* the edges, for example in organic-inorganic hybrid perovskites (e.g. $[Cu(O_2C\text{-}(CH_2)_3\text{-}NH_3)_2]PbBr_4$).[53] A further example is layered phosphatoantimonate $K_3Sb_3P_2O_{14}$, which shows proton conduction after an exchange of K^+ by H^+ (Figure 1.1.1.4b).[54-57]

These layered anionic solids have a wide range of applications. Clays are used as acidic cracking catalysts during crude oil refining for gasoline production.[58] Cu^{2+} incorporated α-zirconium phosphates are catalytically active materials for the oxidation of carbon monoxide in the presence of oxygen.[59] Layered $K_2MnSn_2S_6$ can be used for water purification as it absorbs uranium traces in seawater,[60] triazine-based layered carbon nitrides can produce hydrogen by photochemical water reduction under visible light,[61] layered $LiCoO_2$, $LiNiO_2$ and $LiMnO_2$ are important cathode materials for the current Li^+ ion batteries,[62-63] and $KCa_2Nb_3O_{10}$ is also a photocatalytically active material.[64]

Although these layered materials were already of interest for scientists all over the world, a new “hype” arose in 2004 when A. Geim and K. S. Novoselov reported on the extraordinary properties of a single layer of graphite, called graphene.[3] Graphene was likely already discovered by Boehm *et al*.[65] in 1962, but its physical properties were investigated over 40 years later. The fact that a monolayer of a material can have properties strongly deviating from its bulk structure led to a renewed interest in other 2D materials. A. Geim and K. S. Novoselov obtained their graphene sheets by the famous “scotch-tape method” (see Figure 1.1.2.1), which is a simple mechanical exfoliation route using a thin transparent adhesive tape to peel off atomically thin layers from a crystal. But there exist many other methods as well. In the following chapter, several exfoliation methods are presented with respect to the type of layered bulk material.

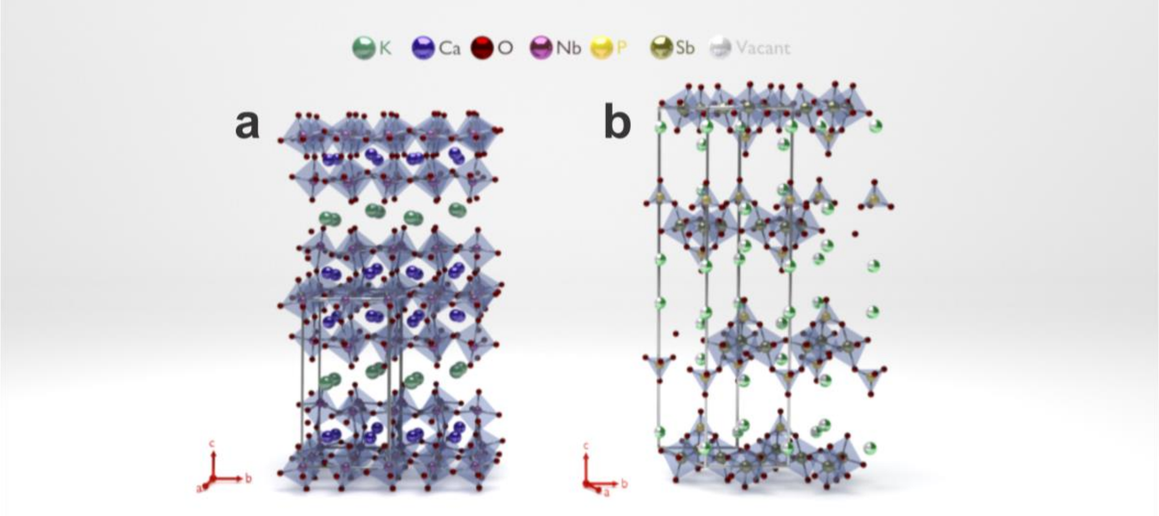

Figure 1.1.1.4 Schematic representation of two anionic layered materials: (a) layered $KCa_2Nb_3O_{10}$ ($P2_1/m$, no. 11) and (b) layered phosphato-antimonate $K_3Sb_3P_2O_{14}$ ($R\bar{3}m$, no. 166).

1.1.2 Exfoliation of layered materials

In general, exfoliation is defined as the decomposition of large aggregates into smaller particles.[66] If this specific decomposition splits the 2D bulk material into individual layers, it is defined as a delamination.[66] The method of choice for preparing nanosheets is dependent on the kind of layered material. While layered van der Waals solids are mostly exfoliated by ultrasonication in organic solvents or lithium intercalation, layered ionic solids are mostly exfoliated *via* ion exchange steps, mainly in aqueous solutions. In the following, some general routes and examples for various layered materials are explained.

Exfoliation of layered van der Waals solids

As layered van der Waals compounds have weak interlayer bonding forces of around 40-70 meV,[9] they can be mechanically exfoliated by the scotch-tape method resulting in high-quality single layers (Figure 1.1.2.1). Nevertheless, the obvious drawback of this method is that it is hardly upscaleable and therefore, liquid exfoliation routes are favored. In 2011, Coleman *et al.*[67] published a detailed investigation on the exfoliation behavior of layered van der Waals solids in various organic solvents using ultrasound. Which solvent is used depends on the material and the appropriate surface tension, e.g. *h*-BN can be exfoliated with cyclohexyl-pyrrolidone (CHP), while for WS_2 dimethylsulfoxide (DMSO) is the best choice. The materials are simply sonicated in the appropriate solvent and centrifuged afterwards to remove residual bulk material. Although this method is easily upscaleable, not only mono- but also few-layered nanosheets are obtained and the nanosheets often have a small lateral size.

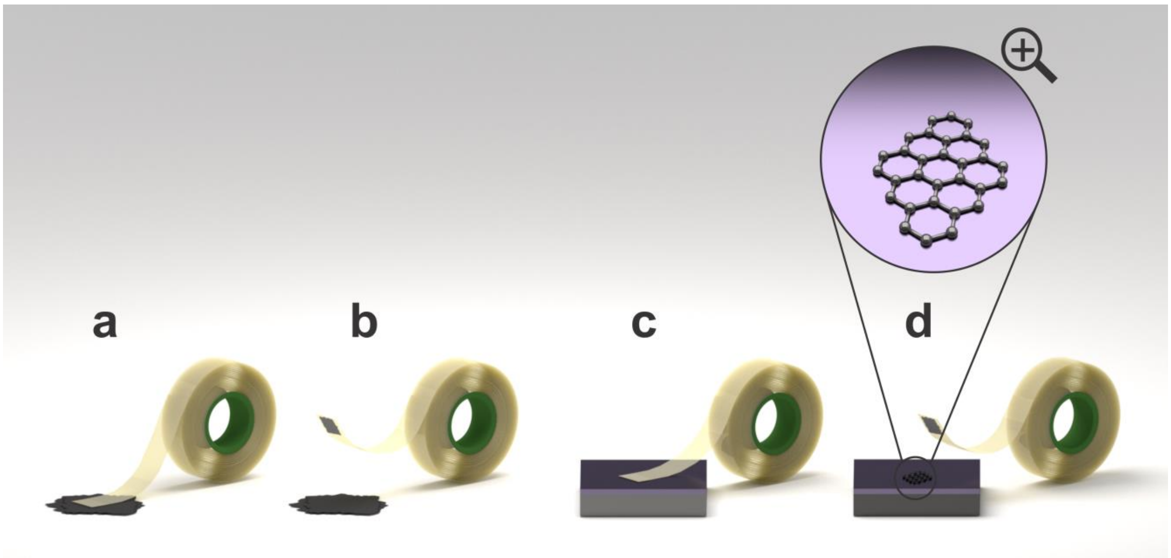

Figure 1.1.2.1 Schematic representation of the several steps of the scotch-tape method. In (a) the scotch-tape is pressed on a graphite crystal. Afterwards, in (b) the scotch-tape is pulled off. In step (c) the removed graphite flake (which is much thinner now than the original crystal) is pressed on a substrate. By removing the scotch-tape, most of the flake stays at the tape while much thinner layers (monolayers after several repetitions) stick on the substrate surface.

Besides sonication, the exfoliation *via* lithium intercalation is a proven route for layered van der Waals solids. Lithium can be intercalated either electrochemically with lithium foil or chemically with *n*-buthyl lithium in hexane under inert gas. The lithiated material is afterwards poured into water and sonicated. The obtained nanosheets can be stabilized either electrostatically by a surface charge[68] or by adding surfactants[69]. It is suspected that lithium reduces the metal center of the covalent layers during the intercalation process and is thereby oxidized to Li^+. If the lithiated material gets into contact with water the metal center is oxidized again, producing H_2 and, due to the gas evolution, the nanosheets are separated and dispersed.[1, 9, 70] This method often leads to single layered sheets with large lateral size. Nevertheless, it also has drawbacks associated with the sensitivity to ambient conditions (e.g. *n*-butyl lithium is not stable in air) and the fact that the material is chemically changed (i.e. change in oxidation state of the metal).[68, 71-72] Figure 1.1.2.2 gives a schematic overview of the exfoliation routes for layered van der Waals solids.

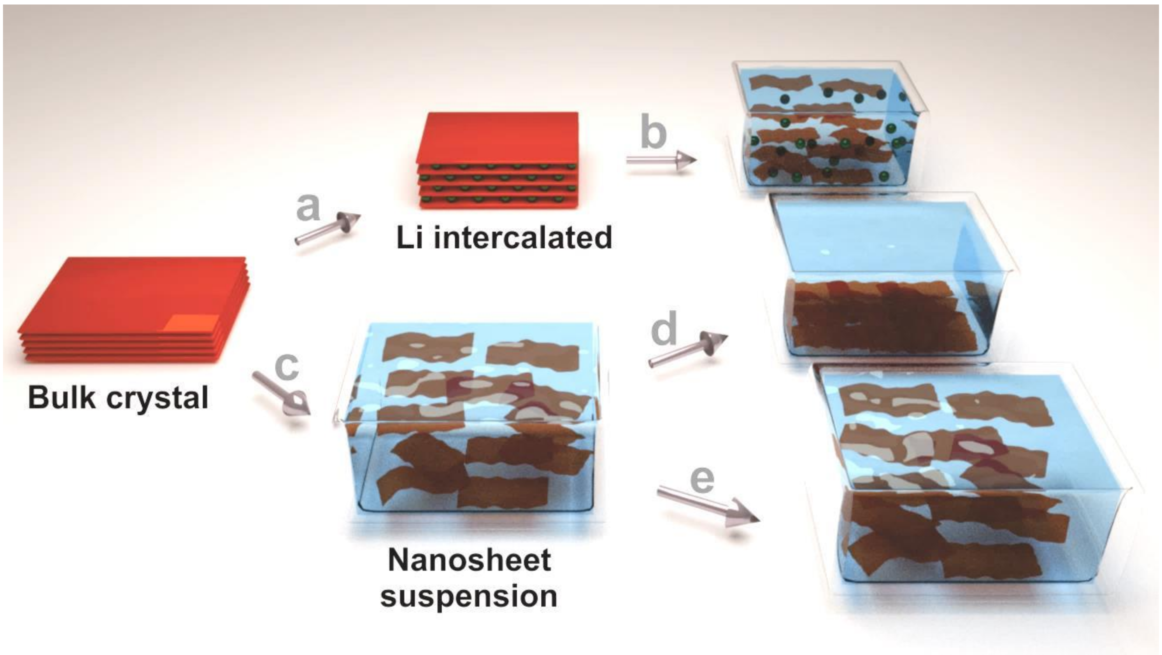

Figure 1.1.2.2. Examples of exfoliation routes for layered van der Waals solids. (a) Intercalation of lithium with (b) a subsequent agitation by ultrasound, resulting in a stable colloidal suspension. (c) Exfoliation by ultrasound in organic solvents. Depending on the appropriate surface tension and the material, (d) a poor solvent results in precipitation of the obtained nanosheets, while (e) a good solvent leads to a stable colloidal suspension.

Exfoliation of layered cationic solids

LDHs were first exfoliated in 2000 by Adachi-Pagano *et al.*[73] They reported that refluxing of Zn^{2+} Al^{3+} LDH dodecylsulfate (DS) in butanol for 16 h led to LDH nanosheets. The substitution of the interlayer water molecules by butanol is the key process for the exfoliation. In general, cationic layered solids are mostly exfoliated *via* an ion exchange step. The choice of the solvent is important for the exfoliation process,[74] e.g. Mg^{2+} Al^{3+} LDH DS can be delaminated in CCl_4 with ultrasonication, but in toluene only swelling occured.[75] All these LDH exfoliation routes have the commonality that they start with an anion exchange step, e.g. in the case of Mn^{2+} Al^{3+} LDH (chloride), the material is dispersed in a highly concentrated solution of sodium DS (2.5 fold excess of dodecylsulfate with respect to chloride anions) until the substitution of chloride by DS is complete (Figure 1.1.2.3). During this exchange, the interlayer distance is drastically increased and thereby the interlayer bonding forces are reduced. Finally, the Mn^{2+} Al^{3+} LDH DS can be exfoliated by sonication in formamide.[76]

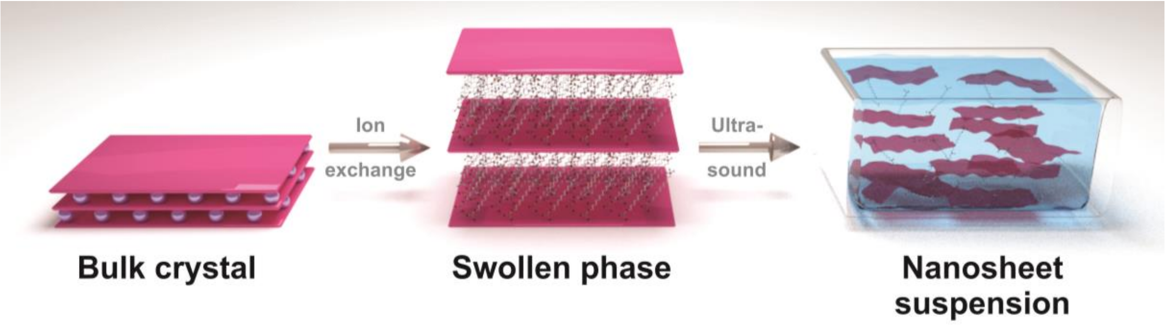

Figure 1.1.2.3 Anion exchange and subsequent exfoliation of a LDH crystal. The interlayer anions are exchanged for (mostly) larger ones (e.g. chloride for DS). As the swollen phase has highly reduced interlayer bonding forces, it can be exfoliated by ultrasound treatment in an appropriate solvent afterwards.

Exfoliation of layered anionic solids

The exfoliation principle of 2D anionic solids is similar to the one for cationic ones. The interlayer ion is exchanged by a larger one, which reduces the interlayer bonding forces and thereby facilitates the delamination of the crystal. Already in 1968 U. Hofman[77] observed that smectite clays undergo an infinite swelling when they are suspended in a low concentrated electrolyte solution which led to an exfoliation of the bulk material into mono- or few layered nanosheets.[77]

In contrast to the spontaneous swelling of smectite clays, layered transition metal oxides are mostly exfoliated *via* a two-step cation exchange procedure. For example, to exfoliate $KCa_2Nb_3O_{10}$, in the first step, K^+ is exchanged by H^+ with a Brønsted acid to obtain $HCa_2Nb_3O_{10}\cdot x\ H_2O$. Afterwards the protons are exchanged by tetra-*n*-butylammonium (TBA^+) cations through an acid-base reaction with an aqueous TBA hydroxide solution resulting in $TBA_{1-y}H_yCa_2Nb_3O_{10}$ ($0<y<1$). During the exchange, the attractive interlayer forces are reduced and the material can be exfoliated by shaking with an orbital shaker.[50] A schematic of the exfoliation process for $KCa_2Nb_3O_{10}$ is presented in Figure 1.1.2.4. Other exfoliation routes include, for example, the exchange of cations under hydrothermal conditions as in the case of $K_4Nb_6O_{17}$. Here, potassium ions are exchanged by *n*-butyl ammonium cations in an autoclave under hydrothermal conditions which automatically leads to the swelling and delamination of the crystal.[78]

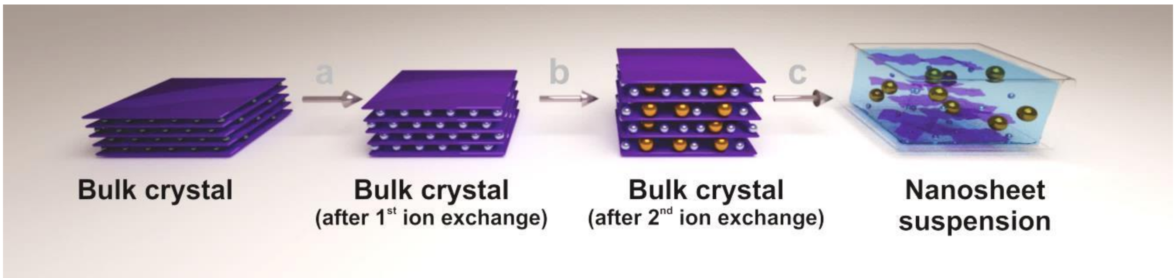

Figure 1.1.2.4 Schematic representation of the exfoliation route for $KCa_2Nb_3O_{10}$. In the first step, potassium is exchanged by protons in a Brønsted acid and in the second step the protons undergo an acid base reaction in TBA hydroxide solution. Thereby protons are partially exchanged by the larger TBA^+ cations. The interlayer forces are drastically reduced and the exfoliation can be achieved by shaking the aqueous solution on in orbital shaker, resulting in a stable colloidal suspension.

1.1.3 Two-dimensional nanosheets

All of the aforementioned exfoliation routes have in common that they attempt to delaminate the bulk crystal into monolayered sheets with a large lateral size and hence a large aspect ratio. The term “nanosheet” was introduced in 1996 by Sasaki *et al.*[79] It reflects two crucial properties of these materials: a layer thickness in the nanometer range and a high 2D anisotropic lateral size. Nanosheets (NS) can be regarded as a new class of materials[50, 80] and in the last decade plenty of layered solids have been exfoliated and investigated for their physical and chemical properties. The simplest property change is the increase of accessible surface area, which can drastically enhance the chemical and physical reactivity, especially for catalytic or surface-active materials. Furthermore, due to the 2D confinement of the electrons, the band structures are altered. This yields new types of electronic or magnetic materials and often leads to unexpected optical and electrical properties. Therefore, compared to their bulk analogues, nanosheets can have vastly different properties. In the following, two prominent examples of nanosheets are presented regarding their special properties and their possible applications.

Graphene

Graphene (Figure 1.1.3.2a) is the archetypal example of a NS material which, with the discovery of its extraordinary properties in 2004, renewed the interest in NS of other materials.[3] Graphene layers display a very high conductivity in *xy* direction (parallel to the layers) that is even higher than the value found for copper. Recent nanoindentation measurements also revealed an intrinsic yield strength of defect-free sheets of 43 N m^{-1}. These experiments established graphene as the strongest material ever measured.[81] The anisotropic characteristics result from its hexagonal lattice of carbon atoms permeated by a "sea" of delocalized electrons.[3, 82-84] This discovery was honored in 2010 with the Nobel Prize in physics "*for groundbreaking experiments regarding the two-dimensional material graphene*".[82]

Offering these promising properties, graphene has been proposed and widely explored for various applications, ranging from energy conversion and storage systems, to next-generation electronic and optical devices such as transistors, sensors, detectors, etc.[85-86] Until now, graphene's commercial success has not yet matched its hype. Graphene is a simple material composed of only one element, which somewhat limits its versatility[87] and as it does not have an intrinsic bandgap, it is not interesting for semiconductor technology. For example, due to the semimetallic properties of graphene, field-effect transistors (FETs) fabricated from graphene cannot be effectively switched off, yielding low on/off switching ratios. Although bandgap engineering in graphene is possible *via* nanostructuring[88-90], chemical functionalization[91] or applying a high electric field to bilayer graphene [92], these methods add complexity and diminish mobility. These intrinsic limits of graphene can potentially be overcome by other semiconducting 2D nanosheets, e.g. MoS_2, that offer a large diversity of composition, structure, and functionality.

Molybdenum sulfide

In contrast to graphene, MoS_2 (Figure 1.1.3.2d) shows semiconducting behavior with an indirect band gap of 1.2 eV. The bandgap changes with the exfoliation state monotonically − with decreasing number of layers per flake it switches from an indirect (1.2 eV) to a direct bandgap (1.9 eV) for a single-layered nanosheet (Figure 1.1.3.1.).[35] Due to the bandgap dependence on the exfoliation state, MoS_2 received a lot of attention and already shows various applications.[37, 93-94] By changing the structure, the bandgap can be tailored as desired.[95] While multilayerd MoS_2 is not photoluminescent, exfoliation-induced changes in the electronic structure lead to photoluminescence in a monolayered nanosheet.[94] It is expected that this behavior may also occur in other layered materials.[96] Field effect transistors (FET) based on monolayered MoS_2 show mobilities of at least 200 $cm^2\ V^{-1}\ s^{-1}$ at ambient conditions with on/off ratios exceeding 10^8[97] and an exceptionally stable transistor operation under large mechanical deformation.[98] Electronic sensors produced from few-layered MoS_2 sheets have an excellent sensitivity towards NO detection[99] and MoS_2 nanosheets are also promising materials for catalytic hydrogenation,[100-101] potential building blocks for thermoelectrics,[102] energy storage devices[103] or top-gate phototransistors.[93]

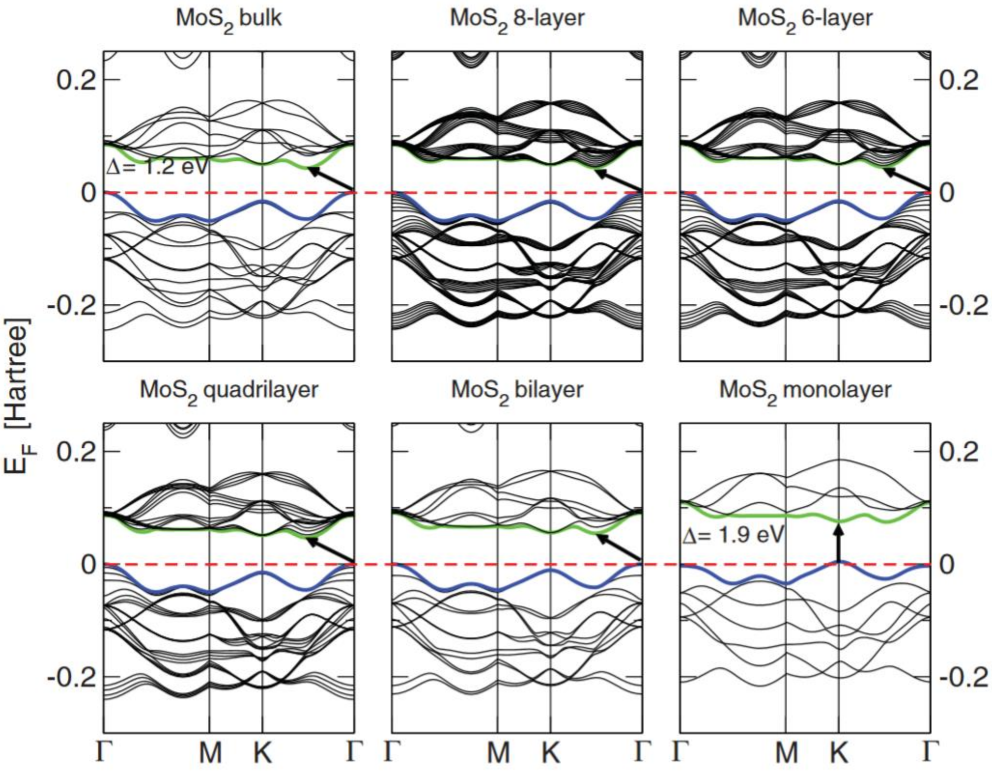

Figure 1.1.3.1. Band structure of bulk and monolayered MoS_2 calculated from first principles.[104] The dashed line represents the Fermi level, the arrows indicate the fundamental band gap. Valence and conductions band are highlighted in blue and green, respectively. Reprinted with permission from the reference [104]. Copyright 2011 by the American Physical Society.

In addition to MoS_2, many other layered materials are of potential interest for nanotechnology, e.g. PTI, *h*-BN, or LDHs. Some of these materials are schematically represented as nanosheets in Figure 1.1.3.2. Another potential class of compounds is the sulfides, i.e. the semiconducting materials SnS or SnS_2. Tin sulfide is a central part of this work and is therefore further introduced in the following chapter (*1.2 Tin sulfides*).

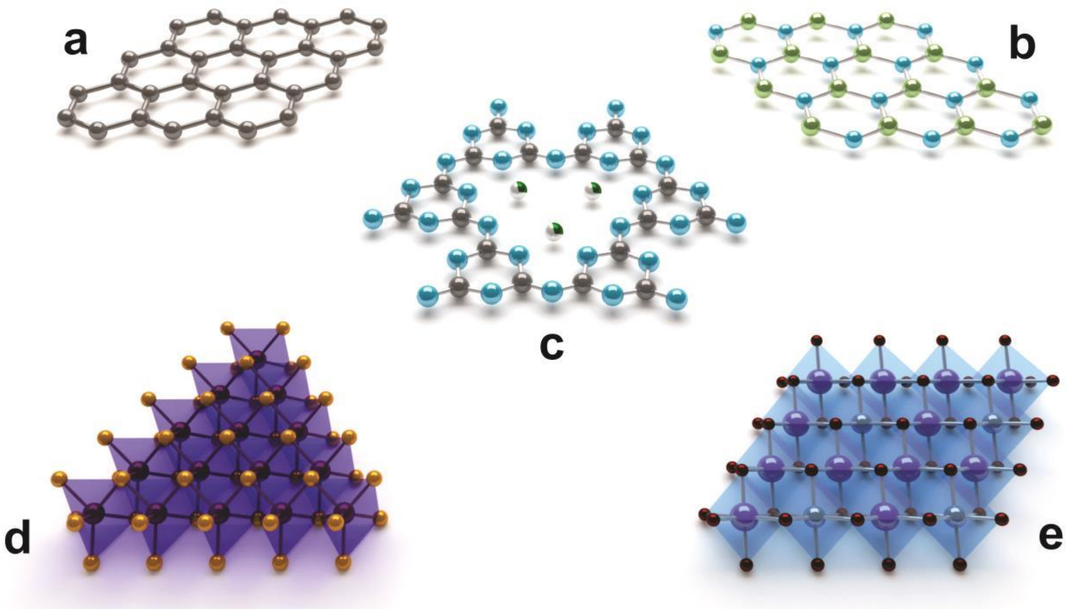

Figure 1.1.3.2. Schematic representation of monolayers of (a) graphite (graphene, hexagonal arrangement of carbon atoms), (b) *h*-BN (hexagonal arrangement of alternating B and N atoms), (c) poly(triazine imide) ((C3N3)2(NH)3LiCl; connected triazine units with intercalated lithium ions), (d) 2H-MoS_2 (edge-sharing MoS_6 trigonal prisms) and (e) a schematic LDH nanosheet (edge-sharing MO_6 octahedra).

1.2 Tin sulfides

Due to its two different oxidation states of +II and +IV, tin can be coordinated by sulfur (-II) either trigonal or tetragonal pyramidal, as well as in octahedral geometry.[105] The most common binary solid-state compounds of tin and sulfur are SnS, SnS_2 and Sn_2S_3 (see Fig. 1.2.1), which can all be synthesized by solid-state reactions of stoichiometric amounts of sulfur and tin.

SnS, also known as the mineral "Herzenbergit", crystallizes in the orthorhombic space group *Pnma* (no. 62) with a = 11.1827(7) Å, b = 3.9767(5) and c = 4.3240(6) Å.[106] Its structural motifs comprise layers of edge-sharing Sn-S tetragonal pyramides (Figure 1.2.1a).

SnS_2 has at least 21 polytypes.[107] The most common one is the 2H phase which is built up of covalent Sn-S layers consisting of edge-sharing SnS_6 octahedra; the separate layers are weakly connected by van der Waals forces. The compound crystallizes in the trigonal space group $P\bar{3}m1$ (no. 164) with a = 3.647(1) Å, b = 3.647(1) Å and c = 5.886(3) Å (Figure 1.2.1b).[108] Two other basic polytypes are 4H ($P6_3mc$, no. 186; a = 3.645 Å, b = 3.645 Å and c = 11.802 Å)[109] and 18R ($R\bar{3}m$, no. 166; a = 3.643 Å, b = 3.643 Å and c = 53.05 Å)[110].

$Sn^{+II}Sn^{+IV}S_3$ was discovered by J. Ottemann who is the originator of its mineral name "ottemannite".[111] It is a mixed-valent compound with a ribbon structure and two different Sn-based structure motifs: the Sn^{+II} site is coordinated in a trigonal pyramidal geometry, whereas the Sn^{+IV} site is octahedrally coordinated by sulfur. Sn_2S_3 crystallizes in the orthorhombic space group *Pnma* (no. 62) with a = 8.878(2) Å, b = 3.751(1) Å, c = 14.020(3) Å (Figure 1.2.1c).[112]

In contrast to Sn_2S_3, SnS and SnS_2 are layered materials and therefore may possibly be exfoliated. SnS and SnS_2 nanosheets can be obtained by bottom-up reactions[113-114] and SnS_2 nanosheets can also be produced by mechanical exfoliation.[115] Both compounds are semiconductors with unique optical and electronic properties and are therefore of interest for various electronic applications. Depending on the synthesis conditions, SnS can be either *n*- or *p*-type semiconductor[116] with both a direct (1.32 eV) and an indirect bandgap (1.0-1.13 eV).[117] Due to these properties, SnS is a potential narrow band gap semiconductor,[118] near-infrared detector,[119-120] photoconductor,[121] photovoltaic material with high energy conversion efficiency,[122] or a potential semiconductor sensor in environmental, industrial or biomedical monitoring.[105] SnS_2 on the other hand has a larger bandgap of 2.21−2.35 eV[16, 123] and shows a strong anisotropy of optical properties due to its layered structure. The photo-conducting properties make it a potential candidate for solar cells and opto-electronic devices.[124] It is further also interesting for holographic recording systems and electrical switching devices.[125-126] Due to the possible exfoliation, SnS_2 and SnS are of special interest for nanotechnology research. SnS_2 nanosheets for example have been explored as nanolayered transistor with high on/off ratio,[115] photocatalyst,[127] or even as electrode material[128-130].

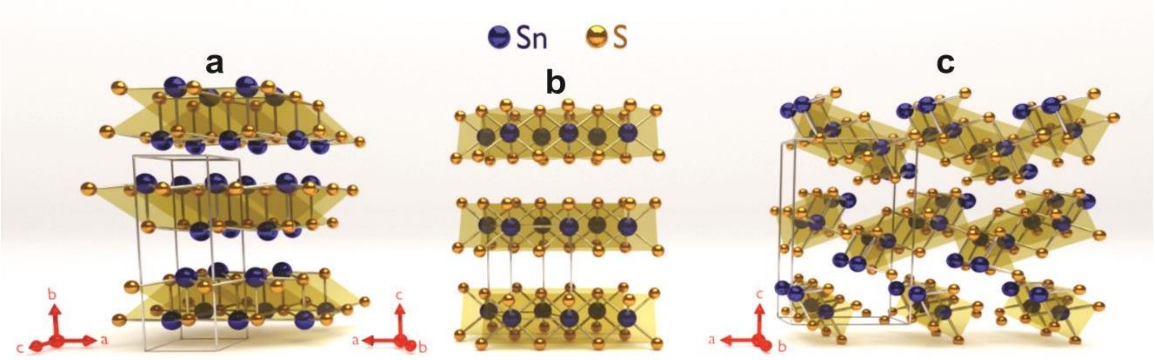

Figure 1.2.1. Crystal structures of (a) SnS (*Pnma*, no.62), (b) SnS_2 ($P\bar{3}m1$, no. 164) and Sn_2S_3 (*Pnma*, no. 62).

In this thesis, tin (IV) sulfide was investigated for its application in field-effect transistors due to its semiconducting behaviour. Furthermore, lithium intercalated tin (IV) sulfide was examined and tested as a solid Li^+ ion conductor for its possible use in all solid-state batteries. The principles of these two electronic devices are described in the sections *1.3 Transistors* and *1.4 All-solid-state Li^+ Ion Batteries.*

1.3 Transistors

In 1947, over 100 years after the discovery of silicon by J. J. Berzelius,[131] a new era of semiconductor technology began with the development of the first transistor by W. B. Shockley, J. Bardeen and W. Brattain (Figure 1.3.1).[132] This groundbreaking invention was honored in 1956 with the Nobel Prize in physics *for their researches on semiconductors and their discovery of the transistor effect*.[133] To date, silicon has become an indispensable part of our technology as it is the most important semiconducting material in electrical circuits.

In general, a transistor is an electronic device built from a semiconductor that is controlled by electronic signals. It has a connection to an external circuit and at least three terminals. A current flowing through one pair of terminals is controlled by a current or a voltage applied to another pair of terminals. Two kinds of transistors can be distinguished: bipolar transistors (BJT; from bipolar junction transistor) and field-effect transistors (FET). A BJT can have two different configurations (*npn* and *pnp*) and the conductivity is controlled by a current. If the transistor uses an electric field to control the conductivity of a channel of one type of charge carriers, it is called a FET (as e.g. in metal-oxide semiconductor FETs; MOSFETs). The FET is often used as a switching device and as the controlled power can be higher than the control power, both BJT and FET can be seen as signal amplifying electronic devices.

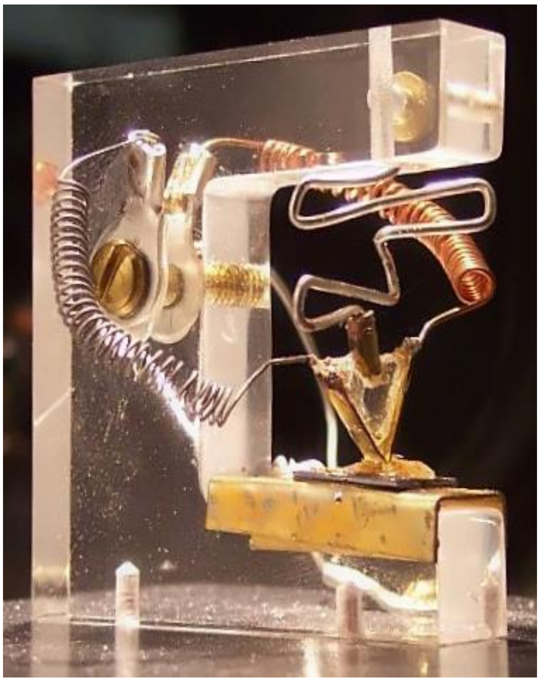

Figure 1.3.1. Replica of the first transistor, built by Shockley, Bardeen and Brattain in 1947/48. (Picture source: DrJunge - de.wikipedia.org – CC Attribution-Share Alike 3.0 Unported license.)

Bipolar transistor

The key to BJTs is the nature of *pn* junctions.[134] Figure 1.3.2 schematically displays such a *pn* junction with holes (in red) in the *p* type material, representing deficiencies of electrons that can act like positive charge carriers, and electrons (in blue), representing available negative charge carriers from the *n* type material. If both materials are brought into contact, electrons can diffuse at the interface from the *n* to the *p* type material and recombine with holes which finally results in a depletion layer consisting of positively and negatively charged ions (see Figure 1.3.2 right). When the Coulombic forces are high enough to prevent further electron migration (i.e. when electrons are repelled from the negative ions in the *p* type material but are attracted by the positive ions in the *n* type material), an equilibrium state is reached.

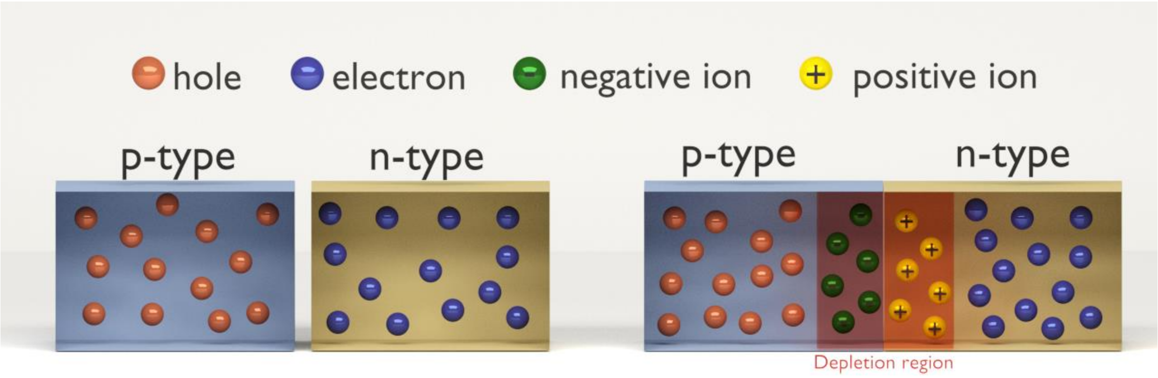

Figure 1.3.2. *pn* junction of two doped silicon materials. Left: Representation of a *p* and *n* doped material. Right: The combination of electrons and holes at the *pn* interface depletes the holes in the *p* and the electrons in the *n* region. The result is a depletion layer of negatively and positively charged ions which accumulate at the interface and thereby block further electron diffusion.

Figure 1.3.3 presents the energy diagram of three different states of *pn* junctions: equilibrium state, reverse-bias and forward-bias mode. In equilibrium, the energy of the valence and conduction band of the *p* doped material is increased. In reverse bias, a reversed voltage (+ at the *n* type material, − at the *p* type material) drives the electrons away from the junction and thereby prevents conduction (Figure 1.3.3 middle). In forward bias mode the applied voltage (− at the *n* type material, + at the *p* type material) assists electrons to overcome the Coulombic forces of the depletion region, resulting in electrons flowing with small resistance in the forward direction (Figure 1.3.3 right).

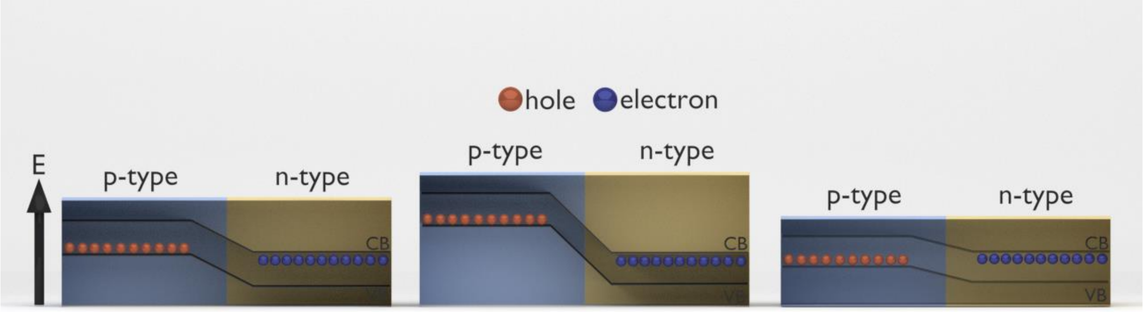

Figure 1.3.3. Energy scheme of a *pn* junction. In equilibrium state (left) Coulombic forces prevent electrons (in blue) from further migration. In reverse bias mode (middle) the reverse voltage drives the electrons away from the junction, preventing conduction. In forward bias mode (right) the applied voltage assists electrons to flow, resulting in small resistance in forward direction.

The BJT consists of two *pn*-junctions and uses both kinds of charge carriers, electrons and holes (Figure 1.3.4.). Without any current applied, the BJT is in an equilibrium state and the depletion layer at the two *pn*-junctions can block an applied current I_c. When a small current I_B is applied to the base, charge carriers can flow between the collector and the emitter. As electron mobility is higher than hole mobility, most of the BJTs are *npn* type (as represented in Figure 1.3.4). The larger collector current I_c is proportional to the base current I_B by a factor β ($I_c = I_B \cdot \beta$). As $I_B << I_c$, a bipolar transistor is called a signal amplifying electronic device.

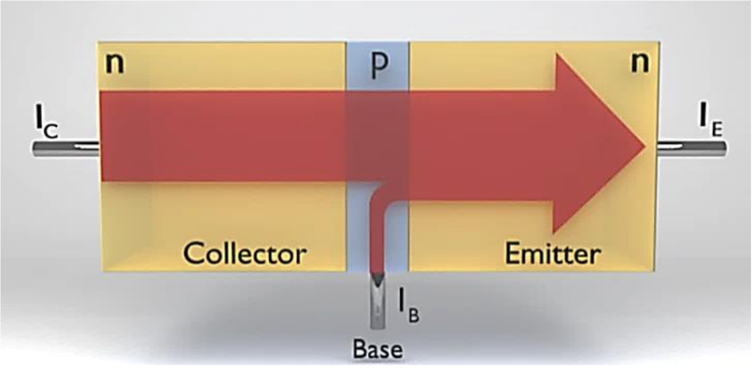

Figure 1.3.4. The structure of a *npn* BJT. A smaller base current I_B is controlling the larger collector current I_C. If $I_B = 0$, the depletion layer is blocking electron migration. If $I_B > 0$, the depletion layer disappears and the current I_C can flow through the transistor. As I_B is much smaller than I_C, the transistor acts as a signal amplifying electronic device.

Metal-oxide-semiconductor FET

The ongoing research on transistors finally resulted in the MOSFET. The MOSFET is nowadays by far the most common transistor in digital and analog circuits. In contrast to a BJT, the FET does not necessarily need a *pn* junction as, for example, in the case of a thin film transistor (see Figure 1.3.5b). The gate (G) terminal in the MOSFET is electrically insulated from the semiconducting channel. It serves to control the electrostatic potential at the semiconductor/insulator interface. In the most commonly used MOSFET the gate is a highly conductive metal which is connected to the *npn* junction through an insulator, e.g. SiO_2 (Figure 1.3.5a). The main advantage of the MOSFET is that it needs only small currents (~1 mA) for switching on while it delivers a much higher current of 10 to 50 A. The MOS layer can be seen as a capacitor. When a voltage U_{GS} is applied to the gate that is larger than the minimum voltage U_{min}, the electric field induces electrons in the channel region close to the insulator-semiconductor interface through band bending processes. Thereby, the channel gets highly conductive and a current I_{DS} can flow after applying a Drain-Source-Voltage U_{DS}. This situation is the “on” state of the transistor. If the applied U_{GS} voltage is smaller than U_{min}, the channel is non-conductive and the transistor is in the “off” state.

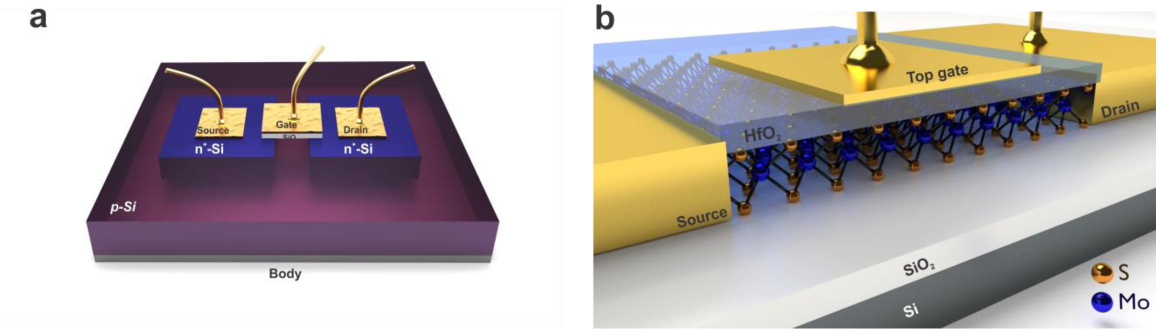

Figure 1.3.5. Schematic representation of a FET (a) with and (b) without a *pn* junction. In (a), the most commonly used MOSFET is presented. It has a *npn* junction and the gate is a highly conductive metal which is connected to the junction through an insulator, e.g. SiO_2. (b) A top gate FET built up from one MoS_2 layer.[97] A *pn* junction is not needed as the applied gate voltage induces an electric field that produces highly conductive electrons by band bending processes.

In future, more and more portable devices such as tablets or smartphones will need powerful CPUs with small sizes. Therefore, these very small FETs should respond quickly to variations in the gate voltage, which requires highly mobile carriers in the channel and short gates. FETs with extremely short gate lengths (<100 nm) however suffer from degraded electrostatics and other problematic short-channel effects.[135] Scaling theory predicts that a FET with a thin barrier (i.e. the semiconductor) and a thin gate (i.e. the oxide layer) will be robust against these short-channel effects down to very short gate lengths.[136] The possibility of having channels that are just a few atomic layers thick (obtained, for example, by exfoliation of layered semiconducting materials) is perhaps the most attractive future option for transistor research. Hence, device engineers devote considerable efforts to developing very small transistors in which short-channel effects are suppressed and series resistances are minimized. Moreover, thin film transistors give the possibility to build transistors on flexible substrates. As SnS_2 can be easily grown in large, anisotropic, flexible crystals (around 1 cm lateral size with a thickness of 0.5 mm), it was tested as a thin film FETs and is presented in Chapter 2.

1.4 All-solid-state Li^+ ion batteries

1.4.1 History

The idea to build Li^+ ion batteries (LIBs) goes back to M. S. Whittingham while he was working for Exxon in 1976. He suggested to use lithium for high energy density storage systems as it is the lightest (M = 6.94 g mol^{-1}) and the most electropositive metal (-3.04 V vs. SHE).[137] He and J. B. Goodenough, who significantly contributed to modern Li^+ ion batteries especially with the discovery of the most important cathode material $LiCoO_2$,[138] are surely candidates for the nobel prize in chemistry as they were laying the scientific foundation for the development of ubiquitous LIBs.[139]

In 1977, the final move to the commercially available LIB of today was made by Samar Basu. He demonstrated the electrochemical intercalation of lithium in graphite, which led to the development of the first working lithium intercalated graphite electrodes at the Bell Labs (LiC_6).[140-142] The first commercialized LIB was launched by Sony Co. in 1991- a rechargeable battery with a carbon anode and a $LiCoO_2$ cathode. It was a high performance, high voltage battery with U = 4 V. Alternatives to $LiCoO_2$ and graphite have been investigated for years now [143-145] and many other materials have been reported. Alternatives to graphite are, for example silicon, $Li_4Ti_5O_{12}$ or SnO_2. However, Li-intercalated graphite has not been replaced yet as it shows the lowest operating voltage against lithium (0-0.25 V), has a high rechargeable capacity of more than 350 mAh g^{-1}, and good reversibility for Li intercalation/deintercalation. $LiCoO_2$ can be replaced for example by $LiNi_{0.33}Co_{0.33}Mn_{0.33}O_2$, $LiNi_{0.8}Co_{0.15}Al_{0.05}O_2$, $LiMn_2O_4$ or $LiFePO_4$. Nickel-based materials such as $LiNi_{0.8}Co_{0.15}Al_{0.05}O_2$ deliver higher capacities of 870-970 mAh cm^{-3} than $LiCoO_2$ with 808 mAh cm^{-3}. SAFT Co. has adopted $LiNi_{0.8}Co_{0.15}Al_{0.05}O_2$ as cathode material in LIBs for electric vehicles.[107] Manganese spinel cathode materials have the advantage that they are rich in resource and therefore cheap. They have been used for LIBs in cellular phones and hybrid electric vehicles from Nissan Co. Ltd.[107] Commercial cells still use mainly $LiCoO_2$ as it shows a flat operating voltage of about 4 V versus Li and a rechargeable capacity of about 140 mA h g^{-1} and due to the good conditions of graphite it is very difficult to replace both materials to improve the energy density of LIBs.[146] The need for these LIBs is meanwhile immense: in 2013, five billion Li^+ ion cells were sold to supply laptops, mobile phones and cameras; the development of electric vehicles and large-scale energy storage devices will further expand the market for LIBs.[147]

1.4.2 Conventional Li^+ ion battery

A battery generally provides two functions: energy storage and energy conversion (from chemical to electrical energy and *vice versa*). The working principle of a Li^+ ion battery is based on Li^+ ions moving between the positive and negative electrode. Figure 1.3.2 schematically displays a typical Li^+ ion battery. The positive electrode (cathode) is e.g. $LiCoO_2$, the negative electrode (anode) is e.g. graphite. During the charging process, Li^+ ions are extracted from $LiCoO_2$ and incorporated into graphite. Both electrodes are separated by a Li^+ ion conducting electrolyte, e.g. $LiPF_6$ dissolved in a mixture of ethylene carbonate (EC) and diethyl carbonate (DEC). The battery is fully charged when the graphite is fully intercalated with Li^+ ions (Figure 1.4.2.1).

Compared to the first commercial LIB, recent devices show twice the efficiency and the technology has been applied to thin, light, and flexible portable electronic devices, and more recently to batteries for transportation systems.[147] Although these common LIBs play a significant role in our daily life, they have some disadvantages. They contain a liquid electrolyte to transport the Li^+ ions between the cathode and anode, which increases the chance of leakage.[148-149] Furthermore, the formation of dendrites of Li combined with overcharging or short-circuiting can lead to high temperatures, often resulting in fire or explosions due to the highly flammable organic electrolytes.[144, 149-150] Many such cases were already reported throughout the world. If LIBs are planned to power manned electric vehicles one day, stricter safety requirements are needed. Besides higher energy and power densities, these safety issues are the main focus on current LIB research.

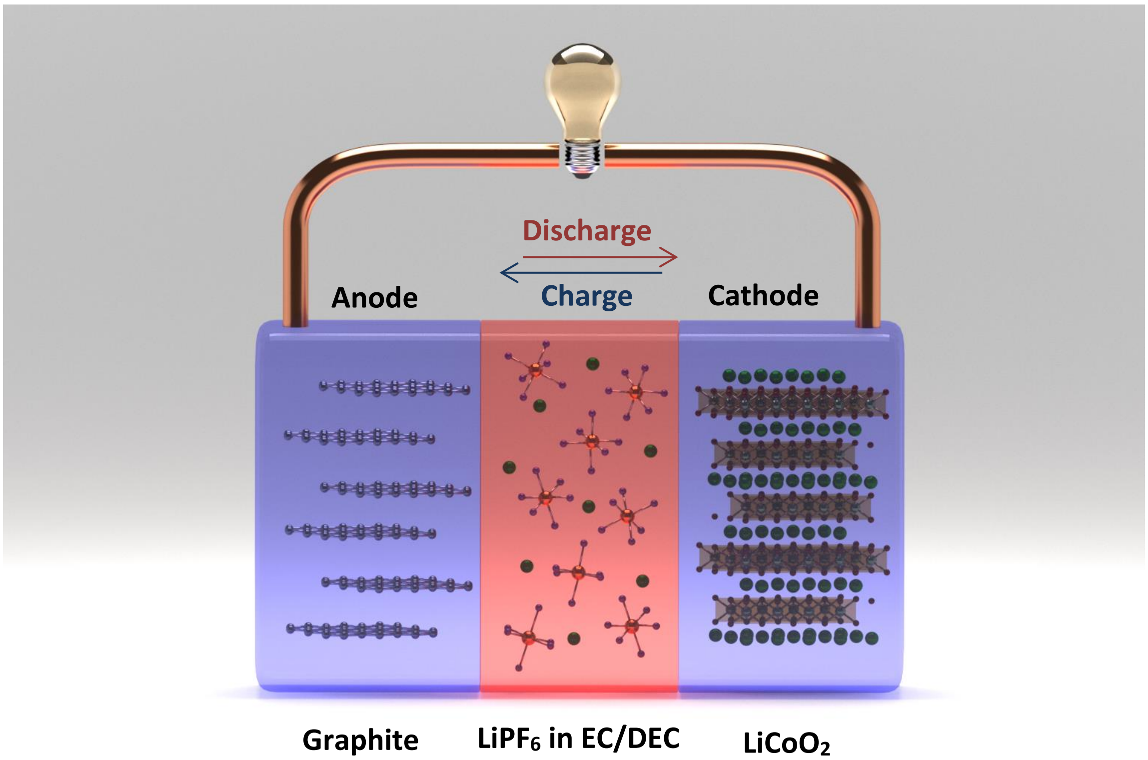

Figure 1.4.2.1. Schematic representation of a typical liquid LIB. Li^+ is intercalated in graphite during the charge process (blue). During discharge, Li^+ moves back to $LiCoO_2$ (red). The liquid electrolyte can be e.g. $LiPF_6$ in DEC/EC.

1.4.3 All-solid-state Li^+ ion battery

One idea to solve the current safety problems is the investigation of all-solid-state LIB (ASSLIB).[144, 148-149, 151-152] The operational principle of ASSLIB is no different from the traditional LIB; it comprises an anode and cathode material separated by a solid electrolyte instead of a liquid electrolyte used in the common LIB, and a metal layer (gold, copper, platinum) at both electrodes to improve the electrical contact.[153-154] The advantages of using a solid electrolyte can be the use of Li metal as the anode material and a reduction in the net weight and volume, and therefore greater energy densities[155] which affords better efficiencies and, of course, the elimination of the leakage problem.[149] An example of an ASSLIB with $LiCoO_2$ as cathode, Li metal as anode and the fast Li^+ ion conductor $Li_{10}GeP_2S_{12}$ (LGPS) as solid electrolyte is shown in Figure 1.4.3.1.

In recent decades, solid-state batteries, especially these based on Li metal anodes have been widely investigated.[152, 156-160] ASS batteries can be grouped by their electrolyte, e.g. polymer solid electrolytes or inorganic solid electrolytes. Until now, all of these ASSLIB have relatively low power densities, high ionic resistances at room temperature and high manufacturing costs.[161] Inorganic solid electrolytes have the advantage compared to polymers that they have high temperature stability, are mechanically stable and non-flammable.[162]

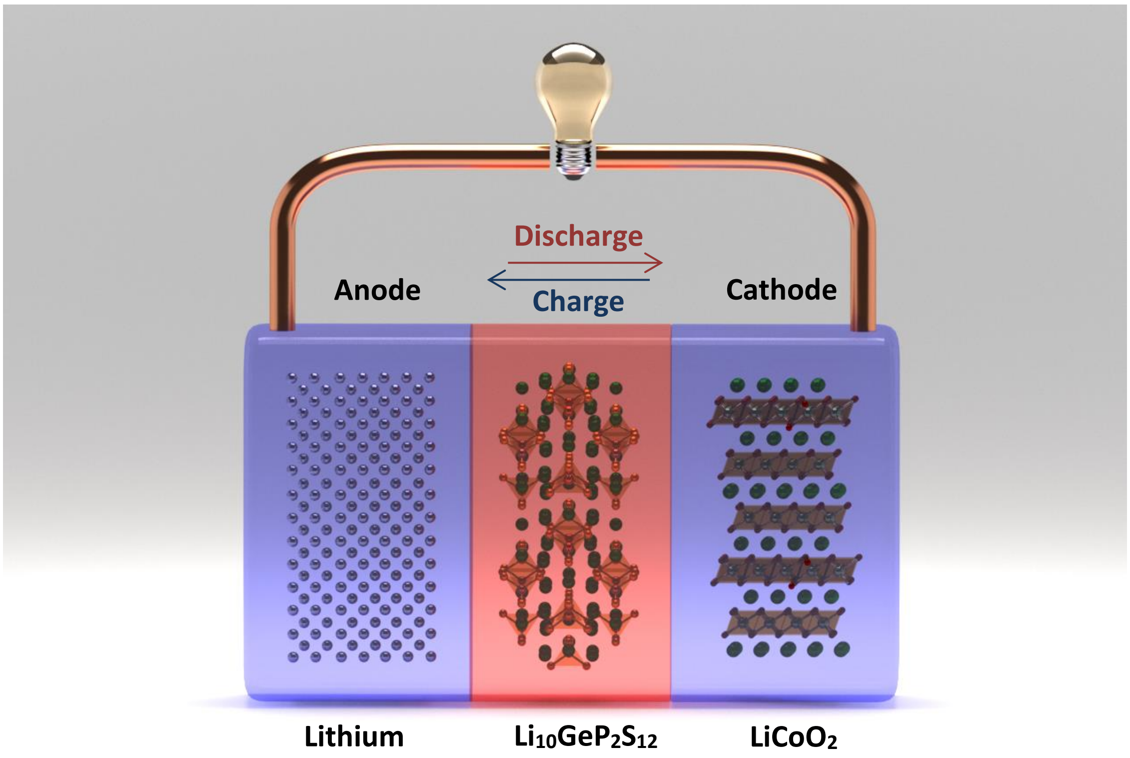

Figure 1.4.3.1. Schematic representation of an ASSLIB with $LiCoO_2$ as cathode, Li metal as anode and $Li_{10}GeP_2S_{12}$ as solid electrolyte. Li^+ migrates to the anode material (here Li metal) during the charging process (blue direction). During discharge, Li^+ moves back to the cathode (here $LiCoO_2$). The liquid electrolyte is replaced by a Li^+ ion conducting solid compound, here $Li_{10}GeP_2S_{12}$.

1.4.4 Inorganic solid electrolytes

The ideal Li solid electrolyte should have a high room temperature conductivity with a low activation energy and a low electron transference number of $t_e < 10^{-4}$ (i.e. a negligible electronic conductivity). The ionic conductivity is thereby dependent on the temperature according to the Arrhenius law $\sigma_T = \sigma_0 \cdot \exp[E_a\ k_B^{-1}\ T^{-1}]$ (T: temperature, σ: ion conductivity, k_B: Boltzmann constant, E_a: activation energy). Between lg σ_T and T^{-1}, there should exist a linear relation. If a polycrystalline material is used as solid electrolyte, the grain-boundary resistance should be negligibly small and for industrial developments the solid electrolyte should be cheap and non-toxic. One of the most important features, however, is the stability against chemical reactions with the electrodes, especially the (electro-) chemical stability against lithium and a large electrochemical window.[156]

Overview of Li^+ ion conductors

Figure 1.4.4.1 presents an overview of various Li^+ ion conductors. Since its discovery in the 1970s, lithium nitride (Li_3N) and its doped variants have been the best Li^+ ion conductors ($\sigma_{298K} = 6 \cdot 10^{-3}$ S cm^{-1}). However, due to its high reactivity and low electrochemical decomposition potential, Li_3N is not suitable for commercial applications.[53, 110] Other Li^+ ion conducting materials with high conductivities are e.g. oxide perovskites ($La_{0.3}Li_{0.5}TiO_3$; $\sigma_{298K} \approx 1 \cdot 10^{-3}$ S cm^{-1}),[163] garnet-type systems such as $Li_7La_3Zr_2O_{12}$ ($\sigma_{298K} \approx 3 \cdot 10^{-4}$ S cm^{-1}) or $Li_6BaLa_2Ta_2O_{12}$ ($\sigma_{298K} = 4 \cdot 10^{-5}$ S cm^{-1}),[164-165] sulfides such as Li_4SnS_4 ($\sigma_{298K} \approx 7 \cdot 10^{-5}$ S cm^{-1})[166] and the 70 $Li_2S \cdot 30$ P_2S_5 glass ceramic ($\sigma_{298K} \approx 3.2 \cdot 10^{-3}$ S cm^{-1})[167] and mixed chalcogenide glassy materials (Li_2S-SiS_2-Li_3PO_4; $\sigma_{298K} \approx 7.6 \cdot 10^{-4}$ S cm^{-1}).[168] During recent years, the initial interest in oxides such as $Li_{14}ZnGe_4O_{16}$ (LISICON)[169] and lithium phosphorous oxynitride (LIPON)[170] was replaced by research into sulfide-based solid electrolytes. One of the first sulfide electrolytes in the Li_2S-SiS_2 system (0.24 SiS_2 - 0.36 Li_2S – 0.40 LiI) was produced by Kennedy *et al.*[171-172] in 1986, using a melt-quenching synthesis method. It showed ion conductivities in the range of 10^{-6} to 10^{-3} S cm^{-1}.[171-172] Kawamoto *et al.*[173] reported in 2002 the ionic conductivity of thio-LISICONS that were found in the Li_2S-SiS_2-Al_2S_3 and Li_2S-SiS_2-P_2S_5 systems. Thereby, $Li_{4-x}Si_{1-x}P_xS_4$ ($x = 0.6$) showed high ionic conductivities of $6.4 \cdot 10^{-4}$ S cm^{-1}.

With the groundbreaking discovery of $Li_{10}GeP_2S_{12}$ (LGPS) in 2011 by Kamaya *et al.*, [174] lithium solid electrolytes reached conductivities comparable to liquid ones for the first time. LGPS is a sulfide based lithium superionic conductor (related to the thio-LiSICONs) with a framework surrounding Li conducting channels, exhibiting one of the highest room temperature Li^+ conductivities known to date ($\sigma_{298K} = 1.2 \cdot 10^{-2}$ S cm^{-1}, Figure 1.4.4.2) and structurally related to the oxide prototype LISICON $Li_{2+2x}Zn_{1-x}GeO_4$ with $\sigma_{298K} \approx 1 \cdot 10^{-7}$ S cm^{-1}.[175-176] This led to a wide range of fundamental studies on ionic mobility in the structurally related tetragonal solid solution with composition $Li_{11-x}M_{2-x}P_{1+x}S_{12}$ (M = Si, Ge, Sn) and promoted the development of next generation batteries.[177-178] After exchanging the expensive element Ge by the much cheaper Si, the conductivity of $Li_{11}Si_2PS_{12}$ was even higher than for $Li_{10}GeP_2S_{12}$ ($D_{NMR,\ RT} = 2.2 \cdot 10^{-12}$ m^2 s^{-1} for Ge,

$D_{\text{NMR, RT}} = 3.5 \cdot 10^{-12}$ m^2 s^{-1} for Si) in the range of 10^{-2} S cm^{-1} as determined by NMR measurements).[179]

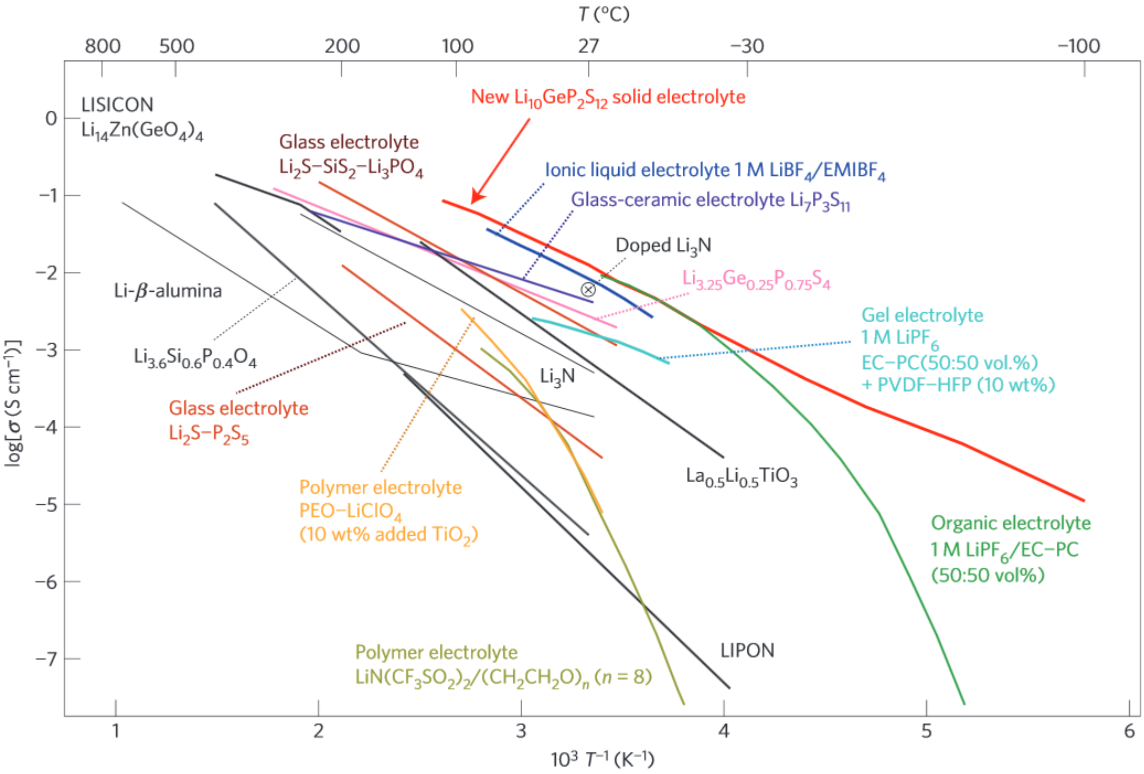

Figure 1.4.4.1. Ionic conductivity vs. temperature of various electrolytes: in the presented image, the highest room temperature Li^+ ion conductivity (12 mS cm^{-1}) is achieved with $Li_{10}GeP_2S_{12}$. The low electron transference number of solid electrolytes increases their conductivity compared to organic electrolytes which have transference numbers of around 0.5.[174] Reprinted with permission from Macmillan Publishers Ltd: Nature Materials[174], copyright 2011.

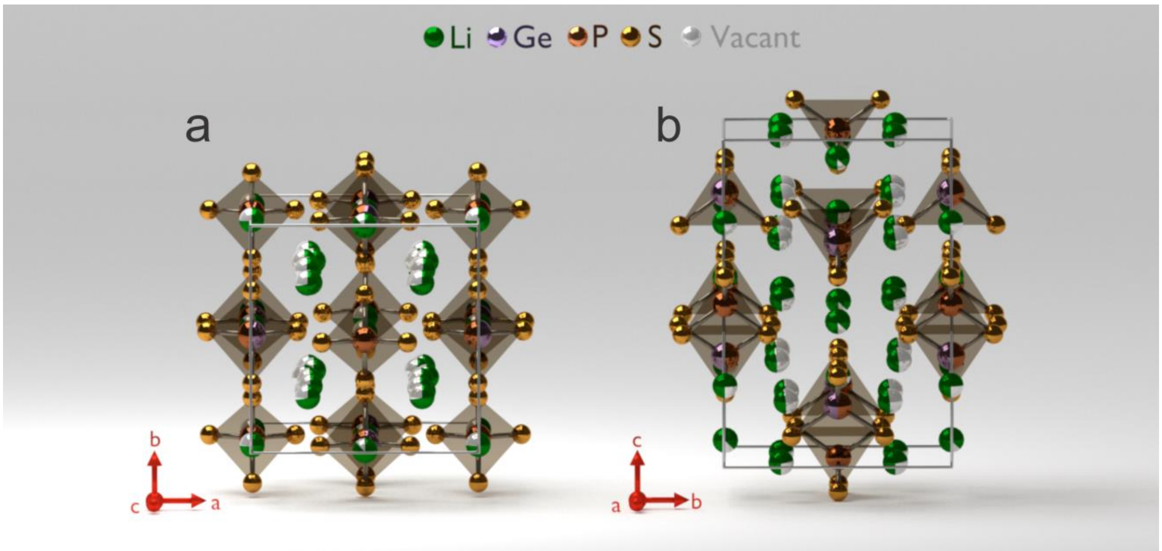

Figure 1.4.4.2. Crystal structure of $Li_{10}GeP_2S_{12}$ ($P4_2/nmc$, no. 137) (a) along [001] and (b) along [100]. P and Ge are tetrahedrally coordinated by sulfur. Lithium can migrate through the crystal along all three dimensions, with the preferred Li trajectory being along [001].

However, the synthesis of $Li_{11}Si_2PS_{12}$ was performed with a multi-anvil press and is therefore not interesting for commercial applications. One of the most recently published discoveries is that, by adding chlorine ($Li_{9.54}Si_{1.74}P_{1.44}S_{11.7}Cl_{0.3}$), the high pressure synthesis could be avoided while the electrochemical stability and the ionic conductivity could be improved even further ($\sigma_{298K} = 2.5\cdot10^{-2}$ S cm^{-1}).[180] Some Li^+ ion conductivities of solid sulfide electrolytes are listed in Table 1.4.4.1.

Table 1.4.4.1. Ionic conductivities σ of various solid sulfide Li^+ ion conductors at room temperature (RT).

Material	σ_{RT} / S cm^{-1}	Material	σ_{RT} / S cm^{-1}
$Li_{9.54}Si_{1.74}P_{1.44}S_{11.7}Cl_{0.3}$[180]	$2.5\cdot10^{-2}$	$Li_7P_3S_{11}$ ($Li_2S\cdot P_2S_5$)[181-182]	$1.7\cdot10^{-2}$
$Li_7P_2S_8$ [183]	$6.3\cdot10^{-4}$	$Li_{10}GeP_2S_{12}$ [174, 177]	$1.2\cdot10^{-2}$
Li_7GePS_8 [177]	$4.0\cdot10^{-3}$	$Li_{10}SnP_2S_{12}$ [179]	$7.0\cdot10^{-3}$

The commercial application of these materials for next-generation ASSLIBs is still ongoing. $Li_{10}GeP_2S_{12}$ which is the most promising solid electrolyte, is currently investigated by Toyota for battery applications.[184] Further search for solid electrolytes with Li^+ ion conductivities of > 1 mS cm^{-1} is of great fundamental interest and of practical importance not only for ASSLIBs but also for other, emerging battery technologies such as Li air batteries which would also benefit from the advantages of solid electrolytes.

1.5 Objectives

The continuous development and size reduction of electronic devices are key challenges in our information and technology age. Field-effect transistors (FETs) are more than ever indispensable as modern computers need to become more efficient. Therefore, modern FETs must become smaller while exhibiting identical computing power. Nevertheless, current silicon transistors are expected to reach their fundamental size limit soon; one idea to overcome this problem is to investigate new technologies for transistors such as thin film devices constructed with nanosheets. The initial idea was to use graphene as it is an ultrathin material showing extremely high mobilities, but due to the absence of a bandgap, other semiconducting nanosheet materials appear more promising for certain applications such as FETs. The first attempts to build FETs with metal dichalcogenide nanosheets were made in 2011. A. Kis *et al*.[97] demonstrated a FET comprising a single-layer MoS_2 nanosheet using a hafnium oxide layer as the gate dielectric (Figure 1.3.5). With this, they could reach RT current on/off ratios in the order of 10^8. They were able to increase the mobility to at least 200 $cm^2\ V^{-1}\ s^{-1}$ compared to MoS_2 transistors without the hafnium oxide layer, which had only 0.5-3 $cm^2\ V^{-1}\ s^{-1}$.[185] Although it is already possible to build FETs from nanosheets, there is no commercialized device yet. SnS_2 is another suitable candidate for these transistors: it is easy to synthesize, can be exfoliated due to its layered structure, and has a bandgap of around 2 eV. Besides the miniaturization, the high aspect ratio of nanosheets offers the possibility of producing transistors on flexible substrates, for example, for smartphone or tablet displays. Chapter 2 of this thesis, entitled *Threshold-voltage control and enhancement-mode characteristics in multilayer tin disulfide field-effect transistors by gate-oxide passivation with an alkylphosphonic acid self-assembled monolayer* was performed in collaboration with the group of Dr. Hagen Klauk from the Max Planck Institute for Solid State Research and is directed towards building FETs from multilayer SnS_2 platelets. We deposited SnS_2 by the scotch-tape method and analyzed the effect of hydrophobic substrate coating on the transistor behavior.

As the scotch-tape method is hard to apply for SnS_2 and it is difficult to obtain single-layer nanosheets with reasonable lateral size, other exfoliation methods were investigated. Liquid chemical exfoliation routes such as intercalation with *n*-butyllithium in hexane under inert gas or electrochemical lithium intercalation followed by ultrasonication are inconvenient and often lead to nanosheets with defects. The next chapter of this thesis, entitled *A facile wet chemistry approach towards unilamellar tin sulfide nanosheets from $Li_{4x}Sn_{1-x}S_2$ solid solutions*, deals with the direct solid-state lithium intercalation of SnS_2 with lithium sulfide to improve the exfoliation process. The obtained solid solution $Li_{4x}Sn_{1-x}S_2$ was analyzed for their exfoliation behavior and optical properties. Additionally, the crystal structure of the mother compound Li_2SnS_3 ($x = 0.33$) was investigated by single crystal X-ray diffraction.

In Chapter 4, entitled *$Li_{0.6}[Li_{0.2}Sn_{0.8}S_2]$ – a layered lithium superionic conductor*, we further investigated $Li_{0.6}[Li_{0.2}Sn_{0.8}S_2]$ ($x = 0.2$) as it showed the best exfoliation properties among the x values tested. The structure solution of $Li_{0.6}[Li_{0.2}Sn_{0.8}S_2]$ showed tetrahedrally coordinated interlayer Li sites in addition to the octahedrally coordinated ones. This is in contrast to Li_2SnS_3, where only the octahedrally coordinated sites are occupied. Furthermore, many vacancies are present in $Li_{0.6}[Li_{0.2}Sn_{0.8}S_2]$. Li_2SnS_3 is known to be a Li^+ ion conductor. In 2015, Brant *et al.*[186] showed that it has a RT conductivity of 10^{-5} S cm^{-1}, a high thermal stability (melting point ~ 750 °C) as well as stability under ambient conditions. Moreover, Ceder *et al.*[187] published in 2015 several design principles for solid state lithium superionic conductors. Through calculations, they revealed a fundamental relationship between anion packing and ionic transport. Li^+ migration *via* tetrahedral sites is most desirable for achieving high ionic conductivities. These tetrahedral sites are available in $Li_{0.6}[Li_{0.2}Sn_{0.8}S_2]$. Therefore, we investigated the Li^+ ion conducting properties of $Li_{0.6}[Li_{0.2}Sn_{0.8}S_2]$ with impedance and PFG NMR measurements.

During our studies, we observed that $Li_{0.6}[Li_{0.2}Sn_{0.8}S_2]$ is hygroscopic. If the powder was left in air, a hydrated compound was formed. The instability of fast solid-state ion conductors to humid air is an immense problem in current research regarding all-solid-state devices such as batteries, supercapacitors, electrochemical sensors or actuators. While the assembly of these devices under inert gas is feasible, a safety risk remains if the packaged compounds show chemical reactions in air, such as in the case of damages to the housing of the device. In the last part of this thesis (Chapter 5), entitled *Air-tolerant Li^+ conductivity in $Li_{0.6}[Li_{0.2}Sn_{0.8}S_2]$*, the air-stability and the subsequent hydration of $Li_{0.6}[Li_{0.2}Sn_{0.8}S_2]$ was investigated. The hygroscopicity was expected to be the reason for the outstanding exfoliation behavior. We analyzed the crystal structure and the water uptake by TGA, ssNMR and PXRD measurements. Furthermore, as $Li_{0.6}[Li_{0.2}Sn_{0.8}S_2]$ is known to be a fast

Li^+ ion conductor (see Chapter 4), the change in Li^+ ion conduction during this hydration process was examined with PFG NMR measurements.

The work presented in this thesis advances the fields of air-tolerant fast solid Li^+ ion conductors for future solid electrolytes and thin film semiconducting layers for FETs. We anticipate the progress made in this thesis will be of importance for next-generation ASSLIBs with improved safety conditions and the production of thin flexible displays.

1.6 Bibliography

[1] V. Nicolosi, M. Chhowalla, M. G. Kanatzidis, M. S. Strano, J. N. Coleman, *Science* **2013**, *340*.

[2] R. H. Friend, A. D. Yoffe, *Advances in Physics* **1987**, *36*, 1.

[3] K. S. Novoselov, A. K. Geim, S. V. Morozov, D. Jiang, Y. Zhang, S. V. Dubonos, I. V. Grigorieva, A. A. Firsov, *Science* **2004**, *306*, 666.

[4] H. Lüschen, *Die Namen der Steine. Das Mineralreich im Spiegel der Sprache., Vol. 2*, Ott Verlag, Thun, **1979**.

[5] M. S. Whittingham, A. J. Jacobson, *Intercalation Chemistry, Vol. 3*, Academic Press, New York, **1982**.

[6] C. Schlenker, J. Dumas, M. Greenblatt, S. van Smaalen, *Physics and Chemistry of Low-Dimensional Inorganic Conductors, Vol. 354*, Plenum Press, New York, **1996**.

[7] D. R. Allan, A. A. Kelsey, S. J. Clark, R. J. Angel, G. J. Ackland, *Physical Review B* **1998**, *57*, 5106.

[8] S. M. Auerbach, K. A. Carrado, R. K. Dutta, *Handbook of layered materials*, Marcel Dekker Inc., New York/Basel, **2004**.

[9] S. Z. Butler, S. M. Hollen, L. Cao, Y. Cui, J. A. Gupta, H. R. Gutiérrez, T. F. Heinz, S. S. Hong, J. Huang, A. F. Ismach, E. Johnston-Halperin, M. Kuno, V. V. Plashnitsa, R. D. Robinson, R. S. Ruoff, S. Salahuddin, J. Shan, L. Shi, M. G. Spencer, M. Terrones, W. Windl, J. E. Goldberger, *ACS Nano* **2013**, *7*, 2898.

[10] P. Miro, M. Audiffred, T. Heine, *Chemical Society Reviews* **2014**, *43*, 6537.

[11] B. Elvers, S. Hawkins, G. Schulz, *Ullmann's Encyclopedia of Industrial Chemistry Vol. A16*, VCH, New York, **1990**.

[12] A. H. Thompson, F. R. Gamble, C. R. Symon, *Materials Research Bulletin* **1975**, *10*, 915.

[13] K. Kourtakis, J. DiCarlo, R. Kershaw, K. Dwight, A. Wold, *Journal of Solid State Chemistry* **1988**, *76*, 186.

[14] L. E. Conroy, K. C. Park, *Inorganic Chemistry* **1968**, *7*, 459.

[15] G. Said, P. A. Lee, *Physica Status Solidi (a)* **1973**, *15*, 99.

[16] D. L. Greenaway, R. Nitsche, *Journal of Physics and Chemistry of Solids* **1965**, *26,* 1445.

[17] C. R. Whitehouse, A. A. Balchin, *Journal of Crystal Growth* **1979**, *47*, 203.

[18] J. George, C. K. Valsala Kumari, *Solid State Communications* **1984**, *49*, 103.

[19] Y. Ishizawa, Y. Fujiki, *Tokyo Sugaku Kaisya Zasshi* **1973**, *35*, 1259.

[20] B. Palosz, W. Palosz, S. Gierlotka, *Bulletin de minéralogie* **1986**, *109*, 143.

[21] A. A. Balchin, *Crystallography and Crystal Chemistry of Materials with Layered Structures*, Springer Netherlands, Dordrecht, **1976**.

[22] L. H. Brixner, *Journal of Inorganic and Nuclear Chemistry* **1962**, *24*, 257.

[23] R. Nitsche, *Journal of Physics and Chemistry of Solids* **1960**, *17*, 163.

[24] R. Nitsche, H. U. Bölsterli, M. Lichtensteiger, *Journal of Physics and Chemistry of Solids* **1961**, *21*, 199.

[25] B. E. Brown, D. J. Beerntsen, *Acta Crystallographica* **1965**, *18*, 31.

[26] R. R. Chianelli, M. B. Dines, *Inorganic Chemistry* **1978**, *17*, 2758.

[27] D. M. Schleich, M. J. Martin, *Journal of Solid State Chemistry* **1986**, *64*, 359.

[28] A. Bensalem, D. M. Schleich, *Materials Research Bulletin* **1988**, *23*, 857.

[29] A. Bensalem, D. M. Schleich, *Materials Research Bulletin* **1990**, *25*, 349.

[30] R. L. Bedard, L. D. Vail, S. T. Wilson, E. M. Flanigen, *Crystalline microporous metal sulfide compositions*, **1989**, US Patent 4880761.

[31] W. K. Hofmann, *Journal of Materials Science* **1988**, *23*, 3981.

[32] J. Cheon, J. E. Gozum, G. S. Girolami, *Chemistry of Materials* **1997**, *9*, 1847.

[33] M. S. Donley, N. T. McDevitt, T. W. Haas, P. T. Murray, J. T. Grant, *Thin Solid Films* **1989**, *168*, 335.

[34] M. S. Donley, P. T. Murray, S. A. Barber, T. W. Haas, *Surface and Coatings Technology* **1988**, *36*, 329.

[35] M. Chhowalla, H. S. Shin, G. Eda, L.-J. Li, K. P. Loh, H. Zhang, *Nature Chemistry* **2013**, *5*, 263.

[36] D. Merki, S. Fierro, H. Vrubel, X. Hu, *Chemical Science* **2011**, *2*, 1262.

[37] Y. Li, H. Wang, L. Xie, Y. Liang, G. Hong, H. Dai, *Journal of the American Chemical Society* **2011**, *133*, 7296.

[38] T. Stephenson, Z. Li, B. Olsen, D. Mitlin, *Energy & Environmental Science* **2014**, *7*, 209.

[39] X. Zong, H. Yan, G. Wu, G. Ma, F. Wen, L. Wang, C. Li, *Journal of the American Chemical Society* **2008**, *130*, 7176.

[40] S. Nagata, T. Aochi, T. Abe, S. Ebisu, T. Hagino, Y. Seki, K. Tsutsumi, *Journal of Physics and Chemistry of Solids* **1992**, *53*, 1259.

[41] A. Beal, W. Liang, *Philosophical Magazine* **1973**, *27*, 1397.

[42] A. I. Khan, D. O'Hare, *Journal of Materials Chemistry* **2002**, *12*, 3191.

[43] D. G. Evans, R. C. T. Slade, in *Layered Double Hydroxides*, Springer, Berlin/Heidelberg, **2006**.

[44] R. Allmann, *Chimica* **1970**, *24*, 99.

[45] Y. Guo, D. Li, C. Hu, Y. Wang, E. Wang, Y. Zhou, S. Feng, *Applied Catalysis B: Environmental* **2001**, *30*, 337.

[46] Y. Guo, D. Li, C. Hu, Y. Wang, E. Wang, *Chemical Journal of Chinese Universities* **2001,** *22*, 1453.

[47] Y. Guo, D. Li, C. Hu, Y. Wang, E. Wang, *International Journal of Inorganic Materials* **2001**, *3*, 347.

[48] A. Gualtieri, A. Viani, G. Banchio, G. Artioli, *Materials Science Forum* **2001**, *378*, 702.

[49] S. Guggenheim, R. Martin, *Clays and clay minerals* **1995**, *43*, 255.

[50] R. Ma, T. Sasaki, *Advanced Materials* **2010**, *22*, 5082.

[51] R. Ma, T. Sasaki, *Accounts of Chemical Research* **2015**, *48*, 136.

[52] M. Dion, M. Ganne, M. Tournoux, *Materials Research Bulletin* **1981**, *16*, 1429.

[53] N. Mercier, A. Riou, *Chemical Communications* **2004**, 844.

[54] Z. Zhang, K. Leinenweber, M. Bauer, L. A. J. Garvie, P. F. McMillan, G. H. Wolf, *Journal of the American Chemical Society* **2001**, *123*, 7788.

[55] E. Wirnhier, M. Döblinger, D. Gunzelmann, J. Senker, B. V. Lotsch, W. Schnick, *Chemistry – A European Journal* **2011**, *17*, 3213.

[56] Y. Piffard, A. Lachgar, M. Tournoux, *Journal of Solid State Chemistry* **1985**, *58*, 253.

[57] J. Phair, S. Badwal, *Ionics* **2006**, *12*, 103.

[58] J. P. Rupert, W. T. Granquist, T. J. Pinnavaia, *Chemistry of clays and clay minerals*, Longman Scientific and Technical, Harlow, **1987**.

[59] T. J. Kalman, M. Dudukovic, A. Clearfield, *Advances in Chemistry* **1974**, *133*, 654.

[60] M. J. Manos, M. G. Kanatzidis, *Journal of the American Chemical Society* **2012**, *134*, 16441.

[61] K. Schwinghammer, B. Tuffy, M. B. Mesch, E. Wirnhier, C. Martineau, F. Taulelle, W. Schnick, J. Senker, B. V. Lotsch, *Angewandte Chemie International Edition* **2013**, *52*, 2435.

[62] K. Dokko, M. Nishizawa, S. Horikoshi, T. Itoh, M. Mohamedi, I. Uchida, *Electrochemical and Solid-State Letters* **2000**, *3*, 125.

[63] A. R. Armstrong, P. G. Bruce, *Nature* **1996**, *381*, 499.

[64] E. M. Sabio, M. Chi, N. D. Browning, F. E. Osterloh, *Langmuir* **2010**, *26*, 7254.

[65] H. P. Boehm, A. Clauss, G. O. Fischer, U. Hofmann, *Zeitschrift für Naturforschung B* **1962**, *17b*, 4.

[66] G. L. F. Bergaya, *Handbook of Clay Science, Vol. A: Fundamentals*, Elsevier, Amsterdam, **2013**.

[67] J. N. Coleman, M. Lotya, A. O'Neill, S. D. Bergin, P. J. King, U. Khan, K. Young, A. Gaucher, S. De, R. J. Smith, *Science* **2011**, *331*, 568.

[68] P. Joensen, R. Frindt, S. R. Morrison, *Materials Research Bulletin* **1986**, *21*, 457.

[69] C.-J. Shih, A. Vijayaraghavan, R. Krishnan, R. Sharma, J.-H. Han, M.-H. Ham, Z. Jin, S. Lin, G. L. Paulus, N. F. Reuel, *Nature Nanotechnology* **2011**, *6*, 439.

[70] Z. Zeng, Z. Yin, X. Huang, H. Li, Q. He, G. Lu, F. Boey, H. Zhang, *Angewandte Chemie International Edition* **2011**, *50*, 11093.

[71] G. Eda, H. Yamaguchi, D. Voiry, T. Fujita, M. Chen, M. Chhowalla, *Nano Letters* **2011**, *11*, 5111.

[72] G. Eda, T. Fujita, H. Yamaguchi, D. Voiry, M. Chen, M. Chhowalla, *ACS Nano* **2012**, *6*, 7311.

[73] M. Adachi-Pagano, C. Forano, J.-P. Besse, *Chemical Communications* **2000**, 91.

[74] B. Venugopal, C. Shivakumara, M. Rajamathi, *Journal of Colloid and Interface Science* **2006**, *294*, 234.

[75] M. Jobbágy, A. E. Regazzoni, *Journal of Colloid and Interface Science* **2004**, *275*, 345.

[76] S. Werner, V. W.-h. Lau, S. Hug, V. Duppel, H. Clausen-Schaumann, B. V. Lotsch, *Langmuir* **2013**, *29*, 9199.

[77] U. Hofmann, *Angewandte Chemie International Edition* **1968**, *7*, 681.

[78] N. Miyamoto, H. Yamamoto, R. Kaito, K. Kuroda, *Chemical Communications* **2002**, 2378.

[79] T. Sasaki, M. Watanabe, H. Hashizume, H. Yamada, H. Nakazawa, *Journal of the American Chemical Society* **1996**, *118*, 8329.

[80] T. Sasaki, *Journal of the Ceramic Society of Japan* **2007**, *115*.

[81] C. Lee, X. Wei, J. W. Kysar, J. Hone, *Science* **2008**, *321*, 385.

[82] The Nobel Prize in Physics 2010, Nobel Media AB 2014, http://www.nobelprize.org/nobel_prizes/physics/laureates/2010/ (December 14th, 2016)

[83] C. Rao, K. Biswas, K. Subrahmanyam, A. Govindaraj, *Journal of Materials Chemistry* **2009**, *19*, 2457.

[84] J. Allen Mattew, C. Tung Vincent, B. Kaner Richard, *Chemical Reviews* **2010**, *110*, 132.

[85] K. S. Novoselov, V. Fal, L. Colombo, P. Gellert, M. Schwab, K. Kim, *Nature* **2012**, *490*, 192.

[86] X. Huang, X. Qi, F. Boey, H. Zhang, *Chemical Society Reviews* **2012**, *41*, 666.

[87] M. Osada, T. Sasaki, *Advanced Materials* **2012**, *24*, 210.

[88] M.-W. Lin, C. Ling, Y. Zhang, H. J. Yoon, M. M.-C. Cheng, L. A. Agapito, N. Kioussis, N. Widjaja, Z. Zhou, *Nanotechnology* **2011**, *22*, 265201.

[89] X. Li, X. Wang, L. Zhang, S. Lee, H. Dai, *Science* **2008**, *319*, 1229.

[90] M. Y. Han, B. Özyilmaz, Y. Zhang, P. Kim, *Physical Review Letters* **2007**, *98*, 206805.

[91] R. Balog, B. Jørgensen, L. Nilsson, M. Andersen, E. Rienks, M. Bianchi, M. Fanetti, E. Lægsgaard, A. Baraldi, S. Lizzit, *Nature Materials* **2010**, *9*, 315.

[92] Y. Zhang, T.-T. Tang, C. Girit, Z. Hao, M. C. Martin, A. Zettl, M. F. Crommie, Y. R. Shen, F. Wang, *Nature* **2009**, *459*, 820.

[93] H. S. Lee, S.-W. Min, Y.-G. Chang, M. K. Park, T. Nam, H. Kim, J. H. Kim, S. Ryu, S. Im, *Nano Letters* **2012**, *12*, 3695.

[94] A. Splendiani, L. Sun, Y. Zhang, T. Li, J. Kim, C.-Y. Chim, G. Galli, F. Wang, *Nano Letters* **2010**, *10*, 1271.

[95] K. F. Mak, C. Lee, J. Hone, J. Shan, T. F. Heinz, *Physical Review Letters* **2010**, *105*, 136805.

[96] Q. H. Wang, K. Kalantar-Zadeh, A. Kis, J. N. Coleman, M. S. Strano, *Nature Nanotechnology* **2012**, *7*, 699.

[97] B. Radisavljevic, A. Radenovic, J. Brivio, V. Giacometti, A. Kis, *Nature Nanotechnology* **2011**, *6*, 147.

[98] J. Pu, Y. Yomogida, K.-K. Liu, L.-J. Li, Y. Iwasa, T. Takenobu, *Nano Letters* **2012**, *12*, 4013.

[99] H. Li, Z. Yin, Q. He, H. Li, X. Huang, G. Lu, D. W. H. Fam, A. I. Y. Tok, Q. Zhang, H. Zhang, *Small* **2012**, *8*, 63.

[100] X. Huang, Z. Zeng, S. Bao, M. Wang, X. Qi, Z. Fan, H. Zhang, *Nature Communications* **2013**, *4*, 1444.

[101] J. Kibsgaard, Z. Chen, B. N. Reinecke, T. F. Jaramillo, *Nature Materials* **2012**, *11*, 963.

[102] R. J. Smith, P. J. King, M. Lotya, C. Wirtz, U. Khan, S. De, A. O'Neill, G. S. Duesberg, J. C. Grunlan, G. Moriarty, *Advanced Materials* **2011**, *23*, 3944.

[103] K. Chang, W. Chen, *ACS Nano* **2011**, *5*, 4720.

[104] A. Kuc, N. Zibouche, T. Heine, *Physical Review B* **2011**, *83*, 245213.

[105] T. Jiang, G. A. Ozin, *Journal of Materials Chemistry* **1998**, *8*, 1099.

[106] D. Eppelsheimer, *Zeitschrift für Kristallographie* **1981**, *156*, 36.

[107] B. Palosz, W. Palosz, S. Gierlotka, *Acta Crystallographica. Section C: Crystal Structure Communications* **1985**, *41*, 807.

[108] J. Morales, J. Santos, J. R. R. Barrado, J. P. Espinós, *Journal of Solid State Chemistry* **2000**, *150*, 391.

[109] J. Guenter, H. Oswald, *Naturwissenschaften* **1968**, *55*, 177.

[110] C. Whitehouse, A. Balchin, *Journal of Materials Science* **1979**, *14*, 2516.

[111] G. H. Moh, *Neues Jahrbuch für Mineralogie* **1969**, *111*, 36.

[112] R. Kniep, D. Mootz, U. Severin, H. Wunderlich, *Acta Crystallographica Section B: Structural Crystallography and Crystal Chemistry* **1982**, *38*, 2022.

[113] Y. Zhang, J. Lu, S. Shen, H. Xu, Q. Wang, *Chemical Communications* **2011**, *47*, 5226.

[114] G. Shen, D. Chen, K. Tang, L. Huang, Y. Qian, G. Zhou, *Inorganic Chemistry Communications* **2003**, *6*, 178.

[115] D. De, J. Manongdo, S. See, V. Zhang, A. Guloy, H. Peng, *Nanotechnology* **2012**, *24*, 025202.

[116] M. Ristov, G. Sinadinovski, I. Grozdanov, M. Mitreski, *Thin Solid Films* **1989**, *173*, 53.

[117] A. Tanuševski, D. Poelman, *Solar Energy Materials and Solar Cells* **2003**, *80*, 297.

[118] S. Lopez, A. Ortiz, *Semiconductor Science and Technology* **1994**, *9*, 2130.

[119] P. Pramanik, P. Basu, S. Biswas, *Thin Solid Films* **1987**, *150*, 269.

[120] N. K. Reddy, K. R. Reddy, *Thin Solid Films* **1998**, *325*, 4.

[121] J. Johnson, H. Jones, B. Latham, J. Parker, R. Engelken, C. Barber, *Semiconductor Science and Technology* **1999**, *14*, 501.

[122] T. Kosugi, K. Murakami, S. Kaneko, *MRS Proceedings* **1997**, *485*, 273.

[123] C. Lokhande, *Journal of Physics D: Applied Physics* **1990**, *23*, 1703.

[124] D. Chen, G. Shen, K. Tang, S. Lei, H. Zheng, Y. Qian, *Journal of Crystal Growth* **2004**, *260*, 469.

[125] S. Patil, R. Tredgold, *Journal of Physics D: Applied Physics* **1971**, *4*, 718.

[126] D. Chun, R. Walser, R. Bene, T. Courtney, *Applied Physics Letters* **1974**, *24*, 479.

[127] W. Du, D. Deng, Z. Han, W. Xiao, C. Bian, X. Qian, *CrystEngComm* **2011**, *13*, 2071.

[128] T.-J. Kim, C. Kim, D. Son, M. Choi, B. Park, *Journal of Power Sources* **2007**, *167*, 529.

[129] T. Momma, N. Shiraishi, A. Yoshizawa, T. Osaka, A. Gedanken, J. Zhu, L. Sominski, *Journal of Power Sources* **2001**, *97–98*, 198.

[130] H. S. Kim, Y. H. Chung, S. H. Kang, Y.-E. Sung, *Electrochimica Acta* **2009**, *54*, 3606.

[131] J. J. Berzelius, *Proceedings of the Royal Science Acadamey* **1824**, *12*, 52.

[132] W. Shockley, J. Bardeen, W. Brattain, *Bell Laboratories (Dec. 16, 1947)* **1947**.

[133] The Nobel Prize in Physics 1956, Nobel Media AB 2014, http://www.nobelprize.org/ nobel_prizes/physics/laureates/1956/

[134] J. S. Yuan, J. J. Liou, *Semiconductor Device Physics and Simulations*, Plenum Press, New York, **2013**.

[135] F. Schwierz, H. Wong, J. J. Liou, *Nanometer CMOS*, Pan Stanford Publishing, **2010**.

[136] D. J. Frank, Y. Taur, H.-S. Wong, *IEEE Electron Device Letters* **1998**, *19*, 385.

[137] M. S. Whittingham, *Science* **1976**, *192*, 1126.

[138] K. Mizushima, P. Jones, P. Wiseman, J. Goodenough, *Materials Research Bulletin* **1980**, *15*, 783.

[139] T. Reuters: Nobel Prize predictions: Chemistry. http://sciencewatch.com/nobel/ 2015-predictions/chemistry-laureates (December 14th, 2016)

[140] S. Basu, *Rechargable battery*, **1983**, US Patent 4304825A.

[141] S. Basu, *Ambient temperature rechargeable battery*, **1981**, US Patent 4423125 A.

[142] S. Basu, C. Zeller, P. Flanders, C. Fuerst, W. Johnson, J. Fischer, *Materials Science and Engineering* **1979**, *38*, 275.

[143] T. Ohzuku, A. Ueda, *Solid State Ionics* **1994**, *69*, 201.

[144] M. S. Whittingham, *Chemical Reviews* **2004**, *104*, 4271.

[145] T. Ohzuku, R. J. Brodd, *Journal of Power Sources* **2007**, *174*, 449.

[146] K. Ozawa, *Lithium Ion Rechargeable Batteries: Materials, Technology, and New Applications*, John Wiley & Sons, **2012**.

[147] R. V. Noorden, *Nature* **2014**, *507*, 3.

[148] P. V. Braun, J. Cho, J. H. Pikul, W. P. King, H. Zhang, *Current Opinion in Solid State and Materials Science* **2012**, *16*, 186.

[149] J. Chen, *Materials* **2013**, *6*, 156.

[150] W. Li, J. R. Dahn, D. S. Wainwright, *Science-AAAS-Weekly Paper Edition-including Guide to Scientific Information* **1994**, *264*, 1115.

[151] S. B. Peterson, J. Apt, J. Whitacre, *Journal of Power Sources* **2010**, *195*, 2385.

[152] J. Janek, W. G. Zeier, *Nature Energy* **2016**, *1*, 16141.

[153] P. G. Bruce, *Chemical Communications* **1997**, 1817.

[154] Y. Yoon, C. Park, J. Kim, D. Shin, *Journal of Power Sources* **2013**, *226*, 186.

[155] Y. Kato, K. Kawamoto, R. Kanno, M. Hirayama, *Electrochemistry* **2012**, *80*, 749.

[156] C. Delmas, M. Menetrier, L. Croguennec, S. Levasseur, J. Peres, C. Pouillerie, G. Prado, L. Fournes, F. Weill, *International Journal of Inorganic Materials* **1999**, *1*, 11.

[157] R. Jasinski, *Journal of Electroanalytical Chemistry and Interfacial Electro-chemistry* **1970**, *26*, 189.

[158] R. Jasinski, *Journal of Electroanalytical Chemistry and Interfacial Electro-chemistry* **1967**, *15*, 89.

[159] J. B. Goodenough, *Solid State Ionics* **1997**, *94*, 17.

[160] V. Kharton, F. Marques, A. Atkinson, *Solid State Ionics* **2004**, *174*, 135.

[161] C. A. Vincent, *Solid State Ionics* **2000**, *134,* 159.

[162] K. Takada, *Acta Materialia* **2013**, *61*, 759.

[163] Y. Inaguma, C. Liquan, M. Itoh, T. Nakamura, T. Uchida, H. Ikuta, M. Wakihara, *Solid State Communications* **1993**, *86*, 689.

[164] R. Murugan, V. Thangadurai, W. Weppner, *Angewandte Chemie International Edition* **2007**, *46*, 7778.

[165] V. Thangadurai, W. Weppner, *Advanced Functional Materials* **2005**, *15,* 107.

[166] T. Kaib, S. Haddadpour, M. Kapitein, P. Bron, C. Schröder, H. Eckert, B. Roling, S. Dehnen, *Chemistry of Materials* **2012**, *24*, 2211.

[167] F. Mizuno, A. Hayashi, K. Tadanaga, M. Tatsumisago, *Advanced Materials* **2005**, *17*, 918.

[168] K. Takada, N. Aotani, S. Kondo, *Journal of Power Sources* **1993**, *43,* 135.

[169] P. G. Bruce, A. West, *Journal of The Electrochemical Society* **1983**, *130,* 662.

[170] X. Yu, J. Bates, G. Jellison, F. Hart, *Journal of the Electrochemical Society* **1997**, *144,* 524.

[171] J. H. Kennedy, Y. Yang, *Journal of The Electrochemical Society* **1986**, *133,* 2437.

[172] J. H. Kennedy, S. Sahami, S. W. Shea, Z. Zhang, *Solid State Ionics* **1986**, *18*, 368.

[173] R. K. M. Murayama, M. Irie, S. Ito, T. Hata, N. Sonoyama, Y. Kawamoto, *Journal of Solid State Chemistry* **2002**, *168,* 140.

[174] N. Kamaya, K. Homma, Y. Yamakawa, M. Hirayama, R. Kanno, M. Yonemura, T. Kamiyama, Y. Kato, S. Hama, K. Kawamoto, *Nature Materials* **2011**, *10*, 682.

[175] H.-P. Hong, *Materials Research Bulletin* **1978**, *13*, 117.

[176] P. Bruce, A. West, *Journal of Solid State Chemistry* **1982**, *44*, 354.

[177] A. Kuhn, V. Duppel, B. V. Lotsch, *Energy & Environmental Science* **2013**, *6*, 3548.

[178] B. R. Shin, Y. J. Nam, D. Y. Oh, D. H. Kim, J. W. Kim, Y. S. Jung, *Electrochimica Acta* **2014**, *146*, 395.

[179] A. Kuhn, O. Gerbig, C. Zhu, F. Falkenberg, J. Maier, B. V. Lotsch, *Physical Chemistry Chemical Physics* **2014**, *16*, 14669.

[180] Y. Kato, S. Hori, T. Saito, K. Suzuki, M. Hirayama, A. Mitsui, M. Yonemura, H. Iba, R. Kanno, *Nature Energy* **2016**, *1*, 16030.

[181] Y. Seino, T. Ota, K. Takada, A. Hayashi, M. Tatsumisago, *Energy & Environmental Science* **2014**, *7*, 627.

[182] H. Yamane, M. Shibata, Y. Shimane, T. Junke, Y. Seino, S. Adams, K. Minami, A. Hayashi, M. Tatsumisago, *Solid State Ionics* **2007**, *178*, 1163.

[183] E. Rangasamy, Z. Liu, M. Gobet, K. Pilar, G. Sahu, W. Zhou, H. Wu, S. Greenbaum, C. Liang, *Journal of the American Chemical Society* **2015**, *137*, 1384.

[184] C. Yada, C. Brasse, *ATZ Elektronik* **2014**, *9*, 10

[185] K. Novoselov, D. Jiang, F. Schedin, T. Booth, V. Khotkevich, S. Morozov, A. Geim, *Proceedings of the National Academy of Sciences of the United States of America* **2005**, *102*, 10451.

[186] J. A. Brant, D. M. Massi, N. Holzwarth, J. H. MacNeil, A. P. Douvalis, T. Bakas, S. W. Martin, M. D. Gross, J. A. Aitken, *Chemistry of Materials* **2014**, *27*, 189.

[187] Y. Wang, W. D. Richards, S. P. Ong, L. J. Miara, J. C. Kim, Y. Mo, G. Ceder, *Nature Materials* **2015**.

2 Threshold-voltage control and enhancement-mode characteristics in multilayer tin disulfide field-effect transistors by gate-oxide passivation with an alkylphosphonic acid self-assembled monolayer

Ute Zschieschang, Tanja Holzmann, Alexander Kuhn, Mahdieh Aghamohammadi, Bettina V. Lotsch, and Hagen Klauk

published in *J. Appl. Phys.* **2015**, *117*, 104509.

DOI: 10.1063/1.4914488

http://dx.doi.org/10.1063/1.4914488

Threshold-voltage control and enhancement-mode characteristics in multilayer tin disulfide field-effect transistors by gate-oxide passivation with an alkylphosphonic acid self-assembled monolayer

Ute Zschieschang,[1] *Tanja Holzmann,*[1,2,3] *Alexander Kuhn,*[1] *Mahdieh Aghamohammadi,*[1,4]
Bettina V. Lotsch,[1,2,3] *and Hagen Klauk*[1,a)]

[1]Max Planck Institute for Solid State Research, Heisenbergstr. 1, 70569 Stuttgart, Germany

[2]Department of Chemistry, Ludwig-Maximilians-Universität München, Butenandtstr. 5-13, 81377 München, Germany

[3]Nanosystems Initiative Munich (NIM) and Center for Nanoscience, Schellingstr. 4, 80799 München, Germany

[4]Instituto de Ciencias Materiales de Barcelona (ICMAB-CSIC), Campus de la UAB, 08193 Bellaterra, Spain

(Received 14 October 2014; accepted 28 February 2015; published online 11 March 2015)

We have synthesized crystals of two-dimensional layered tin disulfide (SnS_2) by chemical vapor transport and fabricated field-effect transistors based on mechanically exfoliated SnS_2 multilayer platelets. We demonstrate that the threshold voltage of these transistors can be modified by passivating the gate-oxide surface with a self-assembled monolayer of an alkylphosphonic acid, affording transistors with desirable enhancement-mode characteristics. In addition to a positive threshold voltage and a large on/off current ratio, these transistors also have a steep subthreshold swing of 4 V/decade. VC 2015 AIP Publishing LLC. [http://dx.doi.org/10.1063/1.4914488]

2.1 Introduction

Tin disulfide (SnS_2) is a two-dimensional layered metal dichalcogenide semiconductor.[1] Many of its electrical, optical, and catalytic properties are similar to those of molybdenum disulfide (MoS_2)[2] which has received significant attention mainly due to the large electron mobilities that have been measured in single- and multilayer MoS_2 field-effect transistors (FETs).[3–5] A potential advantage of SnS_2 over MoS_2 is its larger bandgap (greater than 2 eV for bulk SnS_2,[1] compared to 1.2 eV for bulk MoS_2, and 1.9 eV for single-layer MoS_2; see Ref. 2), which may translate into transistors having smaller off-state leakage currents and larger on/off current ratios. Recently, De *et al*.[6] and Song *et al*.[7] reported field-effect mobilities of 0.8 cm^2/V s for multilayer SnS_2 transistors[6] and 50 cm^2/V s for single-layer SnS_2 transistors.[7] An undesirable feature of many of the previously reported MoS_2 and SnS_2 transistors is that they show depletion-mode behavior,[3–12] i.e., a significant charge-carrier density is present in the semiconductor channel even at a gate-source voltage of zero, so that a negative gate-source voltage must be applied in order to turn these transistors off. Depletion-mode behavior is undesirable for many FET applications, because it means that the circuit or system requires both a negative and a positive supply voltage.[10–12] The ability to control the threshold voltage during the device fabrication in order to obtain enhancement-mode characteristics is thus a valuable benefit in view of efficient circuit and system design. In single-crystalline silicon metal-oxide-semiconductor field-effect transistors (MOSFETs), the threshold voltage is usually adjusted by incorporating small amounts of either electron-donating or electron-accepting impurity atoms (e.g., phosphorus or boron) into the silicon lattice in the channel region of the transistors. An alternative approach to control the threshold voltage during the fabrication is the passivation of the gate-oxide surface with an organic self-assembled monolayer (SAM).[13] By introducing a hydrophobic aliphatic SAM at the interface between the gate oxide and the semiconductor, the density of mobile charges otherwise present in the semiconductor channel at a gate-source voltage of zero can be greatly reduced by eliminating interfacial dipoles and trap states, thus providing a nearly charge-neutral semiconductor-dielectric interface[14] that leads to the desirable enhancement-mode characteristics. Here, we demonstrate multilayer SnS_2 FETs in which enhancement-mode behavior is achieved by passivating the gate-oxide surface with an alkylphosphonic acid SAM prior to the deposition of the semiconductor. For comparison, we also fabricated multilayer SnS_2 FETs without

SAM modification, and these devices show depletion-mode behavior. To our knowledge, this is the first report of SnS_2 FETs with enhancement-mode characteristics.

2.2 Experiment

Tin disulfide (SnS_2) crystals were synthesized by chemical vapor transport in vacuum-sealed ampoules using a horizontal tubular furnace at a temperature of 700 °C, starting from a pellet of elemental tin and a stoichiometric amount of sulfur and using iodine as a carrier agent.[15] Figure 1 shows several photographs and scanning electron microscopy (SEM) images of the vapor-transport-grown SnS_2 crystals. The two-dimensional layered structure consisting of covalently bound layers of edge-sharing SnS_2 octahedra weakly bound by van der Waals forces is clearly visible in the SEM images.

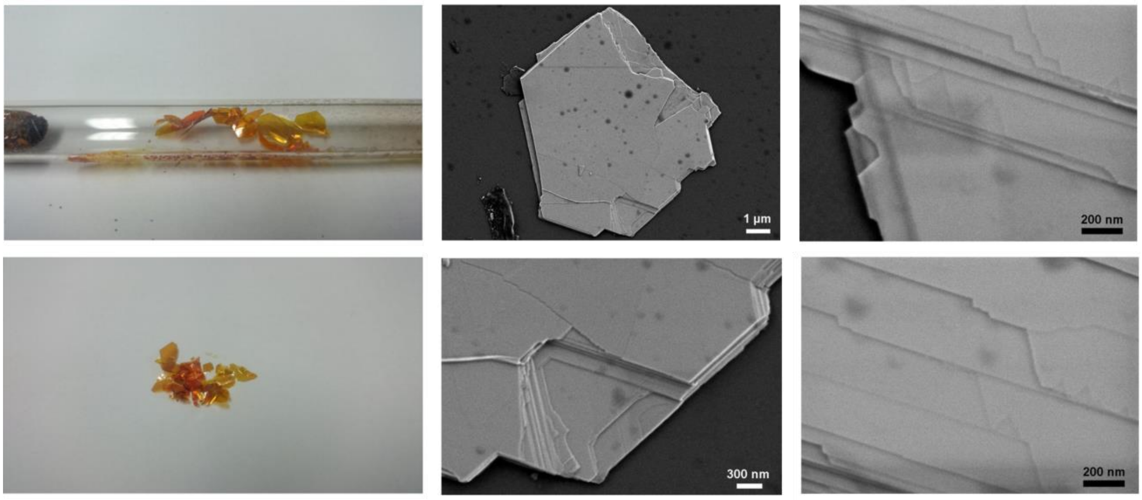

FIG. 1. Photographs and scanning electron microscopy images of SnS_2 crystals produced by chemical vapor transport.

The crystallinity of the SnS_2 platelets was also confirmed by x-ray diffraction (see Figure 2(a)). To estimate the bandgap of the SnS_2 crystals, a diffuse optical reflectance spectrum was measured for wavelengths from 400 to 800 nm (see Figure 2(b)). The reflectance spectrum was transformed according to the Kubelka-Munk formalism, and the bandgap was determined by a linear fit, indicating a bandgap of 2.2 eV.

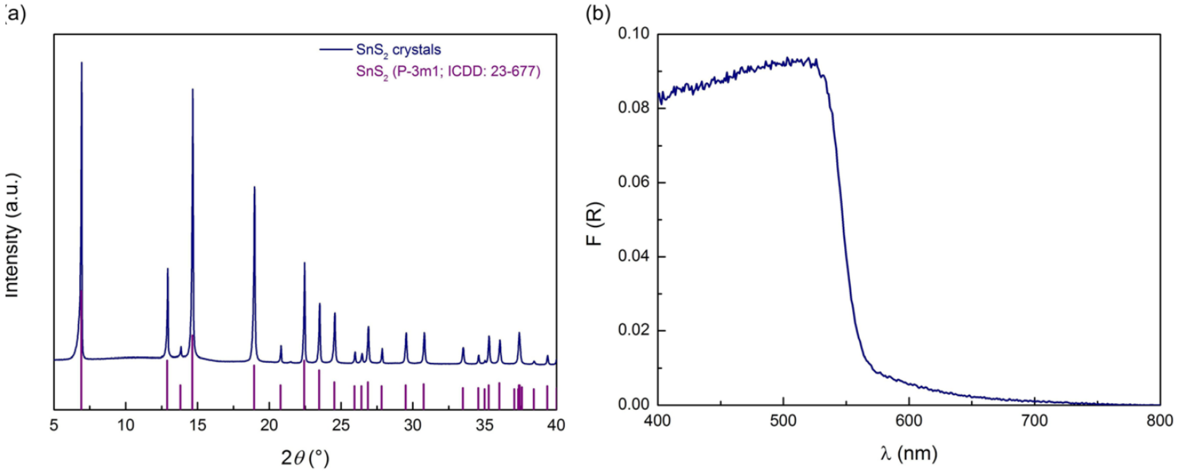

FIG. 2. (a) X-ray diffractogram of one batch of SnS_2 crystals employed in this work. The measured powder pattern is in good agreement with the reference (ICDD: file 23-677). (b) Diffuse optical reflectance spectrum of the same SnS_2 crystal, indicating a bandgap of 2.2 eV (corresponding to an absorption edge of 560 nm).

Transistors were fabricated on heavily boron-doped, thermally oxidized silicon substrates, so that the doped silicon can be used as the gate electrode of the FETs. Prior to the deposition of the semiconductor, the surface of the thermally grown SiO_2 layer was functionalized with a thin layer of aluminum oxide (deposited by atomic layer deposition) and a solution-processed SAM of *n*-tetradecylphosphonic acid.[16] The chemisorption of the alkylphosphonic acid molecules on the Al_2O_3 surface leads to the spontaneous formation of a dense, hydrophobic monolayer, with the alkylphosphonic acid molecules being attached to the Al_2O_3 surface by strong covalent bonds.[17] A beneficial effect of the formation of the SAM is that essentially all hydroxyl groups initially present at the Al_2O_3 surface are eliminated, resulting in a clean, well-defined interface with a greatly reduced density of trap states.[17] The quality of the alkylphosphonic acid SAM was confirmed by contact-angle measurements, which consistently yielded contact angles for water of greater than 110°.[18] The SiO_2/Al_2O_3/SAM gate dielectric has a total thickness of 110 nm and a capacitance per unit area of 34 nF/cm^2.[19] Note that the SAM treatment was performed only in those (relatively small) areas of the substrate in which the transistors were to be fabricated; the remainder of the substrate surface was left hydrophilic, since a completely hydrophobic substrate would have been difficult to uniformly coat with electron-beam resist (which is required for the patterning of the source and drain contacts on the surface of the SnS_2 platelets). Crystalline SnS_2 platelets (flakes) with a thickness of a few hundred nanometers and lateral dimensions of a few tens of microns were then peeled from the SnS_2

crystals by mechanical exfoliation and deposited onto the SAM functionalized Si/SiO_2/Al_2O_3 substrates. We also attempted to produce thinner platelets, but the result were always platelets with very small lateral dimensions, i.e., any platelets with a thickness of less than 100 nm had lateral dimensions of less than 1 µm and were thus not useful for device fabrication. (This problem was recently successfully addressed by Li *et al.*[20] who demonstrated that by exfoliating the flakes first onto a viscoelastic polymeric template and from there onto the hard silicon substrate, very large single-layer MoS_2 flakes can be obtained with excellent yield and quality.) Finally, Ti/Au source and drain contacts were defined on the top surface of the SnS_2 platelets by electron-beam lithography, metal deposition by thermal evaporation in vacuum, and lift-off in organic solvents. All electrical measurements were performed in ambient air at room temperature.

2.3 Results and discussion

Figure 3 shows the schematic cross section and optical as well as SEM images of a transistor with a channel length of 5 µm and a channel width of 20 µm based on a SnS_2 platelet with a thickness of 380 nm. The thickness of the platelet was determined by atomic force microscopy (AFM).

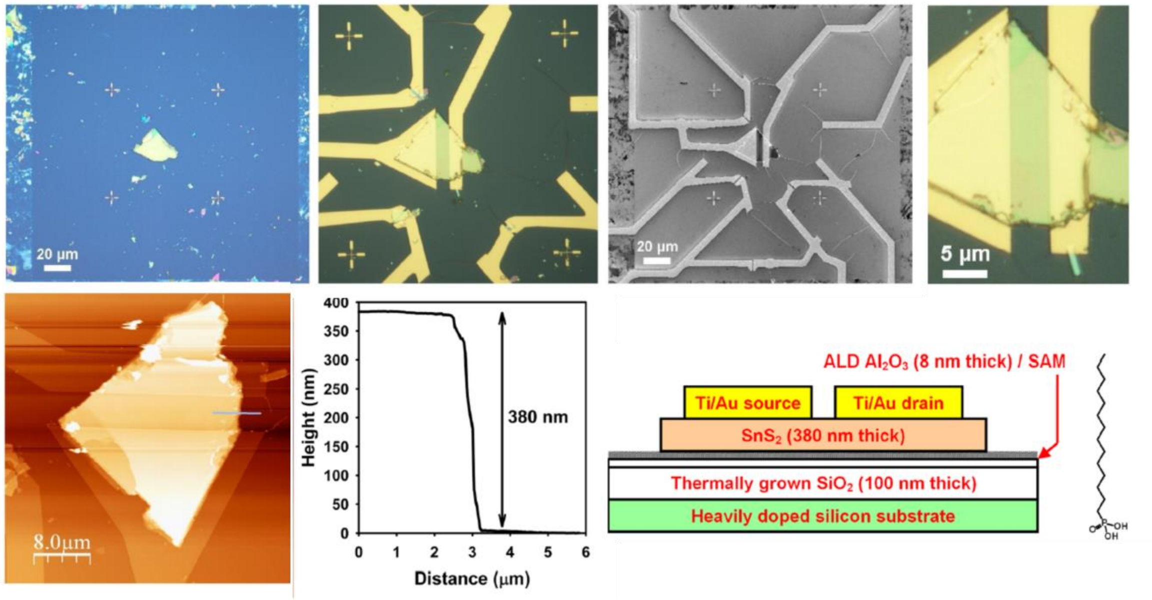

FIG. 3. Schematic cross section, optical micrographs, scanning electron microscopy image, and atomic force microscopy image of a multilayer SnS_2 field-effect transistor with a channel length of 5 μm and a channel width of 20 μm, based on a SnS_2 platelet with a thickness of 380 nm obtained by mechanical exfoliation from a singlecrystal. Prior to depositing the SnS_2 platelet on the thermally oxidized silicon substrate,

the SiO_2 substrate surface was functionalized with an 8-nm thick aluminum oxide layer and a SAM of *n*-tetradecylphosphonic acid (the molecular structure of which is also shown). The Ti/Au source and drain contacts were patterned by electron-beam lithography on the SnS_2 platelet.

For comparison, we also fabricated transistors using SnS_2 platelets with similar dimensions and thickness, but without covering the gate-oxide surface with a SAM. The effect of the SAM passivation of the gate-oxide surface on the threshold voltage of the transistors can be seen in Figure 4(a). The transistor in which the SAM treatment was omitted displays depletion-mode behavior, with a large negative threshold voltage (−10 V) and a significant drain current at a gate-source voltage of zero, similar to many of the previously reported MoS_2 and SnS_2 transistors.[3–12] In contrast, the transistor in which the gate oxide was passivated with an alkylphosphonic acid SAM shows desirable enhancement-mode characteristics, with a positive threshold voltage (+20 V) and a negligible drain current at zero gate-source voltage. Owing to the SAM passivation of the gate dielectric, the transistor can be completely turned off without the need for a negative gate-source voltage. Figure 4(b) shows that the transistor with the SAM-functionalized gate oxide has an on/off current ratio of about 10^6 at a drain-source voltage of 10 V and 5×10^4 at a drain-source voltage of 30 V. From the transfer characteristics, maximum field-effect mobilities of 0.03 cm^2/V s in the saturation regime (Figure 4(c)) and 0.04 cm^2/V s in the linear regime (Figure 4(d)) can be extracted. At small drain-source voltages (1 V), the subthreshold swing is as steep as 4V/decade (Figure 4(e)), which is a significant improvement over the 10 V/decade reported in Ref. 6 for multilayer SnS_2 transistors, although it does not reach the 1.5 V/dec reported in Ref. 7 for single-layer SnS_2 transistors. The output characteristics (Figure 4(f)) display excellent linearity at small drain-source voltages and very good saturation at large drain-source voltages.

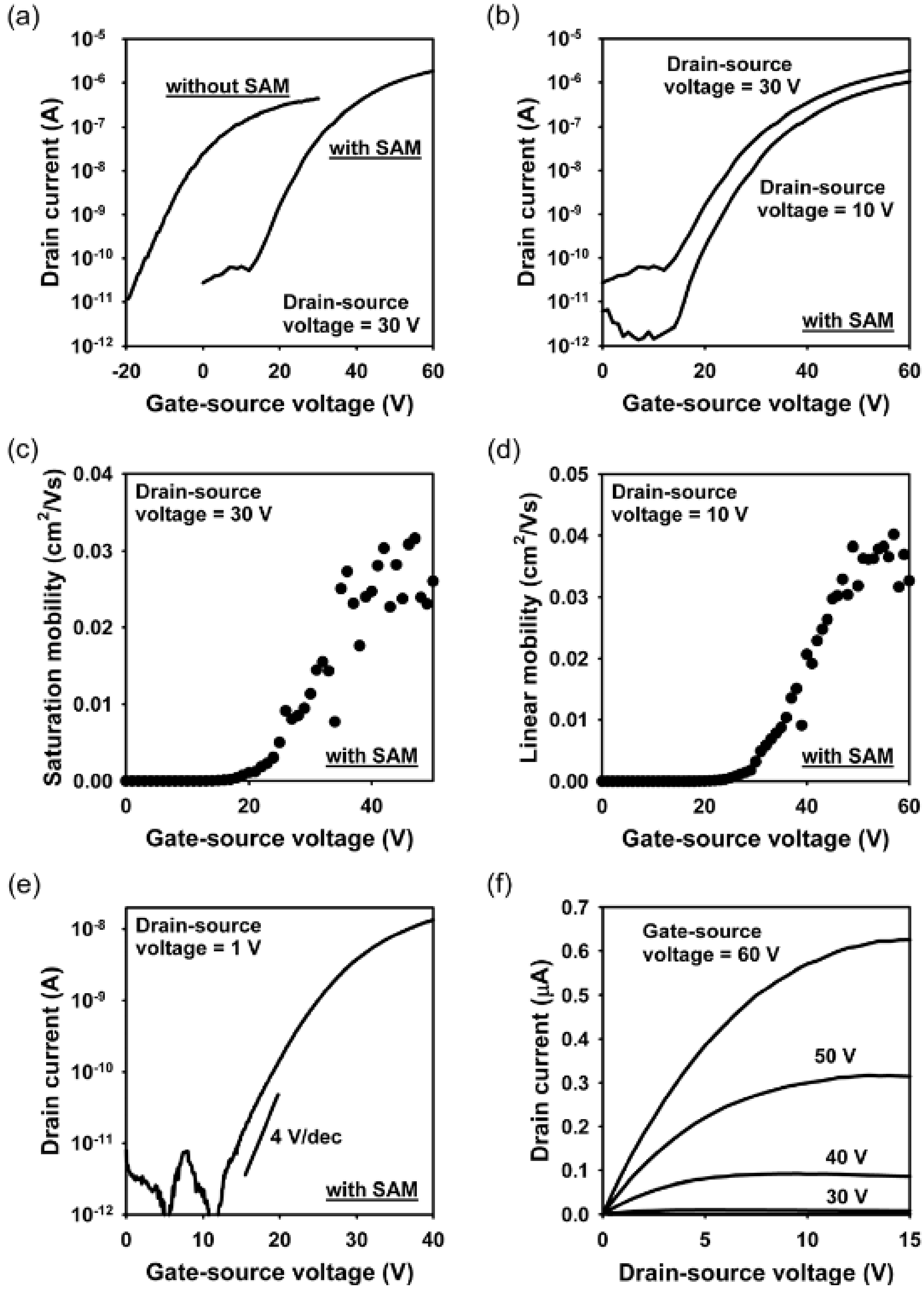

FIG. 4. (a) Transfer characteristics of multilayer SnS_2 FETs with and without SAM passivation of the gate oxide, both measured at a drain-source voltage of 30 V. (b) Transfer characteristics measured at drain-source voltages of 10 V and 30 V. (c) Field-effect mobility in the saturation region (V_{DS} = 30 V). (d) Field-effect mobility in the linear region (V_{DS} = 10 V). (e) Subthreshold characteristics (V_{DS} = 1 V). (f) Output characteristics.

The fact that the field-effect mobility extracted from the current-voltage characteristics (0.04 cm^2/V s) is smaller by several orders of magnitude compared with the field-effect mobilities reported in the literature for FETs based on the same semiconductor (0.8 cm^2/V s for the multilayer SnS_2 transistors in Ref. 6; 50 cm^2 /V s for the single-layer SnS_2 transistors in Ref. 7) is likely related to the substantially greater semiconductor thickness (380 nm in our work, compared to 15 nm in Ref. 6 and 2 nm in Ref. 7). Since the gate-induced carrier channel is located in close proximity to the semiconductor/dielectric interface (see Figure 3(c) in Ref.20), a large semiconductor thickness implies that the charge carriers travel a significant distance from the source contact to the channel and from there to the drain contact through a highly resistive region essentially devoid of charge carriers (labeled “inactive layer” in Figure 3(c) in Ref. 20). Even if the carrier mobility in the crystal was isotropic, the fact that the carrier density is so much smaller in the inactive layer than in the gate-induced carrier channel would mean that the total resistance of the FET is dominated by the access resistance, rather than the channel resistance, resulting in a significantly reduced effective field-effect mobility. However, the layered structure of the SnS_2 crystals implies that the carrier mobility is highly anisotropic, with the out-of-plane mobility likely being substantially smaller than the in-plane mobility, which further reduces the effective mobility extracted from the current-voltage characteristics of FETs based on thicker platelets. For MoS_2 transistors, this trend was recently experimentally verified by Li *et al*. (see Figure 2 in Ref. 21). Our results further emphasize the significant benefit of utilizing thinner crystals (with a maximum thickness of approximately 30 nm) for FET fabrication. Finally, we have also monitored the performance of the multilayer SnS_2 transistor with the SAM-passivated gate oxide over a period of four months during which the substrate was stored in ambient air with a humidity of about 50% under yellow laboratory light. Figure 5 shows that the performance of the transistor remains virtually unchanged over this period of time, indicating that these devices have good shelf-life stability under ambient conditions.

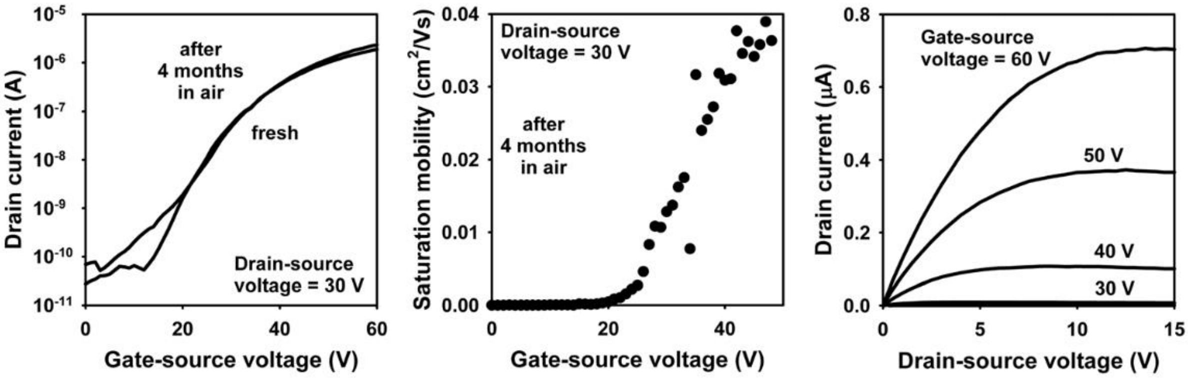

FIG. 5. Shelf-life stability of SnS_2 FETs: Transfer characteristics, saturation mobility, and output characteristics of the same TFT shown in Figures 4(b)–4(f) after four months of storage in ambient air.

2.4 Conclusion

We have synthesized two-dimensional layered tin disulfide (SnS_2) crystals by chemical vapor transport, confirmed their crystallinity and their relatively large bandgap (2.2 eV) by electron microscopy, x-ray diffraction and diffuse optical reflectance spectroscopy measurements, and fabricated field-effect transistors based on mechanically exfoliated SnS_2 platelets with a thickness of a few hundred nanometers. We have demonstrated that the passivation of the gate-oxide surface with an alkylphosphonic acid self-assembled monolayer prior to the deposition of the semiconductor results in FETs that display desirable enhancement-mode characteristics, whereas FETs in which the SAM treatment of the gate oxide is omitted show depletion-mode behavior. To our knowledge, this is the first time that enhancement-mode SnS_2 FETs have been reported. In addition, the transistors also have a large on/off current ratio (10^6) and a steep subthreshold swing (4 V/decade). The small field-effect mobility of our transistors is the result of the large thickness of the platelets (several hundred nanometers) which leads to a large access resistance between the gate-induced carrier channel (located at the semiconductor/dielectric interface) and the source and drain contacts, which further emphasizes the benefit of utilizing thinner crystals for FET fabrication.

ACKNOWLEDGMENTS

The authors would like to thank Marion Hagel, Ulrike Waizmann, and Thomas Reindl at the Max Planck Institute for Solid State Research for expert technical assistance.

[1]C. D. A. Lokhande, “Chemical method for tin disulphide thin film deposition,” J. Phys. D: Appl. Phys. **23**, 1703 (1990).

[2]K. F. Mak, C. Lee, J. Hone, J. Shan, and T. F. Heinz, “Atomically thin MoS_2: A new direct-gap semiconductor,” Phys. Rev. Lett. **105**, 136805 (2010).

[3]B. Radisavljevic, A. Radenovic, J. Brivio, V. Giacometti, and A. Kis, “Single-layer MoS_2 transistors,” Nat. Nanotechnol. **6**, 147 (2011).

[4]B. Radisavljevic and A. Kis, Nat. Nanotechnol. **8**, 147 (2013).

[5]B. W. H. Baugher, H. O. H. Churchill, Y. Yang, and P. Jarillo-Herrero, “Intrinsic electronic transport properties of high-quality monolayer and bilayer MoS_2,” Nano Lett. **13**, 4212 (2013).

[6]D. De, J. Manongdo, S. See, V. Zhang, A. Guloy, and H. Peng, “High on/off ratio field effect transistors based on exfoliated crystalline SnS_2 nanomembranes,” Nanotechnology **24**, 025202 (2013).

[7]H. S. Song, S. L. Li, L. Gao, Y. Xu, K. Ueno, J. Tang, Y. B. Cheng, and K. Tsukagoshi, “High-performance top-gated monolayer SnS_2 field-effect transistors and their integrated logic circuits,” Nanoscale **5**, 9666 (2013).

[8]S. Kim, A. Konar, W.-S. Hwang, J. H. Lee, J. Lee, J. Yang, C. Jung, H. Kim, J.-B. Yoo, J.-Y. Choi, Y. W. Jin, S. Y. Lee, D. Jena, W. Choi, and K. Kim, “High-mobility and low-power thin-film transistors based on multilayer MoS_2 crystals,” Nat. Commun. **3**, 1011 (2012).

[9]D. Krasnozhon, D. Lembke, C. Nyffeler, Y. Leblebici, and A. Kis, “MoS_2 transistors operating at gigahertz frequencies,” Nano Lett. **14**, 5905 (2014).

[10]B. Radisavljevic, M. B. Whitwick, and A. Kis, “Integrated circuits and logic operations based on single-layer MoS_2,” ACS Nano **5**, 9934 (2011).

[11]L. Yu, Y.-H. Lee, X. Ling, E. J. G. Santos, Y. C. Shin, Y. Lin, M. Dubey, E. Kaxiras, J. Kong, H. Wang, and T. Palacios, “Graphene/MoS_2 hybrid technology for large-scale two-dimensional electronics,” Nano Lett. **14**, 3055 (2014).

[12]X. Zou, J. Wang, C.-H. Chiu, Y. Wu, X. Xiao, C. Jiang, W.-W. Wu, L. Mai, T. Chen, J. Li, J. C. Ho, and L. Liao, “Interface engineering for high-performance top-gated MoS_2 field-effect transistors,” Adv. Mater. **26**, 6255 (2014).

[13]S. Kobayashi, T. Nishikawa, T. Takenobu, S. Mori, T. Shimoda, T. Mitani, H. Shimotani, N. Yoshimoto, S. Ogawa, and Y. Iwasa, “Control of carrier density by self-assembled monolayers in organic field-effect transistors,” Nat. Mater. **3**, 317 (2004).

[14]S. K. Possanner, K. Zojer, P. Pacher, E. Zojer, and F. Schürrer, “Threshold voltage shifts in organic thin-film transistors due to self-assembled monolayers at the dielectric surface,” Adv. Funct. Mater. **19**, 958 (2009).

[15]L. A. Burton, D. Colombara, R. D. Abellon, F. C. Grozema, L. M. Peter, T. J. Savenije, G. Dennler, and A. Walsh, “Synthesis, characterization, and electronic structure of single-crystal SnS, Sn_2S_3, and SnS_2,” Chem. Mater. **25**, 4908 (2013).

[16]K. Fukuda, T. Hamamoto, T. Yokota, T. Sekitani, U. Zschieschang, H. Klauk, and T. Someya, “Effects of the alkyl chain length in phosphonic acid self-assembled monolayer gate dielectrics on the performance and stability of low-voltage organic thin-film transistors,” Appl. Phys. Lett. **95**, 203301 (2009).

[17]S. P. Pujari, L. Scheres, A. T. M. Marcelis, and H. Zuilhof, “Covalent surface modification of oxide surfaces,” Angew. Chem. Int. Ed. **53**, 6322 (2014).

[18]U. Zschieschang, F. Ante, M. Schlörholz, M. Schmidt, K. Kern, and H. Klauk, “Mixed self-assembled monolayer gate dielectrics for continuous threshold voltage control in organic transistors and circuits,” Adv. Mater. **22**, 4489 (2010).

[19]R. Hofmockel, U. Zschieschang, U. Kraft, R. Rödel, N. H. Hansen, M. Stolte, F. Würthner, K. Takimiya, K. Kern, J. Pflaum, and H. Klauk, “High-mobility organic thin-

film transistors based on a small-molecule semiconductor deposited in vacuum and by solution shearing," Org. Electron. **14**, 3213 (2013).

[20]S.-L. Li, K. Komatsu, S. Nakaharai, Y.-F. Lin, M. Yamamoto, X. Duan, and K. Tsukagoshi, "Thickness scaling effect on interfacial barrier and electrical contact to two-dimensional MoS_2 layers," ACS Nano **8**, 12836 (2014).

[21]S.-L. Li, K. Wakabayashi, Y. Xu, S. Nakaharai, K. Komatsu, W.-W. Li, Y.-F. Lin, A. Aparecido-Ferreira, and K. Tsukagoshi, "Thickness-dependent interfacial coulomb scattering in atomically thin field-effect transistors," Nano Lett. **13**, 3546 (2013).

3 A facile wet chemistry approach towards unilamellar tin sulfide nanosheets from $Li_{4x}Sn_{1-x}S_2$ solid solutions

Alexander Kuhn, Tanja Holzmann, Jürgen Nuss, and Bettina V. Lotsch

published in J. Mater. Chem. A **2014**, *2*, 6100.

DOI: 10.1039/c3ta14190j

Reproduced by permission of The Royal Society of Chemistry

http://dx.doi.org/10.1039/C3TA14190J


Backcover by Christoph Hohmann (NIM)

A facile wet chemistry approach towards unilamellar tin sulfide nanosheets from $Li_{4x}Sn_{1-x}S_2$ solid solutions

*Alexander Kuhn [a], Tanja Holzmann [abc], Jürgen Nuss, [a] and Bettina V. Lotsch [*abc]*

[a]Max Planck Institute for Solid State Research, Heisenbergstr. 1, 70569 Stuttgart, Germany. E-mail: b.lotsch@fkf.mpg.de

[b]Department of Chemistry, Ludwig-Maximilians-Universität München, Butenandtstr. 5-13, 81377 München, Germany. E-mail: bettina.lotsch@cup.uni-muenchen.de

[c]Nanosystems Initiative Munich (NIM) & Center for Nanoscience, Schellingstr. 4, 80799 München, Germany

Received 18th October 2013, Accepted 14th November 2013

We report on the facile production of single-layered tin sulfide nanosheets by a direct solid-state reaction, followed by quantitative liquid exfoliation in water. The new solid solution of SnS_2 and Li_2S with composition $Li_{4x}Sn_{1-x}S_2$ serves as a versatile solid-state precursor with tunable relative lithium and tin content. The end member Li_2SnS_3, corresponding to the solid solution composition $Li_{3x}[Li_xSn_{1-x}S_2]$, crystallizes in the well-known A_2BO_3 structure type with mixed Li/Sn layers alternating with pure Li layers in the cationic substructure, which is interleaved with sulfur layers. The bonding in the Li layers can be regarded as ionic, while the Sn–S bonds have substantial covalent character. The resulting inherent anisotropy allows for the facile production of unilamellar chalcogenide nanosheets with thicknesses below 1 nm and lateral sizes of tens of microns, simply by shaking the crystalline precursor in water. The quantitative exfoliation into single-layered nanosheets was confirmed using optical microscopy, AFM, TEM, as well as X-ray diffraction of freestanding films produced from the colloidal suspension by centrifugation. Upon annealing, the as-obtained nanosheets are converted into SnS_2 without sacrificing their favorable dispersion properties in water. The presented method allows for the cheap and scalable production of unilamellar chalogenide nanosheets for various potential applications, such as in electronic devices, solar cells, sensors, or battery technology. We expect this method to be generic and transferable to the synthesis of other metal

chalcogenides. The use of solid solutions as solid-state precursors, featuring a large compositional range and potential for doping with other metals, may ultimately allow for the controlled introduction of defect levels and rational band-gap engineering in nanosheet materials.

3.1 Introduction

In the past decade, two-dimensional (2D) crystals have seen an upsurge of interest, owing to their miniature dimensions along with unique electronic and optical properties.[1–5] During the last few years, materials beyond graphene, especially transition metal chalcogenides (TMDs), have increasingly entered the focus of researchers.[2,6,7] Chalcogenide nanosheets, spanning the entire periodic table and covering a host of electronic properties from semiconductors to superconductors, may play a crucial role not only in the development of inexpensive and earth-abundant next-generation technology for transistors,[8,9] thin film solar cells,[10] or photocatalysts[11] – but also in battery technology as fast-chargeable electrode materials.[12]

Among the tin sulfides, there are three common types: SnS, SnS_2 and Sn_2S_3.[13] SnS and SnS_2 nanosheets are usually synthesized by bottom-up synthesis,[14,15] while SnS_2 may be obtained by mechanical exfoliation.[8] As SnS_2 has a bandgap of 2.21 eV,[16] it has been explored as a high on/off ratio transistor,[8] photocatalyst,[11] or electrode material.[12]

In general, the synthesis of chalcogenide nanosheets follows the two generic strategies already well established for graphene and related materials: bottom-up[17–19] or top-down approaches. For top-down synthesis, mechanical exfoliation[1,7,8] and several wet-chemistry based exfoliation methods have been reported. Liquid exfoliation either occurs by Li intercalation and subsequent exfoliation in water,[20,21] or by sonication in solvents, with or without the presence of surfactants as stabilizing agents.[22] All these methods suffer from incomplete exfoliation, producing not only single layers, but rather an – oftentimes broad – distribution of layer thicknesses.

In this study, we report a "green" and efficient exfoliation strategy quantitatively yielding unilamellar nanosheets of a new ternary tin sulfide, simply by pouring the bulk material into water. The precursor, $Li_{4x}Sn_{1-x}S_2$, is composed of layers of $[Sn_{1-x}S_2]^{4x-}$ featuring strong intralayer covalent bonding, while the layers are interleaved by Li^+ ions. In water, facile solvation of Li^+ leads to spontaneous swelling and exfoliation of $Li_{4x}Sn_{1-x}S_2$ into single layers without the need for ultrasonic treatment. The high negative surface potential and the resulting repulsive force between the nanosheets effectively prevent restacking, in sharp contrast to most charge-neutral chalcogenide nanosheets.

3.2 Experimental

Solid-state syntheses

$Li_{4x}Sn_{1-x}S_2$ was prepared from Li_2S (Alfa Aesar, 99.9%), Sn (Alfa Aesar, 99.995%), and S (Alfa Aesar, 99.5%) via a conventional solid-state synthesis. Pellets were pressed from appropriate mixtures of the starting materials and vacuum-sealed in silica tubes. A slight excess of sulfur (30 mg in a tube of approx. 20 ml and 1 g of the material) was used in order to ensure complete oxidation of Sn. For the reaction, the tubes were placed in furnaces and heated to 750 °C (60 K h^{-1}), held at that temperature for several hours and then quenched to room temperature, whereby excess sulfur was condensed on the walls of the silica tube. All steps were carried out under an inert Ar atmosphere or in vacuum.

Exfoliation and production of free-standing films

For exfoliation, the solid-state precursor $Li_{4x}Sn_{1-x}S_2$ was poured into water (1 g l^{-1}) and placed on an orbital shaker (GFL) for a few days. The exfoliability and the time necessary for exfoliation depend on the stoichiometry of the respective bulk material. The orange colloidal nanosheet suspension was stable for several weeks throughout the time of this study; flocculation was never observed. For the production of solid free-standing films, the nanosheet suspension was centrifuged at 15 000 rpm. The supernatant was removed and residual water was evaporated at 100 °C.

X-ray diffraction

Powder X-ray diffraction (XRD) was performed with a STOE Stadi P diffractometer working in Debye–Scherrer geometry with Mo-$K_{\alpha 1}$ radiation and a Ge(111) monochromator. For the measurement, the crystalline samples were ground and the powder was filled in a glass capillary with a diameter of 0.3 mm under an Ar atmosphere. X-ray diffraction of the freestanding film in a flat sample holder was carried out with two geometries: (i) in transmission mode using the above-mentioned STOE Stadi P diffractometer or (ii) in reflectance mode using a

Bruker D8 Advance diffractometer working with Cu $K_{\alpha 1}$ radiation. Rietveld refinement was performed with the software DiffracPlus TOPAS v4.2 (Bruker AXS). For single-crystal X-ray diffraction, a SMART-APEX CCD X-ray diffractometer (Bruker AXS) working with graphite-monochromated Mo-K_α radiation was used. The integration of the reflections was performed with the SAINT software (Bruker AXS). The structure was solved with direct methods and least squares refinement using the SHELXTL program.

Optical microscopy, AFM

The height and lateral dimensions of the nanosheets were analyzed on a silicon wafer covered with a 300 nm thermally grown SiO_2 layer. To adsorb the nanosheets on the wafer surface, the wafer was dipped into the colloidal suspension and the liquid was blown off the wafer after some seconds. The wafer was pre-examined using an optical microscope (Olympus BX51). Images were recorded with the Olympus Stream Essentials 1.7 software. AFM was performed with a Veeco CP II system. The AFM images were analyzed with the Gwyddion software.

TEM

For TEM, a drop of the colloidal nanosheet suspension was placed on a lacey carbon film/copper grid (Plano) and dried under irradiation of IR light. TEM was performed with a Phillips CM30 ST (300 kV, LaB_6 cathode). Bright field images and selected area electron diffraction (SAED) patterns were recorded with a Gatan CCD camera.

SEM, UV/VIS, ICP-AES, Zeta Potential Measurement

Both the crystalline precursors and the freestanding nanosheet film were analyzed by scanning electron microscopy (SEM; Vega TS 5130 MM, Tescan) and SEM-EDX using a Si/Li detector (Oxford). Optical diffuse reflectance spectra of the bulk material and the nanosheet pellet were collected at room temperature with a UV-Vis-NIR diffuse reflectance spectrometer (Agilent Technologies, Cary 5000) at a photometric range of 200–800 nm. Powders were prepared in a sample carrier with a quartz glass window at the edge of the integrating sphere with $BaSO_4$ as the optical standard. Kubelka–Munk spectra were calculated from the reflectance data. ICP-AES was analyzed with a Vista Pro ICP-AES spectrometer. The characteristic wavelengths were separated with an Echelle-Polychromator (Varian, Darmstadt) and detected with a photomultiplier. The zeta potential of the colloidal suspension was determined by a

Malvern Nano ZS Zetasizer (Malvern, Worcestershire) at 20 °C in water using the Smoluchowski method.

3.3 Results and Discussion

Structural characterization of the crystalline precursors

The crystalline precursor $Li_{4x}Sn_{1-x}S_2$ obtained by conventional solid-state synthesis was structurally characterized by means of X-ray diffraction. Single crystals were obtained for the end member of the solid solution, Li_2SnS_3. Li_2SnS_3 is isostructural with Li_2SnO_3 and crystallizes in the monoclinic space group *C*2/*c* (no. 15) with a = 6.3961(7), b = 11.0893(13), c = 12.4157(14), and β = 99.860(2) °.[23] The crystallographic details are listed in Table S1,† the atomic coordinates are given in Table S2.† Fig. 1A shows the idealized structure of Li_2SnS_3, neglecting partial disorder of the Li/Sn sublattice. The layered structure – best described as $Li[Li_{1/3}Sn_{2/3}S_2]$ – is closely related to the delafossite structure, which is often observed for ternary layered oxides or sulfides based on mono- and trivalent-cations. Depending on the synthesis conditions, we obtained Li_2SnS_3 with different degrees of cation ordering (see ESI†). An individual fully ordered $[Li_{1/3}Sn_{2/3}S_2]^-$ layer is shown in Fig. 1B, with the monoclinic unit cell indicated (*C*2/*c*). Random distribution of Li and Sn in the $Li_{1/3}Sn_{2/3}$ layer leads to an average rhombohedral structure of higher symmetry ($R\bar{3}m$) with a smaller unit cell as indicated in Fig. 1B. This average structure has been observed for many delafossite-type compounds, e.g. for the homologous Na_2SnS_3,[24] and, in our experiments, for melt-quenched Li_2SnS_3 (see ESI†). It was argued in the literature that the apparent disorder results from translational stacking faults of individual layers, according to the two vectors shown in Fig. 1B.[25] Note, however, that electron diffraction patterns of individual nanosheets do not show clear superstructure reflections in the *hk*0 plane (see Fig. S7†), as would be expected for an ordered honeycomb-type lattice as implied by Fig. 1B. These results point to the possibility of disorder within individual layers as opposed to disorder due to a superposition structure as a consequence of stacking faults. On the other hand, the Warren-like feature in the XRD pattern of microcrystalline Li_2SnS_3 (Fig. 1C, $7° \leq 2\Theta \leq 9°$) suggests stacking faults of at least partially ordered layers along [001] as a reason for the disorder.[25] The Rietveld refinement shown in Fig. 1C is based on the monoclinic crystal structure (*C*2/*c*) obtained from single-crystal X-ray diffraction.

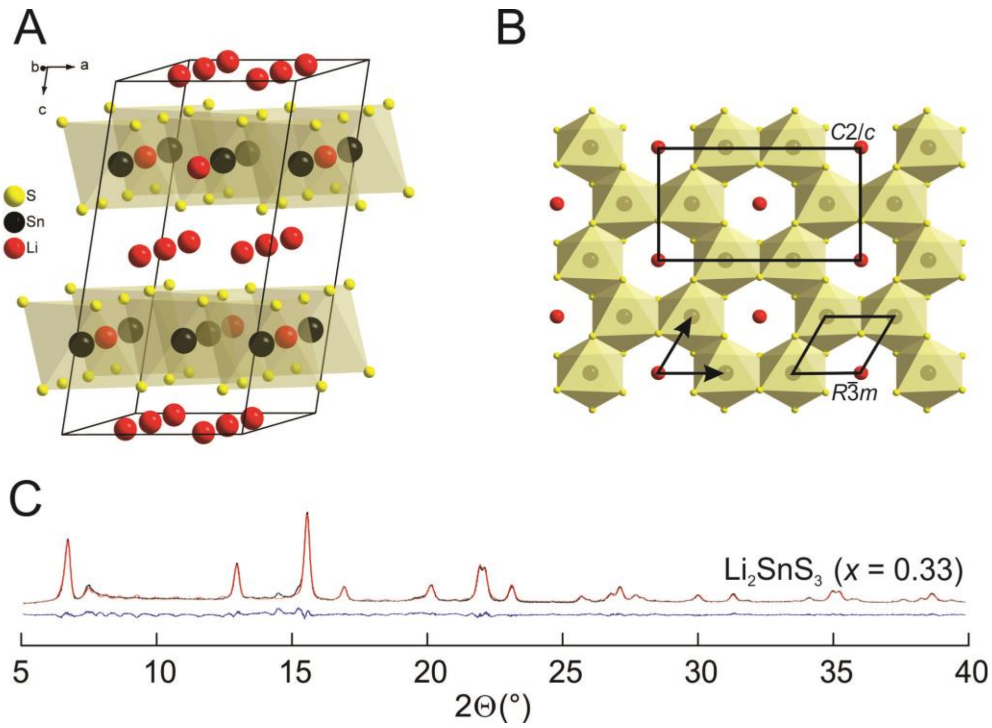

Fig. 1 Crystal structure of Li_2SnS_3. (A) Idealized fully ordered structure of Li_2SnS_3 crystallizing in the monoclinic space group *C*2/*c*. (B) Honeycomb structure of an ideal single $[Li_{1/3}Sn_{2/3}S_2]^-$ layer. The arrows mark the translation vectors of the stacking faults leading to mixed occupancies within these layers in the average rhombohedral structure as discussed in ref. 25. (C): Rietveld refinement of the powder pattern of Li_2SnS_3 (space group *C*2/*c*).

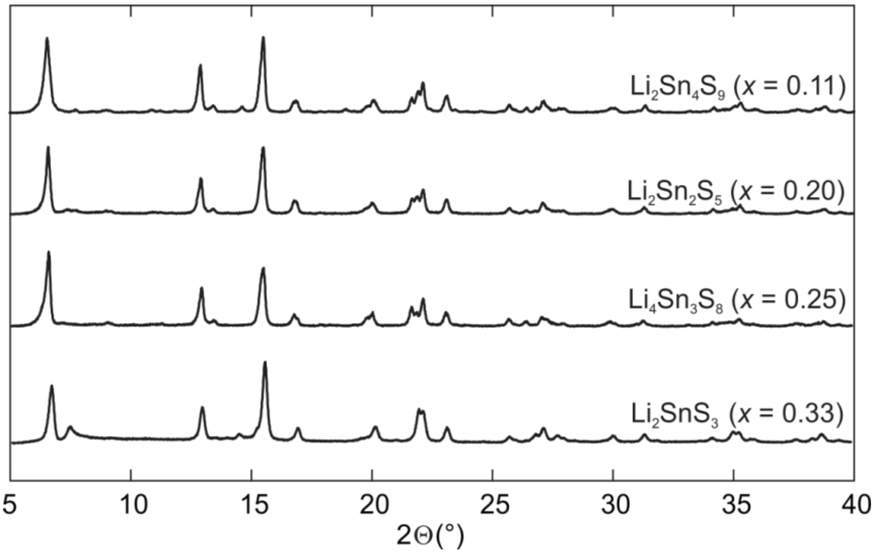

Fig. 2 XRD patterns (Mo-$K_{\alpha 1}$) of $Li_{4x}Sn_{1-x}S_2$ with $0.11 \leq x \leq 0.33$. Note the similarity of the upper powder patterns compared to the pattern of Li_2SnS_3 (bottom).

Fig. 2 shows the PXRD patterns of several samples in the $Li_{4x}Sn_{1-x}S_2$ system with $0.11 \leq x \leq 0.33$, whereby $x = 0.33$ corresponds to Li_2SnS_3 and $x = 0$ corresponds to SnS_2. The formation of a solid solution is hence observed in a wide compositional range and can be understood from Fig. 1 as follows: as one Li atom in the LiSn layer is replaced by a Sn atom, 3 more Li atoms are removed for reasons of charge neutrality, thus decreasing the layer charge density at smaller relative lithium contents. All samples were homogeneous and the crystallites, having a hexagonal morphology, showed the expected Sn : S ratios as measured by SEM-EDX (see Table S3–S6†). A graphical inspection of the XRD patterns of $Li_{4x}Sn_{1-x}S_2$ with $x = 0.25$, 0.20 and 0.11 already reveals that the layered structure is retained for all samples. The monoclinic Li_2SnS_3 structure model (with slightly different lattice constants) was used as the basis for Rietveld refinements which yielded reasonable structure descriptions for all solid solution members (see ESI Fig. S2†), although some minor reflections point to small amounts of side phases or yet undetermined superstructures, depending on x. Likewise, the Sn : S ratios obtained from the refinements are in good agreement with the expectations. In summary, the solid solution of $Li_{4x}Sn_{1-x}S_2$ exhibits a layered 3R structure best written as $Li_{3x}[Li_xSn_{1-x}S_2]$ in a wide compositional range. The structure exhibits alternating layers of (i) $[Sn_{1-x}S_2]^{4x-}$ with intralayer covalent bonding resembling the type of bonding in SnS_2, which is insoluble in water and (ii) Li^+ layers with ionic bonding character, resembling Li_2S, which is soluble in water (see also Fig. 4).

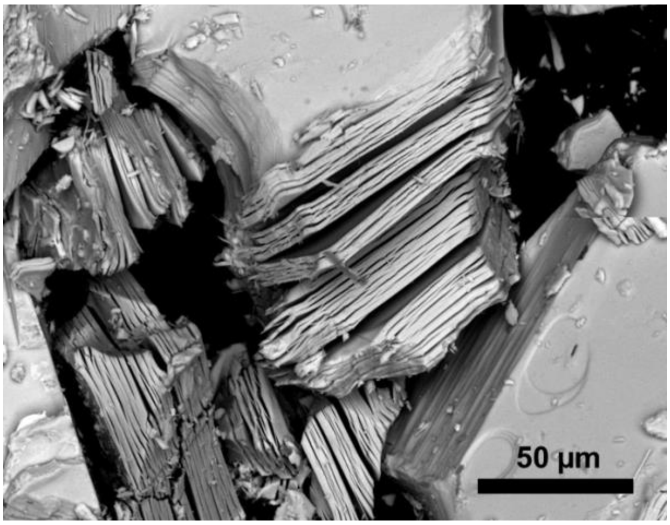

Fig. 3 SEM image of $Li_2Sn_2S_5$ crystals exhibiting a strongly anisotropic, layered crystal morphology with lateral sizes of 20–100 µm.

Exfoliation and Nanosheet Characterization

The crystalline precursor, $Li_{4x}Sn_{1-x}S_2$, can easily be exfoliated in water. A scheme of the proposed exfoliation process is shown in Fig. 4. The success and kinetics of the exfoliation depend on the stoichiometry (see ESI†). While each of the solid solution members can be exfoliated down to the single sheet level, we obtained the best results for $Li_2Sn_2S_5$ ($x = 0.2$), and hence this composition will serve as the basis of our further discussion (see also Fig. 3). Fig. 4 shows the characteristic optical appearance of the obtained colloidal nanosheet suspension with a concentration of 1 g l^{-1}, which is obtained after shaking the crystalline precursor $Li_2Sn_2S_5$ in water for ≈6 h. The observed schlieren texture is reminiscent of the formation of orientationally ordered colloidal particles, as seen in liquid crystals. Fig. 5 displays snapshots of the swelling process recorded with an optical microscope (the real-time movie is provided in the ESI, Movie 1†). To observe the exfoliation process, thoroughly ground $Li_2Sn_2S_5$ powder was placed on a microscope slide, followed by a one-drop addition of water. The spontaneous delamination of the crystal corroborates the assumed exfoliation mechanism shown in Fig. 4. Due to the hydration of the lithium cations and the swelling of the crystal the attractive forces between the layers decrease and the crystal eventually delaminates into separate layers.

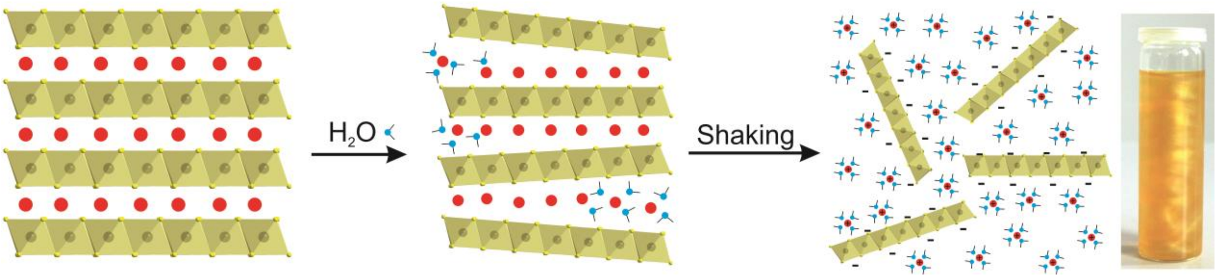

Fig. 4 Scheme outlining the proposed exfoliation mechanism for $Li_{4x}Sn_{1-x}S_2$ and photograph of the obtained colloidal nanosheet suspension ($Li_2Sn_2S_5$, $c = 1$ g l^{-1}).

In order to characterize the morphology and the structure of the dispersed nanosheets, a drop of the colloidal solution of $Li_2Sn_2S_5$ in H_2O was placed on a Si/SiO_2(300 nm) wafer and the deposited nanosheets were analyzed by optical and atomic force microscopy (AFM). Typical images are shown in Fig. 6A and B. The solution consists of well-dispersed single-layer nanosheets with typical lateral sizes of 5–10 μm, which is likely determined by the size of the precursor crystallites. The height of the nanosheets as determined from AFM is 8–10 Å, which is in good agreement with the expectations for a single-layered nanosheet (theoretical height from the crystal structure of Li_2SnS_3 ≈7 Å; Li–Li distance measured along the *c*-axis).

AFM images of Li_2SnS_3, $Li_4Sn_3S_8$ and $Li_2Sn_4S_9$ and additional AFM images of $Li_2Sn_2S_5$ after exfoliation in water are shown in Fig. S3–6.† It is worth noting that for $Li_2Sn_2S_5$ we observed only single sheets, whereas for Li_2SnS_3, $Li_4Sn_3S_8$ and $Li_2Sn_4S_9$ sheets comprising more than one layer were obtained.

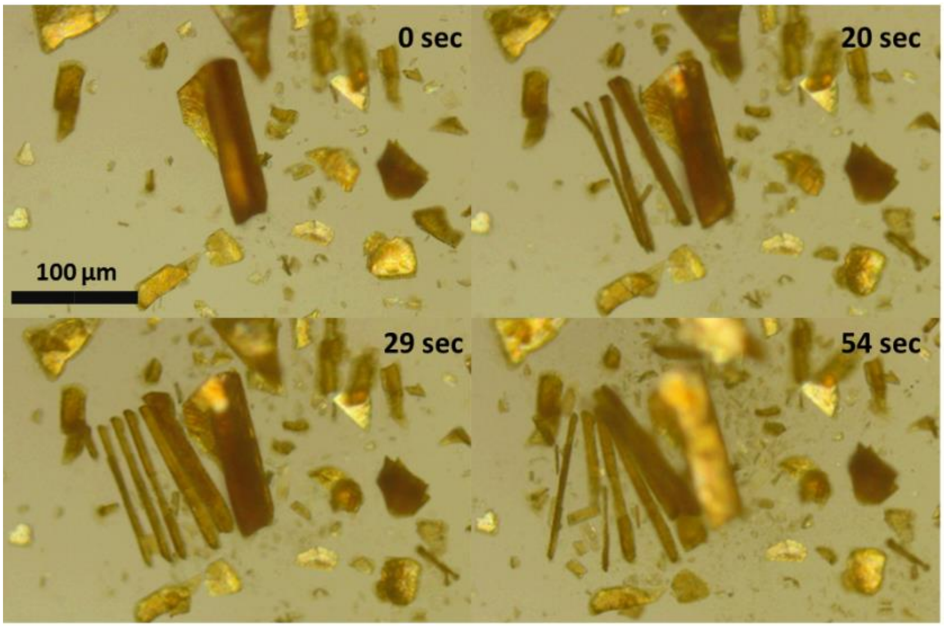

Fig. 5 Exfoliation of $Li_2Sn_2S_5$ in water, recorded with optical microscopy. Time-series images of the spontaneous exfoliation of a $Li_2Sn_2S_5$ crystal after the addition of one drop of water.

TEM was used in order to determine the structure of the nanosheets. Fig. 6C and D show typical images of the $Li_2Sn_2S_5$ nanosheets deposited on a lacey carbon grid of the TEM probe. For higher concentrations, we find several unilamellar nanosheets deposited on top of each another with random orientation (Fig. 6C), while for a lower concentration, the nanosheets tend to crumble and fold during drying (Fig. 6D), presumably due to their large anisotropy. The inset figures show the SAED patterns of the nanosheets. As there are no superstructure reflections observed, the patterns point to a hexagonal plane group for the structure of the nanosheets – plane group $p3m1$ – which is expected for layers of identical edge-sharing octahedra. This is the case for a random distribution of the Sn vacancies in the $[Sn_{1-x}S_2]^{4x-}$ layers. The observed lattice distances are in very good agreement with the expectations from the lattice constants of the crystalline precursors, as discussed in more detail in the next section. In summary, the TEM-SAED results confirm that the $[Sn_{1-x}S_2]^{4x-}$ network is retained in the unilamellar nanosheets after exfoliation. Using TEM-EDX, the average Sn : S ratio of the exfoliated single-layer nanosheets was determined to be 29 : 71 – as expected theoretically for $[Sn_2S_5]^{2-}$ nanosheets (28.6 : 71.4). The zeta potential of the colloidal suspension of $Li_2Sn_2S_5$

in water was determined at 20 °C after one day, using the Smoluchowski method. A value of −44.7 mV was obtained, which rationalizes the observed excellent long-term stability of the colloidal suspension, as well as the fact that only single sheets seem to be present. This is in sharp contrast to the situation encountered with charge-neutral chalcogenide nanosheets, obtained from either exfoliation by sonication in organic solvents or Li intercalation and subsequent exfoliation in water. For such materials originally bearing no layer charge, a broad thickness distribution of the nanosheets is typically obtained, reflecting the comparably much larger electrostatic stabilization of the nanosheets in the present case.

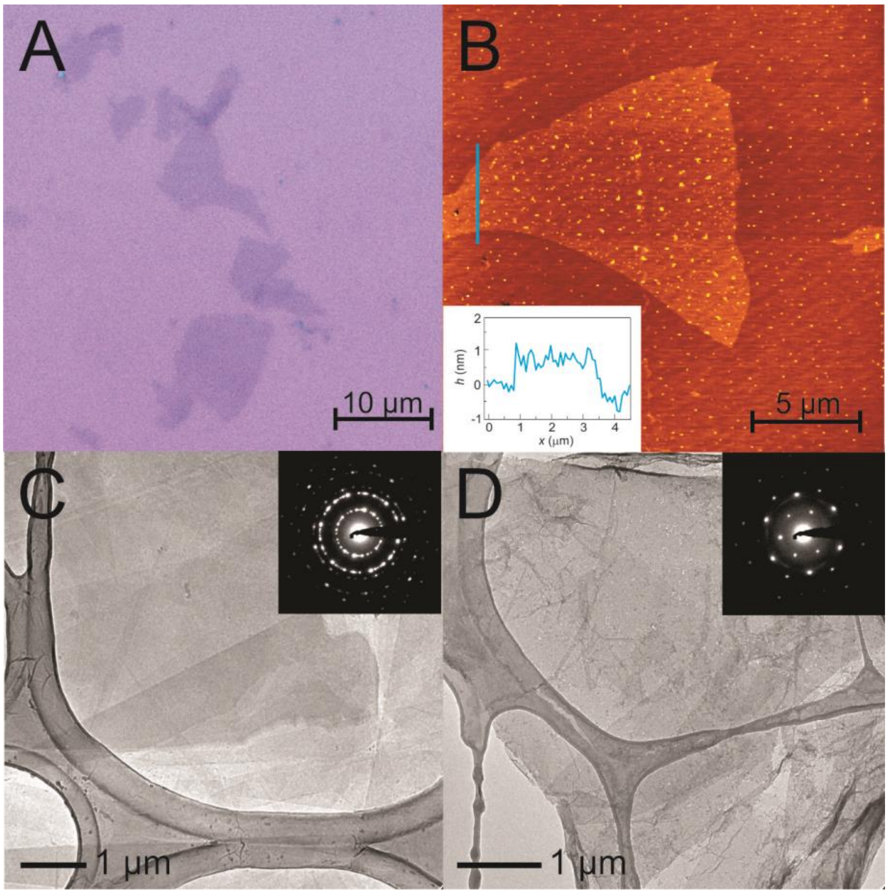

Fig. 6 Characterization of the $[Sn_2S_5]^{2-}$ nanosheets. (A) Optical microscope image of the nanosheets deposited on a Si/SiO_2(300 nm) wafer. (B) AFM image of a nanosheet on the same wafer. The inset picture shows the height of the nanosheet of somewhat less than a nanometer, as expected for a single-layer nanosheet. (C and D) TEM images and SAED patterns for stacks of nanosheets (C) and a single (yet crumbled and folded) nanosheet (D). Note the large aspect ratios in all cases.

Formation of freestanding films

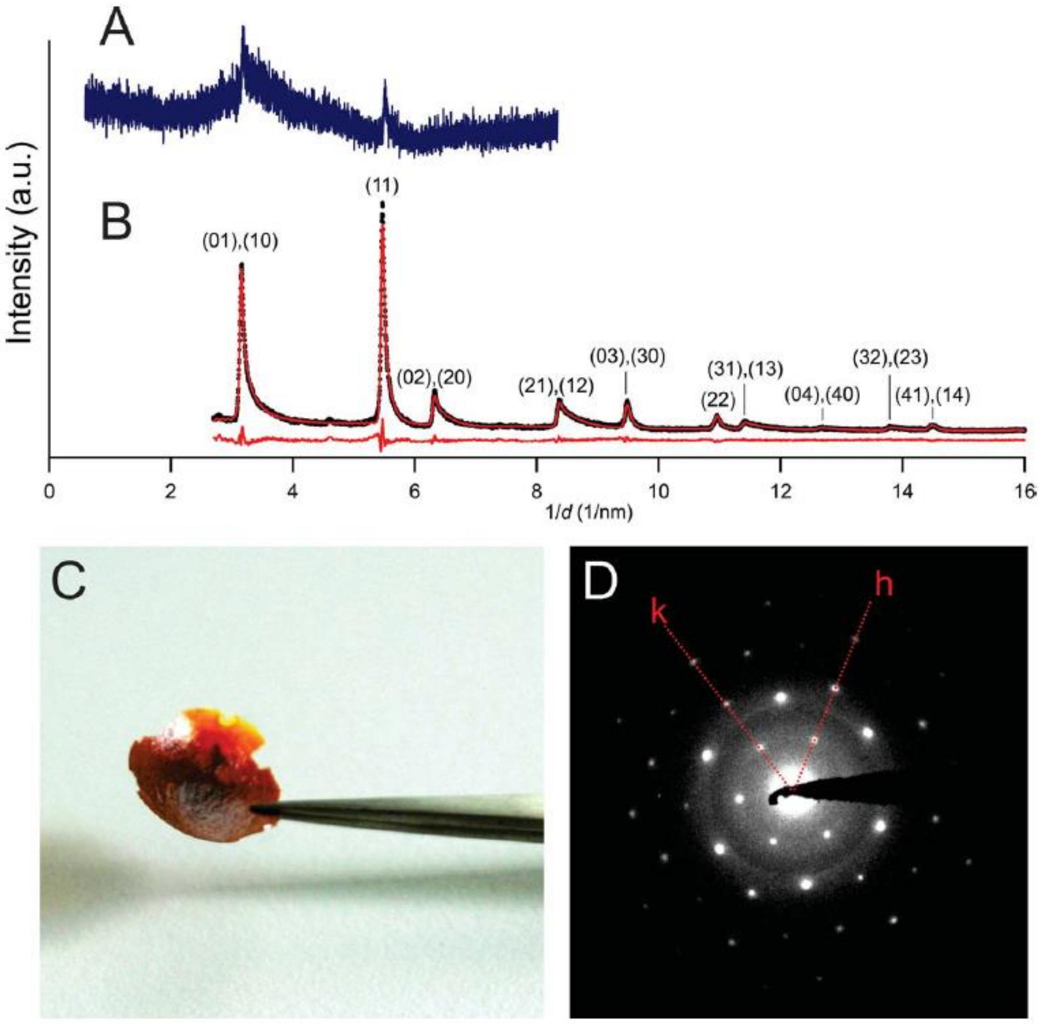

Fig. 7 A) XRD pattern (Cu-$K_{\alpha1}$) of the nanosheet slurry obtained after centrifugation at 25 000 rpm (measured in a capillary in Debye–Scherrer mode). (B) XRD pattern (Mo-$K_{\alpha1}$) of the freestanding nanosheet film shown in (C) with Rietveld refinement (measured in transmission mode). (C) Optical appearance of the freestanding film. (D) SAED pattern of a single-layered nanosheet (cf.Fig. 6), used for indexing.

We used centrifugation in order to prepare freestanding films from the colloidal nanosheet suspension. Hereby, the supernatant was removed from the slurry on the bottom of the vessel. The XRD pattern of the obtained glue-like nanosheet slurry measured with Cu-$K_{\alpha1}$ radiation is shown in Fig. 7A. The pattern features two asymmetric Warren-like reflections which can be assigned to the (01), (10) and the (11) in-plane reflections of the nanosheets in the slurry. The absence of sharp reflections corresponding to the basal spacing in the bulk material clearly supports the picture of complete exfoliation. The slurry was then dried at 100 °C and the freestanding films were produced by centrifugation (see Fig. 7C). In the films, the nanosheets are randomly stacked on top of each other with the sheets being parallel to the top surface of the film, but turbostratically disordered in lateral directions. Fig. 7B shows the X-ray diffraction pattern obtained from the film mounted on a flat sample holder in transmission mode. Hereby, reflections are only measured for planes perpendicular to the sample holder (here: in-plane reflections of the stacked nanosheets). The observed reflections show an asymmetric Warren profile typical of 2D materials – similar to the XRD in Fig. 7A, but with a much better signal-to-noise ratio. As a result of the missing periodicity in the *c* (i.e. stacking) direction, 2D materials are represented by rods along the [001] zone axis in reciprocal space, which leads to the asymmetric peaks in the pattern obtained from radial integration of reciprocal space from the origin (cf. Fig. S1†).[26] For the refinement of the XRD pattern (see Fig. 7B), a single layer of edge-sharing octahedra was assumed with random Li/Sn distribution within the layers. Clearly, the observed and calculated patterns are in very good agreement and the free-standing film consists of randomly stacked 2D layers of edge-sharing octahedra (see ESI† for details of the refinement). The refinement further indicates a Sn : S ratio of 1 : 2 rather than 2 : 5, which is in agreement with the SEM-EDX measurements. Similarly, ICP measurements of the film reveal a depletion in Li down to a Li : Sn ratio of 0.2 : 1 after several washing steps, while the supernatant after centrifugation is enriched in Li (Li : Sn = 4.8 : 1). We therefore propose that Li is formally removed from the sample according to

$$Li_{4x}[Sn_{1-x}S_2] \rightarrow 2x\ Li_2S + [Sn_{1-x}S_{2-2x}] \qquad (1).$$

In line with the concomitant depletion of sulfur we find a lower electron density at the S position in the Rietveld refinement, pointing to a "defective" SnS_2-type structure. In aqueous solution, the sulfur vacancies may be filled by oxygen giving rise, in essence, to hydrated nanosheets according to

$$[Sn_{1-x}S_{2-2x}] + 2x\ H_2O \rightarrow H_{4x}[Sn_{1-x}S_{2-2x}O_{2x}] \qquad (2).$$

It is worth noting that hydrolysis beyond a Sn : S ratio of 1 : 2 was not observed – in agreement with the fact that SnS_2 is rather stable towards degradation in soft acids.

The above rationale is supported by the observation that after annealing the nanosheet film at 450 °C in a vacuum-sealed ampoule the powder pattern matches with that of SnS_2 (space group $P\bar{3}m1$, no. 164, Fig. 8). Interestingly, in contrast to SnS_2 prepared at high temperatures, our product can readily be redispersed in water, suggesting that the above hydration reaction may operate (eqn (2)).

The optical absorption of the crystalline $Li_2Sn_2S_5$, the nanosheet film and the annealed nanosheet film was measured by UV/Vis spectrometry in diffuse reflectance mode (see Fig. 9). In both the crystalline precursor $Li_2Sn_2S_5$ and the annealed nanosheet film the absorption edge points to a bandgap around 1.9 eV. In line with size confinement effects, the nanosheet film displays a slightly larger bandgap of 2.1 eV. All of these values are close to those observed for SnS_2, which has a bandgap of 2.21 eV,[16] thus again emphasizing the similarity of the above tin sulfide species to the prototype material SnS_2.

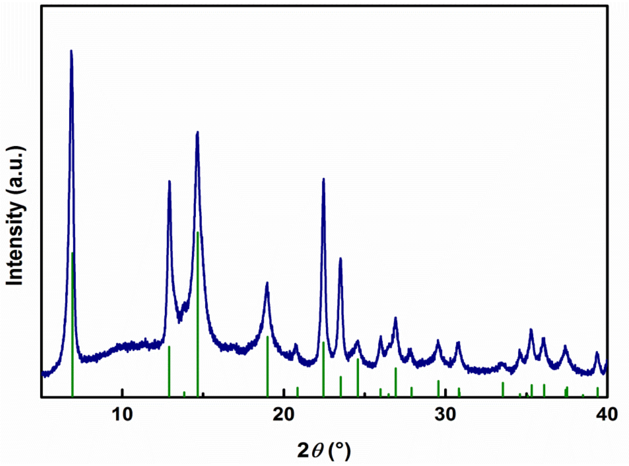

Fig. 8 XRD pattern (Mo-$K_{\alpha1}$) of the nanosheet pellet after annealing in a vacuum-sealed ampoule at 450 °C (blue line). The green lines are the reference reflections of SnS_2 (space group $P\bar{3}m1$, no. 164).

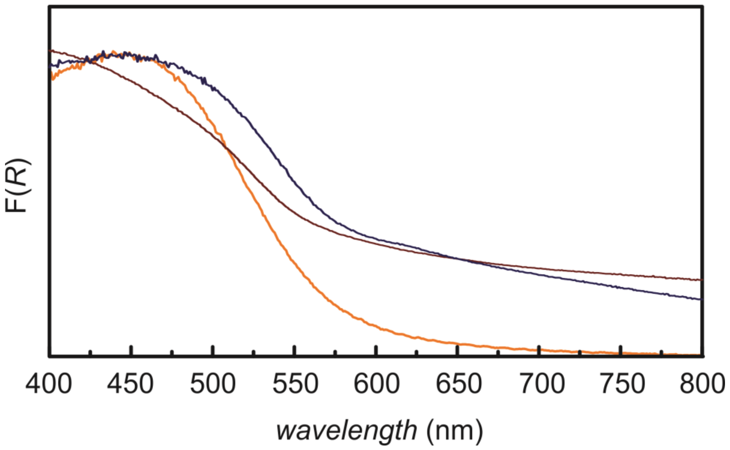

Fig. 9 UV/Vis spectra of bulk $Li_2Sn_2S_5$ (blue line), the nanosheet film after centrifugation and drying (yellow line) and the annealed nanosheet film (brown line). The absorption edges indicate a bandgap of 1.9 eV for the bulk material, 2.1 eV for the nanosheet film and ≈1.9 eV for the annealed nanosheet film (see Fig. S10†).

3.4 Conclusion

We have demonstrated the efficient production of single-layered tin sulfide nanosheets with large aspect ratios from the crystalline solid solution of $Li_{4x}Sn_{1-x}S_2$. The bonding situation and, hence, the morphology of the layered precursors is inherently anisotropic, giving rise to quantitative exfoliation into unilamellar nanosheets in water without mechanical treatment, organic solvents or additives. Freestanding films have been obtained via centrifugation of the nanosheet suspension and transformed into SnS_2 by annealing. We envision that this will enable the fabrication of conformal coatings of tin chalcogenides of desired thickness simply by evaporating the nanosheet suspension. Finally, we expect that the presented exfoliation method, drawing on charge-tunable anionic nanosheets from lithiated solid-solution precursors, will be widely applicable also to other layered chalcogenides.

Acknowledgements

The authors would like to thank V. Duppel for TEM measurements, C. Kamella for SEM-EDX measurements and M.-L. Schreiber for ICP-AES measurements. Financial support by the Max-Planck Society, Nanosystems Initiative Munich (NIM), Center for Nanoscience (CeNS) and Fonds der Chemischen Industrie (FCI) is gratefully acknowledged.

References

1 K. S. Novoselov, A. K. Geim, S. V. Morozov, D. Jian, Y. Zhang, S. V. Dubonos, I. V. Griforieva and A. A. Firsoy, *Science*, 2004, **306**, 666–669.

2 M. Chhowalla, H. Suk Shin, G. Eda, L.-J. Li, K. P. Loh and H. Zhang, *Nature Chem.*, 2013, **5**, 263-275.

3 K. S. Novoselov, D. Jian, F. Schedin, T. J. Booth, V. V. Khotkevich, S. V. Morozov and A. K. Geim, *P. Natl. Acad. Sci. USA*, 2005, **102**, 10451-10453.

4 J. A. Roger, M. G. Lagally and R. G. Nuzzo, *Nature*, 2011, **477**, 45-53.

5 B. Radisavljevic, A. Radenovic, J. Brivio, V. Giacometti and A. Kis, *Nature Nanotechnol*, 2011, **6**, 147-150.

6 K. F. Mak, C. Lee, J. Hone, J. Shan and T. F. Heinz, *Phys. Rev. Lett.*, 2010, **105**, 136805.

7 A. Splendiani, L. Sun, Y. Zhang, T. Li, J. Kim, C.-Y. Chim, G. Galli and F. Wang, *Nano Lett.*, 2010, **10**, 1271-1275.

8 D. De, J. Manongdo, S. See, V. Zhang, A. Guloy and H. Peng, *Nanotechnology*, 2013, **24**, 025202.

9 D. B. Mitzi, L. L. Kosbar, C. E. Murray, M. Copel and A. Afzali, *Nature*, 2004, **428**, 299-303.

10 J. Britt and C. Ferekides, *Appl. Phys. Lett.*, 1993, **62**, 2851-2852.

11 W. Du, D. Deng, Z. Han, W. Xiao, C. Bian and X. Qian, *CrystEngComm*, 2011, **13**, 2071-2076.

12 T.-J. Kim, C. Kim, D. Son, M. Choi and B. Park, *J. Power Sources*, 2007, **167**, 529-535.

13 R. C. Sharma and Y. A. Chang, *Bulletin of Alloy Phase Diagrams*, 1986, **7**, 269-273.

14 G. Shen, D. Chen, K. Tang, L. Huang, Y. Qian and G. Zhou, *Inorg. Chem. Commun.*, 2003, **6**, 178-180.

15 Y. Zhang, J. Lu, S. Shen, H. Xu and Q. Wang, *Chem. Commun.*, 2011, **47**, 5226-5228.

16 D. L. Greenaway and R. Nitsche, *J. Phys. Chem. Solids*, 1965, **26**, 1445-1458.

17 S. Acharya, B. Das, U. Thupakula, K. Ariga, D. D. Sarma, J. Israelachvili and Y. Golan, *Nano Lett.*, 2013, **13**, 409-415.

18 Y. Yu, C. Li, Y. Liu, L. Su, Y. Zhang and L. Cao, *Scientific Reports*, 2013, **3**, 1866.

19 P. Sekar, E. C. Greyson, J. E. Barton and T. W. Odom, *J. Am. Chem. Soc.*, 2005, **127**, 2054-2055.

20 P. Joensen, R. F. Frindt and S. R. Morrison, *Mat. Res. Bull.*, 1986, **21**, 457-461.

21 Z. Zeng, Z. Yin, X. Huang, H. Li, Q. He, G. Lu, F. Boey and H. Zhang, *Angew. Chem. Int. Ed.*, 2011, **50**, 11093-11097.

22 V. Nicolosi, M. Chhowalla, M. G. Kanatzidis, M. S. Strano and J. N. Coleman, *Science*, 2013, **340**, 1226419.

23 G. Lang, *Z. Anorg. Allg. Chem.*, 1954, **276**, 77-94.

24 W. Mark and O. Lindquist, *Acta Cryst.*, 1974, **B30**, 2620-2628.

25 V. Todorova, A. Leineweber, L. Kienle, V. Duppel and M. Jansen, *J. Solid State Chem.*, 2011, **184**, 1112-1119.

26 D. Yang and R. F. Frindt, *J. Appl. Phys.*, 1996, **5**, 2376-2385.

3.5 Supporting Information

A facile wet chemistry approach towards unilamellar tin sulfide nanosheets from $Li_{4x}Sn_{1-x}S_2$ solid solutions

Alexander Kuhn, [a] *Tanja Holzmann,* [a] *Viola Duppel,* [a] *Jürgen Nuss,* [a] *and Bettina V. Lotsch* [a,b*]

a) Max Planck Institute for Solid State Research, Heisenbergstr. 1, 70569 Stuttgart, Germany.

b) Department of Chemistry, Ludwig-Maximilans-Universität München, Butenandtstr. 5-13, 81377 München, and Nanosystems Initiative Munich (NIM) & Center for Nanoscience, Schellingstr. 4, 80799 München, Germany

1. Structural Details

Table S1. Crystallographic details of Li_2SnS_3 as obtained from single-crystal X-ray diffraction using Mo-K_α radiation.

Li_2SnS_3	slowly cooled down	melt-quenched
temperature	298 K	298 K
space group (number)	$C2/c$ (15)	$R\bar{3}m$ (166)
lattice constants	a = 6.3961(7) Å	a = 3.6868(2) Å
	b = 11.0893(13) Å	a = 3.6868(2) Å
	c = 12.4157(14) Å	c = 18.300(2) Å
	β = 99.860(2)°	γ = 120°
cell volume	V = 867.62(17) Å^3	V = 215.42(3) Å^3
unit cell content	Z = 8	Z = 2
radiation	Mo K_α	Mo K_α
max 2Θ	69.42°	69.20°
index range	$-9 \leq h \leq 10$	$-5 \leq h \leq 5$
	$-17 \leq k \leq 17$	$-5 \leq k \leq 5$
	$-19 \leq l \leq 19$	$-28 \leq l \leq 28$
total reflections	6216	1091
unique reflections	1754	143
R_{int}	0.028	0.027
R_1	0.054	0.021
$wR2$	0.162	0.055
$GooF$	1.54	1.48
deposition number	CSD-426848	CSD-426849

Table S2. Atomic coordinates for monoclinic Li_2SnS_3 (space group $C2/c$) and rhombohedral Li_2SnS_3 (space group $R\bar{3}m$) as obtained from single-crystal X-ray diffraction using Mo-K$_\alpha$ radiation.

Li_2SnS_3 average structure in $R\bar{3}m$						
site	Wyck.	*x*	*y*	*z*	*occ.*	U_{eq} (Å^2)
SnLi	3*b*	0	0	1/2	Sn 2/3 Li 1/3	0.00487(19)
Li	3*a*	0	0	0	1	0.0148(25)
S	6*c*	0	0	0.24653(5)	1	0.00867(33)
Li_2SnS_3 superstructure in $C2/c$						
site	Wyck.	*x*	*y*	*z*	*occ.*	U_{eq} (Å^2)
SnLi1	4*e*	0	0.74977(5)	1/4	Sn 0.966(4) Li 0.034(4)	0.0127 (2)
SnLi2	4*e*	0	0.08315(5)	1/4	Sn 0.953(4) Li 0.047(4)	0.0132(3)
SnLi3	4*e*	0	0.4151(6)	1/4	Sn 0.080(6) Li 0.920(6)	0.023(2)
Li1	8*f*	0.248(2)	0.0840(13)	-0.0002(12)	1	0.028(3)
Li2	4*d*	1/4	1/4	1/2	1	0.030(5)
S1	8*f*	0.11268(26)	0.08521(13)	0.63106(14)	1	0.0147(4)
S2	8*f*	0.13487(24)	0.24069(13)	0.13088(13)	1	0.0136(4)
S3	8*f*	0.36583(26)	0.08948(15)	0.37062(14)	1	0.0162(4)

Details of the Rietveld refinement for the 2D freestanding film:

The Rietveld refinement of the XRD pattern shown in Fig 7C was performed with the TOPAS software. Although this software is designed for 3D crystals, we used a quasi 2D model to simulate the structure of the 2D crystals. Therefore, we first analyzed the symmetry of the 2D crystal structure which is constructed of edge-sharing octahedra. Such a layer of equal octahedra has the plane group *p*3*m*1. For the refinement with TOPAS, the space group *P*3*m*1 was used, which results in stacking of identical 2D layers in an eclipsed fashion along the *c*-axis, such that the 2D projection of the 3D structure along *c* is identical to that of a single layer. In order to simulate a quasi 2D structure, we chose an arbitrary but very large value for the separation of the SSnS layers along the *c*-axis (here: 330 Å). Using a very large cell still results in discrete reflections in reciprocal space instead of continuous rods as expected for a true 2D crystal, but already a small broadening of the discrete reflections applied to the model leads to the continuous behavior as expected for a true 2D crystal, which would be obtained as a limit when the layer separation reaches infinity.

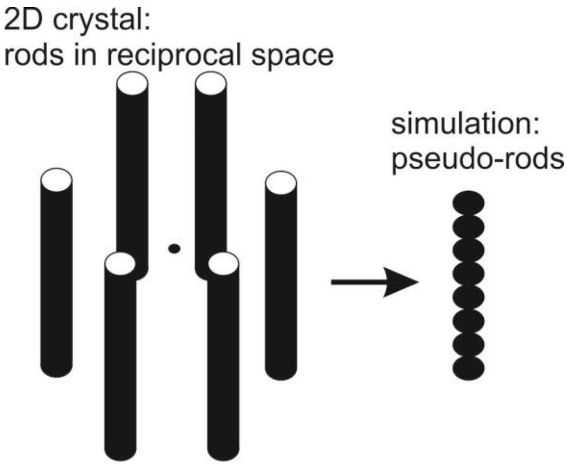

Figure S1. Schematic picture of the representation a 2D crystal in reciprocal space and its simulation with a 3D periodic structure of layers separated by large distances.

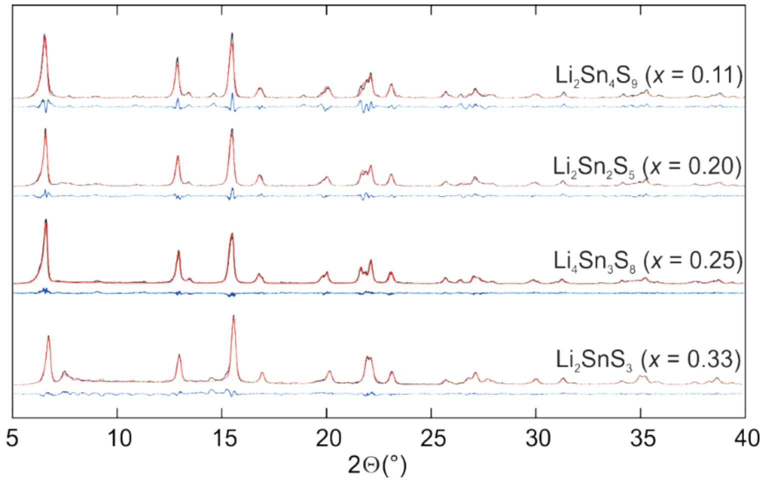

Figure S2. Rietveld refinements of $Li_{4x}Sn_{1-x}S_2$ with $0.11 \leq x \leq 0.33$ (black dots), refined based on the monoclinic crystal structure of Li_2SnS_3 as obtained from single crystal diffraction. Hereby, the occupancies of the SnLi positions (see Table S2) were refined and were equal to the expected values within 5%.

2. Chemical composition

Table S3. SEM-EDX data of Li_2SnS_3 (in at-%).

Spectrum	S	Sn
Spectrum 1	74.60	25.40
Spectrum 2	72.53	27.47
Spectrum 3	74.70	25.30
Spectrum 4	73.10	26.90
Mean	73.73	26.27
Std. deviation	1.08	1.08
Max.	74.70	27.47
Min.	72.53	25.30

Table S4. SEM-EDX data of $Li_4Sn_3S_8$ (in at-%).

Spectrum	S	Sn
Spectrum 1	72.35	27.65
Spectrum 2	71.31	28.69
Spectrum 3	71.81	28.19
Mean	71.82	28.18
Std. deviation	0.52	0.52
Max.	72.35	28.69
Min.	71.31	27.65

Table S5. SEM-EDX data of $Li_2Sn_2S_5$ (in at-%).

Spectrum	S	Sn
Spectrum 1	70.83	29.17
Spectrum 2	70.35	29.65
Spectrum 3	70.86	29.14
Spectrum 4	70.43	29.57
Spectrum 5	70.73	29.27
Spectrum 6	71.34	28.66
Mean	70.76	29.24
Std. deviation	0.35	0.35
Max.	71.34	29.65
Min.	70.35	28.66

Table S6. SEM-EDX data of $Li_2Sn_4S_9$ (in at-%).

Spectrum	S	Sn
Spectrum 1	70.11	29.89
Spectrum 2	69.68	30.32
Spectrum 3	66.87	33.13
Spectrum 4	69.27	30.73
Mean	68.98	31.02
Std. deviation	1.45	1.45
Max.	70.11	33.13
Min.	66.87	29.89

Table S7. SEM-EDX data of the nanosheet pellet after centrifugation at 15000 rpm and drying at 110 °C (in at-%).

Spectrum	S	Sn
Spectrum 1	64.65	35.35
Spectrum 2	65.93	34.07
Spectrum 3	65.31	34.69
Mean	65.30	34.70
Std. deviation	0.64	0.64
Max.	65.93	35.35
Min.	64.65	34.07

Table S8. SEM-EDX data of the nanosheet pellet after rotary evaporation of the solvent at 70 °C (in at-%).

Spectrum	S	Sn
Spectrum 1	71.93	28.07
Spectrum 2	68.80	31.20
Spectrum 3	70.21	29.79
Mean	70.31	29.69
Std. deviation	1.57	1.57
Max.	71.93	31.20
Min.	68.80	28.07

Table S9. ICP-AES results of nanosheet (NS) pellet after centrifugation, NS suspension, supernatant after centrifugation, and bulk material.

Material	Li [wt-%]	Sn [wt-%]	Atomic ratio Li : Sn
NS pellet of $Li_2Sn_2S_5$ after centrifugation (measurement 1)	1.7	47.89	1.00 : 1.64
NS pellet of $Li_2Sn_2S_5$ after centrifugation (measurement 2)	1.69	47.75	1.00 : 1.69
NS pellet of $Li_2Sn_2S_5$ after 3 washing steps and centrifugation (measurement 1)	0.7	65.17	1.00 : 5.44
NS Suspension of $Li_2Sn_2S_5$	29.44	510.14	1.00 : 1.01
Supernatant of NS suspension after centrifugation at 15000 rpm for 30 minutes	15.06	53.44	4.82 : 1.00
Bulk of $Li_2Sn_2S_5$	3.25	56.09	1.00 : 1.00
NS pellet of $Li_2Sn_2S_5$ after annealing at 450 °C (measurement 1)	1.04	63.69	1.00 : 3.58
NS pellet of $Li_2Sn_2S_5$ after annealing at 450 °C (measurement 2)	1.05	65.43	1 : 3.65

3. AFM images

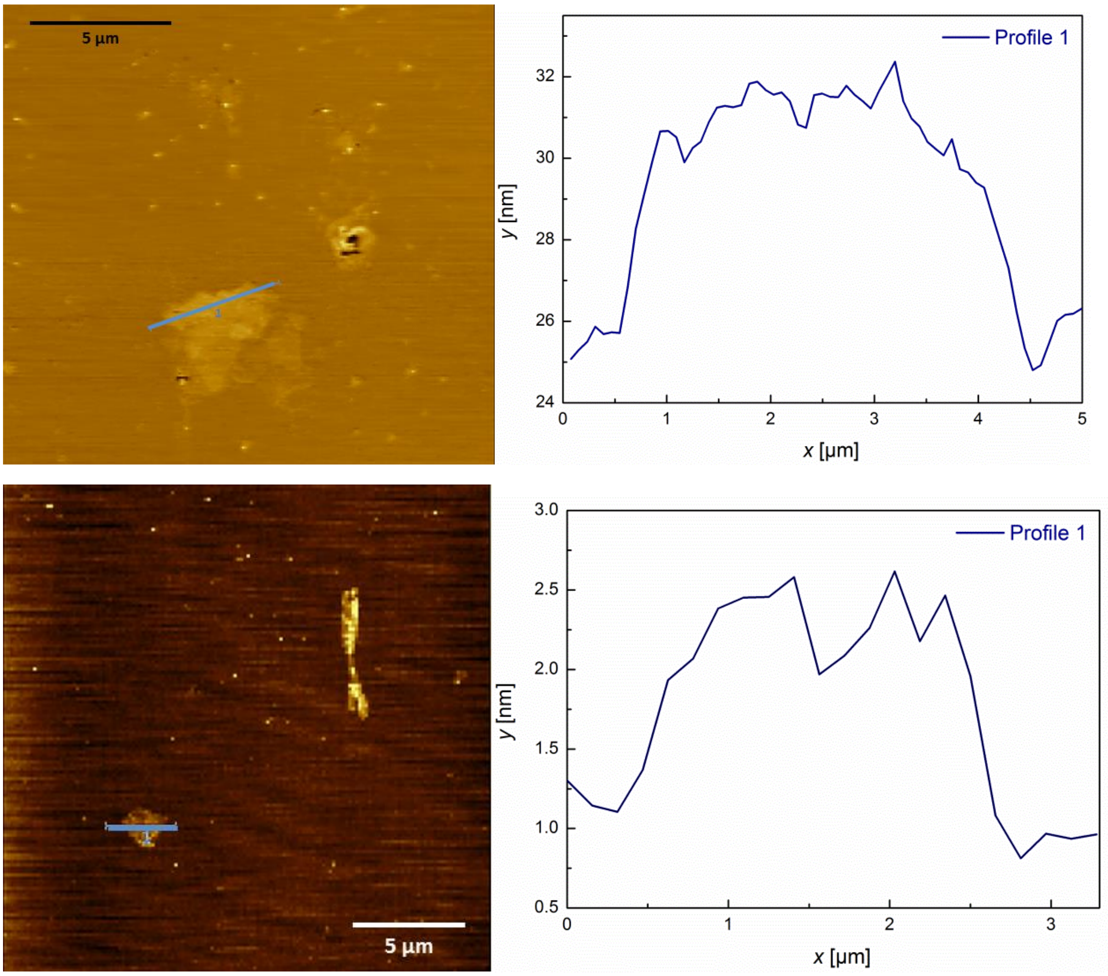

Figure S3. Left: AFM images of nanosheet from a Li_2SnS_3/H_2O nanosheet suspension deposited on a Si/SiO_2(300nm) wafer. Right: Respective height profiles. Height: 4 nm (top), 1.5 nm (bottom)

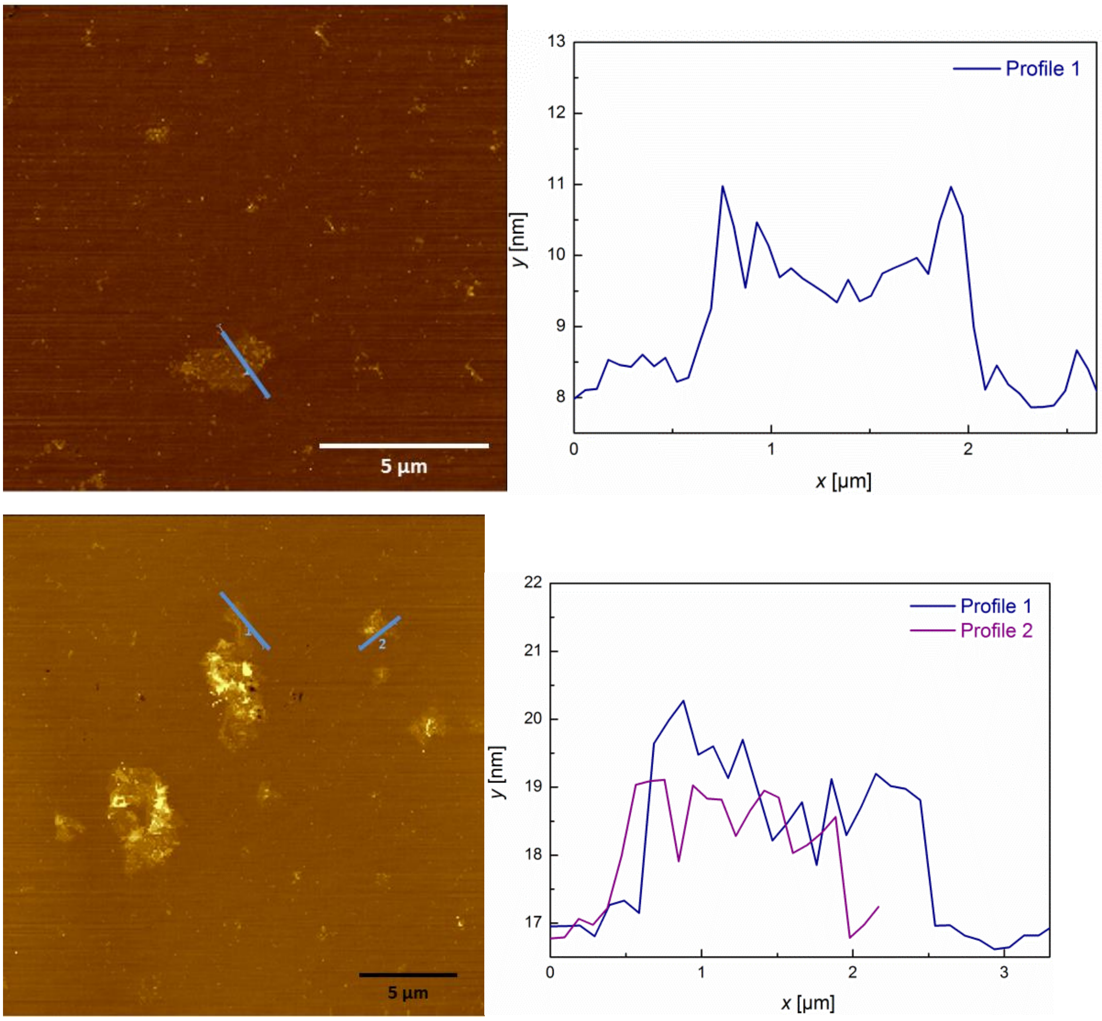

Figure S4. Left: AFM images of nanosheets from a $Li_4Sn_3S_8/H_2O$ nanosheet suspension deposited on a Si/SiO_2(300nm) wafer. Right: Respective height profiles. Height of the nanosheets: approx. 2 nm.

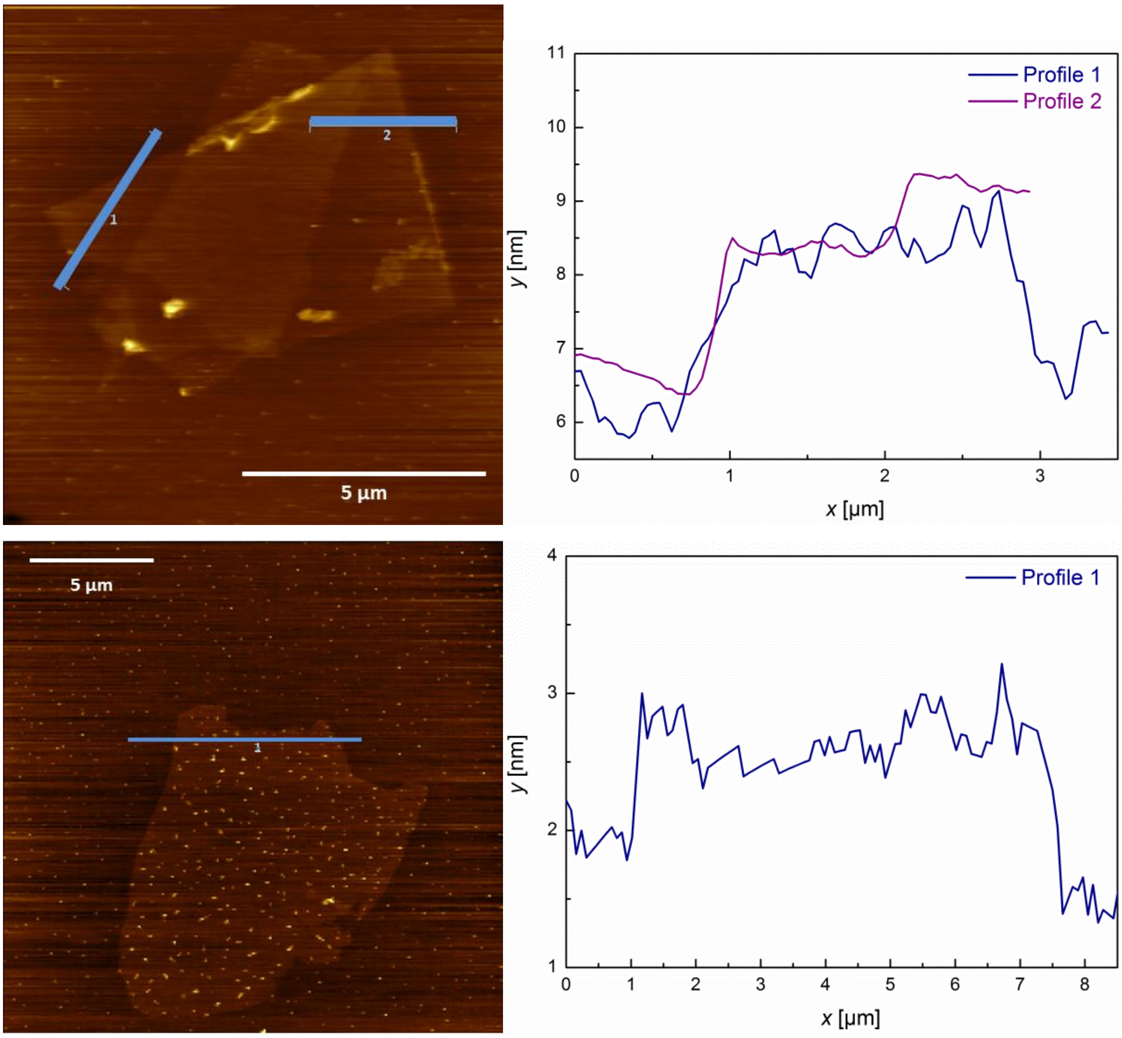

Figure S5. Left: AFM images of nanosheets from a $Li_2Sn_2S_5/H_2O$ nanosheet suspension deposited on a Si/SiO_2(300nm) wafer. Right: Height profile of two overlapping single sheets (top, about 1 nm height) and height profile of a single nanosheet, showing 1 nm height (bottom).

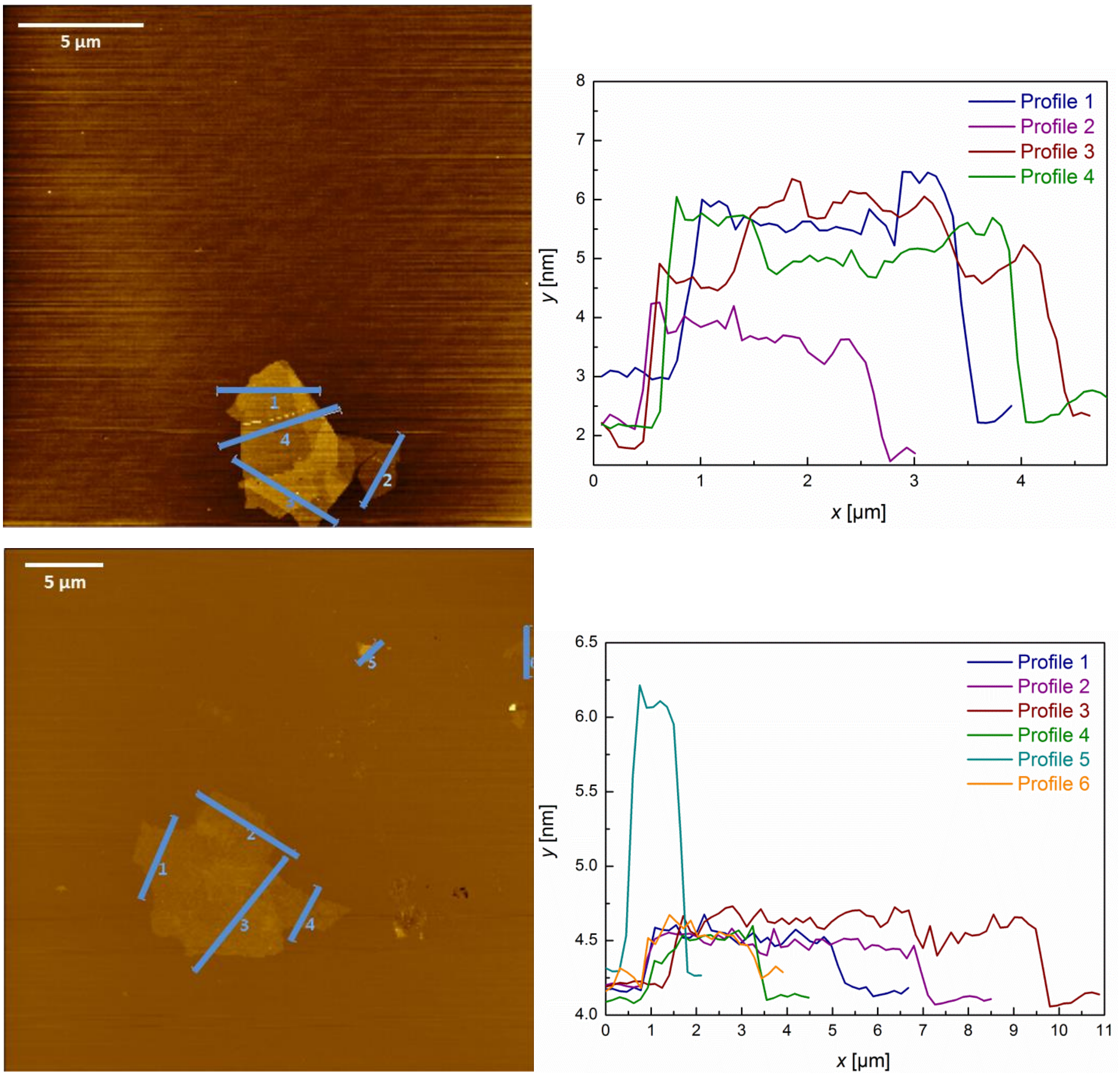

Figure S6. Left: AFM images of nanosheets from a $Li_2Sn_4S_9/H_2O$ nanosheet suspension deposited on a Si/SiO_2(300nm) wafer. Right: Top: folded and stacked sheets with individual height of 2 and 1 nm. Bottom: large nanosheet with a height of 0.6 nm.

4. TEM images

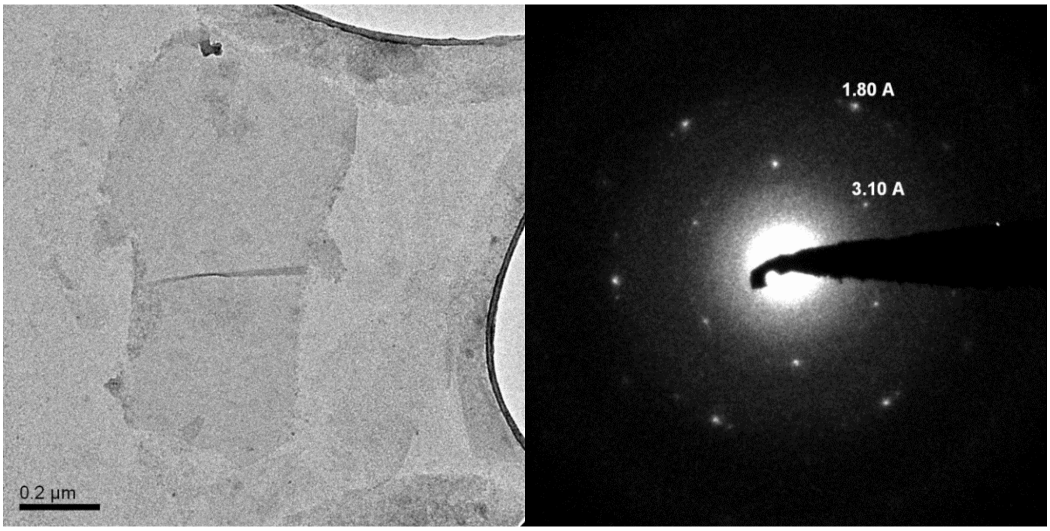

Figure S7. Left: TEM image of a nanosheet obtained by drop-casting a Li_2SnS_3/H_2O nanosheet suspension on a lacey carbon film/copper grid. Right: SAED pattern of the nanosheet shown left.

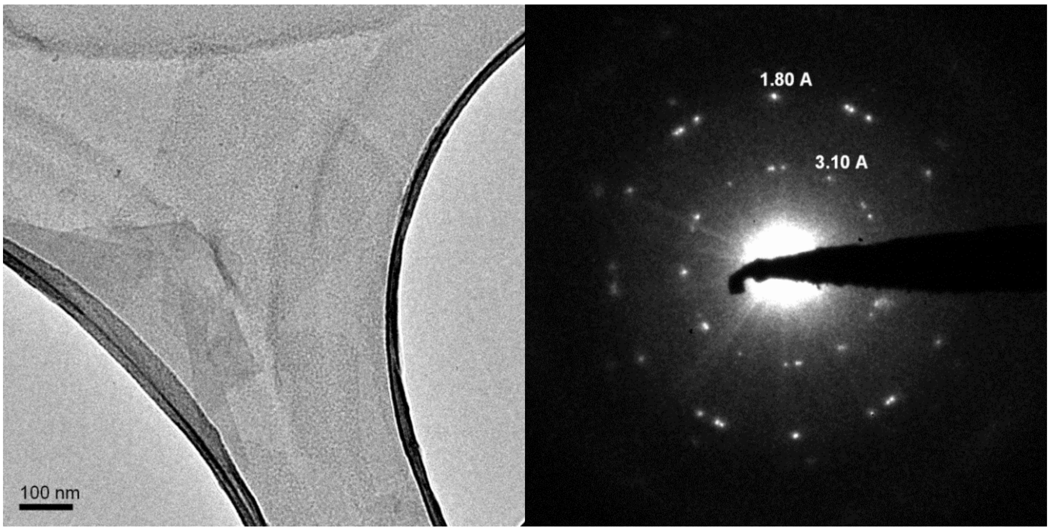

Figure S8. Left: TEM image of a nanosheet obtained by drop-casting the $Li_4Sn_3S_8/H_2O$ nanosheet suspension on a lacey carbon film/copper grid. Right: SAED pattern of the nanosheet shown left.

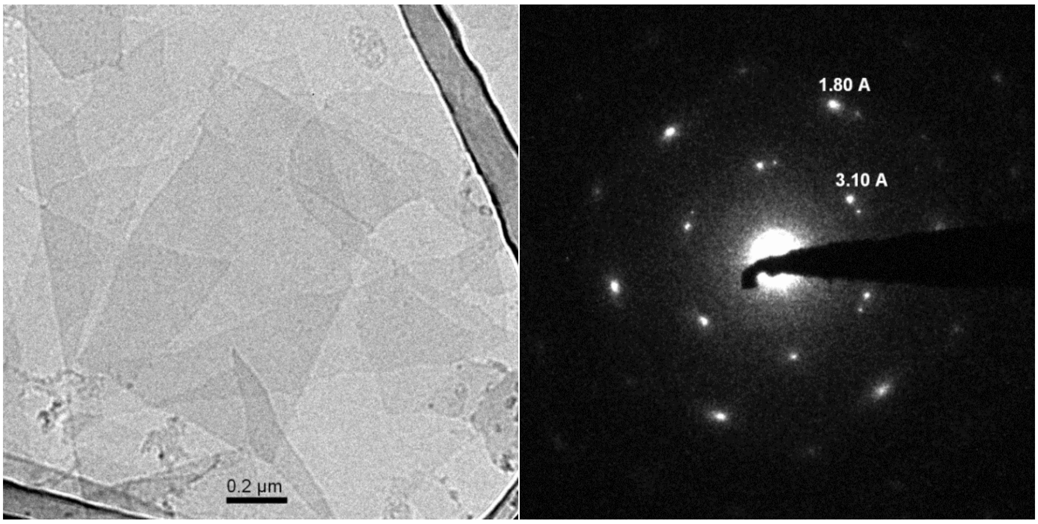

Figure S9. Left: TEM image of a nanosheet obtained by drop-casting the $Li_2Sn_4S_9/H_2O$ nanosheet suspension on a lacey carbon film/copper grid. Right: representative SAED pattern of the nanosheet shown left.

5. Kubelka-Munk spectrum

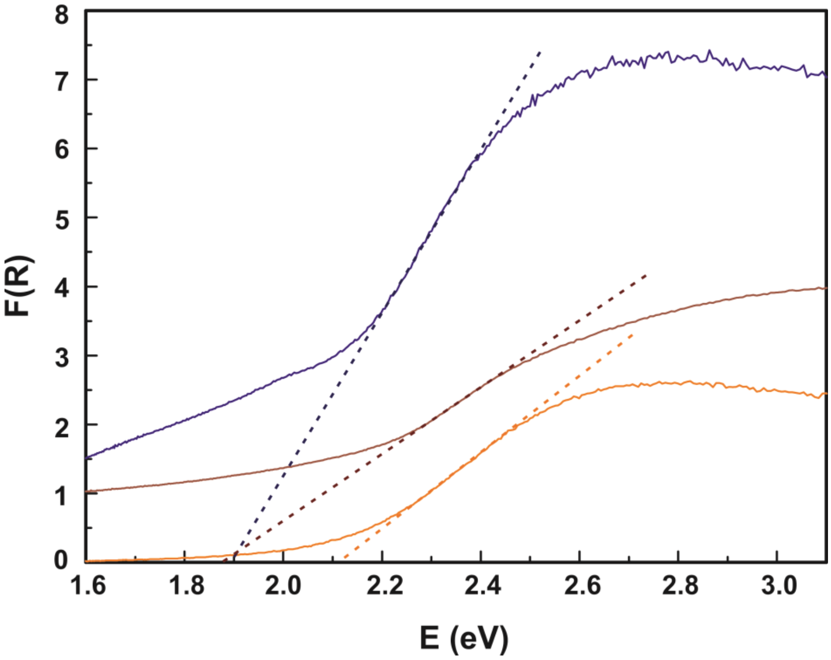

Figure S10. Kubelka-Munk spectra of bulk $Li_2Sn_2S_5$ (blue line), the nanosheet film after centrifugation and drying (yellow line) and the annealed nanosheet film (brown line). The straight lines indicate the linear region of the absorption edges. Their intersection with the *x*-axis gives the optical bandgap of the material, which is ≈ 1.9 eV for the bulk material $Li_2Sn_2S_5$ and the annealed nanosheet pellet, and ≈ 2.1 eV for the nanosheet pellet. Due to the rather smooth absorption edges, these values should only be considered as a rough estimate.

4 $Li_{0.6}[Li_{0.2}Sn_{0.8}S_2]$ – a layered lithium superionic conductor

T. Holzmann, L. M. Schoop, M. N. Ali, I. Moudrakovski, G. Gregori, J. Maier, R. J. Cava, B. V. Lotsch

published in Energy Environ. Sci. **2016**, *9*, 2578-2585.

DOI: 10.1039/c6ee00633g

Reproduced by permission of The Royal Society of Chemistry

http://pubs.rsc.org/en/content/articlepdf/2016/ee/c6ee00633g

Outside front cover image by Christoph Hohmann (NIM)

$Li_{0.6}[Li_{0.2}Sn_{0.8}S_2]$ - a layered lithium superionic conductor

T. Holzmann[†‡§], *L. M. Schoop*[†*], *M. N. Ali*[*], *I. Moudrakovski*[†], *G. Gregori*[†], *J. Maier*[†], *R. J. Cava*[*], *B. V. Lotsch*[†‡§]

[†]Max Planck Institute for Solid State Research, Heisenbergstr. 1, 70569 Stuttgart, Germany

[‡]Department of Chemistry, Ludwig-Maximilians-Universität München, Butenandtstr. 5-13, 81377 München, Germany

[§]Nanosystems Initiative Munich (NIM) & Center for Nanoscience, Schellingstr. 4, 80799 München, Germany

[*]Department of Chemistry, Princeton University, Princeton, NJ 08544, USA.

One of the key challenges of energy research is finding solid electrolytes with high lithium conductivities comparable to those of liquid electrolytes. In this context, developing new structural families of potential Li$^+$ ion conductors and identifying structural descriptors for fast Li$^+$ ion conduction to occur is key to expand the scope of viable Li$^+$ ion conductors. Here, we report that the layered material $Li_{0.6}[Li_{0.2}Sn_{0.8}S_2]$ shows a Li$^+$ ion conductivity comparable to the currently best lithium superionic conductors (LISICONs). $Li_{0.6}[Li_{0.2}Sn_{0.8}S_2]$ is composed of layers comprising edge-sharing Li/SnS_6 octahedra, interleaved with both tetrahedrally and octahedrally coordinated Li$^+$ ions. Pulsed field gradient (PFG) NMR studies on powder samples show intragrain (bulk) diffusion coefficients D_{NMR} on the order of 10^{-11} m^2 s^{-1} at room temperature, which corresponds to a conductivity σ_{NMR} of 9.3×10^{-3} S cm^{-1} assuming the Nernst-Einstein equation, thus putting $Li_{0.6}[Li_{0.2}Sn_{0.8}S_2]$ *en par* with the best Li solid electrolytes reported to date. This is in agreement with impedance spectroscopy on powder pellets, showing a conductivity of 1.5×10^{-2} S cm^{-1}. Direct current galvanostatic polarization/depolarization measurements on such samples show negligible electronic contributions (less than 10^{-9} S cm^{-1}) but indicate significant contact resistance (d.c. conductivity in a reversible cell is 1.2×10^{-4} S cm^{-1} at 298 K). Our results suggest that the partial occupation of interlayer Li$^+$ positions in this

layered material is beneficial for its transport properties, which together with tetrahedrally coordinated Li sites provides facile Li^+ ion diffusion pathways in the intergallery space between the covalent $Sn(Li)S_2$ layers. This work therefore points to a generic design principle for new layered Li^+ ion conductors based on the controlled depletion of Li^+ ions in the interlayer space.

Broader context

Fast solid lithium conductors with negligible electronic contribution are materials of enormous scientific and technological significance. Solid electrolytes enabling rapid ion transport are key ingredients of all-solid-state devices such as batteries, supercapacitors, electrochemical sensors and actuators. Especially in the field of Li-based batteries, appropriate electrolytes with high Li ion conductivities are key ingredients, given the fact that conventional liquid electrolytes suffer from severe safety risks. Therefore, discovering new solid electrolytes composed of earth-abundant elements is in high demand. Here, we describe the first simple ternary ultrafast solid electrolyte and point to a new design principle according to which the implementation of vacant Li sites can drastically enhance the Li ion mobility by orders of magnitude.

4.1 Introduction

Efficient battery systems for mobile applications, particularly in portable devices, are currently in high demand. To date, rechargeable Li^+ ion batteries are leading in performance but suffer from safety concerns augmented by the use of liquid electrolytes. Current lines of research are therefore directed towards the development of non-flammable, non-toxic solid Li electrolytes for use in all-solid-state Li^+ ion batteries with similar power densities In view of the delicate nature of the solid-solid contacts they are particularly relevant for thin film battery applications. Furthermore, solid electrolytes are relevant for various other applications such as electrochemical capacitors, electrochemical sensors and electrochemical actuators.

Since its discovery in the 1970s, lithium nitride (Li_3N) and its doped variants have been the best Li^+ ion conductors ($\sigma_{298K} = 6 \times 10^{-3}$ S cm^{-1}). However, due to its high reactivity and low electrochemical decomposition potential, Li_3N is not suitable for commercial applications.[1,2] Other Li^+ ion conducting materials with high conductivities are e.g. oxide perovskites ($La_{0.3}Li_{0.5}TiO_3$; $\sigma_{298K} \approx 1 \times 10^{-3}$ S cm^{-1}),[3] garnet-type systems such as $Li_7La_3Zr_2O_{12}$ ($\sigma_{298K} \approx 3 \times 10^{-4}$ S cm^{-1}),[4] sulfides such as Li_4SnS_4 ($\sigma_{298K} \approx 7 \times 10^{-5}$ S cm^{-1})[5] and the 70 $Li_2S \cdot 30\ P_2S_5$ glass ceramic ($\sigma_{298K} \approx 3.2 \times 10^{-3}$ S cm^{-1})[6] and mixed chalcogenide glassy materials (Li_2S-SiS_2-Li_3PO_4; $\sigma_{298K} \approx 7.6 \times 10^{-4}$ S cm^{-1}).[7] One of the most prominent classes of *crystalline* Li electrolytes are the so-called lithium superionic conductors (LISICONs), which evolved from the prototype $Li_{2+2x}Zn_{1-x}GeO_4$ with $\sigma_{298K} \approx 1 \times 10^{-7}$ S cm^{-1}.[8,9] The highest Li^+ ion conductivities in this class of materials (up to 10^{-3} S cm^{-1}) are found in the isotypic thio-LISICON solid solutions with composition $Li_{4-x}Ge_{1-x}P_xS_4$ ($x = 0.75$).[10] Recently, Li^+ ion conductivity has been significantly improved in the structurally related tetragonal solid solution with composition $Li_{11-x}M_{2-x}P_{1+x}S_{12}$ (M = Si, Ge, Sn), which displays Li^+ ion conductivities on the order of 10^{-2} S cm^{-1} at room temperature for $Li_{10}GeP_2S_{12}$[11] and $Li_{11}Si_2PS_{12}$.[12]

The crystal structure of the layered lithium intercalated tin sulfide $Li[Li_{0.33}Sn_{0.67}S_2]$ shows Li distributed both in and between Li/Sn-ordered honeycomb sulfide layers.[13,14] Brant *et al.*[14] reported $Li[Li_{0.33}Sn_{0.67}S_2]$ to be a fast Li^+ ion conductor with $\sigma_{298K} = 1.5 \cdot 10^{-5}$ S cm^{-1}, environmental stability under ambient conditions and high thermal stability up to 750 °C. $Li[Li_{0.33}Sn_{0.67}S_2]$ crystallizes in the Na_2IrO_3 structure type (space group *C*2/*c)*, an ordered variant of the layered α-$NaFeO_2$ structure. The structure of Na_2IrO_3 differs from that of α-$NaFeO_2$ (which consists of alternating layers of Na and Fe octahedrally coordinated by oxygen) in having a mixed Na/Ir layer that orders in a honeycomb fashion. Both of these structures are related to the Delafossite structure, which has linear, rather than octahedral, coordination of the interlayer cation. Note that these materials are structurally related to the widely used electrode material $LiCoO_2$.[15,16] We previously reported a related compound with a stoichiometry of $Li_{0.6}[Li_{0.2}Sn_{0.8}S_2]$ to exist in the ternary Li-Sn-S phase diagram, however the details of its crystal structure remained unsolved.[13] Aqueous exfoliation of the layered $Li_{0.6}[Li_{0.2}Sn_{0.8}S_2]$ into single layer nanosheets is extremely facile.

For easier comparison of the two materials $Li[Li_{0.33}Sn_{0.67}S_2]$ and $Li_{0.6}[Li_{0.2}Sn_{0.8}S_2]$ we use the general formula $Li_{3x}[Li_xSn_{1-x}S_2]$, where Li_{3x} corresponds to the interlayer Li atoms and $[Li_xSn_{1-x}S_2]$ to the covalent layers. This representation displays that for each Li atom located in the layers, three times as many Li^+ ions must be found in between the layers. The lithium content within the tin sulfide layer decreases from Li : Sn = 1 : 2 in $Li[Li_{0.33}Sn_{0.67}S_2]$ ($x = 0.33$; Li_2SnS_3) to 1 : 4 in $Li_{0.6}[Li_{0.2}Sn_{0.8}S_2]$ ($x = 0.2$). Similarly, the Li content in the interlayer gallery decreases from full occupation in $Li[Li_{0.33}Sn_{0.67}S_2]$ to only 60 % occupancy in $Li_{0.6}[Li_{0.2}Sn_{0.8}S_2]$. With respect to these interlayer Li^+ ions, $Li_{0.6}[Li_{0.2}Sn_{0.8}S_2]$ can be viewed as a lithium-depleted version. Here the Li^+ deficiency is compensated by Sn^{4+} excess, while in various other layered compounds discussed in the literature the interlayer cation deficiency is compensated by electron holes, corresponding to an oxidation of framework species.[17,18] Here we show that the ionic conductivity of $Li_{0.6}[Li_{0.2}Sn_{0.8}S_2]$ is as high as 10 mS cm^{-1} at room temperature (determined by PFG NMR), which is more than two orders of magnitude higher than the ionic conductivity of $Li[Li_{0.33}Sn_{0.67}S_2]$ on cold pressed powders. This is most likely related to the reduced amount of Li^+ ions in between the layers, in agreement with a recent report concerning Na^+ ion conductivity in $NaFeO_2$-related materials.[19] Our findings therefore strengthen the argument that interlayer cation depleted layered materials can be excellent ion conductors with Li^+ ion conductivities *en par* with those of 3D thio-LISICON materials. The high ionic conductivity of 10 mS cm^{-1} and the very low electronic contribution ($<10^{-9}$ S cm^{-1}) places $Li_{0.6}[Li_{0.2}Sn_{0.8}S_2]$ among the best solid Li^+ electrolytes known to date.

4.2 Experimental section

Polycrystalline $Li_{0.6}[Li_{0.2}Sn_{0.8}S_2]$ was synthesized in three different procedures at 700 – 750 °C, with three different starting reagents. Synthesis 1 was reported by Kuhn *et al.*,[13] synthesis 2 was performed with Li_2CO_3, SnS_2 and S, and synthesis 3 with Li_2S, SnS_2 and S. For synthesis 1 an amorphous phase was found in the NMR spectra which could be avoided by using syntheses 2 or 3. Further details are described in the supporting information. Note that without quenching – for synthesis 2 and 3 - we did not find any evidence for the existence of other ternary compounds in addition to $Li_{1.0}[Li_{0.33}Sn_{0.67}S_2]$ and $Li_{0.6}[Li_{0.2}Sn_{0.8}S_2]$. Other compositions prepared by our method resulted in mixed phases. Small single crystals were obtained by subliming $Li_{0.6}[Li_{0.2}Sn_{0.8}S_2]$ at 750 °C in a vacuum-sealed ampoule for several days.

Single-crystal X-ray diffraction (SXRD) was conducted on a Bruker APEX II diffractometer with Mo-K_α radiation at 100 K. Unit cell refinement and data integration was performed with the Bruker APEX II software and CELL_NOW. The crystal structure was refined using the full-matrix least-squared method on F^2, implemented through SHELXL-2013 and WinGX.

SEM/EDX measurements were performed with a scanning electron microscope (SEM; Vega TS 5130 MM, Tescan) using a Si/Li detector (Oxford). ICP-AES was done with a Vista Pro ICP-AES spectrometer.

^{6}Li and ^{119}Sn solid-state (ss) NMR spectra were obtained on a Bruker Avance III 400 MHz instrument (B_0 = 9.4 T) at Larmor frequencies of 400 MHz, 58.88 MHz and 149.12 MHz, respectively. ^{7}Li T_1 relaxation time measurements at various temperatures were performed to determine the activation energies. Further details are described in the supporting information. ^{7}Li Pulsed Field Gradient (PFG) NMR measurements were performed on a Bruker Avance-III 400 MHz instrument (magnetic field of 9.4 T, and ^{7}Li Larmor frequency of 155.56 MHz), equipped with a diff60 single gradient diffusion probe. The probe allows for pulse field gradients g of up to 30 T/m and variable temperature measurements up to +150 °C. The diffusion measurements were accomplished using a Stimulated Echo pulse sequence.[20] The echo attenuation curves $S(g,\delta,\Delta)$ were processed using the Stejscal-Tanner equation,[21] $S(g,\delta,\Delta) = \mathrm{E}(-\gamma^2\delta^2g^2D(\Delta-\delta)/3)$, where $\gamma = 1.398 \times 10^8$ Hz/T is the ^{7}Li gyromagnetic ratio, g is the strength of the pulse field gradient of duration δ, D is the effective diffusion coefficient, and Δ is the time interval between the field gradients that defines the diffusion time scale. Diffusion constants near room temperature, where diffusion is slow, were obtained by varying the gradient strength between 0.1 and 30 T/m at a fixed $\delta = 1.0$ ms, in a range of Δ = 10-100 ms. At higher temperatures, when diffraction effects in an attenuation curve become apparent, the diffusion measurements were performed by varying δ in a range of 0.25-4.0 ms at a fixed gradient strength g of 900 G, and a fixed Δ of 20 ms.

For electrical conductivity measurements two different configurations were used. In each of them, the thoroughly ground powder was filled into a Teflon die with an inner diameter of 4 mm. The powder was compressed by two stamps (Ø 4 mm) and they were fixed in a uniaxial press during the measurements. The density of the cold-pressed powders is estimated to be 75 %. In configuration 1, in order to avoid any undesired reaction between lithium and the stamp and to ensure a good contact, a 0.1 mm thick gold foil was placed between the plunger and the powder at both sites. Configuration 1 is described therefore as Au|$Li_{0.6}[Li_{0.2}Sn_{0.8}S_2]$|Au. For configuration 2, an additional small layer of LiAl alloy was placed between the sample and the gold foil at both sides (Au|LiAl|$Li_{0.6}[Li_{0.2}Sn_{0.8}S_2]$|LiAl|Au). The alloy acts as a lithium reservoir and allows for both ionic and electronic charge transfer – thereby, concentration polarization effects on the electrodes can be avoided. For each configuration, DC galvanostatic polarization/depolarization measurements were carried out with a Keithley 2604B source-meter, while impedance spectroscopy was performed using a Novocontrol Alpha-A high-performance frequency analyzer at frequencies ranging between 1 MHz and 0.01 Hz (AC voltage of 0.15 V). The impedance spectra were analyzed using the commercial software Z-View by Scribner Assoc.

4.3 Results and discussion

The crystal structure of $Li_{0.6}[Li_{0.2}Sn_{0.8}S_2]$ was solved by single crystal X-ray diffraction in the monoclinic space group $C2/m$ (no. 12) with $a = 19.217(7)$ Å, $b = 3.6996(14)$ Å, $c = 6.529(2)$ Å, and $\beta = 109.056(4)$ ° to a $wR2$ value of 6.6% and a $R1$ ($Fo > 2\sigma(Fo)$) value of 2.4 % . The structure is displayed in Figure 1, the crystallographic details are listed in Table 1, the atomic coordinates and the anisotropic displacement parameters are given in Table S1 and Table S2 (see supporting information). We have confirmed with powder X-ray diffraction that the solution of the single crystal data largely corresponds to the structure of the bulk phase. Slight differences in the powder X-ray pattern compared to the single crystal structure are observed in the 2θ range between 7 and 12°, which is diagnostic of different concentrations of stacking faults in the polycrystalline powder compared to the single crystal, as also observed by J. A. Brant *et al.*[14] for $Li[Li_{0.33}Sn_{0.67}S_2]$. The observed monoclinic superstructure arises from the rhombohedral subcell through cation ordering within the layers, which is commonly observed in materials of this type.[38-41] The chemical formula was confirmed using SEM/EDX and ICP-AES (Figure S2, Table S3 and Table S4, supporting information). SS NMR was performed to confirm the +IV oxidation state of Sn (Figure S3-S6, see supporting information).

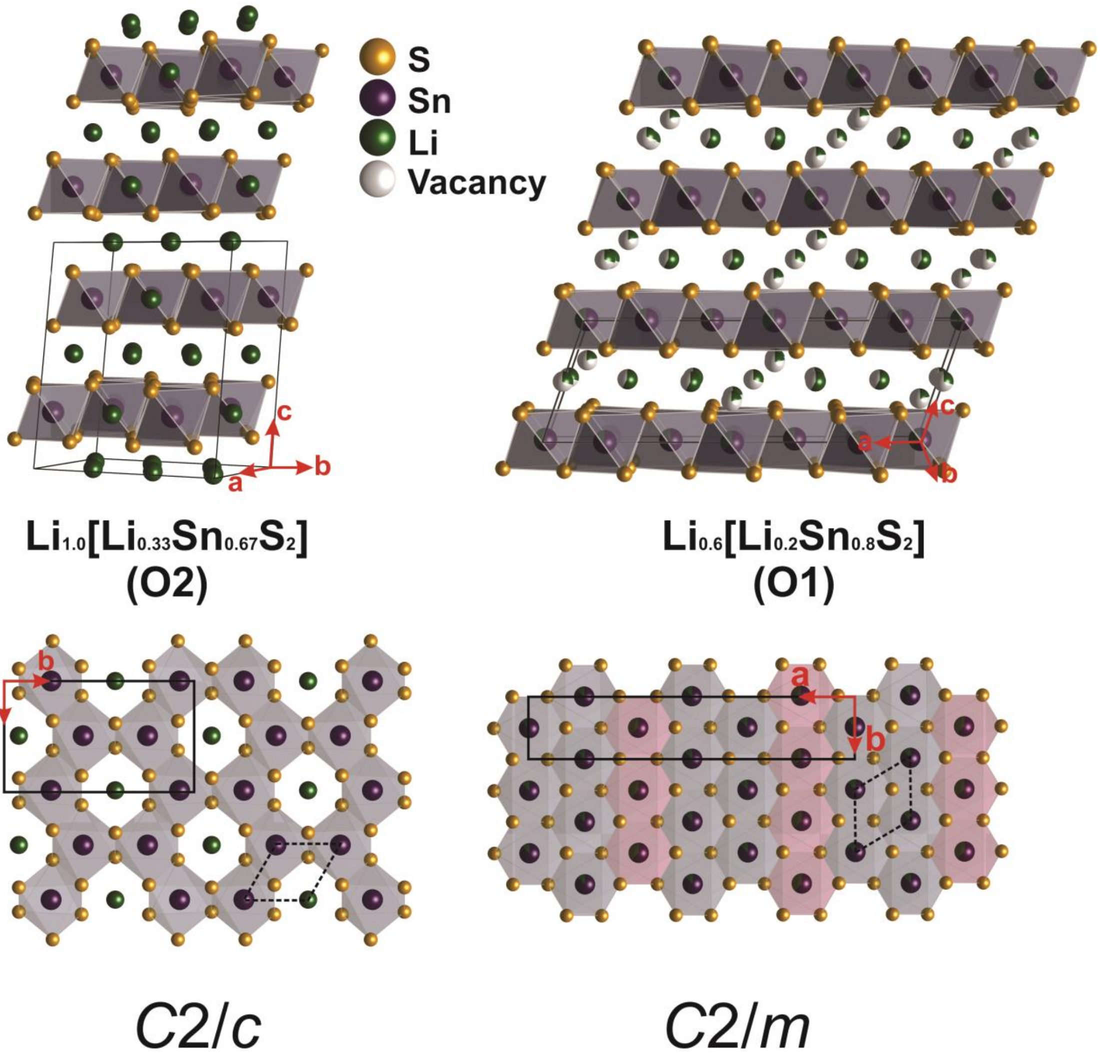

Fig. 1 Left: Crystal structure of $Li[Li_{0.33}Sn_{0.67}S_2]$ with a fully Sn/Li ordered layer and O2 stacking (octahedrally coordinated, two layers per unit cell).[14] Right: Crystal structure of $Li_{0.6}[Li_{0.2}Sn_{0.8}S_2]$ with partially substituted tin positions (displayed by mixed colors of purple and green for tin and lithium, respectively) and an O1 type stacking. A vertical top-view of the layers is shown in the bottom row – the polyhedra of $Li_{0.6}[Li_{0.2}Sn_{0.8}S_2]$ are here displayed in two different colors to clearly illustrate the Sn1/Li1 position (in red) and the Li2/Sn2 position (in grey). The solid lines represent the monoclinic unit cells due to the intralayer ordering obtained by the crystal structure solution, the dashed lines represent the rhombohedral subcells of the monoclinic superstructures.

The structure of $Li_{0.6}[Li_{0.2}Sn_{0.8}S_2]$ is related to the structure of its parent compound $Li[Li_{0.33}Sn_{0.67}S_2]$. Both compounds ($Li[Li_{0.33}Sn_{0.67}S_2]$ in *C*2/*c* and $Li_{0.6}[Li_{0.2}Sn_{0.8}S_2]$ in *C*2/*m*) are composed of layers of edge-sharing tin sulfide octahedra which face in the same direction, and Li$^+$ ions that are sandwiched between the layers (see Figure 1). The Sn atoms are arranged in a hexagonal net; part of the Sn is substituted by Li in both structures and (partial) ordering of the Sn atom in the layer causes a monoclinic supercell. In

$Li[Li_{0.33}Sn_{0.67}S_2]$ the Sn atoms are arranged in a honeycomb order with Li occupying the voids of the honeycomb. In $Li_{0.6}[Li_{0.2}Sn_{0.8}S_2]$, however, the reason for the monoclinic supercell is preferential occupancy of two different Sn positions. This preferential occupancy causes an enlargement of the *a* axis compared to the rhombohedral subcell by a factor of 3√3. Differences in intralayer ordering were also confirmed by ssNMR (see supporting information).

Table 1 Crystallographic details of the single crystal structure solution of $Li_{0.6}[Li_{0.2}Sn_{0.8}S_2]$.

$Li_{0.63}[Li_{0.21}Sn_{0.79}S_2]$	
Temperature	100 K
Symmetry	Monoclinic; *C*2/*m* (12)
Lattice parameters	a = 19.217(7) Å b = 3.6996(14) Å c = 6.529(2) Å β = 109.056(4)°
Cell volume	V = 438.8(3) Å^3
Unit cell content	$Z = 1$
Radiation	Mo-K_α
Θ range	2.24 – 28.12
Index range	$-24 \leq h \leq 24$ $-4 \leq k \leq 4$ $-8 \leq l \leq 8$
Total no. of reflections	2384
Unique reflections	592
R_1 *(all reflections)*	0.041
R_1 $Fo > 2\sigma(Fo)$	0.0241 (434)
wR2	0.0664 (592)
Residual e^- density (e/Å^3)	1.24/-0.96
GooF	1.025
Shape/colour	hexagonal plates/orange
Deposition number	CSD-429584

Upon Li$^+$ ion depopulation of the interlayer Li sites, compensated by increasing the amount of Sn in the honeycomb layers, the interlayer distance *d* slightly increases from 6.11 Å in $Li[Li_{0.33}Sn_{0.67}S_2]$ to 6.17 Å in $Li_{0.6}[Li_{0.2}Sn_{0.8}S_2]$ due to decreased electrostatic attraction forces between the layers, as clearly seen in the PXRD patterns (Figure S1, supporting information).

Both $Li[Li_{0.33}Sn_{0.67}S_2]$ and $Li_{0.6}[Li_{0.2}Sn_{0.8}S_2]$ display O-type stacking of the layers, where the interlayer atoms are octahedrally coordinated by sulfur atoms, which is similar to many other honeycomb type compounds.[22-27] In $Li_{0.6}[Li_{0.2}Sn_{0.8}S_2]$, however, only 77% of the interlayer lithium atoms present occupy those octahedral sites; the other 23% occupy tetrahedral sites that are closer to the covalent layers. We assume that due to the unoccupied positions in the interlayer gallery and the slightly increased distance between the layers, the occupation of both octahedral and tetrahedral sites is possible. The distance between Li in octahedral and tetrahedral positions is about 2.3 Å, which makes it possible, in principle, that lithium occupies adjacent tetrahedral and octahedral sites, according to the Shannon radius of Li$^+$ (0.59 for tetrahedral and 0.76 for octahedral coordination).[28] Nevertheless, it seems more likely that due to the vacant sites either a tetrahedral or an octahedral position is occupied in a particular local region of the structure. This is also supported by the fact that due to the Li depletion, out of all possible octahedral and tetrahedral interlayer Li positions in sum only 38% are occupied.

To add evidence to the distribution of the Li positions, we performed ^{6}Li ssNMR studies on both $Li[Li_{0.33}Sn_{0.67}S_2]$ and $Li_{0.6}[Li_{0.2}Sn_{0.8}S_2]$. The NMR spectra of both samples exhibit narrow, well-resolved signals suggesting phase pure samples with high crystallinity. The ^{6}Li NMR spectrum of $Li[Li_{0.33}Sn_{0.67}S_2]$ shows two signals at -0.2 ppm and 1.5 ppm with an integral ratio of around 75 : 25 (Figure 2, upper panel). This agrees well with the two different types of Li – 75 % (Li1+Li3) between the layers and 25 % (Li2) within the covalent layers – and is in good agreement with the expected fully-ordered honeycomb crystal structure. The ^{6}Li NMR spectrum of $Li_{0.6}[Li_{0.2}Sn_{0.8}S_2]$ displays two signals, at 1.1 ppm and 2.2 ppm, with an integral ratio of 47 : 53. The different integral ratio in $Li_{0.6}[Li_{0.2}Sn_{0.8}S_2]$ supports the structural difference to Li_2SnS_3 and can be rationalized based on the crystal structure (see Table S1, supporting information and Figure 2, lower panel). There are five types of lithium atoms in the unit cell; two (Li1+Li2) are within the layer and three (Li3-Li5) reside in the interlayer gallery, where Li3 and Li4 occupy octahedral positions and Li5 occupies a tetrahedral position. The labelling of each atom position is displayed in Figure 2.

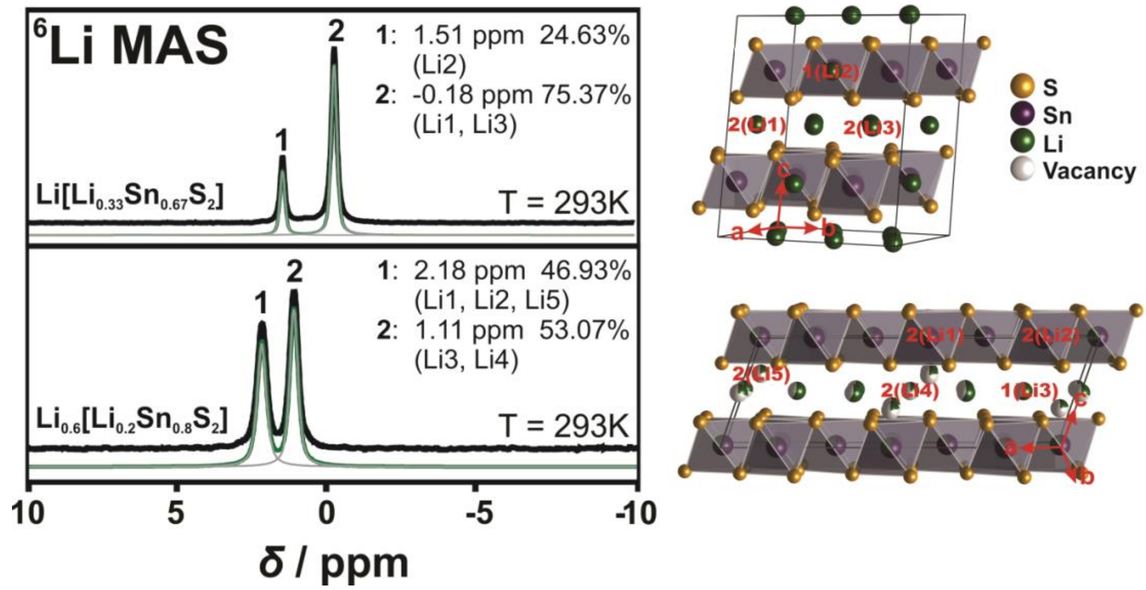

Fig. 2 ^{6}Li NMR measurements of Li[Li$_{0.33}$Sn$_{0.67}$S$_2$] (top left) and Li$_{0.6}$[Li$_{0.2}$Sn$_{0.8}$S$_2$] (bottom left). On the right side, each crystal structure with the labelling of the lithium atoms according to the NMR spectrum is shown. The black line corresponds to the measured spectra, the green line to the sum fit of the different curves (grey lines).

In agreement with Li[Li$_{0.33}$Sn$_{0.67}$S$_2$] the signal of intralayer Li is likely downfield shifted due to the Sn-S environment, hence the intralayer lithium atoms, Li1 and Li2, can be assigned to the signal at 1.1 ppm. Furthermore, we assume that Li5, which is tetrahedrally coordinated, behaves similar to the intralayer Li due to the closeness to the tin sulfide layers. The two octahedrally coordinated Li$^+$ ions Li3 and Li4 can be assigned to the signal at 2.2 ppm. From the crystal structure we then would expect an integral ratio of 42 : 58. This is almost what we see in the NMR spectrum (47 : 53). Note that single crystal XRD data were taken at 100 K and NMR spectra were recorded at room temperature. Since we have more lithium motion at room temperature the integral ratio from NMR spectra and the occupancy ratio from XRD data are expected to not fully match.

Lithium diffusivity was investigated with ^{7}Li PFG NMR at room temperature. Figure 3 (upper panel) displays the diffusion coefficient D_{NMR} as a function of the diffusion time Δ. The longer Δ, the higher is the likelihood of finite crystallite effects on the spectra, since longer diffusion paths will be probed, increasing the chance of intercrystallite diffusion of the Li^+ ions. At shorter diffusion times where intracrystallite diffusion is measured, much higher diffusion coefficients are observed. This dependence on diffusion time indicates that grain boundaries have a significant effect on the transport properties as longer diffusion paths increase the possibility of crossing a grain boundary. Note that the mean free path for diffusion is on the order of ~1μm for diffusion times in the ms range. SEM analysis of the powder samples show that grain sizes vary between 100 μm and less than 1 μm (see Figure S2, supporting information). This indicates that grain boundaries can affect Li^+ ion diffusion at all diffusion times Δ measured here. Note that the values of the room temperature diffusion coefficient D_{NMR} are on the order of 10^{-11} m^2 s^{-1}, which is notably higher than the ones reported for LGPS (~10^{-12} m^2 s^{-1}).[29] We converted D_{NMR} to conductivity σ_{NMR} using the extended Nernst-Einstein relation $\sigma_{NMR} = (D_{NMR}\, n\, z^2\, e^2)\,(k_B\, T)^{-1}$ (see supporting information). We find that for the shortest diffusion time the conductivity reaches a value of $\sigma_{\mathrm{NMR}} = 9.3 \cdot 10^{-3}$ S cm^{-1}. Note that for this analysis we only included interlayer lithium as participants of ion transport (see *TOPOS* calculations below). The overall ^{7}Li NMR signal in the static sample consists of two unresolved components with substantially different spin-spin relaxation times T_2. Only the part of the signal with the longer T_2, however, contributes to the diffusion attenuation curve. That part corresponds to the lithium in the interstitial space and has been consecutively used in all further calculations related to the conductivity (see Figure S10, supporting information).

This was further confirmed by 2D exchange experiments – below ~ 330 K we do not see any exchange between intra and interlayer lithium. The grain boundary conductivity of 9×10^{-4} S cm^{-1} (Δ = 100 ms) assessed by PFG NMR exceeds the value measured with d.c. measurements, 1.2×10^{-4} S cm^{-1}. At an elevated temperature of 407 K, $D_{\mathrm{NMR}} = 2.6 \times 10^{-10}$ m^2 s^{-1} is obtained which corresponds to $\sigma_{\mathrm{NMR}} = 6.7 \times 10^{-2}$ S cm^{-1}. PFG NMR measurements at high temperatures displayed scattering effects that likely arise from the anisotropic lithium movement within the crystals. These problems have been previously observed in different anisotropic materials.[30,31]

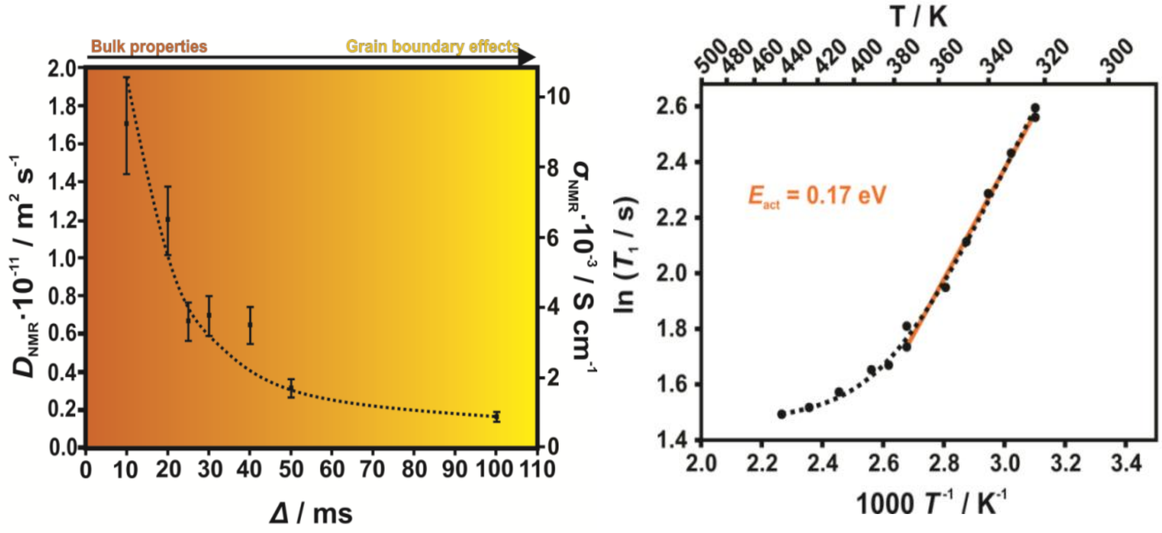

Fig. 3 Left: Diffusion coefficient D_{NMR} determined with PFG NMR at various diffusion times Δ. D_{NMR} is lowered with a longer diffusion time Δ, indicating grain boundary effects in the ion transport that hinder the diffusion. The likelihood for diffusion within one crystallite and hence, bulk diffusion is higher for shorter diffusion times. Hence, ionic conductivity is higher in the bulk. For the calculation of the conductivity σ_{NMR}, the intralayer Li atoms were neglected as they are not assumed to affect the ionic conduction (see Figure S9, supporting information). The experimental error is estimated to be 15%. Right: Activation energy determined by ^{7}Li T_1 relaxation time measurements in the slow motion range at varying temperatures from 320-440 K. The expected shape of the curve according to the BPP model is displayed by a dotted line.

Owing to the scattering effects at high temperatures, we could not determine activation energies with PFG NMR. Further, the preparation of dense samples by sintering suitable for precise impedance spectroscopy measurements was unsuccessful. Therefore, we performed ^{7}Li T_1 relaxation time measurements in a region of slow molecular motion at varying temperatures from 320 – 440 K to determine activation energies (see Figure 3).[32,33] We find an activation energy of $E_{act} = 0.17$ eV that is comparable to values for the currently best LISICONs such as $Li_{10}GeP_2S_{12}$ (0.21 eV) and $Li_{11}Si_2PS_{12}$ (0.19 eV).[12] Nevertheless, different mechanisms can be present simultaneously and we cannot determine which mechanism contributes most.

Figure 4 summarizes the main findings of the electrical conductivity measurements (both d.c. galvanostatic polarization/depolarization and a.c. impedance spectroscopy), which were carried out at room temperature (298 K) and – due to hydration of the material in air - within an argon filled glove box using two different experimental setups with ion-blocking and non-blocking electrodes, respectively (Au|$Li_{0.6}[Li_{0.2}Sn_{0.8}S_2]$|Au and Au|LiAl|$Li_{0.6}[Li_{0.2}Sn_{0.8}S_2]$|LiAl|Au). In the first case (Figure 4, panel a), the voltage change after switching on a d.c. current of 1 nA (at approximately t = 70 min) is characteristic of a slow polarization process due to the accumulation of mobile charge carriers at the sample/electrode interface. Note that turning off the d.c. current (at t = 400 min) results in an equally slow depolarization process. As in this case ion-blocking Au electrodes were used, this clearly indicates that the majority of mobile charge carriers in $Li_{0.6}[Li_{0.2}Sn_{0.8}S_2]$ are ions.

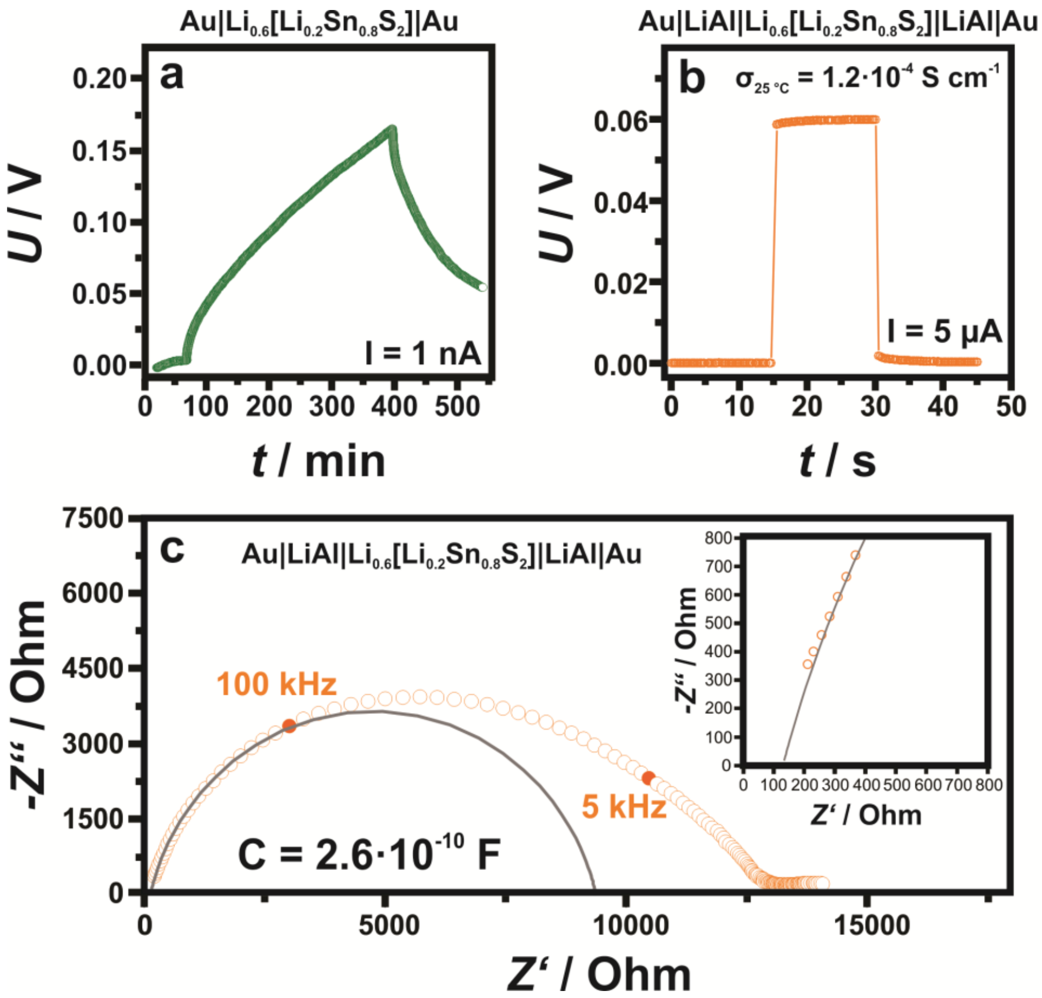

Fig. 4 Electrical measurements on $Li_{0.6}[Li_{0.2}Sn_{0.8}S_2]$ performed at 298 K under argon atmosphere: (a) and (b) display galvanostatic DC measurements of $Li_{0.6}[Li_{0.2}Sn_{0.8}S_2]$ without (a) and with (b) LiAl alloy. In the LiAl configuration there is no polarization effect and the ionic conductivity can easily be determined to $\sigma_{298K} = 1.2 \times 10^{-4}$ S cm^{-1}. Panel (c) displays the impedance spectroscopy measurements ranging between 1 MHz and 0.01 Hz on a non-blocking configuration Au|LiAl|$Li_{0.6}[Li_{0.2}Sn_{0.8}S_2]$|LiAl|Au. The rather distorted spectrum indicates the presence of multiple contributions as expected in the case of cold pressed powders (see main text). The inset shows the finite intercept of the extrapolation of the spectrum towards frequencies exceeding 1 MHz at around 130 Ω (see also Figure S13 in the supporting information) indicating a bulk conductivity that is two orders of magnitudes greater. The intercept of the fitted semicircle in the low fre-

quency range most likely belongs to grain boundary resistance. The suppressed semicircle indicates the presence of a second contact resistance, which is not fitted here. Unlike the high frequency intercept, the low frequency intercept is sensitive to the pressure applied to the powder.

From Figure 4a one can estimate the electronic transference number of $Li_{0.6}[Li_{0.2}Sn_{0.8}S_2]$ to be less than 10^{-4}. Further details for the calculation of the transference number are described in the supporting information; the refined evaluation shifts the upper limit of the transference number to 10^{-9} (see Figure S11). In addition, an impedance spectrum acquired in this configuration (ion blocking electrodes) is shown in Figure S12: a Warburg behavior can be clearly recognized in the low frequency range. The high ionic conductivity is confirmed by the experiments which were performed in the non-blocking Au|LiAl|$Li_{0.6}[Li_{0.2}Sn_{0.8}S_2]$|LiAl|Au configuration (Figure 4, panel b). In this case, the response of the voltage on the application of a d.c. current of 5 μA is instantaneous and corresponds to an effective Li^+ ion conductivity of the sample of $1.2 \cdot 10^{-4}$ S cm^{-1}. In this configuration, also impedance spectroscopy measurements were carried out and a representative complex impedance spectrum is shown in Figure 4c. Here, the spectrum is rather distorted and seems to be composed of at least two contributions. This is not surprising as the sample consists of cold-pressed powders, in which contributions from the bulk, grain boundaries, electrodes and current constrictions (between adjacent particles) can be present. It is noteworthy that, in the low frequency range, the intercept of the spectrum with the real axis (~12500 Ω) is in good agreement with the resistance value that one can extract from the voltage change after the application of the d.c. current (in Figure 4b the change of voltage corresponds to a resistance of 11600 Ω). By fitting the high frequency part of the spectrum with a resistance R in parallel to a constant phase element Q (from which the capacitance can be obtained as $C = (R^{1-n}Q)^{1/n}$ with n being an additional fitting parameter) a capacitance value of 2.6 10^{-10} F is obtained, which corresponds to an apparent relative dielectric constant of 4200. Since $Li_{0.6}[Li_{0.2}Sn_{0.8}S_2]$ is not expected to possess such a large dielectric constant (e.g. it is not a ferroelectric material), this large capacitance cannot be ascribed to the bulk properties of the material, but rather seems to stem from the grain-to-grain contacts. This is supported also by the fact that the extrapolation of the spectrum towards frequencies exceeding 1 MHz results in a finite intercept at about 130 Ω (see inset in Figure 4c), which corresponds most likely to the bulk properties. The supporting information also shows an example (Figure S13) where we extended the measuring range to 10 MHz. Then, in spite of the increased noise, the transition to the bulk semi-circle is visible. Converting this into conductivity, a value of 1.5×10^{-2} S cm^{-1} is obtained, which conforms with the PFG NMR results ($\sigma_{NMR} = 9.3 \times 10^{-3}$ S cm^{-1} for Δ = 10 ms). For different samples, we observe a scatter in the enormously high conductivity, which we propose either stems from variations in the composition or in the distribution of the anisotropic grains (see Table S6, supporting information). At any rate, for optimized single crystalline conditions a conductivity of at least 10 mS cm^{-1} is to be expected. Note that, irrespective of these variations, the high frequency intercept of impedance spectroscopy measurement and the PFG NMR results at low Δ, which both describe bulk properties, are in good agreement in all cases. The conductivity values we obtain for our samples indicate very fast ionic bulk transport and negligible electron transport ($<10^{-9}$ S cm^{-1}), placing $Li_{0.6}[Li_{0.2}Sn_{0.8}S_2]$ among the materials with the highest ionic conductivities known to date. Moreover, even including the contact resistance of the cold-pressed powder, the resulting conductivity is an order of magnitude higher than the one of related, Li rich $Li[Li_{0.33}Sn_{0.67}S_2]$.

The reason for the much higher ionic conductivity in Li depleted $Li_{0.6}[Li_{0.2}Sn_{0.8}S_2]$ compared to fully occupied $Li[Li_{0.33}Sn_{0.67}S_2]$ is most likely connected to its crystal structure. Not only is the amount of Li between the layers decreased, giving rise to unoccupied sites which facilitate Li movement; Li was also found to occupy octahedral as well as tetrahedral sites, which already indicates that the energies associated with these sites are similar, making Li diffusion along a trajectory containing adjacent face-sharing octahedral and tetrahedral sites facile.

To further address these ideas we show difference Fourier maps ($F_{obs} - F_{calc}$) of the single crystal diffraction data where no Li is modeled in the refinement (Figure 5). It is important to keep in mind that those data were recorded at 100 K, a temperature at which Li is less mobile than at room temperature. While the Li in the octahedral layer is well localized, indeed, we find evidence for smeared out extra electron density around the tetrahedral positions. This implies that even at 100 K there is some Li mobility *via* the tetrahedral positions, suggesting that the ionic transport involves the tetrahedral Li sites.[34] In contrast, all Li atoms are located on the octahedral positions in $Li[Li_{0.33}Sn_{0.67}S_2]$, which likely explains its lower conductivity.

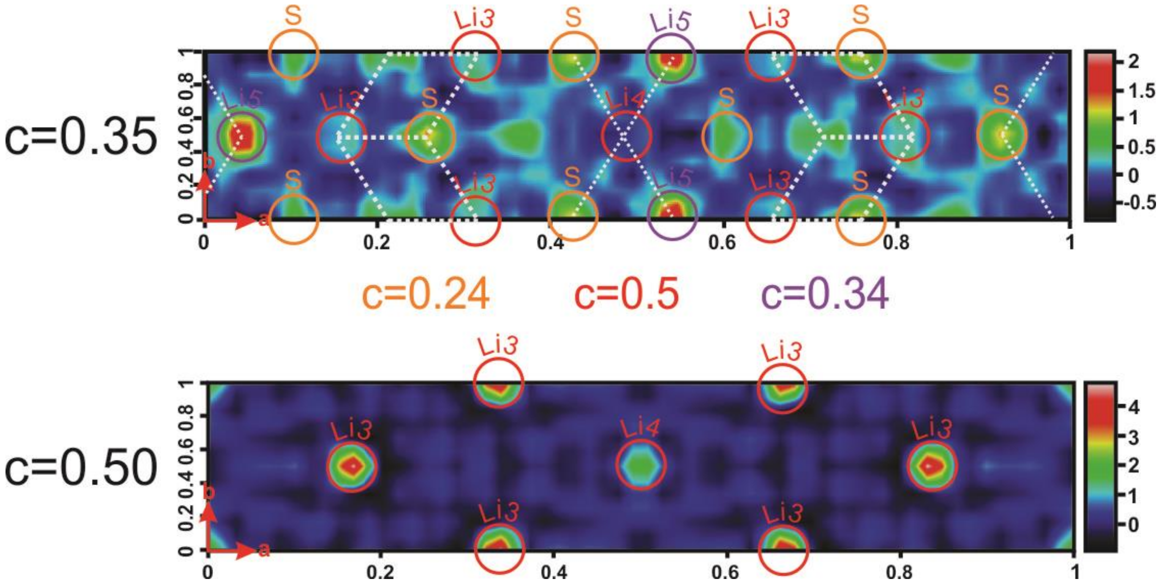

Fig. 5 Electron density difference maps ($F_{obs} - F_{calc}$) of $Li_{0.6}[Li_{0.2}Sn_{0.8}S_2]$ measured at 100 K. Li was not modeled for the difference maps so that its position can be determined by means of the recorded electron density. Top: View along *c* at *c* = 0.35 (this corresponds to the layer of the tetrahedrally coordinated lithium atom, Li5). Residual electron density is observed; it partially appears from adjacent layers (octahedral lithium positions at *c* = 0.5 (in red) and sulfur atoms at *c* = 0.24 (in orange)). The Li migration pathway calculated by *TOPOS* is highlighted with white dotted lines. Bottom: View along *c* perpendicular to the *ab* plane at *c* = 0.5; the layer of octahedral Li positions. No residual electron density is observed and the Li ions are very well localized.

The reason as to why tetrahedral positions can be easier occupied in $Li_{0.6}[Li_{0.2}Sn_{0.8}S_2]$ than in $Li[Li_{0.33}Sn_{0.67}S_2]$ is most likely associated with the partial occupancy of the Li positions in the interlayer space, reducing repulsive forces due to the fewer Li atoms that have to be accommodated between the layers in $Li_{0.6}[Li_{0.2}Sn_{0.8}S_2]$. This leaves some of the octahedral sites vacant, such that Li^+ ions can reside in the adjacent tetrahedral sites and interlayer diffusion pathways through face-sharing tetrahedral-octahedral-tetrahedral sites become accessible. The white dotted lines in Figure 5 display the expected Li migration pathway according to our *TOPOS* calculations (see below).

Additionally, we performed estimates of the possible lithium migration pathways and voids with the program package *TOPOS.*[35-37] As the program relies only on geometric and topological arguments and does not refer to the local energetics, we consider the outcome of this analysis only as providing a guideline. For this purpose, the voids in the crystal structure are calculated with the help of Voronoi-Dirichlet polyhedra and Li^+ ions are assumed to be able to jump between different sites if open channels between two sites exist. A channel is considered to be accessible for lithium motion if the sum of the radii of a lithium and a framework atom (here sulfur) does not exceed the channel radius by more than 10-15 %. For $Li[Li_{0.33}Sn_{0.67}S_2]$ we find that Li migrates through the covalent Li/SnS_2 layers, along the [101] direction (see Figure S8). Following the calculated pathways, lithium migration is only possible passing through unoccupied tetrahedral sites. The calculation for $Li_{0.6}[Li_{0.2}Sn_{0.8}S_2]$ is more difficult as *TOPOS* is not able to handle mixed occupancies. Therefore, we chose four different configurations: (i) all Sn/Li positions are fully occupied by tin and all interlayer positions are fully occupied by lithium, (ii) all Sn2/Li2 positions are occupied by tin and Sn1/Li1 positions as well as interlayer positions are occupied by lithium, (iii) all Sn1/Li1 positions are occupied by tin and Sn2/Li2 positions as well as interlayer positions are occupied by lithium, (iv) all tin and all lithium positions are fully occupied by lithium. All these configurations can be seen as borderline cases which only partially reflect the single-crystal X-ray structure. (Note, however, that charge balance is not considered by *TOPOS* and the calculations are purely geometrical in nature). Interestingly, the migration pathway analysis leads to chains along *b* in all four cases (see Figure S9, supporting information). This can arise from the fact that the anion framework (here sulfur), which greatly influences the Li motion, is the same in all calculations. In contrast to $Li[Li_{0.33}Sn_{0.67}S_2]$ though, the migration pathway does not cross the covalent layers. The calculated migration pathway of lithium is marked by white dotted lines in the electron density maps (Figure 5, top). These calculations lend further evidence that lithium movement is only possible *via* tetrahedrally coordinated sites. There is no hopping from octahedral to octahedral voids in both structures but only hopping from octahedral to tetrahedral sites and *vice versa*.

4.4 Conclusions

We have shown that $Li_{0.6}[Li_{0.2}Sn_{0.8}S_2]$ is a fast Li$^+$ ion conductor with a bulk conductivity of ~10^{-2} S cm^{-1} at room temperature, exceeding electronic contributions by at least 7 orders of magnitude. This places $Li_{0.6}[Li_{0.2}Sn_{0.8}S_2]$ among the best solid Li electrolyte materials known to date. While being compositionally simpler, the new superionic conductor $Li_{0.6}[Li_{0.2}Sn_{0.8}S_2]$ is also structurally distinct from the known LGPS solid electrolytes and can be viewed formally as a Li sulfide-depleted version of $Li[Li_{0.33}Sn_{0.67}S_2]$, a recently reported Li$^+$ ion conductor with a much lower conductivity. By analyzing the structure –

property relationships in the two compounds by means of single crystal X-ray diffraction and ssNMR - we demonstrate that removal of Li^+ ions from the interlayer gallery significantly improves the ionic conductivity. Clearly, such partial occupancy slightly decreases the number of mobile Li^+ ions while at the same time it facilitates Li^+ ion motion by increasing the mobility of the Li^+ ions. Therefore, besides a distinctly different Sn/Li order in the mixed Li/SnS_2 layers, the Li^+ ions in $Li_{0.6}[Li_{0.2}Sn_{0.8}S_2]$ have more space to move, due to the slightly larger layer distance in $Li_{0.6}[Li_{0.2}Sn_{0.8}S_2]$, but also due to the lower occupancy of the Li sites located in between the layers. Importantly, we show that interlayer Li does not only occupy the central octahedral but also tetrahedral sites, which is critical for facile ion movement as it opens up a Li trajectory involving face-sharing octahedral and tetrahedral voids with lower activation energies for Li hopping. In $Li[Li_{0.33}Sn_{0.67}S_2]$, however, Li^+ ions are only found in the octahedral positions which are fully occupied, rendering movement of those Li^+ ions more difficult. Our study therefore proves that the partial occupancy of interlayer cation sites in layered NaCl-analogues and Delafossite-related structure types can significantly enhance ionic conductivity as recently also seen in $Na_{3-x}Sn_{2-x}Sb_xNaO_6$.[19] This effect can be very important for further studies on those materials since many Delafossite-related compounds have been reported to also exist in cation depleted versions.[17,18] In the non-optimized cold-pressed samples, the transport measurements indicate high bulk conductivities (~10^{-2} S cm^{-1}) along with significant contact resistances (~10^{-4} S cm^{-1}). Given the structural anisotropy of $Li_{0.6}[Li_{0.2}Sn_{0.8}S_2]$, even higher conductivity can be expected for a single crystalline sample along the *ab* plane. Further studies on large enough single crystals and densified sintered samples are required for a deeper analysis. As far as the applicability of the new solid electrolyte is concerned, it will be key to combine it with electrodes of moderate Li chemical potential, or to find ways of kinetic passivation. Studies along those lines are currently ongoing in our lab.

Acknowledgments

We thank Marie-Luise Schreiber for ICP-AES measurements. Financial support by the Max Planck Society, Nanosystems Initiative Munich (NIM), Center for Nanoscience (CeNS) and Fonds der Chemischen Industrie is gratefully acknowledged. Work at Princeton was supported by the NSF-sponsored MRSEC at Princeton University, grant DMR-

1005438. LMS gratefully acknowledge support from the Minerva fast track fellowship by the Max Planck Society.

References

1 U. v. Alpen, A. Rabenau and G. H. Talat, *Appl. Phys. Lett.*, 1977, **30**, 621.

2 T. Lapp, S. Skaarup and S. Hooper, *Solid State Ionics*, 1983, **11**, 97.

3 Y. Inaguma, C. Liquan, M. Itoh and T. Nakamura, *Solid Sate Commun.*, 1993, **86**, 689.

4 R. Murugan, V. Thangadurai and W. Weppner, *Angew. Chem. Int. Ed.*, 2007, **46**, 7778.

5 T. Kaib, S. Haddadpour, M. Kapitein, P. Bron, C. Schröder, H. Eckert, B. Roling and S. Dehnen, *Chem. Mater*., 2012, **24**, 2211.

6 F. Mizuno, A. Hayashi, K. Tadanaga and M. Tatsumisago, *Adv. Mater*., 2005, **17**, 918.

7 K. Takada, N. Aotani and S. Kondo, *J. Power Sources*, 1993, **43-44**, 135.

8 H. Y-P. Hong, *Mat. Res. Bul*., 1978, **13**, 117.

9 P. G. Bruce and A. R. West, *J. Sol. State Chem*., 1982, **44**, 354.

10 R. Kanno and M. Murayama, *J. Electrochem. Soc*., 2001, **148**, A742.

11 N. Kamaya, K. Homma, Y. Yamakawa, M. Hirayama, R. Kanno, M. Yonemura, T. Kamiyama, Y. Kato, S. Hama, K. Kawamoto and A. Mitsui, *Nat. Mater*., 2011, **10**, 682.

12 A. Kuhn, O. Gerbig, C. Zhu, F. Falkenberg, J. Maier and B. V. Lotsch, *Phys. Chem. Chem. Phys*., 2014, **16**, 14669.

13 A. Kuhn, T. Holzmann, J. Nuss and B. V. Lotsch, *J. Mater. Chem. A*, 2014, **2**, 6100.

14 J. A. Brant, D. M. Massi, N. A. W. Holzwarth, J. H. MacNeil, A. P. Douvalis, T. Bakas, S. W. Martin, M. D. Gross and J. A. Aitken, *Chem. Mater*., 2015, **27**, 189.

15 K. Mizushima, P. C. Jones, P. J. Wiseman and J. B. Goodenough, *Solid State Ionics*, 1981, **3/4**, 171.

16 E. Plichta, M. Salomon, S. Slane and M. Uchiyama, *J. Power Sources,* 1987, **21**, 25.

17 E. M. Seibel, J. H. Roudebush, M. N. Ali, K. A. Ross and R. J. Cava, *Inorg. Chem*., 2014, **53**, 10989.

18 J. H. Roudebush and R. J. Cava., *J. Solid State Chem*., 2013, **204**, 178.

19 R. W. Smaha, J. H. Roudebush, J. T. Herb, E. M. Seibel, J. W. Krizan, G. M. Fox, Q. Huang, C. B. Arnold and R. J. Cava, *Inorg. Chem*., 2015, **54**, 7985.

20 J. E. Tanner, *J.Chem.Phys*., 1970, **52**, 2523.

21 E. O. Stejskal and J. E. Tanner, *J. Chem. Phys*., 1965, **42**, 288.

22 M. Bréger, M. Jiang, N. Dupré, Y. S. Meng, Y. Shao-Horn, G. Ceder and C. P. Grey, *J. Solid State Chem*., 2005, **178**, 2575.

23 O. A. Smirnova, V. B. Nalbandyan, A. A. Petrenko and M. Avdeev, *J. Solid State Chem*., 2005, **178**, 1165.

24 V. V. Politaev, V. B. Nalbandyan, A. A. Petrenko, I. L. Shukaev, V. A. Volotchaev and B. S. Medvedev, *J. Solid State Chem*., 2010, **183**, 684.

25 R. Berthelot, W. Schmidt, S. Muir, J. Eilertsen, L. Etienne, A. W. Sleight and M. A. Subramanian, *Inorg. Chem*., 2012, **51**, 5377.

26 E. A. Zvereva, M. A. Evstigneeva, V. B. Nalbandyan, O. A. Savelieva, S. A. Ibragimov, O. S. Volkova, L. I. Medvedeva, A. N. Vasiliev, R. Klingeler and B. Buechner, *Dalton Trans*., 2012, **41**, 572.

27 C. Greaves and S. M. A. Katib, *Mater. Res. Bull*., 1990, **25**, 1175.

28 R. D. Shannon, *Acta Cryst*. **1976**, *A32*, 751.

29 A. Kuhn, V. Duppel and B. V. Lotsch, *Energy Environ. Sci.*, 2013, **6**, 3548.

30 K. Hayamizu, Y. Aihara and N. Machida, *Solid State Ionics*, 2014, **259**, 59.

31 K. Hayamizu, Y. Matsuda, M. Matsui and N. Imanishi, *Solid State Nucl. Magn. Reson.,* 2015, **70**, 21.

32 Y. Deng, C. Eames, J.-N. Chotard, F. Lalere, V. Seznec, S. Emge, O. Pecher, C. P. Grey, C. Masquelier and M. S. Islam, *J. Am. Chem. Soc*., 2015, **137**, 9136.

33 L. Zhou, M. Leskes, T. Liu and C. P. Grey, *Angew. Chem. Int. Ed.*, 2015, **54**, 14782.

34 Y. Wang, W. D. Richards, S. P. Ong, L. J. Miara, J. C. Kim, Y. Mo and G. Ceder, *Nat. Mater*., 2015, **14**, 1026.

35 V. A. Blatov, *Acta Cryst.*, 2000, **A56**, 178.

36 V. A. Blatov, A. P. Shevchenko and V. N. Serezhkin, *J. Appl. Cryst.*, 1999, **32**, 377.

37 V. A. Blatov, *IUCr Comp. Comm. Newsletter,* 2006, **7**, 4.

38 A. C. W. P. James and J. B. Goodenough, *J. Sol. State Chem.*, 1988, **74**, 287.

39 J. Claverie, C. Foussier and P. Hagenmuller, *Bull. Soc. Chim. Fr.*, 1966, 244.

40 K. M. Mogare, K. Friese, W. Klein and M. Jansen, *Z. Anorg. Allg. Chem.*, 2004, **630**, 547.

41 G. Lang, *Z. Anorg. Allg. Chem.*, 1954, **276**, 77.

4.5 Supporting Information

$Li_{0.6}[Li_{0.2}Sn_{0.8}S_2]$ – a layered lithium superionic conductor

T. Holzmann[†‡§], *L. M. Schoop*[†*], *M. N. Ali*[*], *I. Moudrakovski*[†], *G. Gregori*[†], *J. Maier*[†], *R. J. Cava*[*], *B. V. Lotsch*[†‡§]

[†]Max-Planck-Institute for Solid State Research, Heisenbergstr. 1, 70569 Stuttgart, Germany

[‡]Department of Chemistry, Ludwig-Maximilians-Universität München, Butenandtstr. 5-13, 81377 München, Germany

[§]Nanosystems Initiative Munich (NIM) & Center for Nanoscience, Schellingstr. 4, 80799 München, Germany

[*]Department of Chemistry, Princeton University, Princeton, NJ 08544, USA.

Synthesis: Polycrystalline $Li_{0.6}[Li_{0.2}Sn_{0.8}S_2]$ was synthesized using three different routes. Synthesis 1 was already reported by *Kuhn* et *al.* and is described in ref. 1. For synthesis 2, Li_2CO_3 (Alfa Aesar, 99.0 % min), SnS_2 (Johnson Matthey Electronics brand, 99.5 % metals basis) and S (Alfa Aesar, 99.5 %) were mixed in a stoichiometric ratio with a slight excess of sulfur (2 wt% with regard to the product). Synthesis 3 uses a stoichiometric amount of Li_2S (Alfa Aesar, 99.9 %), SnS_2 (Johnson Matthey Electronics brand, 99.5 % metals basis) and S (Alfa Aesar, 99.5%). For $Li[Li_{0.33}Sn_{0.67}S_2]$, all synthesis procedures gave the same material according to NMR and PXRD. In the case of $Li_{0.6}[Li_{0.2}Sn_{0.8}S_2]$, synthesis 1 resulted in an amorphous side phase detected by NMR, which could be avoided by using syntheses 2 or 3. The starting materials were thoroughly ground and vacuum-sealed in silica tubes within a carbon crucible – this carbon crucible prevents the reaction of lithium with the silica tube and in the case of synthesis 2 it further reduces the Li_2CO_3 and therefore prevents formation of the oxide compound. For reaction 2 and 3 a furnace was heated to 700 °C (120 °C h^{-1}), held at that temperature for 3 days and then cooled down to room temperature (180 °C h^{-1}). All preparation steps were carried out under inert atmosphere or vacuum.

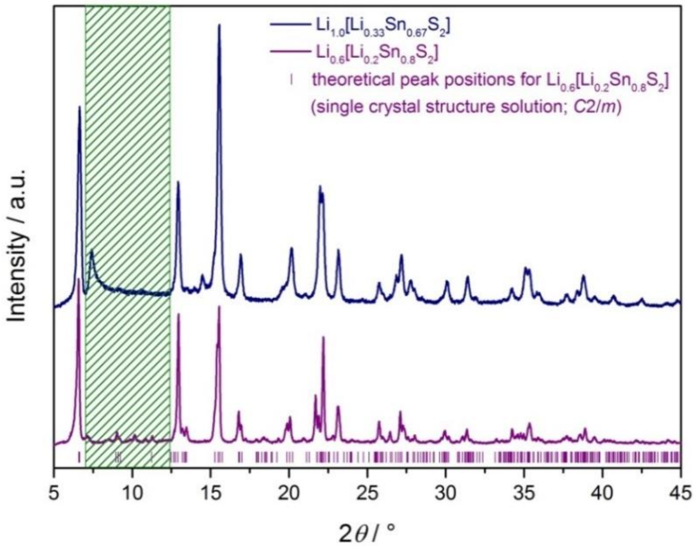

Figure S1. Mo-K_α PXRD pattern of $Li_{0.6}[Li_{0.2}Sn_{0.8}S_2]$ (bottom, purple) in comparison with $Li[Li_{0.33}Sn_{0.67}S_2]$ (top, blue). The purple scatter mark the theoretical peak positions of $Li_{0.6}[Li_{0.2}Sn_{0.8}S_2]$, according to the single crystal structure solution. The reflections in the highlighted region of 7-12 °2θ belong to the monoclinic superstructure cell. Differences between single crystal structure solution and powder X-ray data arise from varying concentrations of stacking faults in the powder.

Table S1. Atomic coordinates of the single crystal structure solution of $Li_{0.6}[Li_{0.2}Sn_{0.8}S_2]$.

Site	Wyck.	*x*	*y*	*z*	*occ.*
Sn1	2b	0	1/2	0	0.625
Li1A	2b	0	1/2	0	0.375
Sn2	4i	0.16471(2)	0	0.99600(7)	0.872
Li2A	4i	0.16471(2)	0	0.99600(7)	0.128
S3	4i	0.91344(7)	1/2	0.2420(2)	1
S4	4i	0.08395(8)	0	0.2351(2)	1
S5	4i	0.25193(8)	0	0.7669(2)	1
Li3	4i	0.8360(9)	1/2	0.502(3)	0.58
Li4	2c	0	0	1/2	0.3
Li5	4i	0.0391(18)	1/2	0.340(6)	0.216

Table S2. Anisotropic displacement parameters of the single crystal structure solution of $Li_{0.6}[Li_{0.2}Sn_{0.8}S_2]$.

Anisotropic displacement parameters, in Å^2				
Atom	U_{11}	U_{22}	U_{33}	U_{13}
Sn1	0.0033(4)	0.0050(4)	0.0095(5)	0.0022(3)
Li1A	0.0033(4)	0.0050(4)	0.0095(5)	0.0022(3)
Sn2	0.0061(2)	0.0053(2)	0.0126(3)	0.00492(16)
Li2A	0.0061(2)	0.0053(2)	0.0126(3)	0.00492(16)
S3	0.0128(8)	0.0106(7)	0.0147(8)	0.0034(6)
S4	0.0142(8)	0.0174(7)	0.0131(8)	0.0075(6)
S5	0.0102(7)	0.0093(7)	0.0117(8)	0.0067(5)
Li3	0.028(10)	0.010(9)	0.014(11)	0.003(7)

Li4	0.01100	0.00700	0.02100	0.00600
Li5	0.01500	0.00800	0.01300	0.00100

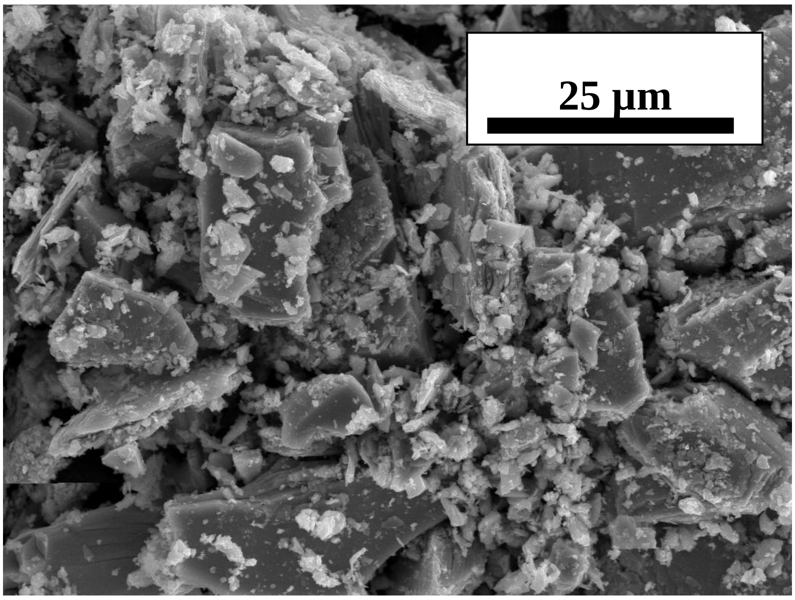

Figure S2. SE-SEM image (20 kV) of a typical $Li_{0.6}[Li_{0.2}Sn_{0.8}S_2]$ powder with a grain size in the range of <1µm – 100 µm.

Table S3. EDX data of $Li_{0.6}[Li_{0.2}Sn_{0.8}S_2]$ crystals.

Spectrum	**S**	**Sn**
Expected	71.43	28.57
Spectrum 1	70.60	29.40
Spectrum 2	70.59	29.41
Spectrum 3	70.14	29.86
Spectrum 4	70.55	29.45
Spectrum 5	70.69	29.31
Mean	70.51	29.49

Table S4. ICP-AES data of $Li_{0.6}[Li_{0.2}Sn_{0.8}S_2]$ in atomic- and weight-%. Two measurements of each sample were performed.

$Li_{0.6}[Li_{0.2}Sn_{0.8}S_2]$	**Li**	**Sn**
wt%	2.83 2.80	50.42 50.79
at%	1.0 1.0	1.04 1.08
Expected (at%)	1.0	1.0

Solid-state NMR spectroscopy

Experimental Details: ^{6}Li and ^{119}Sn SS NMR spectra were obtained on a Bruker Avance III 400 MHz instrument (B_0 = 9.4 T) at Larmor frequencies of 400 MHz, 58.88 MHz and 149.12 MHz, respectively. All measurements were performed with a Bruker 4 mm triple-channel Magic Angle Spinning (MAS) probe in ZrO_2-spinners at spinning speeds between 5 kHz and 14 kHz. In most cases the spectra were collected using a simple Bloch decay ($\pi/2$-pulse-acquire-delay) with $\pi/2$-pulses for ^{6}Li and ^{119}Sn set to 5.8 μs (B_1 = 43.1 kHz) and 4 μs (B_1 = 62.5 kHz), respectively. ^{119}Sn spectra are externally referenced to neat tetramethyltin ($Sn(CH_3)_4$, δ_{iso} = 0.0 ppm) with solid SnO_2 used as a secondary chemical shift standard (δ_{iso}-603.0 ppm relative to $Sn(CH_3)_4$).[2] ^{6}Li spectra are referenced to a 9.7 M aqueous solution of LiCl (δ_{iso} = 0.0 ppm).[2] ^{6}Li spectra employed delays between 30 and 500 s, and ^{119}Sn experiments used delays between 200 and 400 s. In every case the relaxation delays were set to provide for quantitative spectra, which was validated by the estimates of the relaxation times performed for every specific situation. The temperature of the samples in the MAS experiments was controlled using a Bruker BVT3000 temperature controller and was calibrated using the ^{207}Pb signal in $Pb(NO_3)_2$.[3] Analytical simulations and integration of experimental spectra were carried out with the DMFit and Bruker TopSpin 3.2 Lineshape Analysis Tool simulation packages.[4,5]

^{119}Sn NMR:

^{119}Sn NMR measurements were performed on $Li[Li_{0.33}Sn_{0.67}S_2]$, $Li_{0.6}[Li_{0.2}Sn_{0.8}S_2]$ as well as on SnS_2 for comparison. As expected due to the high crystallinity and the well-defined tin environment, SnS_2 gave a single signal at -764.7 ppm (Figure S3).

^{119}Sn NMR of $Li[Li_{0.33}Sn_{0.67}S_2]$ displays one signal at -765.9 ppm, which is slightly shifted compared to SnS_2, indicating less shielding at the tin atoms in $Li[Li_{0.33}Sn_{0.67}S_2]$ (Figure S5). As both crystallographic tin positions in $Li[Li_{0.33}Sn_{0.67}S_2]$ have the same chemical environment, the single signal is in good agreement with our expectations.

$Li_{0.6}[Li_{0.2}Sn_{0.8}S_2]$ shows three ^{119}Sn NMR peaks at -747.6 ppm, -750.1 ppm and -754.6 ppm with an integral ratio of around 39 : 21 : 40. According to the literature[6,7] this chemical shifts proves that only Sn(+IV) atoms are present, which are presumably all octahedrally coordinated by sulfur. Sn(+II) would show signals with a much smaller chemical shift. According to the crystal structure solution there are two crystallographically different Sn atoms. 26 % of all Sn atoms are located on the position Sn1 whereas 74% are located on Sn2. As the first coordination sphere is octahedrally coordinated sulfur for both tin positions, a clear assignment of the peaks cannot be made. Nevertheless, with respect to the integral ratios it seems likely that the two peaks at -747.6 ppm and -754.6 ppm belong to Sn2 with an integral sum of 79 % and the third peak at -750.1 ppm belongs to Sn1 with an integral of 21 %. As we expect a ratio of 26 : 74 for Sn1 : Sn2 this is in quite good agreement. This assumption is further confirmed by low temperature measurements, as the two Sn2 peaks are shifted to higher negative ppm values and the Sn1 peaks remains at -750.1 ppm. As we have lithium motion in the sample and the crystal structure solution gives us mixed occupancies we assume that the splitting into two peaks for the Sn2 position arises from small differences in local chemical environments, e.g. differences in the second coordination sphere (one, two or more Li atoms, see Figure S7) or slightly distorted sulfur octahedra. A similar situation was previously observed in powdered SnS_2 where several signals in the range of -755 ppm to -780 ppm appeared, mainly due to different stacking periodicities and distortions.[6]

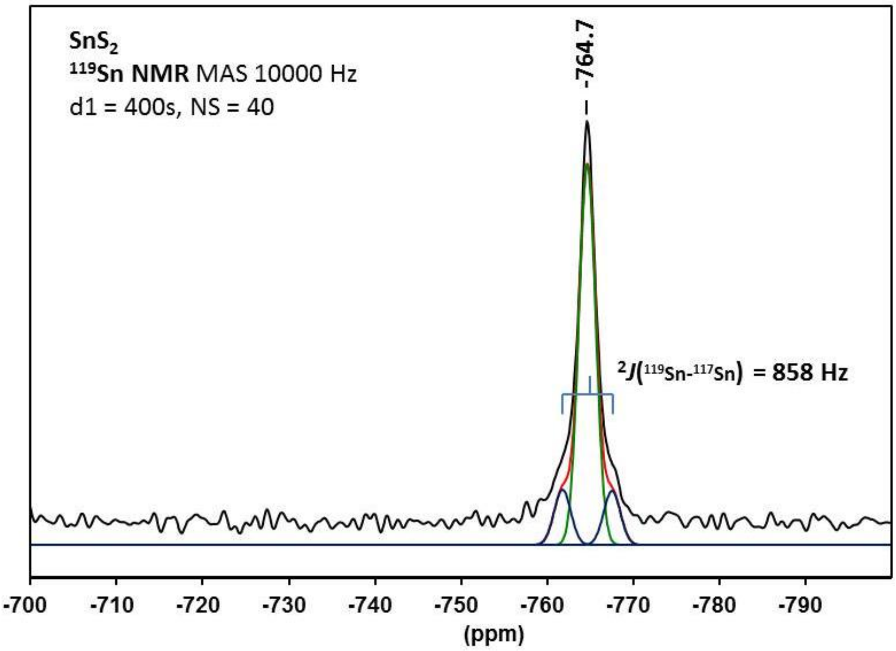

Figure S3. ^{119}Sn NMR spectrum of SnS_2 flakes ground with glass powder. The black line corresponds to the measured spectrum, the red line corresponds to the overall fit out of the single curves (in blue and green). The shoulders belong to a ^{119}Sn-^{117}Sn scalar coupling.

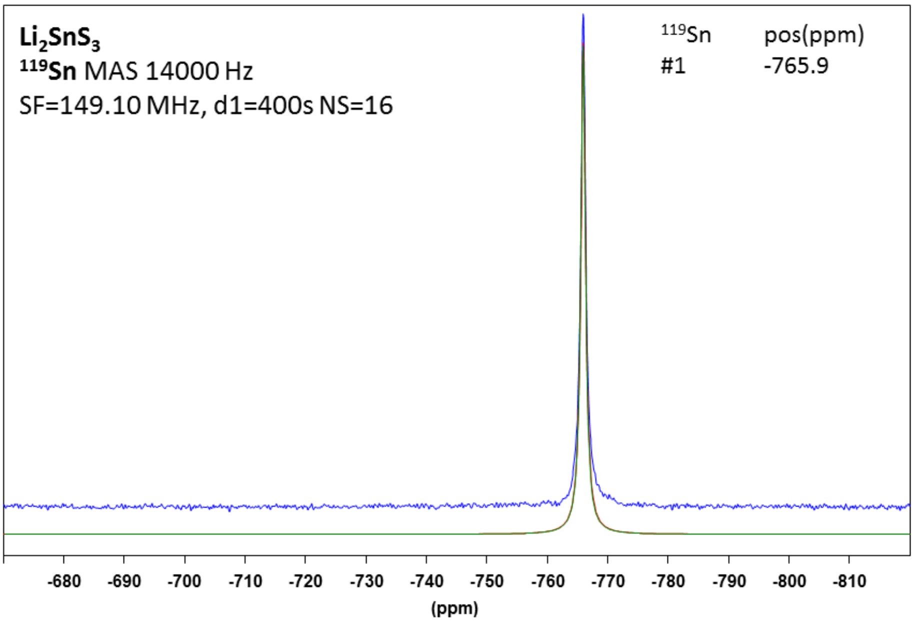

Figure S4. ^{119}Sn NMR spectrum of $Li[Li_{0.33}Sn_{0.67}S_2]$. In blue: measured spectrum, in green: single fit and in red: overall fit.

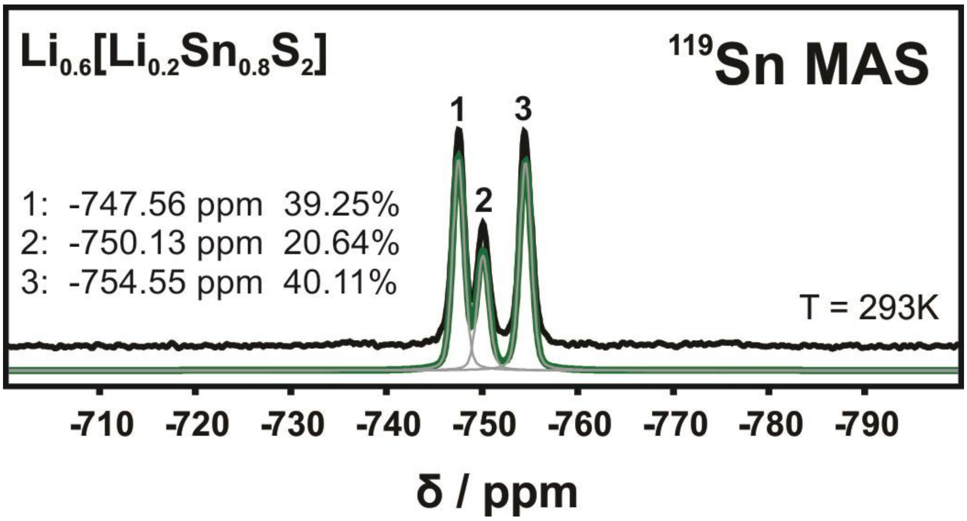

Figure S5. ^{119}Sn NMR spectrum of $Li_{0.6}[Li_{0.2}Sn_{0.8}S_2]$. In black: measured spectrum, in green: overall fit, in grey: single fits.

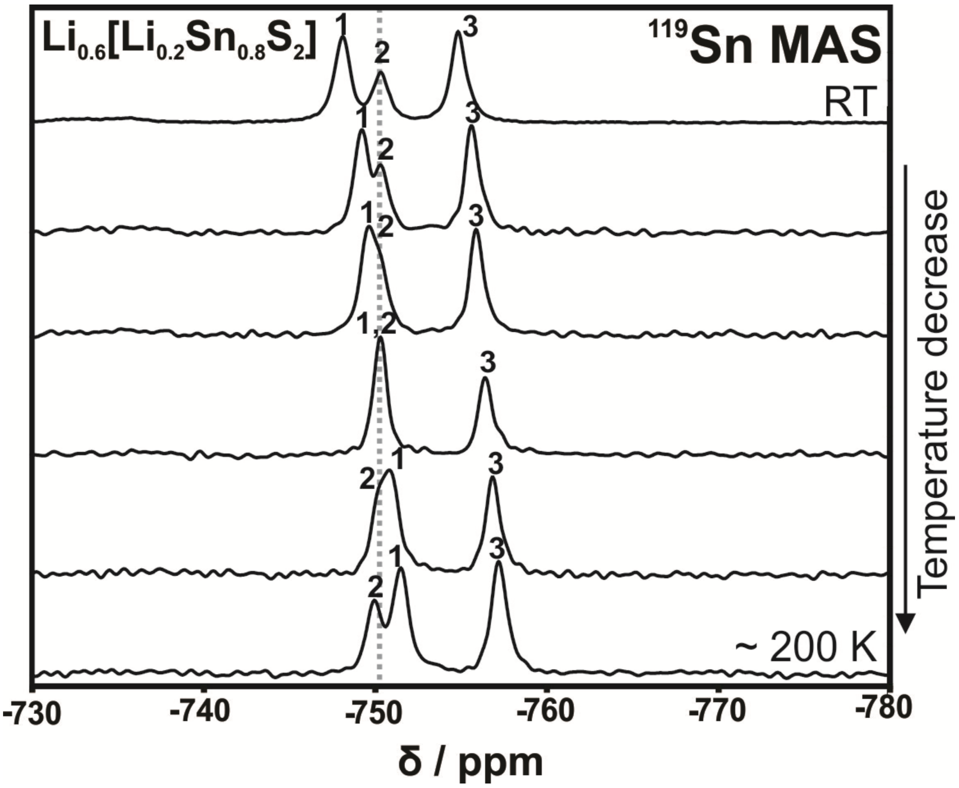

Figure S6. ^{119}Sn NMR spectrum of $Li_{0.6}[Li_{0.2}Sn_{0.8}S_2]$ at varying temperatures. Temperature is decreased downwards. Note that only peak 1 and peak 3 are highfield shifted with a decreased temperature, indicating that both peaks belong to the same tin position.

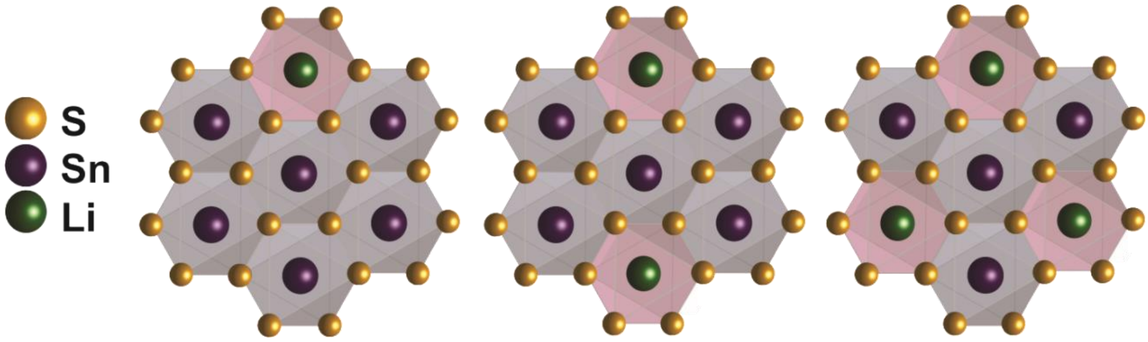

Figure S7. Schematic representation of three possible chemical environments of the tin atoms in the covalent layers of $Li_{0.6}[Li_{0.2}Sn_{0.8}S_2]$ surrounded by one (left), two (middle) or three (right) lithium atoms. Not that these are just examples which do not necessarily occur in the material with the same abundance.

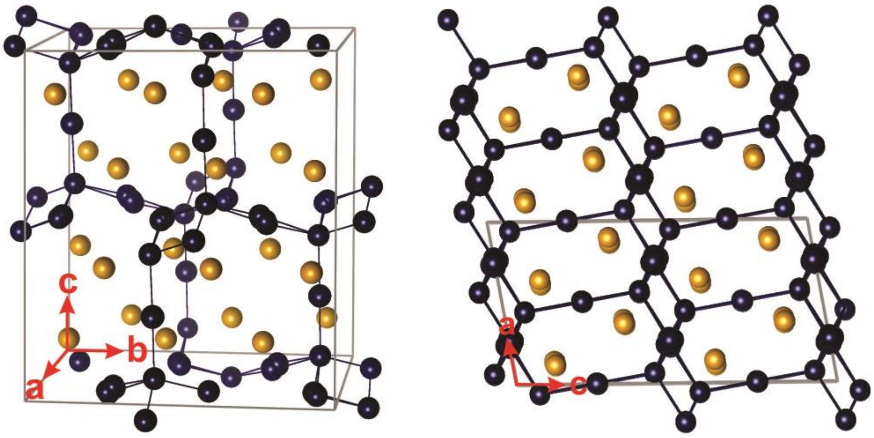

Figure S8. Calculated lithium migration path in $Li[Li_{0.33}Sn_{0.67}S_2]$. Sulfur as framework atom in yellow and voids in dark blue. The lines connecting the voids display the possible migration pathway. Note that this migration pathway consists of connected chains that cross the covalent layers.

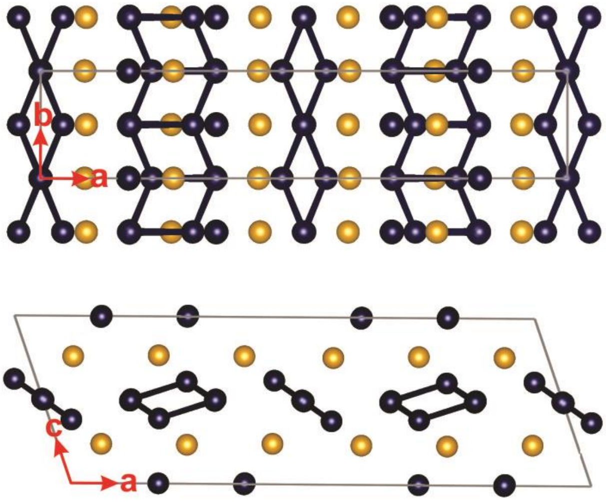

Figure S9. Calculated lithium migration path in $Li_{0.6}[Li_{0.2}Sn_{0.8}S_2]$. Sulfur as framework atom in yellow and voids in dark blue. The lines connecting the voids display the possible migration pathway. Note that this migration pathway does not cross the covalent layers.

Conductivity estimation using the Nernst-Einstein-Equation:

$$\sigma_{NMR} = \frac{D_{NMR}\, n\, z^2\, e^2}{k_B T} \quad (1)$$

D_{NMR}: Diffusion coefficient determined by PFG NMR (m^2 s^{-1}); n: concentration of diffusing species that take part in the ion conduction (if only interlayer Li$^+$ ions: $8.62 \cdot 10^{27}$ m^{-3}, if all Li$^+$ ions: $1.15 \cdot 10^{28}$ m^{-3}); z: charge number of diffusion species, here +1 for Li$^+$; e: elemental charge ($1.60 \cdot 10^{-19}$ C); k_B: Boltzmann constant ($1.38 \cdot 10^{-23}$ kg m^2 s^{-2} K^{-1}), T: Temperature (293 K).

The conductivity was calculated for each PFG NMR measurement with varying Δ values. The results are listed in Table S5. We calculated σ_{NMR} for the case that – according to the TOPOS calculations - only the interlayer Li$^+$ ions are responsible for the conduction. Note that Δ = 10 ms is closest to the bulk conductivity and if all lithium ions would take part into the conduction σ_{NMR} would be slightly above 10^{-2} S cm^{-1}, which is in the range of the best known solid-state electrolytes.

Table S5. Conductivity determined by PFG NMR according to equation (1).

Δ / ms	D_{NMR} / m^2 s^{-1}	σ_{NMR} (only interlayer Li$^+$ ions) / S cm^{-1}
10	$1.7\cdot10^{-11}$	$9.2\cdot10^{-3}$
20	$1.2\cdot10^{-11}$	$6.5\cdot10^{-3}$
25	$6.7\cdot10^{-12}$	$3.6\cdot10^{-3}$
30	$7.0\cdot10^{-12}$	$3.8\cdot10^{-3}$
40	$6.5\cdot10^{-12}$	$3.5\cdot10^{-3}$
50	$3.2\cdot10^{-12}$	$1.7\cdot10^{-3}$
100	$1.7\cdot10^{-12}$	$9.1\cdot10^{-4}$

Table S6. Bulk conductivity σ of three different samples determined by PFG NMR (σ_{NMR}) and impedance spectroscopy ($\sigma_{298\mathrm{K}}$). The samples are expected to differ in particle distribution and possibly also in their exact composition.

	σ_{NMR} / S cm^{-1}	$\sigma_{298\mathrm{K}}$ / S cm^{-1}
Sample 1	$9\cdot10^{-3}$	$2\cdot10^{-2}$
Sample 2	$3\cdot10^{-3}$	$4\cdot10^{-3}$
Sample 3*	$5\cdot10^{-4}$	$5\cdot10^{-4}$

*Partially hydrated.

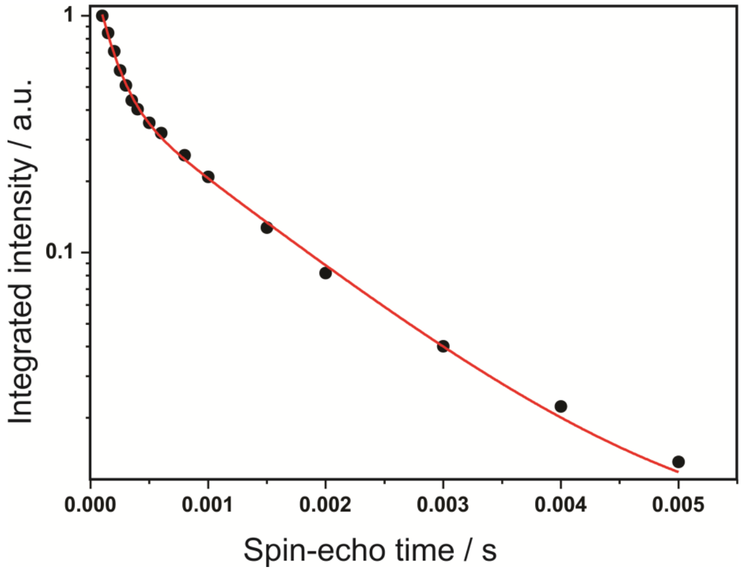

Figure S10. Signal attenuation of the ^{7}Li central transition as a function of the duration of the spin-echo time. The experimental points are fitted with a bi-exponential function characterized by spin-spin relaxation times of T_2’ = 1.13 ms and T_2’’ = 0.144 ms.

Estimation of the electronic contribution to the conductivity

As we did not reach the steady state we can only estimate an upper limit for the electronic contribution U_e to the conductivity. After applying a current of $I = 1$ nA for more than 6 h we reach a voltage of $U_\infty = 163.80$ mV. In the galvanostatic experiment, the sudden *IR* drop (U_0) after having switched on the current yields $U_0 = U_i + U_{contact}$ as 0.53 mV. (Note that U_i refers to the bulk response, whereas $U_{contact}$ comprises the contributions stemming from grain boundaries and contacts between particles that can be easily estimated from impedance spectra). PFG NMR data show that the bulk conductivity is on the order of $9.3 \cdot 10^{-3}$ S cm^{-1}, from which $U_i \sim 2 \cdot 10^{-4}$ mV results. The electronic transference number follows as

$$t_e = \frac{U_\mathrm{i}}{\qquad} \approx U_i / U_e = 10^{-6},$$

where

$$U_\mathrm{e} = U_\infty - U_\mathrm{contact}$$

and U_∞ is the steady state voltage.

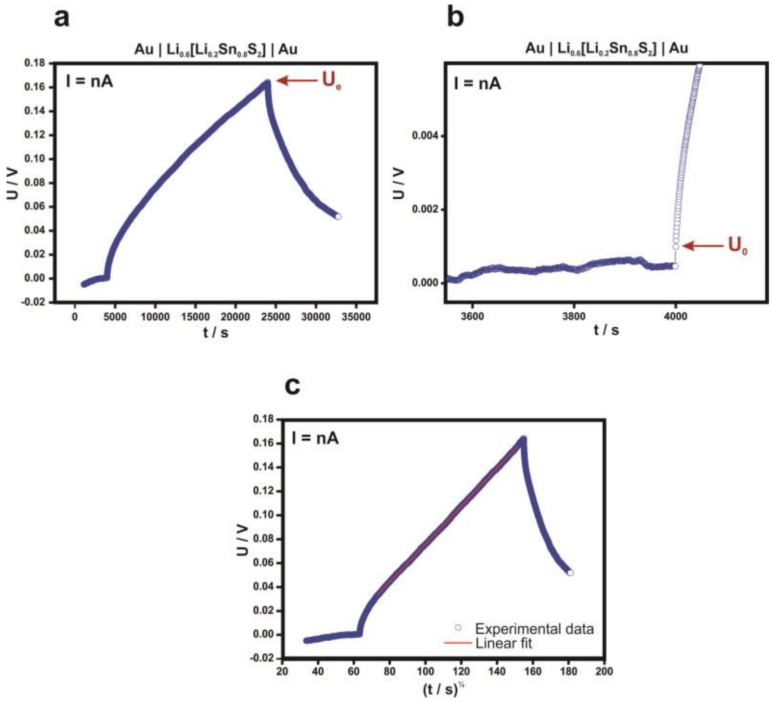

Figure S11. Electrical measurements on $Li_{0.6}[Li_{0.2}Sn_{0.8}S_2]$ performed at 298 K under argon atmosphere. (a) Full spectrum of the galvanostatic DC measurements of $Li_{0.6}[Li_{0.2}Sn_{0.8}S_2]$ without LiAl alloy. (b) Magnification of the first step after adding the current. (c) Voltage as a function of the square root of time. The maximum voltage value corresponds to U_e, the first step after adding the current corresponds to U_0.

The data collected during the transient of the polarization measurements can be used to independently support the considerations made above. The upper limit of the electronic conductivity can be estimated by considering the following expression [8], which holds for $t < \tau^{\delta}$ (τ^{δ} being the characteristic chemical diffusion time).

$$U - U_{contact} = \frac{IL}{\sigma} + \frac{\sigma_{ion}}{\sigma} \cdot \frac{IL}{\sigma_{eon}} \cdot \frac{4}{\pi^{3/2}} \sqrt{\frac{t}{\tau^{\delta}}} \, ,$$

where I is the current (1 nA) and L the diffusion length (i.e. the thickness of the sample ca. 2 mm).

As the evolution of the voltage fits well the square root law and since $\sigma \cong \sigma_{ion}$ and $\tau^{\delta} >$ 15000 s (Fig. S10 c), $\sigma_{eon} < 10^{-9}$ S·cm^{-1} results, which is consistent with the transference number value obtained above.

Additional impedance measurements on Li$_{0.6}$[Li$_{0.2}$Sn$_{0.8}$S$_2$]

1) Figure S12 shows a Nyquist plot of the complex impedance recorded using ion-blocking (Au) electrodes. In the low frequency range, a typical Warburg behavior can be recognized.

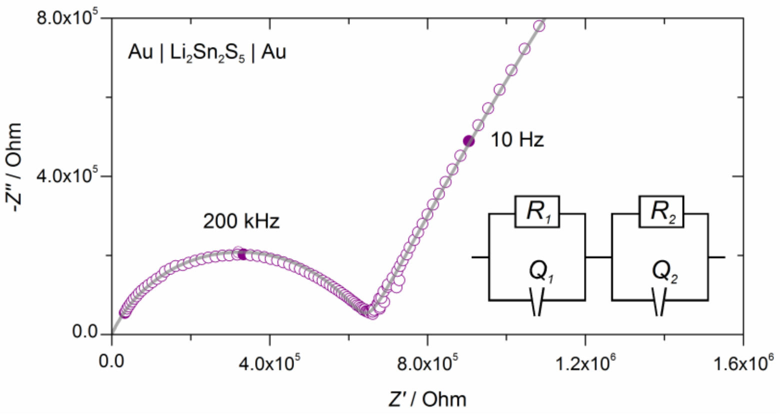

Figure S12. Nyquist plot of the complex impedance of the Li$_{0.6}$[Li$_{0.2}$Sn$_{0.8}$S$_2$] sample acquired using Au electrodes. The open circles correspond to the experimental data, while the grey line was obtained by fitting the data with the equivalent circuit shown in the bottom right corner.

2) In Figure S13 an additional impedance spectrum is presented, which was acquired using an extended frequency range, namely up to 10 MHz. Here, despite the increased noise, the transition to the bulk semi-circle (at high frequency) can be clearly recognized.

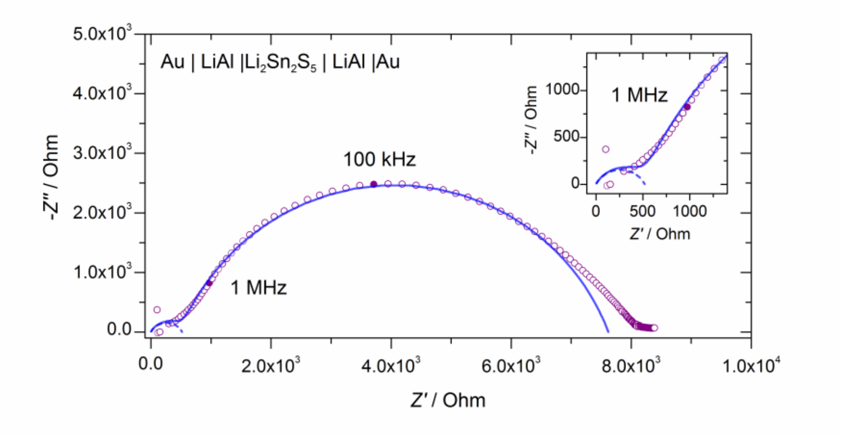

Figure S13. Nyquist plot of the complex impedance acquired in the non-blocking configuration Au|LiAl|Li$_{0.6}$[Li$_{0.2}$Sn$_{0.8}$S$_2$]|LiAl|Au at frequencies up to 10 MHz indicating the transition to the bulk response. The inset highlights the frequency range above 1 MHz and the dashed line correspond to the high frequency contribution. The high frequency behavior demonstrates that the high frequency intercept referred to in the main text is not an artefact of inductive phenomena.

Electrical measurements on $Li[Li_{0.33}Sn_{0.67}S_2]$

Electrical measurements were performed also on the related compound $Li[Li_{0.33}Sn_{0.67}S_2]$ under the same conditions used for $Li_{0.6}[Li_{0.2}Sn_{0.8}S_2]$. Figure S14(a) displays the Nyquist plot of the complex impedance, which can be fitted (grey line) by the equivalent circuit consisting of 3*RQ* elements, where *Q* is a constant phase element, whose capacitance is defined as $C = (R^{1-n}Q)^{1/n}$ (*n* is an additional fitting parameter). The resulting bulk conductivity is $6\cdot10^{-8}$ S cm^{-1}.

The results of the corresponding d.c. galvanostatic measurement are shown in Figure S14b. It is noteworthy that the value of the low frequency intercept with the *x*-axis of Figure S14a is in good agreement with the resistance value resulting from the d.c. measurement shown in Figure S14b.

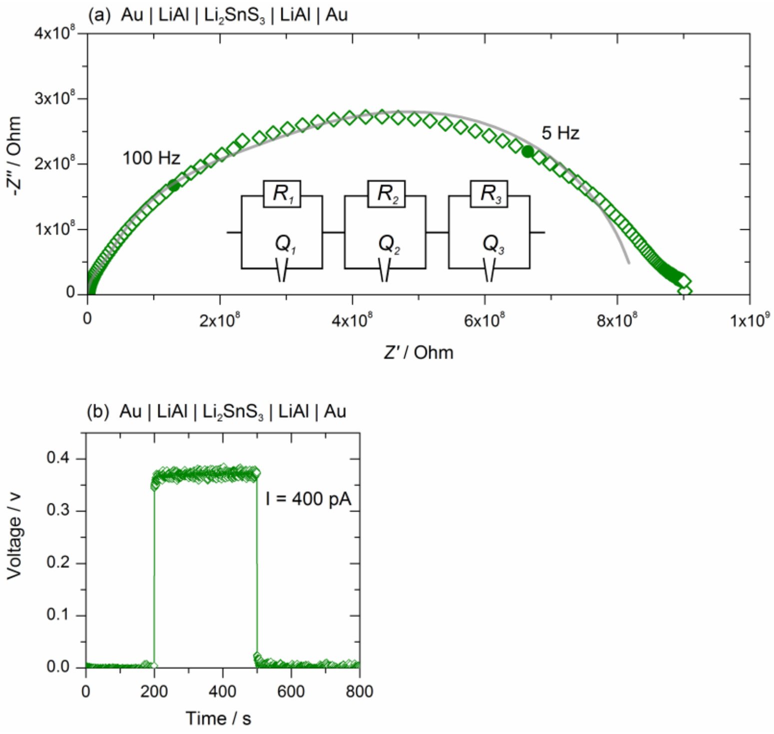

Figure S14. (a) Nyquist plot of the complex impedance and (b) d.c. galvanostatic measurement of $Li[Li_{0.33}Sn_{0.67}S_2]$. In (a) the open diamonds correspond to the experimental data whereas the grey line represents the fitting, which was obtained by using the equivalent circuit shown in the figure.

Literature:

[1] A. Kuhn, T. Holzmann, J. Nuss and B. V. Lotsch, *J. Mater. Chem. A*, 2014, **2**, 6100.

[2] R. K. Harris, E. D. Becker, S. M. Cabral De Menezes, P. Granger, R. E. Hoffman and K. W. Zilm, *Pure and Applied Chemistry*, 2008, **80**, 59.

[3] A. Bielecki and D. P. Burum, *J. Magn. Reson. Ser. A*, 1995, **116**, 215.

[4] D. Massiot, F. Fayon, M. Capron, I. King, S. Le Calvé, B. Alonso, J. O. Durand, B. Bujoli, Z. Gan and G. Hoatson, *Magn. Reson. Chem.*, 2002, **40**, 70.

[5] J. Rohonczy, Bruker BioSpin GmbH: Rheinstetten, Germany, 2009.

[6] T. Pietrass and F. Taulelle, *Magn. Reson. Chem.*, 1997, **35**, 363.

[7] T. Pietrass and F. Taulelle, *J. Phys. Chem. B*, 1997, **101**, 6715.

[8] J. Maier, *Physical Chemistry of Ionic Materials*, John Wiley & Sons, Chichester England (2004).

[9] J. A. Brant, D. M. Massi, N. A. W. Holzwarth, J. H. MacNeil, A. P. Douvalis, T. Bakas, S. W. Martin, M. D. Gross and J. A. Aitken, *Chem. Mater.*, 2015, **27**, 189.

5 Air-tolerant Li ion conduction in the superionic conductor $Li_{0.6}[Li_{0.2}Sn_{0.8}S_2]$

Tanja Holzmann, Leslie M. Schoop, Igor Moudrakovski, Mazhar N. Ali, Robert J. Cava, Bettina V. Lotsch

To be submitted.

Air-tolerant Li ion conduction in the superionic conductor $Li_{0.6}[Li_{0.2}Sn_{0.8}S_2]$

Tanja Holzmann[†‡§], *Leslie M. Schoop*[†*], *Igor Moudrakovski*[†], *Mazhar N. Ali*[*], *Robert J. Cava*[*], *Bettina V. Lotsch*[†‡§]

[†]Max Planck Institute for Solid State Research, Heisenbergstr. 1, 70569 Stuttgart, Germany

[‡]Department of Chemistry, Ludwig-Maximilians-Universität München, Butenandtstr. 5-13, 81377 München, Germany

[§]Nanosystems Initiative Munich (NIM) & Center for Nanoscience, Schellingstr. 4, 80799 München, Germany

[*]Department of Chemistry, Princeton University, Princeton, NJ 08544, USA.

We study the environmental stability of the lithium superionic conductor $Li_{0.6}[Li_{0.2}Sn_{0.8}S_2]$ and show that its high ionic diffusivity is not substantially affected by hydration, thus rendering this material the first humidity-tolerant sulfide superionic conductor. Layered $Li_{0.6}[Li_{0.2}Sn_{0.8}S_2]$ is hygroscopic, displaying a two-step hydration process in air that results in a large increase in interlayer distance. Ambient hydration first yields a monohydrate phase by a topochemical transformation, followed by swelling of the powder if the relative humidity is above ≈ 65%. We report the crystal structure of the monohydrate $Li_{0.6}[Li_{0.2}Sn_{0.8}S_2]\cdot H_2O$ and analyze it by thermogravimetric analysis (TGA), powder X-ray diffraction (PXRD) and solid-state NMR (ssNMR) measurements, observing a stacking change from O1 in $Li_{0.6}[Li_{0.2}Sn_{0.8}S_2]$ to P3 in $Li_{0.6}[Li_{0.2}Sn_{0.8}S_2]\cdot H_2O$. As in the case of $Li_{0.6}[Li_{0.2}Sn_{0.8}S_2]$, [4] we study the Li diffusivity in the hydrated state by pulsed field gradient (PFG) NMR measurements. Hydration slightly reduces the NMR-defined Li conductivity in the monohydrate (σ_{NMR} = 2 mS cm^{-1}) compared to the anhydrate, while Li diffusivity is fully restored in the swollen phase (here $Li_{0.6}[Li_{0.2}Sn_{0.8}S_2]\cdot 1.6\ H_2O$; σ_{NMR} = 10 mS cm^{-1}). To the best of our knowledge, this is the first air-stable sulfide-based lithium superionic conductor reaching Li ion conductivities

up to σ_{NMR} = 10 mS cm^{-1} even after hydration, in contrast to LGPS-type superionic conductors, which are known to rapidly degrade in air.

5.1 Introduction

Safety issues are of key importance in developing advanced energy storage technologies. Solid-state (ss) Li ion conductors with negligible electronic conduction and liquid-like ion conductivities are vital ingredients to develop next-generation all-solid-state devices such as batteries, supercapacitors, electrochemical sensors or actuators. Therefore, the discovery of new ultrafast solid electrolytes composed of earth-abundant elements that are (electro-)chemically stable is of enormous scientific and technological interest.[38] Since the groundbreaking discovery of $Li_{10}GeP_2S_{12}$ (LGPS) with an ionic conductivity of σ = 12 mS cm^{-1} at room temperature, solid electrolytes have become competitive with liquid ones.[1] However, most of the currently best Li ion conductors are sulfide systems (thio-LISICONs [2-4], the related LGPS-type phases [1,5] and glassy ceramics such as $Li_7P_3S_{11}$ [6,7]) and need to be handled under inert conditions as they are unstable in air.[8] As the prediction of new possible candidates based on computational approaches alone is challenging, the discovery of new Li ion conductors is contingent on extending known superionic compounds into new compositional spaces and on unraveling mechanistic details of Li ion transport that are still not fully understood.[9]

Recently, we reported fast Li ion conduction in layered $Li_{0.6}[Li_{0.2}Sn_{0.8}S_2]$, with a room temperature, NMR defined, conductivity of σ ~ 9 mS cm^{-1}.[10] The ionic conductivity measured with impedance spectroscopy exceeded 15 mS cm^{-1} . The monoclinic crystal structure of $Li_{0.6}[Li_{0.2}Sn_{0.8}S_2]$ ($C2/m$; $Li_2Sn_2S_5$) derives from $Li_{1.0}[Li_{0.33}Sn_{0.67}S_2]$ ($C2/c$; Li_2SnS_3), but instead of a honeycomb ordered layer all tin positions are partially occupied by lithium and vice versa.[10-12] Due to the decreased Li content in $Li_{0.6}[Li_{0.2}Sn_{0.8}S_2]$ as compared to $Li_{1.0}[Li_{0.33}Sn_{0.67}S_2]$, the interlayer distance slightly increases.[10] These lithium tin sulfide compounds are of special interest due to their tunable lithium ion conducting properties. $Li_{1.0}[Li_{0.33}Sn_{0.67}S_2]$ has a room temperature Li ion conductivity of σ ~ 10^{-2} mS cm^{-1}, whereas in the Li depleted version $Li_{0.6}[Li_{0.2}Sn_{0.8}S_2]$ the conductivity is roughly three orders of magnitude higher (σ ~ 9-15 mS cm^{-1}). This is connected to the fact that the interlayer Li positions are partially vacant and that Li can occupy tetrahedral positions in the interlayer space.[10] Geometrical considerations render the ion transport in $Li_{0.6}[Li_{0.2}Sn_{0.8}S_2]$ and $Li_{1.0}[Li_{0.33}Sn_{0.67}S_2]$ to be possible only *via* face-sharing octahedrally and tetrahedrally coordinated positions (i.e. O-T-O),[10] in line with the generally acknowledged influence of the anion lattice topology on the energetics of the Li trajectories. [9,13,14]

Here we report on the effect of $Li_{0.6}[Li_{0.2}Sn_{0.8}S_2]$ exposure to air, resulting in a hydrated compound. Hydration happens as a two-step process, during which the monohydrate $Li_{0.6}[Li_{0.2}Sn_{0.8}S_2]\cdot H_2O$ is formed first, and, upon longer exposure to air (humidity > 65%), a swollen layered phase is created with the degree of hydration depending on the relative humidity. We present the single crystal structure of the monohydrate and investigate the Li ion conducting properties of the anhydrate, monohydrate and the swollen phase. In contrast to other, typically highly air-sensitive lithium superionic conductors, $Li_{0.6}[Li_{0.2}Sn_{0.8}S_2]$ does not lose its high Li diffusivity upon absorbing water, and results in an increased interlayer distance of ≈ 5 Å. PFG NMR measurements as a function of the hydration state reveal that while the conductivity σ_{NMR} is slightly decreased in the monohydrate (from 9 mS cm^{-1} in the anhydrous sample to 2 mS cm^{-1} in the monohydrate), it is fully restored after further swelling (here: $Li_{0.6}[Li_{0.2}Sn_{0.8}S_2]\cdot 1.6\ H_2O$; 10 mS cm^{-1}). This observation sheds light on the mechanism of ion transport in this material and points towards the crucial role of both structural features (stacking sequence and layer distance) and the rigidity of interlayer water molecules, which may give rise to water-assisted Li ion transport.

5.2 Experimental Details

Polycrystalline $Li_{0.6}[Li_{0.2}Sn_{0.8}S_2]$ powder was synthesized in a classical solid state reaction according to the literature.[10] Exposure to air resulted in the monohydrate $Li_{0.6}[Li_{0.2}Sn_{0.8}S_2]\cdot H_2O$, which was stable over several weeks if the relative humidity was less than ≈ 65%. If the relative humidity was above ≈ 65%, further water uptake was observed. For PFG NMR measurements, the powder was stored in a desiccator above a water vessel for one hour. Thereby, a swollen phase with 1.6 H_2O molecules per formula unit ($Li_{0.6}[Li_{0.2}Sn_{0.8}S_2]\cdot 1.6H_2O$) was obtained. The exfoliation was performed in water with a $Li_{0.6}[Li_{0.2}Sn_{0.8}S_2]$ concentration of $c = 1$ g L^{-1}.[11]

All powders were characterized by powder X-ray diffraction (PXRD) using a STOE Stadi P diffractometer working in Debye-Scherrer geometry with either Mo-K_α or Cu- K_α radiation and a Ge(111) monochromator. Single crystals of $Li_{0.6}[Li_{0.2}Sn_{0.8}S_2]$ were obtained by subliming the powder at 750 °C in a vacuum-sealed ampoule for several days. When kept in air, the crystals hydrated to $Li_{0.6}[Li_{0.2}Sn_{0.8}S_2]\cdot H_2O$. Single-crystal X-ray diffraction (SXRD) was conducted on a Bruker APEX II diffractometer with Mo-K_α radiation at 100 K. Unit cell refinement and data integration was performed with Bruker APEX II software and CELL_NOW. The crystal structures were refined using the full-matrix least-squared method on F^2, implemented through SHELXL-2013 and WinGX.

^{1}H, ^{6}Li and ^{119}Sn ssNMR spectra were obtained on a Bruker Advance III 400 MHz instrument (B_0 = 9.4 T) at Larmor frequencies of 400 MHz, 58.88 MHz and 149.12 MHz, respectively. Further information is provided in the supporting information. ^{7}Li Pulsed Field Gradient (PFG) NMR measurements were performed on a Bruker Avance-III 400 MHz instrument (magnetic field of 9.4 T, and ^{7}Li Larmor frequency of 155.56 MHz), equipped with a diff60 single gradient diffusion probe. The probe allows for pulse field gradients g of up to 30 T/m and variable temperature measurements up to +150 °C. The diffusion measurements were accomplished using a Stimulated Echo pulse sequence.[36] The echo attenuation curves $S(g,\delta,\Delta)$ were processed using the Stejscal-Tanner equation,[37] $S(g,\delta,\Delta) = E(-\gamma^2\delta^2 g^2 D(\Delta-\delta)/3)$, where $\gamma = 1.398\cdot10^8$ Hz/T is the ^{7}Li gyromagnetic ratio, g is the strength of the pulse field gradient of duration δ, D is the effective diffusion coefficient, and Δ is the time interval between the field gradients that defines the diffusion time scale.

DTA and TG data of the various powders were collected in an aluminum crucible, using a NETZSCH STA 409CD thermoanalyzer.

For the TEM and SAED measurements, a drop of the colloidal nanosheet suspension was placed on a lacey carbon film/copper grid (Plano) and dried under irradiation of IR light. TEM was performed with a Phillips CM30 ST (300 kV, LaB_6 cathode). Bright field images and selected area electron diffraction (SAED) patterns were recorded with a Gatan CCD camera. SEM/EDX measurements were performed with a scanning electron microscope (SEM; Vega TS 5130 MM, Tescan) using a Si/Li detector (Oxford).

AFM was performed with a Veeco CP II system. The AFM images were analyzed with the Gwyddion software.

ICP-AES was analyzed with a Vista Pro ICP-AES spectrometer. The characteristic wavelengths are separated with an Echelle-Polychromator (Varian, Darmstadt) and detected with a photomultiplier.

5.3 Results and Discussion

Figure 1 displays the Cu-K_α powder X-ray diffraction patterns of $Li_{0.6}[Li_{0.2}Sn_{0.8}S_2]$ and $Li_{0.6}[Li_{0.2}Sn_{0.8}S_2]\cdot H_2O$. The hydration process leads to an increase in the layer distance from 6.2 Å to 8.4 Å, which corresponds to an enlargement of the *c* axis by more than 2 Å. To determine the chemical composition of the monohydrate, EDX (Sn : S = 1 : 2.4; expected 1 : 2.5) and ICP-AES (Li : Sn = 1 : 1.06; expected 1 : 1.0) was performed (Table S1 and S2, supporting information).

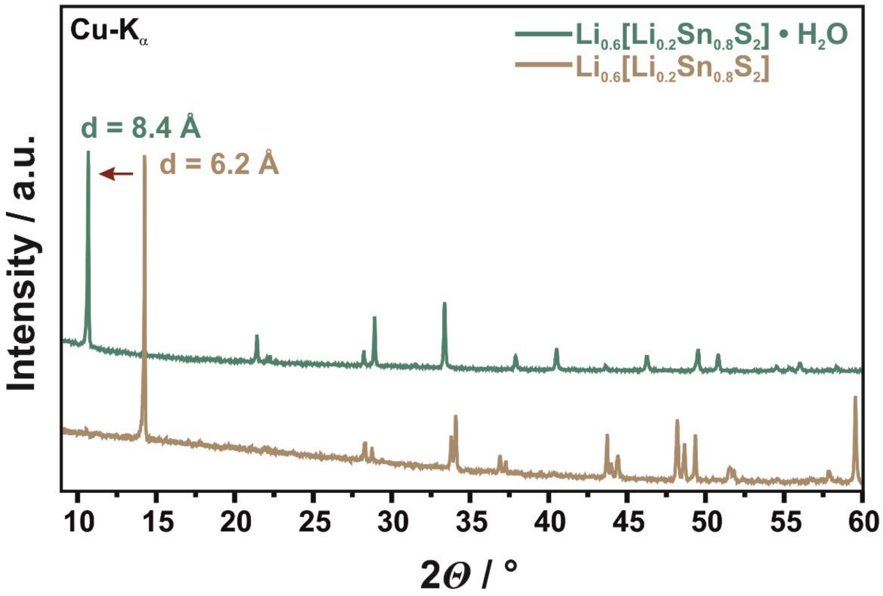

Figure 1. PXRD patterns (Cu-K_α) of anhydrous $Li_{0.6}[Li_{0.2}Sn_{0.8}S_2]$ (bottom) and the monohydrate $Li_{0.6}[Li_{0.2}Sn_{0.8}S_2]\cdot H_2O$ (top). The corresponding stacking reflections display the increased layer distance after swelling from $d_{(001)}$ = 6.17 Å (14.34 °2Θ) in $Li_{0.6}[Li_{0.2}Sn_{0.8}S_2]$ to $d_{(003)}$ = 8.39 Å (10.54 °2Θ) in $Li_{0.6}[Li_{0.2}Sn_{0.8}S_2]\cdot H_2O$. The Mo-$K_\alpha$ PXRD patterns are presented in Figure S1 (supporting information).

The hydration state was analyzed by TGA measurements (Figure S3, supporting information). The weight increase after the first hydration step is about 10%, which corresponds to an uptake of one molecule of water per formula unit by anhydrous

$Li_{0.6}[Li_{0.2}Sn_{0.8}S_2]$ (M = 164.65 g mol^{-1}), therefore transforming to the monohydrate $Li_{0.6}[Li_{0.2}Sn_{0.8}S_2]\cdot H_2O$ (M = 182.67 g mol^{-1}). Combined ICP and TG analysis reveal a Li : Sn : S : H_2O ratio of about 1 : 1 : 2.5 : 1.25. The structure of the monohydrate was solved by means of single-crystal X-ray diffraction in the rhombohedral space group $R\bar{3}m$ (no. 166) with a = 3.685(3) Å and c = 25.164 Å and shows a P3 type layer stacking (Figure 2). The observed stacking change from O1 in the anhydrous sample to P3 in the hydrated sample is a common occurrence for layered hygroscopic materials.[15,16]

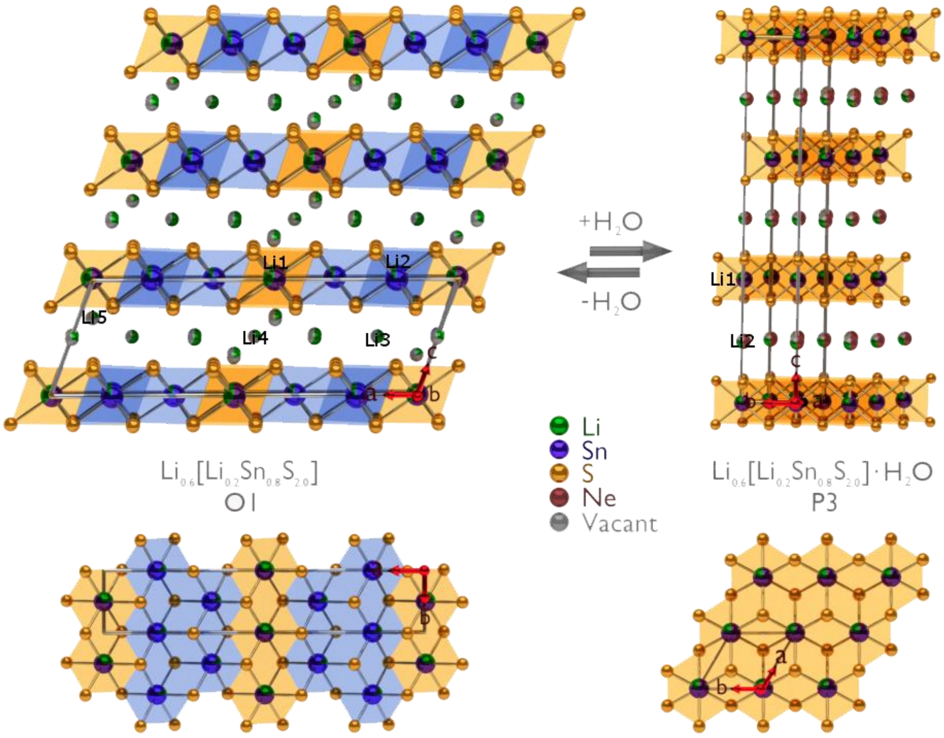

Figure 2. Crystal structure of $Li_{0.6}[Li_{0.2}Sn_{0.8}S_2]$ [4] with partially substituted tin positions (left, displayed by mixed colors) and O1 type stacking and a schematic representation of $Li_{0.6}[Li_{0.2}Sn_{0.8}S_2]\cdot H_2O$ (right) with lithium and water between the layers and P3 stacking. Water was substituted by neon to simplify the structure solution and to ensure charge neutrality. A vertical top-view of the layers is shown in the bottom row. The solid lines represent the unit cell obtained by the crystal structure solution. The two different Li/Sn positions in $Li_{0.6}[Li_{0.2}Sn_{0.8}S_2]$ are highlighted by different polyhedra colors.

Owing to the low quality of the crystal data, the intralayer Li/Sn/S site occupancies in the hydrate were kept the same as those in the anhydrate while assuming random distribution of the Li and Sn atoms within the layer. The interlayer water molecules were modeled as neon atoms in order to simplify the structure solution and to ensure charge neutrality at the same time; the interlayer Li ions were assumed to share the same positions as the water molecules. Note that the water molecules display in the ^1H NMR spectrum a Pake doublet, a lineshape diagnostic of rigidly bound water molecules (Figure 3).[17] The large splitting of about 40 kHz indicates that the motion of water molecules in the crystal is highly restricted. The crystallographic details for the monohydrate, including the atomic coordinates and the anisotropic displacement parameters are given in Table S3-S5 (supporting information). Although no supercell reflections pointing to a preferential intralayer occupation of the Li/Sn sites were observed in the single crystal X-ray diffraction pattern of the monohydrate, it still appears likely that the monoclinic superstructure (*C*2/*m* symmetry) adopted by $Li_{0.6}[Li_{0.2}Sn_{0.8}S_2]$ through intralayer Li/Sn ordering is maintained during water insertion. To test this hypothesis, we exfoliated $Li_{0.6}[Li_{0.2}Sn_{0.8}S_2]$ in an aqueous solution as previously reported[11] and confirmed by AFM measurements. Figure 4c shows a SAED pattern viewed along the [001] direction, with the corresponding simulation of the monoclinic *C*2/*m* structure of the anhydrate (Figure 4d). The measured and calculated *d* values are in good agreement and are presented in Table S6 (supporting information). The presence of supercell reflections in the exfoliated sheets indicates that the intralayer ordering (resulting from preferred occupancies of the Sn1 and Sn2 positions as seen in anhydrous $Li_{0.6}[Li_{0.2}Sn_{0.8}S_2]$ [10]) persists upon hydration. Hence, the here reported crystal structure of the monohydrate only describes the averaged rhombohedral subcell with random Li/Sn positions.

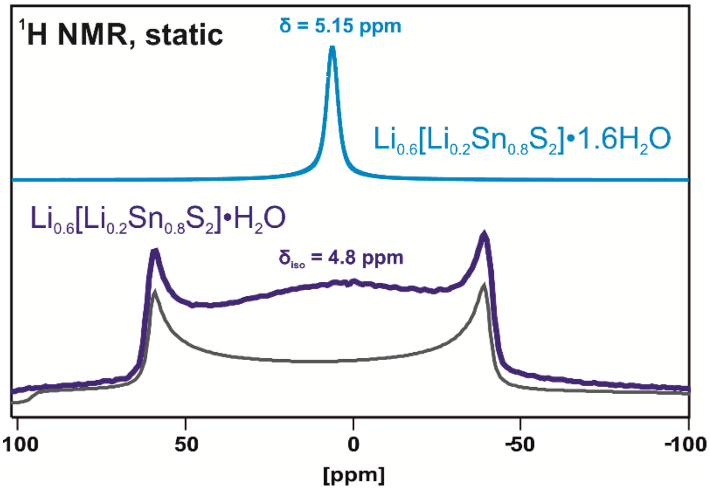

Figure 3. Static ^1H NMR spectra of the monohydrate $Li_{0.6}[Li_{0.2}Sn_{0.8}S_2]·H_2O$ (bottom) and the swollen phase $Li_{0.6}[Li_{0.2}Sn_{0.8}S_2]·1.6\ H_2O$ (top). Note that the water molecules in the monohydrate display a characteristic Pake doublet, a lineshape that is typical for rigidly bound water molecules, meaning that the motion

of water in the crystal is restricted. For comparison, the splitting in the spectrum of gypsum ($CaSO_4·2H_2O$) is 46 kHz, corresponding to immobile water molecules with proton internuclear distances of 1.58 Å.[25] The spectrum of the swollen phase displays a single peak with a FWHM of about 1600 Hz. Such a small linewidth indicates that in contrast to the monohydrate the water in the swollen phase is very mobile.

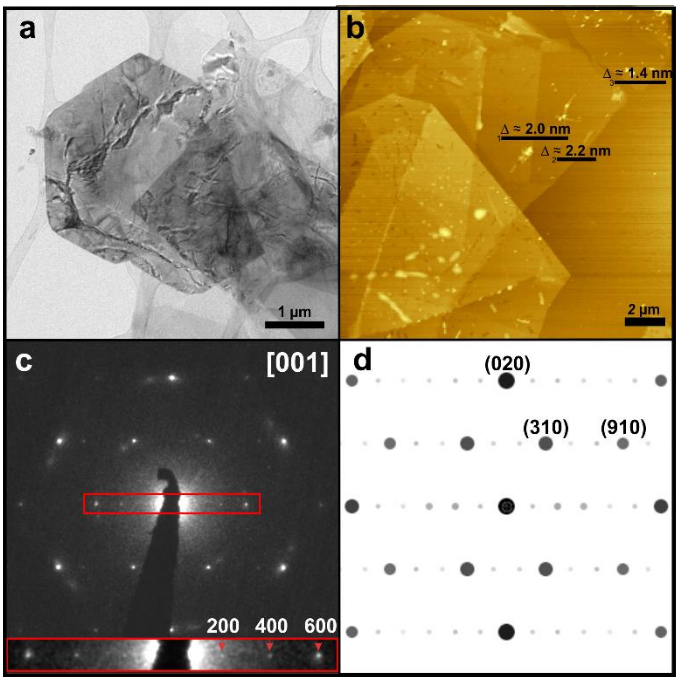

Figure 4. (a) Bright field image of a $Li_{0.6}[Li_{0.2}Sn_{0.8}S_2]$ nanosheet after exfoliation in water, displaying hexagonal morphology, and (b) thickness of the nanosheets measured by AFM under ambient conditions. The height is in the range of 1.5-2.2 nm (height profiles are presented in Figure S7, supporting information), likely corresponding to single or double layered sheets (double layered sheets arise presumably from folding). The deviation to the expected height of ≈ 0.6 nm based on the crystallographic thickness of a Li/SnS_x monolayer was previously reported to result from adsorbed water layers.[5] (c) SAED pattern of the nanosheets with a magnification of the superstructure reflections (highlighted by a red box) in the [001] viewing direction. Note that a second nanosheet lies on top, slightly twisted. (d) The corresponding SAED simulation assuming the monoclinic structure of the anhydrate. The measured and simulated reflections are in good agreement (see also Table S6, supporting information).

Both solid-state (ss) NMR and PXRD measurements indicate a direct phase transformation from anhydrate to monohydrate without passing through an amorphous state (see Figure 5 and Figures S2 and S5, supporting information); likewise, no crystalline intermediate phase with less than one water molecule per formula unit has been detected. Figure 2 displays the structural change of $Li_{0.6}[Li_{0.2}Sn_{0.8}S_2]$ to $Li_{0.6}[Li_{0.2}Sn_{0.8}S_2]·H_2O$.

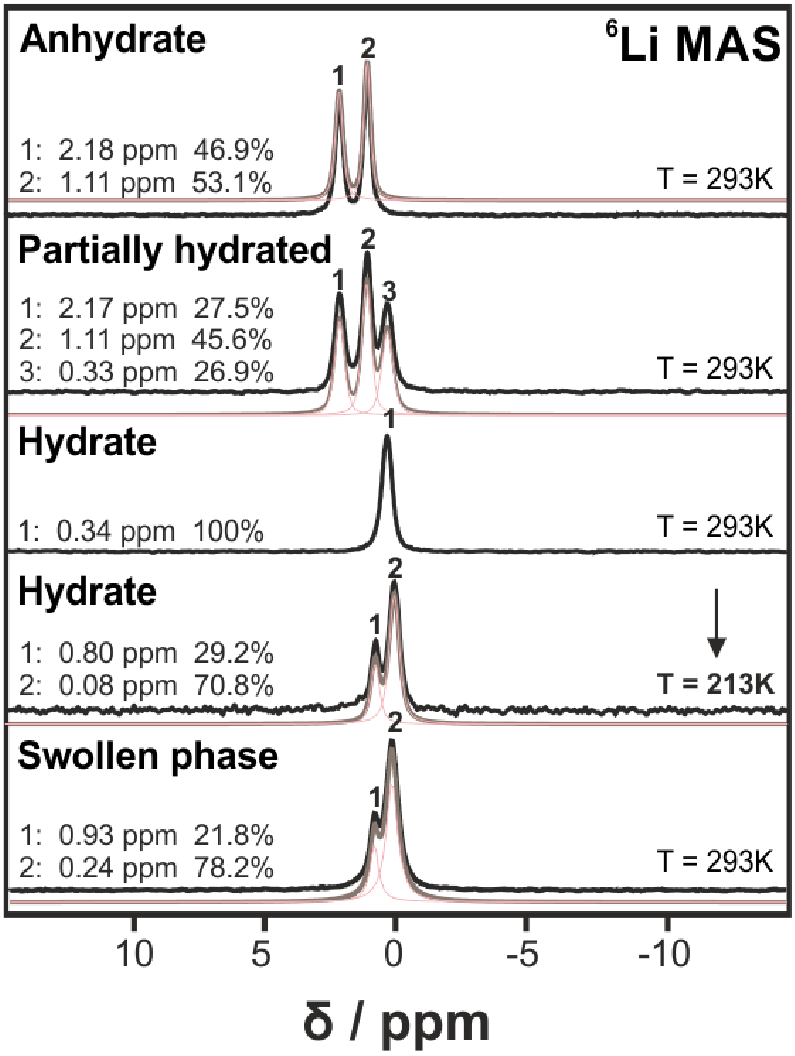

Figure 5. ^6Li NMR measurements of $Li_{0.6}[Li_{0.2}Sn_{0.8}S_2]$ (anhydrate), a partially hydrated powder, $Li_{0.6}[Li_{0.2}Sn_{0.8}S_2]\cdot H_2O$ (monohydrate, measured at room temperature and 213 K) and $Li_{0.6}[Li_{0.2}Sn_{0.8}S_2]\cdot 1.6\ H_2O$ (swollen phase). The partially hydrated powder displays two phases, anhydrate and monohydrate. The black line corresponds to the measured spectra, the grey line is the summary fit of the different curves (red lines).

If the monohydrate is left in humid air (RH close to 100%), a swollen phase forms after several hours, identified by the 00*l* stacking peak shifted to 7.78 °2θ, corresponding to d = 11.4 Å (Figure S1, supporting information). This additional adsorption of water is strongly dependent on the humidity. Below a RH of ≈ 65%, the monohydrate was stable over several weeks. The humidity above ≈ 65% results in a water content above 1 molecule per formula unit. To track and quantify the swelling process, we performed TGA measurements on the anhydrous powder under an argon/water vapour flow (Figure S3 and S4, supporting information). After the formation of the monohydrate, the swelling process continues. After 900 min, 4.3 H_2O molecules per formula unit were absorbed, but no saturation was reached. We thus expect that hydration under a water vapor flow is a continuous process, similar to osmotic swelling, ultimately leading to exfoliation of the powder.[11] Next, we performed TGA measurements on the swollen powder that was used for PFG NMR measurements. We obtained a water content corresponding to $Li_{0.6}[Li_{0.2}Sn_{0.8}S_2]\cdot 1.6\ H_2O$ (Figure S4, supporting information) which correlates with a stacking peak in the PXRD at 7.78 °2θ. The fact that only the lithium-depleted compound $Li_{0.6}[Li_{0.2}Sn_{0.8}S_2]$ forms a hydrate while the related $Li[Li_{0.33}Sn_{0.67}S_2]$ does not, is expected to be the reason for the outstanding exfoliation behavior reported by us earlier.[11] Likewise, many other layered compounds swell before they exfoliate, e.g. Na_xCoO_2 [39,40], $CsTi_{(2-x/4)}\square_{x/4}O_4\cdot H_2O$ [18-21], hydrated $HCa_2Nb_3O_{10}$ [22,23] α-$[Zr(HPO_4)_2]\cdot H_2O$ [24,25] or $HTaP_2O_8\cdot 2H_2O$.[26]

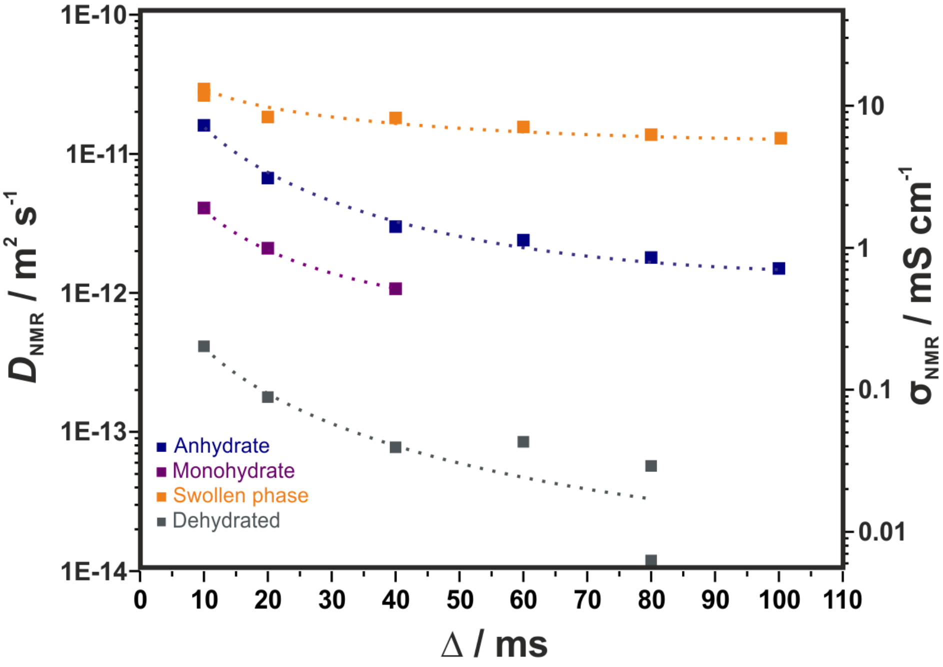

Figure 6. PFG NMR data of $Li_{0.6}[Li_{0.2}Sn_{0.8}S_2]$ (anhydrate) at various hydration steps at different time intervals between the field gradient pulses, defining the diffusion time Δ which was set between 10 and 100 ms. The hydration of the powder was performed in humid air and was detected by PXRD measurements (see Figure S6, supporting information). For dehydration, the powder was heated for around 30 min with a heat gun under high vacuum (~10^{-3} bar). Monohydrate: $Li_{0.6}[Li_{0.2}Sn_{0.8}S_2]\cdot H_2O$, swollen phase: $Li_{0.6}[Li_{0.2}Sn_{0.8}S_2]\cdot 1.6\ H_2O$, dehydrated sample $Li_{0.6}[Li_{0.2}Sn_{0.8}S_2]$. Although ssNMR and PXRD measurements indicate a reversibility of the hydration, the Li ion conduction is significantly reduced in the dehydrated powder. Note that short Δ values correspond to the bulk conductivities, while the probability of Li ions crossing grain boundaries increases with increasing Δ, which hinders the Li migration and reduces

conductivity. Ionic conductivities were calculated according to the Nernst-Einstein-equation as described in reference 4.

We measured the ^{6}Li and ^{119}Sn ssNMR spectra of the hydrated samples and compared them to the anhydrate (Figure 5). ^{6}Li NMR of the anhydrous powder shows two signals at 2.18 ppm (46.9%) and 1.11 ppm (53.1%), which were assigned to Li1, Li2 and Li5 (peak 1) and to Li3 and Li4 (peak 2), respectively.[10] The monohydrate displays a single peak at 0.33 ppm, which is consistent with a higher shielding of Li^+ upon coordination to H_2O, in agreement with the literature.[27] Note that the simultaneous presence of both phases in the partially hydrated sample indicates that there is no distinct intermediate phase with less than one water molecule per formula unit. When the first hydration step leading to $Li_{0.6}[Li_{0.2}Sn_{0.8}S_2]\cdot H_2O$ is complete, the spectrum at RT consists of one signal at 0.34 ppm, that splits at lower temperature (213K) into two signals at 0.80 ppm and 0.08 ppm. The integral ratio of 71 :29 is close to what one could expect for inter- and intralayer lithium (75 : 25). The splitting is rationalized by different water environments of the intra- and interlayer Li at low temperature when the water exchange dynamics is slowed down. In the swollen phase we observe two signals already at room temperature, which appears similar to the spectrum of the monohydrate at low temperatures. The integral ratio of the two peaks at 0.93 ppm and 0.24 ppm (78 : 22) is in good agreement with inter- and intralayer lithium distribution (75 : 25). We tentatively assign signal 2 at 0.24 ppm (78 %) to the interlayer lithium ions as they are more effectively shielded compared to the intralayer Li due to the water molecules inserted between the layers. The ^{119}Sn NMR spectra further confirm the direct phase change during the hydration process and indicate that hydration is reversible, which is in agreement with the PXRD measurements (see Figure S1 and S5, supporting information). In the ^{119}Sn NMR - like in the PXRD patterns (Figure S1, supporting information) - we observe a reversibility of the hydration process accompanied by a loss in crystallinity: After heating the hydrated sample for 30 min in high vacuum, the ^{119}Sn NMR signals return to their original positions but show significant line broadening, consistent with a loss of crystallinity. Further details concerning the ^{119} Sn NMR spectra can be found in the supporting information.

$Li_{0.6}[Li_{0.2}Sn_{0.8}S_2]$ was recently identified as a very fast Li ion conductor with conductivities σ in the range of 9-15 mS cm^{-1}.[10] To probe the influence of hydration on the long-range ionic conductivity, we investigated the Li ion migration in the hydrated samples compared to the anhydrous powder with ^{7}Li PFG NMR spectroscopy (Figure 6), converting the NMR diffusion coefficients D_{NMR} into conductivity σ_{NMR} via the extended Nernst-Einstein relation, assuming that the Li is the only mobile ion in the compounds (for further details see supporting information). The hydration degree was determined by PXRD and TGA measurements (see discussion above and Figure S6, supporting information). While the anhydrous sample displays a bulk conductivity of $\sigma_{\mathrm{NMR}} = 8.6$ mS cm^{-1} (slightly lower than previously observed, but within range of error), the conductivity decreases to $\sigma_{\mathrm{NMR}} = 1.7$ mS cm^{-1} in the monohydrate. Note that, although the hydration impairs the conductivity, the value is still two orders of magnitude higher than for the fully lithiated material $Li_{1.0}[Li_{0.33}Sn_{0.67}S_2]$ ($\sigma = 1.5\cdot10^{-2}$ mS cm^{-1}).[12] After further hydration in humid air (RH ≈ 100%) 1.6 H_2O molecules per formula unit are taken up by the sample. This causes an increase in conductivity to $\sigma_{\mathrm{NMR}} = 10$ mS cm^{-1}, thus roughly restoring the value found the anhydrous starting material. These results suggest that $Li_{0.6}[Li_{0.2}Sn_{0.8}S_2]$ is an air-tolerant lithium superionic conductor and that prolonged hydration with concomitant swelling does not adversely affect the ion conducting properties. ^{119}Sn NMR and PXRD measurements indicate that the hydration process is reversible with a clear loss in crystallinity but no signs of sample decomposition. Loss of crystallinity can strongly affect Li diffusivity, i.e. by a reduction in crystal size causing an increased number of grain boundaries, and possibly by a decrease in the registry of the layers, leading to an obstruction of the interlayer Li diffusion pathways, as sketched in Figure 7. Such changes in morphology result in a reduced conductivity in the dehydrated sample of $\sigma_{\mathrm{NMR}} = 0.2$ mS cm^{-1} (Figure S6, supporting information). While we see clear signs of high Li diffusivity in the PFG NMR measurements, we cannot exclude simultaneous proton diffusion in the swollen phase. The observed ^{1}H NMR chemical shift is close to that of pure water and no signs of acidic protons have been detected suggesting that only mobile neutral water molecules are present in the structure. Further experiments to elucidate the mechanism of possible water-mediated Li$^+$ diffusion are currently in progress. Note that impedance measurements in blocking configuration did not permit determination of the bulk conductivity of the monohydrate and swollen phase, while the use of a non-blocking configuration led to a chemical reaction between the hydration water and the LiAl alloy, thus excluding the use of impedance spectroscopy as a suitable tool to determine ion specific conductivities.

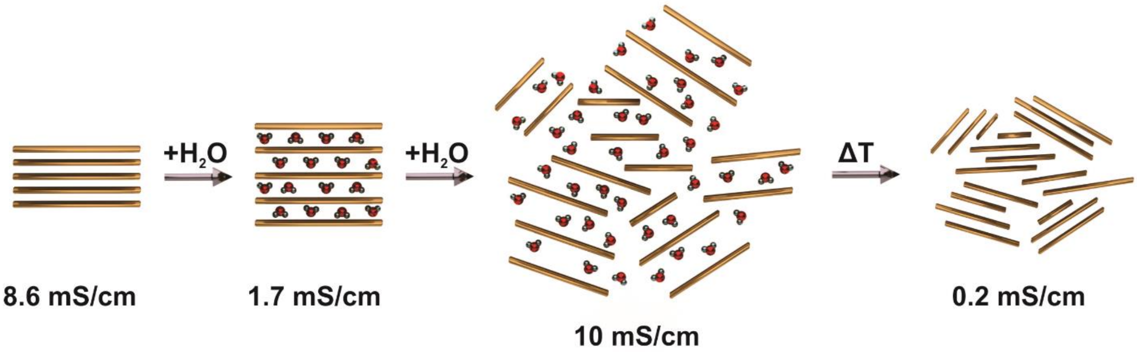

Figure 7. Schematic representation of the two-step water adsorption and dehydration of $Li_{0.6}[Li_{0.2}Sn_{0.8}S_2]$ with the corresponding ionic conductivities. While the conductivity decreases after the formation of the monohydrate, it increases again with further swelling. Although the structure remains intact with dehydration according to PXRD and solid-state NMR measurements, the conductivity is nevertheless negatively affected by the reduced crystallinity, which possibly leads to an obstruction of the Li diffusion pathways.

Figure 7 presents a summary overview of the two-step hydration and dehydration process and the corresponding Li ion conductivities determined by PFG NMR measurements (Figure 6). The anhydrous powder $Li_{0.6}[Li_{0.2}Sn_{0.8}S_2]$ is known to be a fast Li ion conductor and the sample studied here has a bulk conductivity of σ_{NMR} = 8.6 mS cm^{-1}. Upon air contact water is absorbed between the covalent layers, resulting in a monohydrate with an increased layer distance by 2 Å (see Figure 1). In this structure (Figure 2), water occupies interlayer lithium positions rather than distinct water sites. Since the water is strongly bound in the lattice (as shown by ^1H NMR measurements, Figure 3), steric hindrance for the Li ion motion is expected. It is known from other layered intercalation compounds, e.g. Li_xTiS_2, that migration barriers are very sensitive to the *c* lattice parameter.[13, 28] Further, it has been reported for electrode materials such as Li_xCoO_2 that the stacking order as well as the type of stacking (here, O1 in $Li_{0.6}[Li_{0.2}Sn_{0.8}S_2]$ vs P3 in $Li_{0.6}[Li_{0.2}Sn_{0.8}S_2]\cdot H_2O$) has profound influence on the Li migration, mainly through enabling or disabling Li diffusion through specific octahedral or tretrahedral sites, and by changing the size and geometry of the anion “window”.[29-32] Both factors, the type of stacking and the increased layer distance, can affect the ion conduction, as likewise seen for example in Na_xCoO_2 [33,34]. While in principle the interlayer water in the monohydrate is expected to negatively affect the conductivity due to steric hindrance and blocking of the Li trajectories, the increased layer distance and the change in stacking sequence may have positive effects, leading to the unexpectedly high conductivity σ_{NMR} = 1.7 mS cm^{-1}. Although the value is lower than that for the anhydrous sample, it is still two orders of magnitude better than in the fully lithiated version $Li_{1.0}[Li_{0.33}Sn_{0.67}S_2]$.[12] Upon further hydration, the materials display reduced crystallinity and a further increase of interlayer distance to 11.4 Å. In contrast to the monohydrate, the water molecules in the swollen phase according to ^{1}H NMR are very mobile (Figure 3). Its significantly increased interlayer distance, combined with liquid-like mobility of the water molecules, are the likely reasons for a more facile lithium diffusion, resulting in similar or maybe increased conductivities compared to those found for the anhydrous sample (σ_{NMR} = 10 mS cm^{-1} *vs.* 8.6 mS cm^{-1}) (note that within the range of error they are very similar). We hypothesize that another mechanism potentially enhancing long-range Li motion operates in the swollen phase: The mobile water molecules may screen the positive charge through facile reorientation of their dipoles as Li ions move through the interlayer space. This dielectric relaxation mechanism may mitigate the otherwise strong Coulombic interactions immobilizing the Li ions in their interlayer potential wells. In addition, the water molecules may act like vehicles to transport the Li ions, similar to the vehicle mechanism found in several protonic conductors [35]. Finally, the increase in interlayer distance and the possible turbostratic layer stacking likely opens up additional, facile pathways for Li ion movement with potentially lower energies of activation for Li hopping as compared to the rigid lattices of the anhydrate and the monohydrate. Note that although in this respect solvation of the Li ions may be beneficial for Li motion, it may be detrimental for interfacial kinetics in batteries when the Li ions need to strip off their solvation shell before they can cross the electrode interface. Likewise, the presence of water in the solid electrolyte can be highly critical in present all-solid-state-batteries as hydrogen and oxygen may be evolved electrolytically as gaseous byproducts.

5.4 Conclusion

In summary, we have studied the impact of hydration – dehydration on the anhydrous fast Li ion conductor $Li_{0.6}[Li_{0.2}Sn_{0.8}S_2]$. Upon air exposure, the material forms a stoichiometric monohydrate, which is accompanied by a change in stacking from O1 to P3 and an increase of the interlayer distance by 2 Å. The hygroscopic nature of $Li_{0.6}[Li_{0.2}Sn_{0.8}S_2]$ is most likely the reason for its previously observed excellent exfoliation behavior in water. In addition to retaining its chemical integrity, the monohydrate exhibits a rather high ionic conductivity of σ_{NMR} = 1.7 mS cm^{-1}, demonstrating that hydration does not significantly reduce or even prevent Li ion conduction. Upon further hydration to $Li_{0.6}[Li_{0.2}Sn_{0.8}S_2]\cdot 1.6H_2O$, the ionic conductivity reaches σ_{NMR} = 10 mS cm^{-1}, making $Li_{0.6}[Li_{0.2}Sn_{0.8}S_2]$ the first sulfide-based air-tolerant lithium superionic conductor with Li conductivities competitive with those of liquid electrolytes. Further understanding of the nature of ionic transport in the fully hydrated phase may open the door to the rational design of air and water stable superionic conductors. Also, due to its similarity in ionic conductivity to state-of-the-art superionic conductors and its air stability, $Li_{0.6}[Li_{0.2}Sn_{0.8}S_2]\cdot 1.6H_2O$ itself may be used as a solid electrolyte in electrochemical devices operating in a potential range where water electrolysis cannot adversely affect device operation.

Acknowledgement

We thank Marie-Luise Schreiber for ICP-AES measurements, Viola Duppel for TEM meaurements and Willi Hoelle and Daniel Weber for TGA measurements. Financial support by the Max Planck Society, Nanosystems Initiative Munich (NIM), Center for Nanoscience (CeNS) and Fonds der Chemischen Industrie is gratefully acknowledged. Work at Princeton was supported by the NSF-sponsored MRSEC at Princeton University, grant DMR-1420541. LMS gratefully acknowledges support from the Minerva fast track fellowship by the Max Planck Society.

References

[1] Kamaya, N.; Homma, K.; Yamakawa, Y.; Hirayama, M.; Kanno, R.; Yonemura, M.; Kamiyama, T.; Kato, Y.; Hama, S.; Kawamoto, K. *Nature Mat.* **2011**, *10*, 682-686.

[2] Kanno, R.; Hata, T.; Kawamoto, Y.; Irie, M. *Solid State Ionics* **2000**, *130*, 97-104.

[3] Murayama, M.; Kanno, R.; Irie, M.; Ito, S.; Hata, T.; Sonoyama, N. Kawamoto, Y. *J. Solid State Chem.* **2002**, *168*, 140-148.

[4] Kanno, R.; Murayama, M. *J. Electrochem. Soc.* **2001**, *148***,** A742.

[5] Kuhn, A.; Gerbig, O.; Zhu, C.; Falkenberg F.; Maier, J.; Lotsch, B. V. *Phys. Chem. Chem. Phys.* **2014**, *16*, 14669-14674.

[6] Seino, Y.; Ota, T.; Takada, K.; Hayashi, A.; Tatsumisago, M.; *Energy Environ. Sci*. 2014, *7*, 627.

[7] Yamane, H. et al. *Solid State Ion.* **2007**, *178*, 1163-1167.

[8] Ong, S. P.; Mo, Y.; Richards, W. D.; Miara, L. Lee, H. S.; Ceder, G. *Environ. Sci.* **2013**, *6*, 148

[9] Wang, Y.; Richards, W. D.; Ong, S. P.; Miara, J.; Kim, J. C.; Mo, Y.; Ceder, G. *Nature Material* **2015**, *14*, 1026-1031

[10] Holzmann, T.; Schoop, L. M.; Ali, M. N.; Moudrakovski, I.; Gregori, G.; Maier, J.; Cava, R. J.; Lotsch B. V. *Energy Environ. Sci.* **2016**, *9*, 2578-2585.

[11] Kuhn, A.; Holzmann, T.; Nuss, J.; Lotsch, B. V. *J. Mater. Chem. A* **2014**, *2*, 6100.

[12] Brant, J. A.; Massi, D. M.; Holzwarth, N. A. W.; MacNeil, J. H.; Douvalis, A. P.; Bakas, T.; Martin, S. W.; Gross, M. D.; Aitken, J. A. *Chem. Mater.* **2015**, *27*, 189-196.

[13] Van der Ven, A.; Bhattacharya, J.; Belak, A. A. *Acc. Chem. Res.* **2013**, *46*, 1216-1225.

[14] Urban, A.; Lee, J.; Ceder, G. *Adv. Energy Mater.* **2014**, *4*, 1400478.

[15] Roudebush, J. H.; Cava, R. J. *J. Sol. State Chem.* **2013**, *204*, 178-185.

[16] Seibel, E. M.; Roudebush, J. H.; Ali, M. N.; Ross, K. A.; Cava, R. J. *Inorg. Chem.* **2014**, *53*, 10989-10995

[17] Pake, G. E. *J. Chem. Phys.* **1948**, *16*, 327.

[18] Sasaki, T.; Komatsu, Y.; Fujiki, Y. *J. Chem. Soc., Chem. Comm.* **1991**, *12*, 817-818.

[19] Sasaki, T.; Watanabe, M.; Hashizume, H.; Yamada, H.; Nakazawa, H. *J. Am. Chem. Soc.* **1996**, *118*, 8329.

[20] Sasaki, T.; Nakano, S.; Yamauchi, S.; Watanabe, M. *Chem. Mater.* **1997**, *9*, 602.

[21] Sasaki, T.; Watanabe, M. *J. Am. Chem. Soc.* **1998**, *120*, 4682.

[22] Ebina, Y.; Sasaki, T.; Harada, M.; Watanabe, M. *Chem. Mater*. 2002, *14*, 4390.

[23] Ma, R.; Sasaki, T. *Adv. Mater.* **2010**, *22*, 5082-5104.

[24] Tindwa, R. M.; Ellis, D. K.; Peng, G. Z.; Clearfield, A. *J. Chemical Society, Faraday Transactions 1* **1985**, *81*, 545.

[25] Kim, H. N.; Keller, S. W.; Mallouk, T. E. *Chem. Mater.* **1997**, *9*, 1414.

[26] Ganter, P.; Schoop, L. M.; Lotsch, B. V. *Adv. Mater.* **2016**.

[27] Alam, T. M.; Hart, D.; Repe, S. L. B. *Phys. Chem. Chem. Phys.* **2011**, *13*, 13629-13637.

[28] Van der Ven, A.; Thomas, J. C.; Xu, Q. *Phys. Rev. B* **2008**, *78*, 104306.

[29] Van der Ven, A.; Ceder G. *Electrochemical and Solid-State Letters* **2000**, *3*, 301-304.

[30] Reimers, J. N.; Dahn, J. R. *J. Electrochem. Soc*. **1992**, *139*, 2091-2097

[31] Carlier, D.; Van der Ven, A.; Delmas, C.; Ceder G. *Chem. Mater.* **2003**, *15*, 2651-2660.

[32] Ceder, G.; Van der Ven, Aydinol, M. K. *JOM* **1998**, *50*, 35-40.

[33] Mo, Y.; Ong, S. P.; Ceder, G. *Chem. Mater.* **2014**, *26*, 5208.

[34] Clément, R. J.; Bruce, P. G.; Grey, C. P. *J. Electrochem. Soc.* **2015**, *162*, A2589.

[35] Kreuer, K.-D.; Rabenau, A.; Weppner, W. *Angew. Chem. Int. Ed. Engl.* **1982**, *21*, 208-209.

[36] Tanner, J. E. *J.Chem.Phys*. **1970**, *52*, 2523 .

[37] Stejskal, E. O.; Tanner, J. E. *J. Chem. Phys*. **1965**, *42*, 288.

[38] Janek, J.; Zeier, W. G. *Nature Energy* **2016**, *1*, 16141.

[39] Masuda,Y.; Hamada, Y.; Seo, W. S.; Koumoto, K. *J. Nanosci. Nanotechnol.* **2006**, *6*, 1632-1638.

[40] Foo, M. L.; Klimczuk, T.; Cava, R. J. *Materials Research Bulletin* **2005**, *40*, 665-670.

5.5 Supporting Information

Air-tolerant Li ion conduction in the superionic conductor $Li_{0.6}[Li_{0.2}Sn_{0.8}S_2]$

Tanja Holzmann[‡†§], *Leslie M. Schoop*[*†], *Igor Moudrakovski*[†], *Mazhar N. Ali*[*], *Robert J. Cava*[*], *Bettina V. Lotsch*[†‡§]

[†] Max Planck Institute for Solid State Research, Heisenbergstr. 1, 70569 Stuttgart, Germany

[‡] Department of Chemistry, Ludwig-Maximilians-Universität München, Butenandtstr. 5-13, 81377 München, Germany

[§] Nanosystems Initiative Munich (NIM) & Center for Nanoscience, Schellingstr. 4, 80799 München, Germany

[*] Department of Chemistry, Princeton University, Princeton, NJ 08544, USA.

1. X-ray diffraction

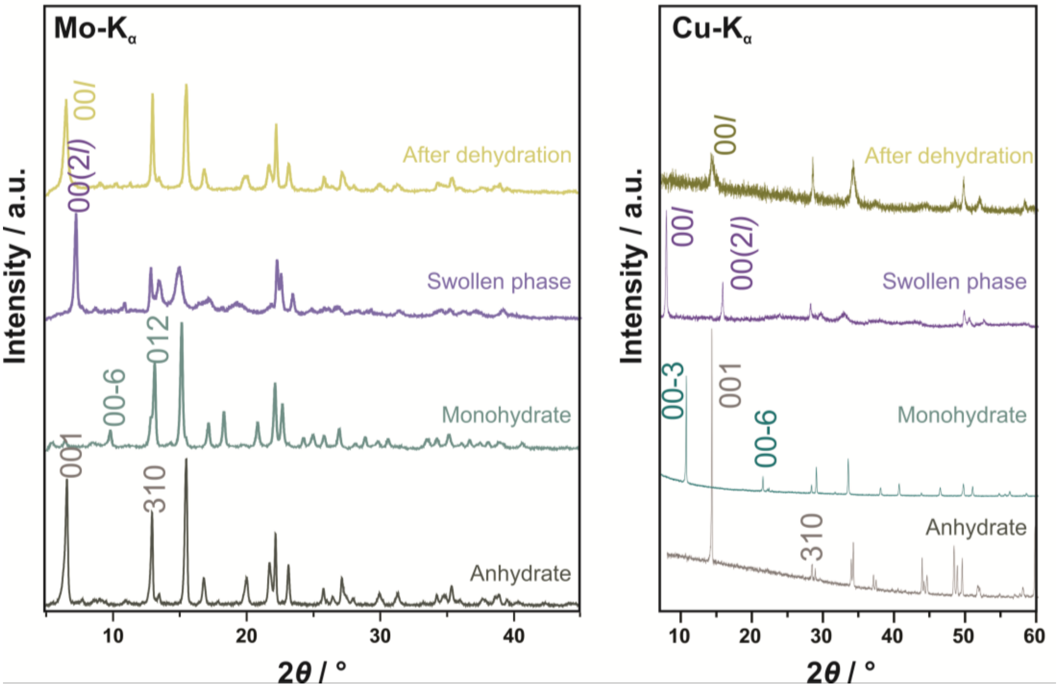

Figure S1. Mo-Kα (left) and Cu-Kα (right) PXRD patterns of $Li_{0.6}[Li_{0.2}Sn_{0.8}S_2]$ (anhydrate), $Li_{0.6}[Li_{0.2}Sn_{0.8}S_2]\cdot H_2O$ (monohydrate), $Li_{0.6}[Li_{0.2}Sn_{0.8}S_2]\cdot 1.6\ H_2O$ (swollen phase) and the dehydrated powder. The swollen sample was dehydrated with a heat gun for 30 min under vacuum. Note the reduced crystallinity of the dehydrated powder, probably arising from smaller grain sizes.

Hydration process tracked with PXRD

To track the hydration process with PXRD measurements, two different configurations were tested. First, the anhydrate powder was poured on a flat sample holder and measured in reflectance mode. After the first scan (8 min long), the powder was already fully transformed to the monohydrate. To slow down the hydration process, the anhydrate powder was transferred into a glass capillary. After measuring the sample under argon, the capillary was opened to allow slow hydration of the powder (see Figure S2). These measurements in 6 min intervals display a slow hydration process, visible by the decrease of the peak at $2\theta = 14.3°$ (stacking peak of the anhydrate) and a simultaneous increase of the peak at $2\theta = 10.5°$ (stacking peak of the monohydrate). After 42 min about half of the sample was hydrated. No intermediate phase between anhydrate and monohydrate could be observed.

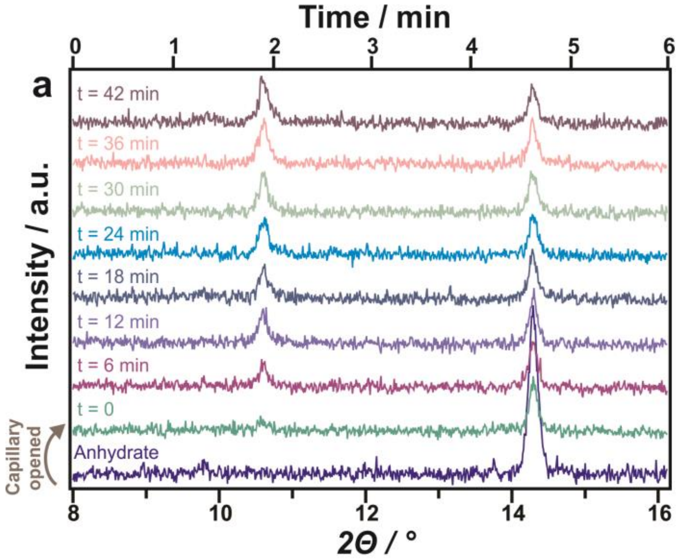

Figure S2. Cu-K_{α} PXRD patterns recording the hydration of $Li_{0.6}[Li_{0.2}Sn_{0.8}S_2]$ to $Li_{0.6}[Li_{0.2}Sn_{0.8}S_2]\cdot H_2O$. 8 ranges à 6 min were measured. The reference pattern of the anhydrate is presented in dark purple (bottom line). After opening the capillary, the powder hydrates in air. The reflection at 14.3 °2θ represents the anhydrate phase. With increasing time, the hydration becomes visible at 10.5 °2θ. Due to the geometry of the capillary the air penetration and thereby the hydration process is delayed. Note that using a flat sample holder led to immediate full hydration.

2. Chemical composition

Table S1. EDX data of $Li_{0.6}[Li_{0.2}Sn_{0.8}S_2]\cdot H_2O$ in atomic-%.

Spectrum	S	Sn
Expected	71.43	28.57
Spectrum 1	70.60	29.40
Spectrum 2	70.59	29.41
Spectrum 3	70.14	29.86
Spectrum 4	70.55	29.45
Spectrum 5	70.69	29.31
Mean	70.51	29.49

Table S2. ICP-AES data of $Li_{0.6}[Li_{0.2}Sn_{0.8}S_2]$•$H_2O$ in atomic- and weight-%. Two measurements were performed.

$Li_{0.6}[Li_{0.2}Sn_{0.8}S_2]$	Li	Sn
wt%	2.83	50.42
	2.80	50.79
at%	1.0	1.04
	1.0	1.08

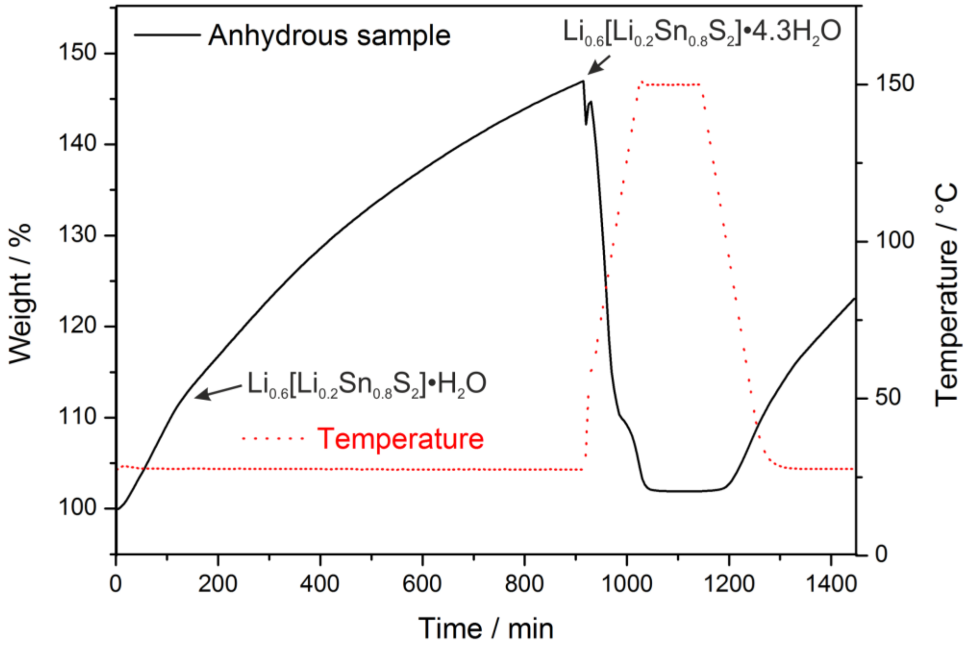

Figure S3. TGA measurements of $Li_{0.6}[Li_{0.2}Sn_{0.8}S_2]$ under a constant flow of argon/water vapor. In the first step, the monohydrate $Li_{0.6}[Li_{0.2}Sn_{0.8}S_2]\cdot H_2O$ is formed (see kink at around 110 min, +10 %), afterwards the sample gradually swells further. After 900 min, a water uptake of 4.3 H_2O molecules per formula unit was obtained and the heating process to 150 °C started (1°C/min). Note that the hydration of the powder was not complete. The dehydration also shows a two-step behavior: the "kink" in the curve is seen at the same weight as during hydration, indicating the formation of the monohydrate.

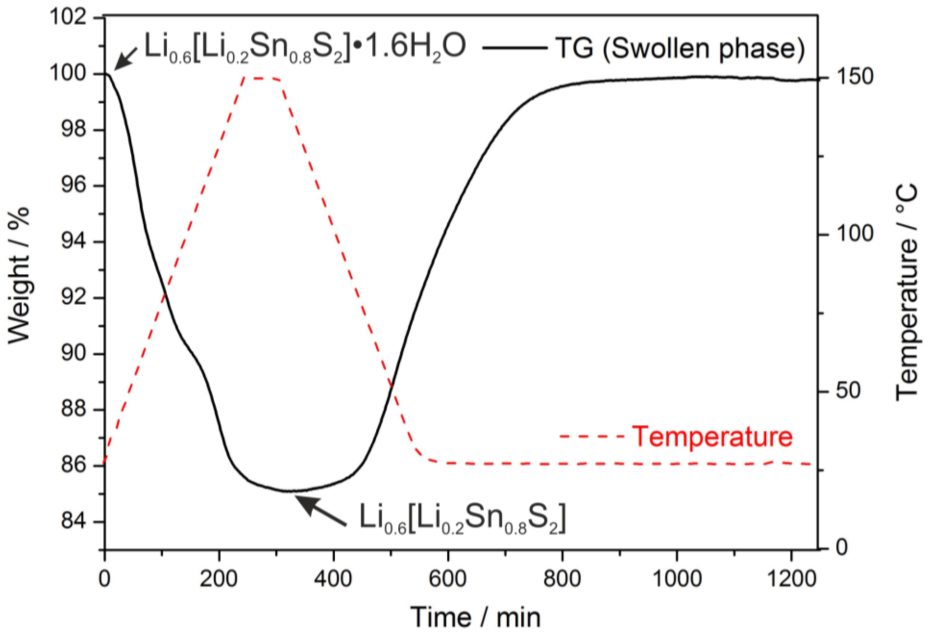

Figure S4. TGA measurements of swollen $Li_{0.6}[Li_{0.2}Sn_{0.8}S_2]\cdot1.6H_2O$ that was used for ^{7}Li PFG NMR measurements after several days in air. The heating process was performed with 0.5 °C min^{-1} up to 150 °C. The sample was held at that temperature for 60 min and cooled down with 0.5 °C min^{-1}. The weight loss is about 15%, which corresponds to 1.6 water molecules per formula unit. Note that this particular water amount is presumably dependent on the relative humidity in air.

3. Structural details

Table S3. Crystallographic details of the single crystal structure solution of $Li_{0.6}[Li_{0.2}Sn_{0.8}S_2]\cdot H_2O$.

$Li_{0.64}[Li_{0.21}Sn_{0.79}S_2]\cdot H_2O$	
Temperature	100 K
Symmetry	Trigonal; $R\bar{3}m$ (166)
Lattice constants	a = 3.685(3) Å c = 25.164(18) Å
Cell volume	V = 296.0(4) Å^3
Unit cell content	Z = 3

Radiation	Mo K_α
Θ range	2.43 – 26.01
Index range	$-4 \leq h \leq 4$ $-4 \leq k \leq 4$ $-29 \leq l \leq 30$
Total no. of reflections	673
Unique reflections	100
R_1 (all reflections)	0.0574
R_1 $Fo > 2\sigma(Fo)$	0.0413 (86)
wR2	0.0992 (100)
Residual e^- density (e/Å^3)	1.71/-0.84
GooF	1.080

Table S4. Atomic coordinates of the single crystal structure solution of $Li_{0.6}[Li_{0.2}Sn_{0.8}S_2]\cdot H_2O$.

Site	Wyck.	*x*	*y*	*z*	*occ.*
Sn1	3a	0	0	0	0.79
Li1	3a	0	0	0	0.21
S2	6c	0	0	0.60915(17)	1
Ne = H_2O	6c	1/3	-1/3	0.4991(14)	0.5
Li2	6c	1/3	-1/3	0.4991(14)	0.32

Table S5. Anisotropic displacement parameters of the single crystal structure solution of $Li_{0.6}[Li_{0.2}Sn_{0.8}S_2]\cdot H_2O$

Anisotropic displacement parameters, in Å^2				
Atom	U_{11}	U_{22}	U_{33}	U_{12}
Sn1	0.0046(8)	0.0046(8)	0.0252(17)	0.0023(4)
Li1	0.0046(8)	0.0046(8)	0.0252(17)	0.0023(4)
S2	0.0090(13)	0.0090(13)	0.022(3)	0.0045(7)
O3	0.16(3)	0.16(3)	0.033(19)	0.078(14)
Li2	0.16(3)	0.16(3)	0.033(19)	0.078(14)

4. NMR measurements

All solid-state (ss) MAS NMR measurements were performed with a Bruker 4 mm triple-channel Magic Angle Spinning (MAS) probe at spinning speeds between 5 kHz - 14 kHz. Most of the time the spectra were collected using a simple Bloch decay (π/2-pulse-acquire-delay) with π/2-pulses for ^{6}Li and ^{119}Sn set to 5.8 μs (B_1 = 43.1 kHz) and 4 μs (B_1 = 62.5 kHz), respectively. ^{119}Sn spectra are externally referenced to tetramethyltin ($Sn(CH_3)_4$, δ_{iso} = 0.0 ppm) with solid SnO_2 as secondary chemical shift standard (δ_{iso} = -603.0 ppm relative to $Sn(CH_3)_4$).[1] ^{6}Li spectra are referenced to 9.7 M aqueous solution of LiCl (δ_{iso} = 0.0 ppm).[1] ^{1}H spectra are referenced to neat tetramethylsilane (TMS, δ_{iso} = 0.0 ppm). Broadband high power proton-decoupling (SPINAL-64 pulse sequence at nutation proton frequency $B_1(^1H)$ = 78.1 kHz) was used when acquiring spectra of hydrated $Li_{0.6}[Li_{0.2}Sn_{0.8}S_2]$. Some of the hydrated samples were also acquired with Cross Polarization (CP) transfer from protons to ^{6}Li or ^{119}Sn. These spectra are recorded using a ramp on the proton channel during the spin-lock and contact times of 1 to 10 ms. Normally, between 16 and 128 scans were accumulated in the spectra obtained with the direct excitation, and up to 4000 accumulations were collected for the CP spectra. The relaxations delays in ^{1}H and CP experiments were 2 s, ^{6}Li spectra employed delays between 30 and 500 s, and ^{119}Sn experiments used delays between 200 and 400 s. In every case the relaxation delays were set to provide for quantitative spectra, which was validated by the estimates of the relaxation times performed for every specific situation. During the MAS experiments the temperature of the samples was controlled using a Bruker BVT3000 temperature controller and was calibrated using the ^{207}Pb signal in $Pb(NO_3)_2$.[2] Analytical simulations and integration of experimental spectra were carried out with the DMFit [3] and Bruker TopSpin 3.2 Lineshape Analysis Tool simulation packages.[4]

^{119}Sn NMR

As previously reported,[5] $Li_{0.6}[Li_{0.2}Sn_{0.8}S_2]$ shows 3 peaks at -747.6 ppm, -750.1 ppm and -754.6 ppm with an integral ratio of around 39 : 21 : 40. Due to the close positions of the signals and the possible differences in short range chemical environments, they cannot be clearly assigned, but it is presumed that the two peaks at -747.6 ppm and -754.6 ppm belong to Sn2 sites with a combined integral sum of 79% and the third peak at -750.1 ppm belongs to Sn1 with an integral of 21%.[5] We observe that during the hydration peak 2 is shifted to lower frequencies (from -750.13 ppm to -756.03 ppm; named peak 3 in the hydrated sample) while peak 1 and 3 are shifted to higher frequencies (here peak 1 and 2 in the hydrated sample).The fact that the peaks are shifted in different directions (peak 1 and 3 to higher, peak 2 to lower frequencies) can be explained by a preferred intercalation site for water.

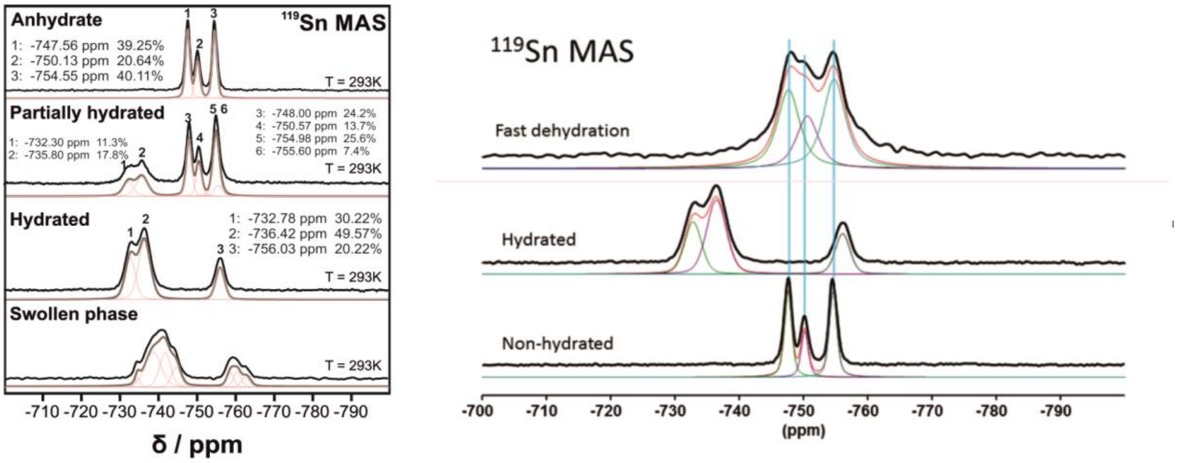

Figure S5. ^{119}Sn NMR spectra of $Li_{0.6}[Li_{0.2}Sn_{0.8}S_2]$ before and after various hydration steps and after the dehydration under vacuum. Note that the peak positions after fast dehydration are in the same range as for the anhydrate although the peaks are broadened, which is consistent with the lower crystallinity observed in the PXRD measurements. In accord with the PXRD measurements, no intermediate phase between hydrate and anhydrate can be observed.

^{7}Li PFG NMR

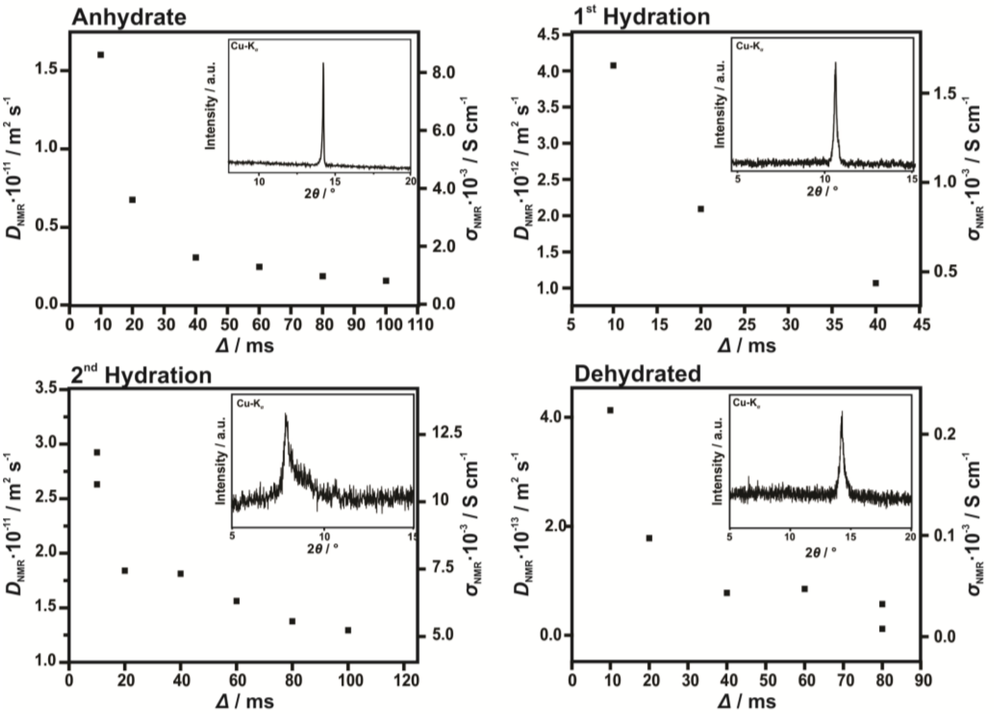

Figure S6. PFG NMR data of $Li_{0.6}[Li_{0.2}Sn_{0.8}S_2]$ at various hydration steps with the corresponding PXRD data. For each hydration step, the powder was poured into a mortar and stored for 1h in a dessiccator at 100% humidity. For dehydration, the powder was heated for around 30 min with a heat gun under vacuum.

The lithium conductivity σ_{NMR} was calculated according to the extended Nernst-Einstein equation, using the diffusion coefficient determined by ^{7}Li PFG NMR:

$$\boldsymbol{\sigma_{NMR} = \frac{D_{NMR}\, n\, z^2\, e^2}{k_B T}} \quad \textbf{(1)}$$

D_{NMR}: Diffusion coefficient determined by PFG NMR ($m^2\ s^{-1}$); n: concentration of diffusing species that take part in the ion conduction; z: charge number of diffusion species, here +1 for Li^+; e: elemental charge ($1.60\cdot10^{-19}$ C); k_{B}: Boltzmann constant ($1.38\cdot10^{-23}$ kg $m^2\ s^{-2}\ K^{-1}$), T: Temperature (293 K).

The conductivity was calculated for each PFG NMR measurement with varying Δ values. Note that Δ = 10 ms is closest to the bulk conductivity.

5. TEM measurements

As previously reported, TEM-EDX measurements of the nanosheets gave an average Sn : S ratio of 1 : 2.1 (expected 1 : 2.5).[6]

Table S6. Comparison of *d* values measured with TEM-SAED and calculated according to the space group *C*2/*m*. The values are in good agreement, confirming our assumption that the intralayer ordering of the anhydrous sample is still present in the exfoliated nanosheets and, hence, in the hydrated samples.

Reflection	d_{measured} [Å]	d_{calc} [Å] ($C2/m$)
200	9.12	9.08
400	4.59	4.54
600	3.07	3.03
020	1.82	1.85
310	3.15	3.16
910	1.78	1.77

6. AFM measurements of exfoliated $[Li_{0.2}Sn_{0.8}S_2]^{0.6-}$ nansosheets

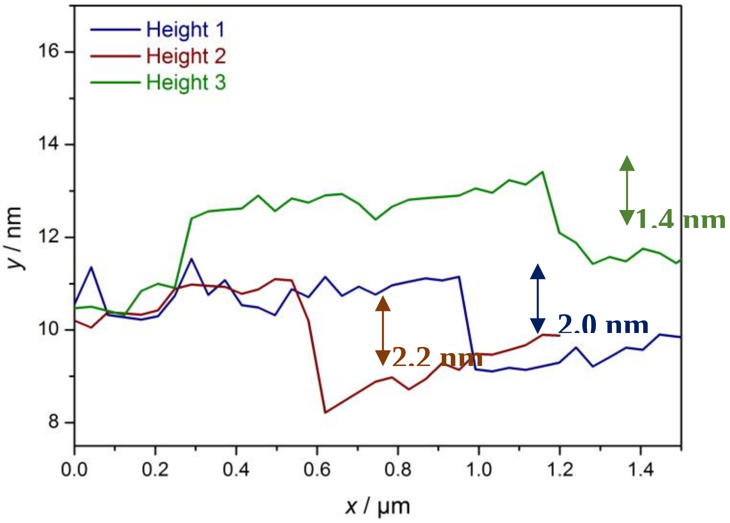

Figure S7. Height profiles of AFM measurements (see Figure 3b). The estimated heights are 2.0 nm (blue line), 2.2 nm (red line) and 1.4 nm (green line).

Literature

[1] Harris, R. K.; Becker, E. D.; Cabral de Menezes, S. M.; Granger, P.; Hoffmann, R. E.; Zilm, K. W. *Pure and Applied Chemistry* **2008**, *80*, 59.

[2] Bielecki, A.; Burum, D. P.; *J. Magn. Reson. Ser. A* **1995**, *116*, 215.

[3] Massiot, D.; Favon, F.; Capron, M.; King, I.; Le Calvé, S.; Alonso, B.; Durand, J. O.; Bujoli, B.; Gan, Z.; Hoatson, G. *Magn. Reson. Chem.* **2002**, *40*, 70.

[4] Rohonczy, J. Bruker BioSpin GmbH: Rheinstetten, Germany, 2009.

[5] Holzmann, T.; Schoop, L. M.; Ali, M. N.; Moudrakovski, I.; Gregori, G.; Maier, J.; Cava, R. J.; Lotsch B. V. *Energy Environ. Sci.* **2016**, *9*, 2578-2585.

[6] Kuhn, A.; Holzmann, T.; Nuss, J.; Lotsch, B. V. *J. Mater. Chem. A* **2014**, *2*, 6100.

6 Conclusion and Outlook

With the advent and proliferation of personal computers in the middle of the 20th century, the digital revolution started and is still ongoing. While the first all-in-one personal computer, the Commodore PET 2001 (release date 1977[1]) had a CPU with 1 MHz frequency,[1] recent models achieve up to 4 GHz at half the size. The number of embedded transistors thereby increased from 3510[2] to more than 1 billion[3]. This development was described in 1965 by Gordon Earle Moore and is commonly known as “Moore's law”, predicting a duplication of transistors per area every 18 months. Although this constant increase has proven true, it is expected to reach its fundamental limit around 2020 due to economical, technical and physical limits. Recent transistors are still manufactured from silicon and, at a transistor size of around 5-7 nm, the silicon layer has a height of only 17 silicon atoms. Fewer silicon atoms would lead to a lack of mobile charge carriers, quantum-mechanical effects and leakage currents due to tunneling electrons. Besides the possibility of building quantum computers, researchers are also investigating new design concepts. One example is the application of atomically thin films which can be achieved by the exfoliation of bulk semiconducting layered materials. We could demonstrate the functionality of such a thin-film FET out of the layered semiconductor SnS_2. This FET shows no leakage currents, an on/off ratio of 10^6, and displayed a constant current flow once the threshold voltage was reached. The key challenge, however, was to obtain single-layered nanosheets with lateral sizes that allow an electrical contacting *via* standard lithography processes. The scotch-tape method proves to be unsuitable because reducing the height of the nanoflakes was accompanied by a decrease in lateral size. In addition, such a non-scalable and thus time-consuming method would not be economically useful. We therefore aimed to improve the exfoliation route of tin disulfide-type materials. By adding the lithium precursor (Li_2S) directly to the starting reactants, a new solid solution, $Li_{3x}[Li_xSn_{1-x}S_2]$, with outstanding exfoliation behavior was obtained. Common exfoliation methods are either complex (e.g. post-lithium-insertion) or lead to a broad range of Li contents and height distributions of the resulting nanolayers consisting of more than one nanosheet (e.g. by sonication in organic solvents). This thesis presents a new method that enables a quantitative extraction of single-layered nanosheets, resulting in the possibility to fabricate conformal coatings of tin disulfide-type materials of desired thickness. It is conceivable that this design principle can be extended to other layered chalcogenides and may result in a more efficient production of single-layered metal chalcogenide nanosheets. For a deeper insight into the exfoliation of $Li_{0.6}[Li_{0.2}Sn_{0.8}S_2]$, the material that displayed the best exfoliation properties, we performed further investigations on this material. $Li_{0.6}[Li_{0.2}Sn_{0.8}S_2]$ is the lithium depleted version of Li_2SnS_3. The reduction of the lithium content results in unoccupied interlayer lithium positions that result in a spontaneous hydration in air to $Li_{0.6}[Li_{0.2}Sn_{0.8}S_2]\cdot H_2O$. This hydration is not observed in Li_2SnS_3. The generated vacancies open up the possibility of water penetration, increasing the layer distances and thereby facilitating the exfoliation due to reduced electrostatic forces. This concept can be seen as a key finding for future access to nanosheets and can be transferred to many other layered ionic solids.

The continuing acceleration of processor performance is accompanied by an increasing energy demand, especially due to the ever increasing proliferation of portable devices like smartphones or notebooks and the future plans for building electrical vehicles. The main problem with existing Li ion batteries are their relatively low energy and power densities as well as safety risks associated primarily with the use of flammable liquid electrolytes. Thus, the batteries are vulnerable to leakage in case of damages to the battery casing. Further, the formation of lithium dendrites at the separator layer may result in short circuiting, which makes the battery prone to explosion. These safety risks need to be overcome if manned electrical vehicles shall be realized one day. The most commonly pursued approach is to use all-solid-state batteries, which are batteries where the liquid electrolyte is replaced by a solid one, using ultrafast lithium ion conducting solid state compounds. We were able to identify $Li_{0.6}[Li_{0.2}Sn_{0.8}S_2]$ as such a material. Unlike common lithium superionic conductors, it shows an anisotropic, 2D lithium migration pathway. With conductivities in the range of 10^{-2} S cm^{-1}, it is in the range of the best lithium superionic conductors currently. It is important to note that the design principles that we investigated for the spontaneous hydration in air are also important for the lithium ion conduction. The conductivity of $Li_{0.6}[Li_{0.2}Sn_{0.8}S_2]$ is three orders of magnitude better than the one for Li_2SnS_3. The implemented vacancies are therefore especially important as they generate tetrahedrally coordinated lithium sites. The migration pathway from tetrahedral to octahedral sites and *vice versa* is known to be associated with lower activation energies and are thus energetically favorable. This effect can be very important for further studies on these materials as many layered compounds (e.g. Delafossite-related ones) have been reported to also exist in cation depleted versions. As the conductivities of 10^{-2} S cm^{-1} presented herein were measured on polycrystalline powder, single crystals should also be investigated in the future with respect to the anisotropic conductivity. However, as far as applicability allows it, these new solid electrolytes should be included into future all-solid-state batteries in combination with electrodes of moderate Li chemical potential or by finding ways of kinetic passivation. Some of the currently best Li^+ ion conductors such as LGPS-type materials are already investigated for all-solid-state devices, but these compounds are not air-stable. Although the substitution of liquid electrolytes has advantages, a risk remains if solid electrolytes show chemical reactions if they get into contact with high/low voltage electrodes as well as humid air, for example, if the housing has damages. Besides the high Li mobility of $Li_{0.6}[Li_{0.2}Sn_{0.8}S_2]$, we could demonstrate that this conductivity is not dramatically sensitive to air. Although $Li_{0.6}[Li_{0.2}Sn_{0.8}S_2]$ forms a hydrate in air, the Li^+ conductivity is still in the range of 1.7 – 10 mS cm^{-1}. To the best of our knowledge, $Li_{0.6}[Li_{0.2}Sn_{0.8}S_2]$ is not only one of the best solid Li^+ ion conductors, it is furthermore the only lithium superionic conductor that does not show chemical decomposition in air beyond hydrate formation and, although it hydrates, its exceptional conduction properties are largely maintained.

6.1 Bibliography

[1] I. Matthews: Commodore PET History. http://www.commodore.ca/commodore-products/commodore-pet-the-worlds-first-personal-computer/ (December 14th, 2016).

[2] G. James: Visualizing a Classic CPU in Action: The 6502. http://visual6502.org/docs/6502_in_action_14_web.pdf (December 14th, 2016).

[3] Intel Corporation: Transistors to Transformations – From Sand to Circuits. http://www.intel.com/content/www/us/en/history/museum-transistors-to-transformations-brochure.html (December 14th, 2016).

7 Appendix

7.1 Experimental and analytical details

7.1.1 Syntheses

The synthesis procedures for SnS_2, $Li_{4x}Sn_{1-x}S_2$ as well as the hydration and the exfoliation routes are described in the following.

SnS_2

Tin disulfide (SnS_2) was synthesized in a common solid state reaction from the elements tin and sulfur with a stoichiometric ratio of 1 : 2. The powders were thoroughly ground and pressed into pellets. The pellets were vacuum sealed in quartz ampoules and heated to 700 °C with a heating rate of 60° h^{-1} and hold for at least 12 h. The ampoules were afterwards either quenched or cooled down with around 180 °C h^{-1} to room temperature (for both methods, no chemical difference was observed). The powder obtained was afterwards used for the synthesis of $Li_{4x}Sn_{1-x}S_2$.

For the synthesis of large SnS_2 crystals, iodine was added to the ampoule before sealing it. Iodine acts as a transport agent to obtain large (up to a diameter of 1 cm), plate-like, transparent orange SnS_2 crystals.

$Li_{4x}Sn_{1-x}S_2$

The ternary lithium tin sulfide compounds were synthesized in different ways. Compared to SnS_2 all products were handled under inert gas to avoid hydration or oxidation. The solid solution character of $Li_{4x}Sn_{1-x}S_2$ was only observed for synthesis 1: stoichiometric amounts of tin, sulfur and lithium sulfide were thoroughly ground and pressed to pellets. These pellets were sealed in quartz ampoules under vacuum and were afterwards heated to 750 °C with around 60 °C h^{-1}. Depending on the stoichiometry, the composition could be varied from $x = 0.33$ to $x = 0.11$. For synthesis 1 an amorphous side phase was observed by NMR measurements which could be avoided by synthesis 2: stoichiometric ratios of lithium sulfide and SnS_2 were thoroughly ground and pressed into pellets. The pellets were vacuum sealed in quartz ampoules and heated to 700 °C with 60 °C h^{-1}. After 2 d reaction time, the ampoule were cooled down with 180 °C h^{-1}. For synthesis 2 no solid solution character was observed and no amorphous side phase was detected in solid-state NMR measurements. In both synthesis routes an excess of sulfur was added to ensure complete oxidation of tin.

$Li_{0.6}[Li_{0.2}Sn_{0.8}S_2]•H_2O$

Exposure of polycrystalline powder $Li_{0.6}[Li_{0.2}Sn_{0.8}S_2]$ to air resulted in the monohydrate $Li_{0.6}[Li_{0.2}Sn_{0.8}S_2]•H_2O$. The speed of the hydration depends on the humidity and the grain size, but in general around 15 min of air contact resulted in fully hydrated material. The hydration degree can be detected by PXRD measurements, observing the stacking reflection shift from ~14 °2θ to ~10 °2θ.

Exfoliation of $Li_{0.6}[Li_{0.2}Sn_{0.8}S_2]$

If the monohydrate $Li_{0.6}[Li_{0.2}Sn_{0.8}S_2]•H_2O$ was further exposed to humid air the hydration went on and resulted in an exfoliated powder. If the stacking reflection is fully shifted to ~8 °2θ the material is exfoliated. Thereby often a Warren shaped peak can be observed.

To obtain a colloidal nanosheet suspension, $Li_{0.6}[Li_{0.2}Sn_{0.8}S_2]•H_2O$ was poured into water with c = 1 g l^{-1}. After several hours a swelling of the powder gets visible. The exfoliation can be obtained by shaking the vessel. Besides $Li_{0.6}[Li_{0.2}Sn_{0.8}S_2]$ also other stoichiometries could be exfoliated. The exfoliability and the time necessary for exfoliation thereby depend on the stoichiometry of the respective bulk material. In some cases ultrasonication of the suspension for 10-30 min was necessary.

7.1.2 X-ray diffraction

Powder X-ray diffraction (XRD) was performed with a STOE Stadi P diffractometer working in Debye–Scherrer geometry with Mo-$K_{\alpha 1}$ radiation and a Ge(111) monochromator. For the measurement, the crystalline samples were ground and the powder was filled in a glass capillary with a diameter between 0.3 – 0.7 mm. X-ray diffraction of the free-standing film in a flat sample holder was carried out with two geometries: (i) in transmission mode using the above-mentioned STOE Stadi P diffractometer or (ii) in reflectance mode using a Bruker D8 Advance diffractometer working with Cu-$K_{\alpha 1}$ radiation. Rietveld refinement was performed with the software DiffracPlus TOPAS v4.2 (Bruker AXS). For single-crystal X-ray diffraction, a SMART-APEX CCD X-ray diffractometer (Bruker AXS) working with graphite-monochromated Mo-$K_{\alpha 1}$ radiation was used. The integration of the reflections was performed with the SAINT software (Bruker AXS). The structure was solved with direct methods and least squares refinement using the SHELXTL program. Single-crystal X-ray diffraction (SXRD) was further conducted on a Bruker APEX II diffractometer with Mo-$K_{\alpha 1}$ radiation at 100 K. Unit cell refinement and data integration was performed with the Bruker APEX II software and CELL_NOW. The crystal structure was refined using the full-matrix least-squared method on F^2, implemented through SHELXL-2013 and WinGX.

7.1.3 Optical microscopy

The height and lateral dimensions of the nanosheets were analyzed on a silicon wafer covered with a 100 or 300 nm thermally grown SiO_2 layer. To adsorb the nanosheets on the wafer surface, the wafer was dipped into the colloidal suspension and the liquid was blown off the wafer after some seconds. The wafer was pre-examined using an optical microscope (Olympus BX51). Images were recorded with the Olympus Stream Essentials 1.7 software.

7.1.4 TEM

For TEM, a drop of the colloidal nanosheet suspension or ground bulk powder was placed on a lacey carbon film/copper grid (Plano). The nanosheet suspensions were afterwards dried under irradiation of IR light. TEM was performed with a Phillips CM30 ST (300 kV, LaB_6 cathode). Bright field images and selected area electron diffraction (SAED) patterns were recorded with a Gatan CCD camera.

7.1.5 SEM/EDX

Scanning electron microscopy was performed on a Vega TS 5130 MM (Tescan), for EDX measurements a Si/Li detector (Oxford) was used.

7.1.6 UV/VIS

Optical diffuse reflectance spectra were collected at room temperature with a UV-Vis-NIR diffuse reflectance spectrometer (Agilent Technologies, Cary 5000) at a photometric range of 200–800 nm. Samples were prepared in a sample carrier with a quartz glass window at the edge of the integrating sphere with $BaSO_4$ as the optical standard. Kubelka–Munk spectra were calculated from the diffuse reflectance data.

7.1.7 ICP-AES

ICP-AES was analyzed with a Vista Pro ICP-AES spectrometer. The characteristic wavelengths were separated with an Echelle-Polychromator (Varian, Darmstadt) and detected with a photomultiplier.

7.1.8 Zeta potential

The zeta potential of the colloidal suspension was determined by a Malvern Nano ZS Zetasizer (Malvern, Worcestershire) at 20 °C in water using the Smoluchowski method.

7.1.9 Electrical Measurements

For electrical conductivity measurements two different configurations have been used. In each of them, the thoroughly ground powder was filled into a Teflon die with an inner diameter of 4 mm. The powder was compressed by two aluminum stamps (Ø 4 mm) and they were fixed in a uniaxial press during the measurements. In configuration 1, in order to avoid any undesired reaction between lithium and aluminum and to ensure a good contact, a 0.1 mm thick gold foil was placed between the plunger and the powder at both sites. Configuration 1 is described therefore as $Au|Li_{0.6}[Li_{0.2}Sn_{0.8}S_2]|Au$. For configuration 2, an additional small layer of LiAl alloy was placed between the sample and the gold foil at both sides ($Au|LiAl|Li_{0.6}[Li_{0.2}Sn_{0.8}S_2]|LiAl|Au$). For each configuration, DC galvanostatic polarization/depolarization measurements were carried out with a Keithley 2604B source-meter, while impedance spectroscopy was performed using a Novocontrol Alpha-A high-performance frequency analyzer at frequencies ranging between 1 MHz and 0.01

Hz (AC voltage of 0.15 V). The impedance spectra were analyzed using the commercial software Z-View by Scribner Assoc.

7.1.10 AFM

AFM was performed with a Veeco CP II system. The AFM images were analyzed with the Gwyddion software.

7.1.11 NMR

^{1}H, ^{6}Li and ^{119}Sn ssNMR spectra were obtained on a Bruker Avance III 400 MHz instrument (B_0 = 9.4 T) at Larmor frequencies of 400 MHz, 58.88 MHz and 149.12 MHz, respectively. ^{7}Li T_1 relaxation time measurements at various temperatures were performed to determine the activation energies. All measurements were performed with a Bruker 4 mm triple-channel Magic Angle Spinning (MAS) probe in ZrO_2-spinners at spinning speeds between 5 kHz - 14 kHz. Most of the time the spectra were collected using simple Bloch Decay (π/2-pulse-acquire-delay) with π/2-pulses for ^{6}Li and ^{119}Sn set to 5.8 µs (B_1 = 43.1 kHz) and 4 µs (B_1 = 62.5 kHz), respectively. ^{119}Sn spectra are externally referenced to tetramethyltin ($Sn(CH_3)_4$, δ_{iso} = 0.0 ppm) with solid SnO_2 as secondary chemical shift standard (δ_{iso}-603.0 ppm relative to $Sn(CH_3)_4$). ^{6}Li spectra are referenced to 9.7 M aqueous solution of LiCl (δ_{iso} = 0.0 ppm). ^{1}H spectra are referenced to neat tetramethylsilane (TMS, δ_{iso} = 0.0 ppm). Broadband high power proton-decoupling (SPINAL-64 pulse sequence at nutation proton frequency $B_1(^1H)$ = 78.1 kHz) was used when acquiring spectra of $Li_{0.6}[Li_{0.2}Sn_{0.8}S_2]\cdot H_2O$. Some of the hydrated samples were also acquired with Cross Polarization (CP) transfer from protons to ^{6}Li or ^{119}Sn. These spectra are recorded using a ramp on the proton channel during the spin-lock and contact times of 1 to 10 ms. Normally, between 16 and 128 scans were accumulated in the spectra obtained with the direct excitation, and up to 4000 accumulations were collected for the CP spectra. The relaxations delays in ^{1}H and CP experiments were 2 s, ^{6}Li spectra employed the delays between 30 and 500 s, and ^{119}Sn experiments used the delays between 200 and 400 s. In every case the relaxation delays were set to provide for quantitative spectra, which was validated by the estimates of the relaxation times performed for every specific situation. During the MAS experiments the temperature of the samples was controlled using a Bruker BVT3000 temperature controller and was calibrated using the ^{207}Pb signal in $Pb(NO_3)_2$ Analytical simulations and integration of experimental spectra were carried out with the DMFit and Bruker TopSpin 3.2 Lineshape Analysis Tool simulation

^{7}Li Pulsed Field Gradient (PFG) NMR measurements were performed on a Bruker Avance-III 400 MHz instrument (magnetic field of 9.4 T, and ^{7}Li Larmor frequency of 155.56 MHz), equipped with a diff60 single gradient diffusion probe. The probe allows for pulse field gradients g of up to 30 T/m and variable temperature measurements up to +150 °C. The diffusion measurements were accomplished using a Stimulated Echo pulse sequence. The echo attenuation curves $S(g,\delta,\Delta)$ were processed using the Stejscal-Tanner equation, $S(g,\delta,\Delta) = E(-\gamma^2\delta^2g^2D(\Delta-\delta)/3)$, where $\gamma = 1.398\cdot10^8$ Hz/T is the ^{7}Li gyromagnetic ratio, g is the strength of the pulse field gradient of duration δ, D is the effective diffusion coefficient, and Δ is the time interval between the field gradients that defines the diffusion time scale. Diffusion constants near room temperature, where diffusion is slow, were obtained by varying the gradient strength between 0.1 and 30 T/m at a fixed $\delta = 1.0$ ms, in a range of Δ = 10-100 ms. At higher temperatures, when diffraction effects in an attenuation curve become apparent, the diffusion measurements were performed by varying δ in a range of 0.25-4.0 ms at a fixed gradient strength g of 900 G, and a fixed Δ of 20 ms.

7.2 List of publications

Basic results compiled in this thesis were published in scientific journals according to the below-mentioned list.

1. A facile wet chemistry approach towards unilamellar tin sulfide nanosheets from $Li_{4x}Sn_{1-x}S_2$ solid solutions

Alexander Kuhn, Tanja Holzmann, Jürgen Nuss, and Bettina V. Lotsch

J. Mater. Chem. A **2014**, *2*, 6100. DOI: 10.1039/c3ta14190j

The single crystal structure was solved by A. Kuhn and J. Nuss. The main part of the paper was written by A.Kuhn. Literature screening was mainly performed by T. Holzmann. Images were created by A. Kuhn, T. Holzmann and V. Duppel. PXRD, SEM/EDX, *UV/Vis, optical microscopy and AFM measurements, as well as the exfoliation (including the exfoliation movie) of the material was performed, analyzed and interpreted by T. Holzmann. TEM measurements were performed by V. Duppel and were interpreted by A. Kuhn and V. Duppel. B. V. Lotsch led the research and wrote parts of the paper. All authors analyzed and discussed the data.*

2. Threshold-Voltage Control and Enhancement-Mode Characteristics in Multilayer Tin Disulfide Field-Effect Transistors by Gate-Oxide Passivation with an Alkylphosphonic Acid Self-Assembled Monolayer

Ute Zschieschang, Tanja Holzmann, Alexander Kuhn, Mahdieh Aghamohammadi, Bettina V. Lotsch, Hagen Klauk

J. Appl. Phys. **2015**, *117*, 104509. DOI: 10.1063/1.4914488

The main part of the paper was written by H. Klauk. T. Holzmann performed the synthesis of the SnS_2 *crystals, the scotch-tape process and the localization of the flakes under the optical microscope as well as AFM, SEM/EDX, PXRD and UV/Vis measurements and the interpretation of these data. The lithography process (adding the mask to the silicon wafers and contacting the* SnS_2 *flakes), the covering process with hydrophobic SAMs and further AFM measurements were performed by U. Zschieschang. The electrical measurements on the crystals were performed by U. Zschieschang and H. Klauk. All authors analyzed and discussed the data.*

3. $Li_{0.6}[Li_{0.2}Sn_{0.8}S_2]$ – a layered lithium superionic conductor

Tanja Holzmann, Leslie M. Schoop, Mazhar N. Ali, Igor Moudrakovski, Giuliano Gregori, Joachim Maier, Robert J. Cava, Bettina V. Lotsch

Energy Environ. Sci. **2016**, *9*, 2578-2585. DOI: 10.1039/c6ee00633g

T. Holzmann led the organization and wrote the main part of the paper. The synthesis was performed by T. Holzmann, the single crystal X-ray diffraction measurements and the structure solution of $Li_{0.6}[Li_{0.2}Sn_{0.8}S_2]$ *was performed by M. Ali and L. Schoop. Solid-state* *as well as PFG NMR measurements were done by I. Moudrakovski. The analysis and interpretation of NMR data was done by I. Moudrakovski and T. Holzmann. SEM/EDX measurements were done by T. Holzmann. electrical conductivity measurements were performed by G. Gregori. Figures were done by T. Holzmann. B. V. Lotsch led the research and wrote parts of the paper. All authors analyzed and discussed the data.*

4. Air-tolerant Li ion conduction in the superionic conductor $Li_{0.6}[Li_{0.2}Sn_{0.8}S_2]$

Tanja Holzmann, Leslie M. Schoop, Igor Moudrakovski, Mazhar N. Ali, Robert J. Cava, Bettina V. Lotsch

To be submitted.

T. Holzmann led the organization and wrote the paper. The syntheses of the various anhydrous and hydrated samples were performed by T. Holzmann, the single crystal X-ray diffraction measurements and the structure solution of $Li_{0.6}[Li_{0.2}Sn_{0.8}S_2]\cdot H_2O$ *was performed by M. Ali and L. Schoop. Solid-state as well as PFG NMR measurements were done by I. Moudrakovski and interpreted by T. Holzmann. PXRD patterns and AFM images were recorded and analyzed by T. Holzmann, TGA data and TEM data were performed by Willi Hoelle/Daniel Weber and Viola Duppel, respectively, and interpreted by T. Holzmann. B. V. Lotsch led the research and wrote parts of the paper. All authors analyzed and discussed the data.*

7.3 Deposited crystallographic data

Crystallographic data were deposited with the Fachinformationszentrum Karlsruhe (FIZ), Germany (fax: +49-7247-808-666, e-mail: crysdata@fiz-karlsruhe.de) and are available on quoting the respective CSD depository numbers.

Li_2SnS_3 ($C2/c$)	426848
Li_2SnS_3 ($R\bar{3}m$)	426849
$Li_{0.6}[Li_{0.2}Sn_{0.8}S_2]$ ($C2/m$)	42958

You can know the name of a bird in all the languages of the world, but when you're finished, you'll know absolutely nothing whatever about the bird. So let's look at the bird and see what it's doing – that's what counts. I learned very early the difference between knowing the name of something and knowing something.

— Richard P. Feynman